The University Of Sheffield.

Thesis for PHD

Optimisation of GaAsBi Based Semiconductors

Zhize Zhou

A thesis submitted for the degree of Doctor of Philosophy

Department of Electronic and Electrical Engineering

The University of Sheffield

March 2017

Content

Acknowledgement I
Abstract III
Chapter 1: Introduction 1
1. The major characteristics of GaAsBi 1
2. Valence band anti-crossing 2
3. Applications of GaAsBi 4
3.1. Light sources 4
3.2. Detectors 4
3.3. Heterojunction bipolar transistors 6
3.4. THz Devices 6
4. The lattice balanced GaAsBiN 7
5. Growth of Bismides and Bismuth as a surfactant 8
6. Bismuth as Dopants 8
7. Thesis organization 10
Chapter 2: Molecular Beam Epitaxy (MBE) technology 11
1. Concept 11
2. The structure of MBE system 11
2.1. Deposition chamber 12
2.2. Ultra-high vacuum system 13
2.3. Substrate holder 16
2.4. Beam generators, controllers and monitors 16
2.5. RHEED 17
2.6. System maintenance 21
3. Substrate preparation 21
4. Static phase investigation of GaAs surface 22
4.1. GaAs lattice structure 22
4.2. Surface structure at different RHEED patterns 23
4.3. Substrate surface temperature calibration 25
5. GaAs growth conditions 26
5.1. Growth rate 26
5.2. Growth temperature range 27
5.3. Ga flux rate 27
5.4. As flux rate calibration and adjustment 28

5.5. Dopants ... 29
6. Summary ... 29
Chapter 3: Technologies for investigating GaAsBi ... 31
1. X-ray Diffraction ... 31
2. Photoluminescence ... 33
2.1. Principle ... 33
2.2. Setup ... 35
3. Capacitance-Voltage and Current-Voltage measurement ... 36
3.1. Capacitance-Voltage ... 36
3.2. Current-Voltage ... 39
4. Photocurrent ... 40
5. Impact ionisation and avalanche multiplication ... 41
5.1. Impact ionisation ... 41
5.2. Avalanche multiplication ... 42
5.3. Photo-multiplication measurement ... 43
6. Summary ... 44
Chapter 4: Analysis for the MBE growth of GaAsBi material ... 45
1. Background study of Bismuth growth ... 45
2. Growth conditions for GaAsBi ... 45
3. Surface reconstructions of GaAsBi growth ... 48
4. The GaAsBi growth models ... 51
4.1. Lu's model ... 51
4.2. Lewis's model ... 52
4.3. Analysis of previous models ... 54
5. Summary ... 62
Chapter 5: Absorption Properties of GaAsBi Based p-i-n Heterojunction Diodes ... 62
1. Growth structure of GaAsBi samples ... 65
2. IVCV measurements ... 67
2.1. Capacitance-Voltage ... 67
2.2. Current-Voltage ... 69
3. Photocurrent measurements ... 71
3.1. Photoresponsivity and quantum efficiency ... 71
3.2. Absorption coefficient ... 73
3.3. Investigation of diffusion length at samples with thick i-region thickness ... 76
4. Summary ... 81
Chapter 6: The electrical and optical properties of p-i-n and n-i-p structure diodes ... 83

1. The structure and related analysis of PINs and NIPs ... 83
1.1. The analysis of the surface profile ... 84
1.2. X-ray diffraction results ... 90
1.3. Room temperature photoluminescence results ... 94
1.4. Capacitance-Voltage measurements ... 96
1.5. Current-voltage measurements ... 98
1.6. Low-temperature current-voltage behaviour ... 100
1.7. Photocurrent ... 102
2. Low-temperature photoluminescence ... 106
2.1. The investigation of the band-gap change with temperature ... 106
2.2. Experiment ... 111
3. Photo-multiplication behaviour ... 115
3.1. Background study of photo-multiplication ... 115
3.2. Multiplication behaviour of GaAs ... 117
3.3. Experimental Results ... 119
4. Summary ... 127
Chapter 7: Future plan ... 129
1. Sample growth ... 129
2. Photoluminescence measurements ... 129
3. Device fabrication ... 130
4. Measurements of device properties ... 130
Appendices ... 131
Appendix 1: Summary of previous GaAsBi samples grown by STM-MBE ... 131
Appendix 2: The theory of time resolved photoluminescence ... 132
Appendix 3: A simple way of calculating Capacitance ... 135
Appendix 4: Photocurrent Calculation ... 136
Appendix 5: Photo-multiplication results of STF8 and STFA series ... 141
Bibliography ... 1
Publications ... 13
Journals ... 13
Conferences ... 13

Acknowledgement

First I would like to thank Professor John David for his support and guidance throughout the project. Without him I would not have this nice study experience in England, and I would not accomplish this challenging doctoral task. Thanks are also due to Dr. Robert Richards, Thomas Rockett, and Yuchen Liu for all their help and for giving feedback on my work. During the research, Rob gave me most of the instructive advises. Tom provided me some GaAsBi samples with good qualities, and XRD and Nomaski measurements as well. Yuchen helped me a lot with the electrical and optical measurements. All three are such nice and easy going guys. We four spent a long time together in that small MBE room, trying to get more useful samples from the machine. I learnt quite a lot in that period, and I am really grateful of having those days with them.

I would like to thank other members of the small GaAsBi growth group. Faezah Harun did quite a lot of work on the photoluminescence measurements and device fabrications for the lab. Without her, I could not have so many devices with nice electrical and optical behaviours. Thanks also go to Danuta who gave me her legacy when she left where I have my first paper out of it. Chris Hunter's work gave me a clear instruction of doing photocurrent measurements. Yi Gu gave me his ideas of doing research, especially in the area of XRD and PL.

I would like to thank members of the Impact Ionisation Group. The first person I knew after John in Sheffield is Jingjing Xie, and she provided an accommodation for me. I spent a lot of time with Xiao Meng, Xinxin Zhou, Liang Qiao together. They warmed me, making me feel not lonely as I was studying and living in a foreign country. Aina and Cheong provided their hands on photo-multiplication measurements. Benjamin White helped me significantly on low temperature IV measurements. Besides, I established a nice friendship with Manuel, my first foreign friend.

I would like to thank everyone who I encountered and spent time with in Sheffield. The life would not be so colourful without you. I would thank Andy Jones for his friendship and helping with my English. He is such a nice person that I appreciated so much of knowing him. I would thank my roommates: Weigang Yang, Gang Luo, Sheng Liu, Wei Wang, etc. I would thank Jingxuan Zhu. It was a nice journey to be together with her. I would thank all the people whose names are not listed in this acknowledgement. The place is too small to put all my thanks.

I would like to thank my parents whose support is the most important power source for me to finish this program. I would like to thank all my friends. I would thank the life itself, which gave me these good and bad experiences, which made me grow up, which made me as now I am.

Abstract

GaAsBi has recently attracted much attention due to its large band gap reduction, a less temperature dependence of the band gap, and the giant spin orbiting properties. The large band gap reduction of GaAsBi is explained by valence band anti-crossing (VBAC) model. It has been proposed that a resonant energy state is introduced in the valence band, and the interaction between that state and the original valence states leads to a splitting of the valence band into two sub-bands and therefore a reduction of the band gap.

Molecular beam epitaxy (MBE) has been implemented to grow GaAsBi layers. Two growth conditions should be satisfied to get bismuth incorporated into GaAs: the growth temperature should be low enough (usually lower than 400 °C), and the As:Ga atomic flux ratio should be near stoichiometry. Four parameters can affect the final bismuth incorporation: growth rate, As:Ga atomic flux ratio, Bi:Ga atomic flux ratio, and growth temperature. The relationships have been investigated in the previous research, and also explored in this thesis.

Absorption properties are the key properties of an optoelectronic device. Through measuring the photoresponse of GaAsBi based p-i-n heterojunction devices, the absorption coefficient as a function of the incident light energy is obtained. The results reveal that the absorption coefficient follows the square law of the Tauc relation, which indicates that the material is a direct band gap material. The diffusion length is a combination of the lifetime and the mobility of carriers, and it is the diffusion length that directly reflects the performance of carrier transportation. Especially in a device which requires high absorption of photons such as a solar cell, a long diffusion length becomes even more important. In this thesis, a model has been established to calculate the diffusion length of GaAsBi based on the photocurrent measurements, and results show that the diffusion length is around 1 μm.

Photoluminescence (PL) measurements are used to decide the bismuth content based on the relation between the bismuth content and the band gap obtained from VBAC. Temperature dependence of the band gap of GaAsBi is also investigated using PL measurements. The s-shape of the PL peak position against the temperature reveals the existence of localized states. The source of localized states is claimed to be from bismuth clusters in some papers. Low temperature behaviours of GaAsBi have further been investigated using low temperature current-voltage measurements. It seems that the results also reflected the existence of localized states.

For low noise avalanche photodiodes (APDs), it is important that the electron-initiated and hole-initiated impact ionization coefficients α and β are very different in magnitude. Photo-multiplication measurements were taken in this thesis to investigate the impact ionization property of GaAsBi p-i-n and n-i-p diodes. A relatively large ionization coefficient ratio α/β for GaAsBi heterojunctions was obtained, which shows a promising use of GaAsBi as low-noise electron-initiated APDs.

Chapter 1: Introduction

1. The major characteristics of GaAsBi

The material $GaAs_{1-x}Bi_x$ has attracted much attention in recent years due to several advantages. The most important characteristic of GaAsBi is its large band gap reduction [1][2] via incorporating small fractions of bismuth (Bi), which allows absorption and emission of light at longer wavelengths than for GaAs. Incorporating Bi into GaAs leads to a decrease of the band gap by a linearized rate of ~84 meV/% Bi, which is much larger than ~16 meV/% of indium (In) and ~21 meV/% of antimony (Sb), and only lower than ~125 meV/% for alloying with nitrogen (N). However, since N alloying decreases the band gap by reducing the conduction band edge, incorporating nitrogen generally leads to degradation in electron mobility. In contrast, it is expected that using bismuth will maintain good electron transport properties, because the band gap is reduced by increasing the valence band maximum. The most acceptable mechanism used to explain the large band gap reduction, valence band anti-crossing model, will be introduced in the next section.

Another important characteristic of GaAsBi is the relatively insensitive band gap change with temperature, which was first proposed in [1]. The wavelength of the peak in the electro-luminescence (EL) spectra of GaAsBi was independent of temperature in the range of 100-300K while the GaAs peak shifted with temperature as expected [3]. The author of [1] claimed that this characteristic is possibly because of the combination of a semiconductor (GaAs) and a semimetal (GaBi), since semiconductors and semimetals have reverse temperature dependences. This effect has also been seen in InAsBi [4] and Titanium alloys [5]. However in [6], the author asserted that this characteristic may have less to do with the semi-metallic behaviour of GaBi. It is believed that Bi-cluster traps (localized states) behave as deep donors. Deep levels do not follow the change in the band edge when the temperature is changed, and when Bi incorporation reaches a reasonable level, the Bi impurity band from deep levels becomes the new valence band edge of GaAsBi. This assertion is subverted by [7], which claimed that Bi impurity band would majorly form from the isovalent resonant level below the valence band maximum. Until now, although several hypotheses have been proposed, the reason for the temperature independent behaviour of GaAsBi is still a mystery.

GaAsBi also has a giant spin-orbit bowing making it potentially suitable for spintronic applications [8][9]. Spintronics have been developed since the 1980s, when spin-dependent electron transportation was discovered [10]. The most important discovery and application in spintronics is giant magnetoresistance (GMR) [11][12][13], for which the 2007 Nobel Prize in Physics was awarded. The main application of GMR is magnetic field sensors which are used to read data in hard disk drives, biosensors, microelectromechanical systems (MEMS) and other devices. Spin-based

semiconductor usage was first reported on InAlAs [14]. With the discovery of giant spin-obit bowing on GaAsBi, it opens up the possibility of tailoring the spin-orbit splitting in semiconductors. Tunnel magnetoresistance (TMR) could be created using semiconductors as well, since the GaAsBi-insulator-GaAsBi structure could be realized using semiconductor growth techniques.

The incorporation of Bi into GaAs to form $GaAs_{1-x}Bi_x$ with $x > 10\%$ leads to a band structure in which the magnitude of the spin-orbit-splitting exceeds the band gap ($\Delta_{SO} > E_g$). This band structure condition offers the possibility to suppress the hot-hole-producing non-radiative CHSH Auger recombination pathway, a loss mechanism that strongly increases the threshold current and temperature sensitivity, which effects exist in conventional InP-based quantum well (QW) lasers operating at telecommunication wavelengths [15].

The major characteristics of GaAsBi have been introduced in the above paragraphs. In this chapter, more bismuth related research topics (not only GaAsBi) will be introduced as background information to give a more complete image of this material.

2. Valence band anti-crossing

The valence band anti-crossing (VBAC) model has been adopted to explain the large reduction of band gap with Bi incorporation [16][17], since a strong possibility of the existence of a Bi resonant state below the valence band maximum (VBM) has been indicated by theory. Although the Bi isovalent defect level was first calculated at 0.18 eV above the VBM [18], the calculation results in [7] showed that no Bi-bound states above VBM could exist, and only one resonant Bi level at 0.08 eV below VBM was found. Nowadays, the mainstream of the research results tend to support the latter.

The perturbation of the Bi isovalent resonant state would split the heavy-hole and light-hole valence bands near VBM into E_+ and E_- levels (as shown in Figure 1.1). In Figure 1.1, CB means conduction band, and HH, LH and SO are heavy-hole, light-hole and spin-orbit states respectively. The large band-gap reduction with Bi incorporation thus results from the upward motion of the heavy-hole and light-hole E_+ bands. Besides, the anti-crossing interaction of the Bi defect level with GaAs can also explain the shift in the spin-orbit splitting energy. The VBAC model described in [16] considered the perturbation of a Bi impurity to split the degenerate four Γ_8 primary and two Γ_7 spin-orbit states of host semiconductor (GaAs). Furthermore, the hole effective mass would be increased with the broadening of the heavy-hole E_+ band, and the impact ionisation coefficient of holes would therefore be suppressed, which will be discussed in Section 3, Chapter 6.

Figure 1.1 illustrates qualitatively the band structure change with Bi incorporation. Besides the normal introduced single Bi impurity level, Figure 1.1 also shows a possible interaction of Bi cluster states which lie above the valence band maximum. Hypotheses were proposed that these cluster states

are localized states which can be used to explain the temperature independence of GaAsBi. Detailed discussion about the influence of localized states can be found in Chapter 6, Section 2.

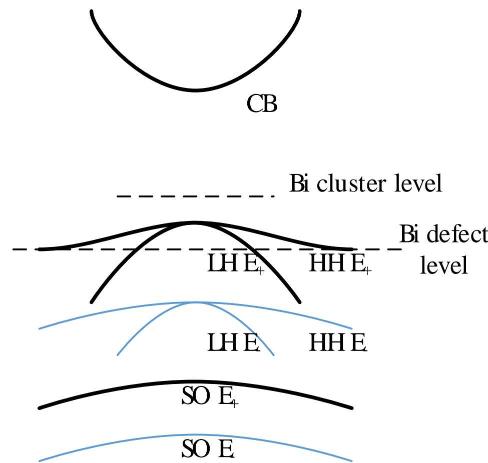

Figure 1.1. The diagram of band structure change with Bi incorporation (symbols are explained in the description of this figure)

A simplified equation was proposed assuming that the perturbation happens on the valence band edge, which was adapted from the band anti-crossing of GaAsN on the conduction band [19]. The band anti-crossing equation can be written as:

$$\begin{vmatrix} E - E_{Bi} & -V \\ -V & E - E_{VBM} \end{vmatrix} = 0 \tag{1.1}$$

where E_{Bi} is the energy of the localized state, E_{VBM} is the energy of VBM, and $V = C_{Bi}\sqrt{x}$ is the coupling between these two states according to [16]. C_A is a constant, and x is the fraction of Bi in GaAsBi. The band-gap change with bismuth incorporation calculated from equation 1.1 is shown in Figure 1.2.

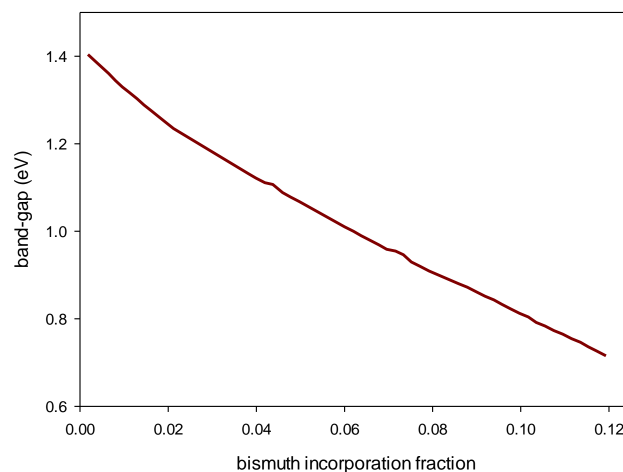

Figure 1.2. band-gap change with bismuth incorporation to GaAs, data adapted from [20]

3. Applications of GaAsBi

Based on the property of giant band-gap reduction in GaAsBi, the wavelength of photons which can be emitted or absorbed by the material can be increased to longer than 1 μm. In this case, GaAsBi usually works at near-infrared region (0.75-1.4 μm). Based on its properties (especially the large band gap reduction), GaAsBi is supposed to provide a wide range of exciting potential device applications, including IR light sources and detectors, high efficiency solar cells, spintronics, HBTs, THz sources and detectors, and thermoelectrics.

3.1. Light sources

Opto-devices can be divided into sources and detectors, which provide and absorb light respectively. On the source side, GaAsBi can be used to form the active region in light-emitting structures such as light-emitting diodes (LEDs) and lasers. The working principles of these devices can either be electro-luminescence (EL) or photo-luminescence (PL), which mechanism is introduced in Chapter 3.

When GaAsBi was first grown by MOVPE, the temperature independent character of the band gap of this material had already been discovered [1]. This property makes this material suitable for semiconductor lasers, since the emitted wavelength remains nearly constant with the variation of ambient temperature. An optically-pumped (PL implementation) GaAsBi laser has been reported in [21] and an electrically-pumped GaAsBi laser operating at room temperature has been demonstrated in [22].

LEDs do not require the same level of temperature stability as lasers do. GaAsBi layers have shown strong room temperature PL which makes it a good candidate for LED as well. Some results of the PL and EL characteristics of Bismide LEDs have been reported in [3].

3.2. Detectors

The applications of GaAsBi are mainly on the detector side. Photo-detectors are capable of converting light into electric current or voltage. They work in 2 working modes: photovoltaic mode and photoconductive mode, which are distinguished by the need for bias voltage or not on the device. Solar cells are used to generate power from sunlight. A typical solar cell, which is usually a large area photodiode, works in photovoltaic mode, since it generates electric solar power without any voltage bias.

The dramatic bandgap reduction [2] makes GaAsBi a good candidate material for tandem solar cells [23]. A tandem solar cell is consisted of multi-junctions with different semiconductor materials. Since different materials would have different optical properties of sunlight absorption, each junction can be adjusted to capture a portion of the solar spectrum, and reduces the wasted energy. The potential efficiency of a triple-junction InGaP/GaAs/Ge solar cell could be increased by adding a

fourth junction with a 1 eV band gap using GaAsBi [24]. In this case, the photonic behaviour of GaAsBi layers becomes interesting, especially the shift of photoresponsivity and absorption coefficient when bismuth is incorporated into GaAs [25]. A quadruple-junction solar cell with GaAsBi was patented in 2003 [26], which structure is shown in Figure 1.3. Boron is co-doped with bismuth into GaAs to make the material latticed matched to GaAs.

Optical Window
AlInP
n
GaInP (1.90 eV) p
AlGaInP p
p++
n++
GaInP n
n
GaAs (1.42 eV) p
p
p++
n++
GaAs:Bi:B n
n
GaAs:Bi:B (1.05 eV) p
GaAs:Bi:B p
p++
n++
n
Ge Substrate (0.67 eV) p
Back Contact

Figure 1.3. A structure of Tandem Solar Cell with inserting a GaAsBiB junction to absorb sunlight at ~1.05 eV.

When a photodiode is working at photoconductive mode, a reverse bias voltage is added, and the electrical conductivity changes as a function of the intensity of the incident light. This is usually required for high sensitivity and high speed of response, which are two key parameters for telecommunication photodetector design. Furthermore, avalanche photodiodes (APDs) have the advantage of higher sensitivity over conventional p-i-n photodiodes by providing an internal gain through impact ionisation process. A large difference between the electron and hole impact ionisation coefficients (α and β) is important to produce low noise and high quality APDs, which will be introduced in Section 3, Chapter 6. Since the Bi resonant states would only affect the valence band, it has a high probability that incorporating Bi into GaAs would change β significantly and thus lead to a large difference between α and β. In this case, GaAsBi might also be a good candidate for making APDs.

3.3. Heterojunction bipolar transistors

A heterojunction bipolar transistor (HBT) is a bipolar transistor with its emitter made of a semiconductor material with a wider band gap than its base material. A high injection efficiency of electrons would therefore be achieved even when the base layer has an impurity concentration higher than the emitter layer. Based on this, HBTs are regarded as excellent devices which achieve fast operation and high breakdown voltage. One of the implementations of HBTs is to be used as power amplifiers in mobile phones due to high current drive capability, and the low threshold could significantly reduce power consumption.

The hole mobility in GaAsBi has been found to decrease with increasing Bi-content due to the interaction of Bi on the valence band [27]. In the contrast, Bi is not found to strongly affect the electron mobility as N does [28]. Due to the large band gap reduction with the Bi incorporation by increasing VBM combined with the little effect on electron mobility and conduction band alignment, GaAsBi becomes a suitable material for low threshold voltage HBTs. An HBT using GaAsBi as the base layer has been patented in 2006 [29], which structure is shown in Figure 1.4.

Layer	Doping
InGaAs (collector)	n++
GaAs	n-
InGaP	n-
GaAsBi (base)	p+
GaAs	n-
GaAs (emitter)	n+
GaAs Substrate	

Figure 1.4. A HBT structure using GaAsBi as the base layer.

3.4. THz Devices

Conventional semiconductors have long carrier recombination times (in the nanosecond range), which impede their usage for ultrafast photo-response. In order to get fast response to photons (e.g. terahertz), GaAs layers has been deliberately grown at low temperature. The carrier lifetime of low growth temperature (LGT) layers can be as short as sub-100-fs, and high resistivity of the layers is also obtained. LGT-GaAs is therefore useful for the fast photoconductive semiconductor switches (PCSSs) used to generate and detect THz radiation. However, the non-adjustable band gap of GaAs (at ~ 1.42 eV) limits its application at longer wavelengths (1-1.5 μm). LGT-InGaAs was grown to work in the longer wavelength region as a replacement of GaAs [30]. However, unfortunately not only its shortest carrier lifetimes are only ~ 2 ps, but also its resistivity is low.

GaAsBi might be suitable for such a high frequency application working at longer wavelength as mentioned in [31]. The GaAsBi layers grown at extremely low temperature (<280 °C) can get a carrier lifetime less than 1 ps. Besides, GaAsBi photoconductive switches can be pumped with a wider range of laser sources due to its band gap reduction. A GaAsBi THz source which is designed to be pumped by sources operating at wavelengths shorter than 1030 nm with emission bandwidth up to 5 THz is commercially available in Ekspla, a Lithuanian optoelectronics company. Especially, this GaAsBi THz source from Ekspla reveals the first commercial usage of this material, inspiring researchers to put more effort on excavating its industrial possibilities.

4. The lattice balanced GaAsBiN

Although GaAsBi can largely reduce the band gap, the lattice constant of GaAsBi varies with Bi content through Bi incorporation. The lattice mismatch of GaAsBi with 4.5% Bi from GaAs is between 0.45-0.89% according to [32]. Lattice mismatch will cause strained or relaxed GaAsBi layer when growing GaAsBi on GaAs, leading to interfacial defects which reduce electron mobility, carrier concentration and optical efficiency. Detailed discussion of lattice mismatch of GaAsBi/GaAs can be found in Section 1, Chapter 6.

The co-doped GaAsBiN has been proposed to compensate for the lattice mismatch [6], and realized by MBE [33–35]. The small size of N substituting for As on the group V sublattice can be balanced by the large size of Bi substituting on the same sublattice in GaAs. This facilitates coherent epitaxial growth of the isoelectronically co-doped GaAsBiN alloy on GaAs substrates. Besides, GaAsBiN is claimed to have the advantage which offers a wider scope of band structure design, since N mainly influences the conduction band whereas Bi influences the valence band [6].

The lattice constants of GaBi and GaN have been calculated in [18] as 6.324Å and 4.488Å respectively. Since the lattice constant of GaAs is 5.653Å, the lattice mismatches are approximately 12% and -20.4% for GaBi and GaN respectively. According to Vegard's Law [36], The lattice constant of $GaAs_{1-x-y}Bi_yN_x$ is given by:

$$a = (1 - x - y)a_{GaAs} + xa_{GaN} + ya_{GaBi} \tag{1.2}$$

In this case, if the quaternary alloy is lattice matched with GaAs, $y = 1.7x$. The author of [18] also calculated the bowing coefficient of band gap, and found that 5.6% of N and 9.5% of Bi should be incorporated to get a 1 eV bandgap which can be used in tandem solar cells. This result is not very encouraging, since on the contrary, only 5% Bi incorporation is needed to reach the goal of 1 eV for GaAsBi.

5. Growth of Bismides and Bismuth as a surfactant

Metal-Organic Vapour Phase Epitaxy (MOVPE) was first used to grow GaAsBi samples in 1998 [1]. After that, a significant amount of investigations of GaAsBi growth have been moved to Molecular Beam Epitaxy (MBE) after the first successful MBE growth in 2003 [2]. In this thesis, we use MBE to grow GaAsBi layers. The MBE growth technique, as one of the most important topics in this thesis, will be discussed in detail in Chapter 2 and 4.

It has been found that bismuth is hard to incorporate into layers during normal growth conditions [37][2]. Instead, the bismuth atoms would rather remain on the surface. This characteristic of bismuth makes it a good candidate to act as a surfactant. Introducing a surfactant can sometimes dramatically reduce the defects, especially those caused by the strain at the interface of the heterojunction. The adatom diffusion is believed to be enhanced by the presence of Bi on the surface, possibly due to the interface energy reduction between the semiconductor surface and the vacuum.

Bismuth was first used as a surfactant in Ge/Si/Ge heterojunctions [37][38], before being used in InGaAs[39], InGaAsN and GaAsN [40][41], and BGaAs [42] growth on GaAs substrates. According to the results in [40], the surface roughness of GaNAs was reduced by an order of magnitude, and thus the PL intensity was increased by more than two times compared with the surfactant-free samples.

When Bi works as a surfactant, a metallic layer would be formed on the surface, and the coverage depends on the Bi flux [41] which follows the Langmuir isotherm [43]:

$$\theta_{Bi} = \frac{bF_{Bi}}{1+bF_{Bi}} \tag{1.3}$$

where θ_{Bi} is the fraction of bismuth metallic layer covered on the surface, and F_{Bi} is the flux rate of bismuth. b is a fitting parameter, and the calculation of b has been given in [41]. The author used the RHEED intensity as a reference for the Bi coverage, and assumed that the intensity is proportional to the Bi coverage.

The existence of the metallic layer was also indirectly proven in [44] by testing the resistance of the (2×1) surface layer with scanning tunnelling microscope (more information can be found in Section 3, Chapter 4 in this thesis). This theoretical explanation of the working mechanism of Bi as a surfactant also provides a possible explanation of Bi incorporation mechanism, which is discussed in detail in Section 4, Chapter 4.

6. Bismuth as Dopants

Even though supplying a Bi flux during growth can enhance surface migration of the constituent atoms and result in a lower density of As and/or Ga related defects [45] due to the surfactant function,

the doping density of pure GaAsBi would still reach a level around 10^{16} cm^{-3} because of the low growth temperature.

How bismuth acts as a dopant has been widely investigated [47–49]. Bi incorporation is an isovalent atomic substitution process (Bi atoms replace As atoms Bi_{As}). Isovalent atoms may act as impurities [49]. For example, if a P atom is replaced by a much less electronegative Bi atom in GaP, the Bi would give rise to a tightly bound hole and a weakly bound electron. Thus Bi is an isovalent donor in GaP. However in the meantime, far-infrared (FIR) absorption measurements have revealed the presence of acceptor states related to Bi exclusively in the low-concentration "anomalous" region [48].

Another possible way of introducing doping is by forming anion hetero-antisites (Bi_{Ga}, i.e. Bi replaces Ga site), which has been discovered in GaAsBi [46]. In this case, Bi behaves as a strong donor. Magnetic circular dichroism (MCD) is used to find the antisites [46]. MCD is a phenomenon that left and right circularly polarized (LCP and RCP) light would have different absorption coefficients in a material when a strong magnetic field which is oriented parallel to the direction of light propagation is implemented on that material. Its working principle is similar to electron spin resonance (ESR), which is a technique for studying materials with unpaired electrons. If an external magnetic field is supplied, the spin nature of electrons causes them to split into two states (parallel and antiparallel) with an energy difference of $g_e \mu_B B_0$, due to the Zeeman effect. If multi-wavelength photons (e.g. white light) are incident on the sample, photons with energy $hv = g_e \mu_B B_0$ would be absorbed.

In conclusion, the possibility of Bi multivalency and multisite occupancy would enable four different impurity configurations: isovalent impurity as donor or double accepter for Bi_{As} or isovalent impurity as donor or double donor for Bi_{Ga} [47]. According to [47], Bi_{Ga} is very rare in GaAsBi layers (less than 5%). Besides, whether Bi atoms act as an acceptor or donor is unfortunately still under discussion. In this thesis, the doping type of Bi was investigated by observing the absorption behaviour under partially depleted GaAs/GaAsBi/GaAs p-i-n diodes, and the results are recorded in Chapter 5.

Usually the perturbation caused by doping (such as Be and Si to GaAs) to the host lattice is small and produces an energetically shallow and delocalized state that remains unnoticeable. However, since Bi and As atoms have distinct characteristics (large difference in atomic size and core potential), the perturbation becomes important. The state would trap a charge carrier (become localized) via a short-range potential [50], and the properties of the host semiconductor would be altered significantly.

As the binding energy increases, the localization of the carrier becomes important and its interaction with lattice vibrations becomes stronger. So when the temperature is low, the luminescence of localized centres becomes power dependent. Localized states quickly ionize as

temperature increases. At 300 K, the luminescence is insensitive to excitation intensity, indicating that all Bi-related bound states are ionized.

7. Thesis organization

The first 3 chapters are about the background information in this research area. In this chapter, the major characteristics of GaAsBi were introduced, and several interesting bismuth related research topics were provided as background information of this thesis. Most importantly, several possible applications of GaAsBi were introduced which revealed its potential industrial value. In Chapter 2, MBE, the growth technique for GaAsBi layers, will be introduced in detail. The techniques of measuring the optical and electrical properties of GaAsBi will be introduced in Chapter 3.

Chapter 4 is mainly about the work on MBE, and a growth model is established as an attempt to investigate the Bi content under different growth conditions. The optical properties of GaAsBi, especially the absorption properties, are investigated in Chapter 5. Chapter 6 includes several different research aspects, such as the PL and dark current behaviours with the change of temperature, and the photo-multiplication behaviour which shows a good potential of GaAsBi for making avalanche photo diodes.

The further investigation work which could be done in the future is presented in Chapter 7.

Chapter 2: Molecular Beam Epitaxy (MBE) technology

1. Concept

As mentioned in Chapter 1, Section 5, molecular beam epitaxy (MBE) has become a major technique for the growth of GaAsBi for a long time. A whole chapter here is to introduce MBE in detail, not only because it is the growth technique adopted in this thesis to grow GaAsBi, but also it is a very important research topic through this thesis.

MBE is an epitaxial growth process. The name MBE was first used in 1970 [51]. During epitaxy, one or more beams of atoms or molecules evaporated thermally from sources interact on a heated crystalline substrate to produce a single-crystal layer.

MBE distinguishes itself from previous vacuum evaporation techniques (e.g. liquid phase epitaxy, sputtering, metalorganic vapour phase epitaxy) with two aspects. First, the deposition in MBE is under ultrahigh-vacuum (UHV) conditions (idle pressure $<10^{-10}$ mBar), which is essential to get a high quality growth layer. Second, substrate surface temperature and flux rates (arrival rate of beam atoms or molecules onto the substrate surface) are critical and should be controlled precisely during growth.

Due to the precise controlling of growth temperature and flux rates for MBE growth, the composition and structure of the growth layer can be predicted more easily. This makes MBE a powerful growth technique for scientific research on new materials.

2. The structure of MBE system

The design criteria of MBE system are generally based on three principles. First, it should of course be managed to generate molecular beams for growth. Second, the growth environment should be under ultrahigh vacuum to make sure that less impurities are incorporated. Third, the growth process should better be observed, in which case the growth results can be predictable, and the procedure can thus be improved.

The industrial implementation of MBE growth usually requires high sample throughput, but the ultraclean environment makes the requirement hard to achieve. To satisfy these two conflicting requirements, an MBE system is usually designed to comprise multiple chambers. Buffer chambers with less rigorous vacuum conditions are used to allow samples to be transferred into the growth chamber without exposing the samples to atmosphere. Besides, chambers are usually made with stainless steel, and separated by gate valves.

The fast entry lock (FEL) is one of the buffer chambers, through which samples are introduced from atmosphere into the machine. It works under medium high vacuum (10^{-6}~10^{-7} mBar). Usually a

separate UHV buffer chamber is adopted by most modern MBE systems between the FEL and the growth environment. Sample preparation (e.g., outgassing) can be done in this chamber. The most important chamber in MBE is the main chamber (also called the growth chamber, or the deposition chamber), which is used for the epitaxy of materials. The deposition chamber will be introduced in the following section in detail.

MBE machine used in this work is a small Omicron MBE-STM (scanning tunnelling microscope) reactor, which only has an FEL and a main chamber, with the sample preparation done in the main chamber. Figure 2.1 shows a general schematic plot of our MBE system. A photo of our MBE-STM machine is shown in Figure 2.2 (in the next page).

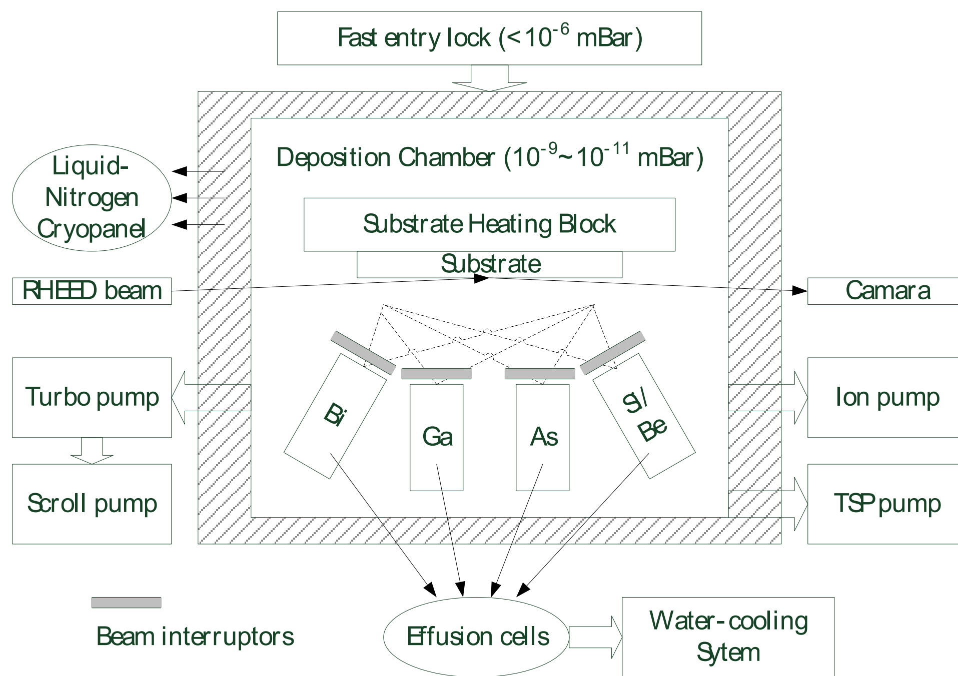

Figure 2.1. Schematic plot of Omicron MBE system

Sample transfer between chambers is usually realized in two ways: to use a direct mechanically coupled drive with remote levers, or a magnetically coupled transfer arm. In our machine, a latter one is used to load samples.

2.1. Deposition chamber

The deposition chamber as the most important part of an MBE system, as the name it is, is used to grow materials. As shown in Figure 2.1, the main systems in the deposition chamber are substrate holder, beam generators, beam controls, ultra-high vacuum system and monitors. Details of the components of each system in our machine can be found in Table 2.1, and each system would be introduced in the following several parts.

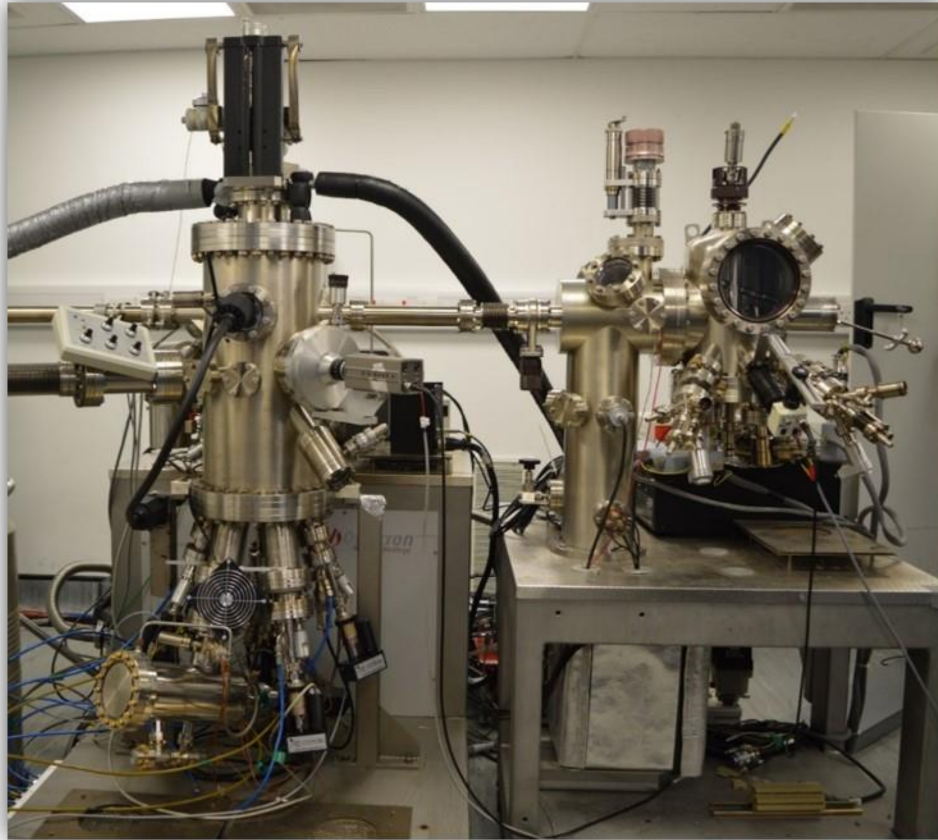

Figure 2.2. A photo of Omicron MBE-STM machine

Table 2.1. The components of systems in the deposition chamber

Systems	Components	Functions
Ultra-high vacuum system	Various pumps Liquid-nitrogen cryopanel	To provide ultra-clean growth environment
Substrate holder	Sample heater Thermocouple	To adjust position and change surface temperature of samples
Beam generators	Knudsen cells Dissociation cells	To generate atomic or molecular beams
Beam controls	Fast-action shutters As cracker	To control the beam flux between source and substrate
Beam and growth monitors	RHEED Ion gauge Spectrometer	To monitor the growth environment

2.2. Ultra-high vacuum system

To provide an ultra-clean growth environment in the deposition chamber, primary and secondary pumping stages are used to form the whole ultra-high vacuum system. Primary pumping is used to ensure that the whole deposition chamber is at ultra-high vacuum (<10^{-10} mBar). Secondary pumping

surrounding the growth region is used to make sure that the residual gas levels are low (<10^{-11} mBar) in the growth region. The pumps commonly used in the two pumping stages and their pumping abilities are listed in Table 2.2.

Table 2.2. Pumps used in MBE

Methods	**Function**	**Pressure (mBar)**	**In our chamber**
Sorption pump	Prepump of Ion pump	10^{-7}-10^{-2}	
Scroll pump	Backing Turbo pump	<10^{-1}	Yes
Rotary vane pump	Backing Diffusion pump	10^{-6}	
Ion pump	Primary pump	<10^{-10}	Yes
Turbo-molecular pump		10^{-10}-10^{-4}	Yes
Diffusion pump		<10^{-9}	
Helium cryo-pump			
LN2 cryo-panel	Secondary pump	<10^{-11}	Yes
TSP			Yes

A combination of ion and sorption pumps is commonly used in the standard MBE primary pumping stage. The other optional pumps can be turbo-molecular pumps, oil diffusion pumps, or helium cryopumps. In our machine, a turbo-molecular pump works together with an ion pump as the primary pumping stage.

A secondary pumping system is essential to get high quality thin films in MBE systems, especially since most of the group V elements would condense on secondary pumping panels. The secondary pumping stage in our machine comprises a liquid-nitrogen cryopanel together with a titanium sublimation pump (TSP). The pumps used in our machine will be introduced in detail below, and the pressure of ~ 2×10^{-9} mBar is achieved.

Turbo-molecular pump and scroll pump

In a turbo-molecular pump, rotor/stator pairs are stacked to compose a multi-stage structure [52]. The turbine rotors spin rapidly during operation, while the stators maintain static. In this case, gas molecules from the deposition chamber or the above stator channels (shown in Figure 2.3) would be transported into the next stator channels by the spinning of rotor blades. Through this process, the captured gas is compressed from the chamber to exhaust, and finally reaches the pressure level of the scroll pump.

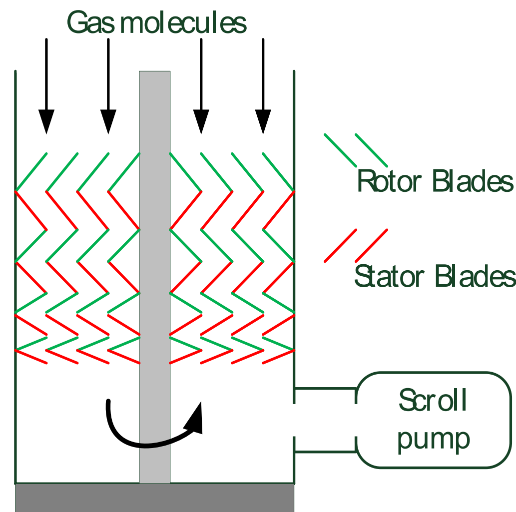

Figure 2.3. The structure of turbo pump

The scroll pump is usually used as a backing pump for the turbo-molecular pump. A typical scroll pump uses two interleaving scrolls with one of them being fixed. The other one orbits eccentrically without rotating, thereby trapping and pumping pockets of gas between the scrolls [53].

Ion pump

The ion pump is the major primary pump in our MBE machine. An ion pump uses the anode of a Penning trap to temporarily store electrons generated by an electric discharge [54]. Gas atoms and molecules would be ionized by the electrons when they come into the pump from the deposition chamber. The resultant ions are then accelerated by a strong electrical potential (typically 3 kV to 7 kV) to strike a chemically active cathode (usually titanium). After collision with the cathode, either the accelerated ions would be buried to the cathode, or cathode material would be sputtered onto the walls by the ions. Besides, the chamber can be further cleaned by freshly sputtered material, since they can act as a getter of gas by chemisorption and physisorption.

Liquid-nitrogen cryopanel

As a part of the secondary pumping system, a liquid-nitrogen (LN_2) cryopanel surrounds all the beam sources and the growth environment to minimize unintentional impurity incorporation to the growth layers from the residual background. The larger the area and the more complete the enclosure around the sources and the substrate, the more effective the cryopanel is in removing any background contaminants.

With the surrounding of the cryopanel, impurities would collide with the panel at least once before they get to the growth environment. During collision, impurities tend to stick to the panel surface due to the rapid loss of their thermal momentum. However, the impurity absorbing ability of the LN_2 cryopanel varies with different types of gas molecules because of their different freezing and boiling points.

Titanium sublimation pump

Titanium sublimation pump (TSP) is another part of the secondary pumping state in our MBE chamber. The core component of a TSP is a titanium filament with a high current (typically around 40 A) periodically passed through it. Titanium would then be thermally sublimated from the filament to the surrounding walls by the heat generated from the high current. When the residual gas molecules collide with the sublimated titanium, they are likely to react and form a stable, solid product on the walls, since the titanium is very reactive. Similar to the LN2 cryopanel, the gas sorption ability of the TSP depends on the reactivity of residual gas [55].

2.3. Substrate holder

The substrate holder can help to adjust the substrate position and temperature. The holder itself is a refractory metal block (usually Molybdenum). The heater element used to adjust the substrate temperature is usually manufactured from high purity Tantalum, and thermocouple is used to measure the substrate temperature. The sample can be heated either resistively or radiatively (used in our machine). Usually, the substrate holder provides the function of substrate rotation [56], in order to make sure the growth on the whole substrate surface is uniform. The substrate rotation function is not available in our MBE-STM machine, partly because the sample holder itself is very small, in which case the variation of fluxes can be ignored.

2.4. Beam generators, controllers and monitors

In MBE systems, various kinds of beam sources are used to generate different kinds of material beams in the chamber. Each source is separated from the others by a cryo-baffle (cooled by water in our machine), to reduce chemical and thermal interaction. Material sources can be mounted vertically or semi-horizontally to the chamber. Modern machines mostly use semi-horizontal mounting, reducing the risk of flakes of condensed matter falling into the sources and causing contamination. Unfortunately, vertically mounted sources are used in our small Omicron machine.

In our MBE-STM machine, all the beam sources are Knudsen effusion cells [57]–[61] apart from the arsenic cell (dissociation cell). In a Knudsen cell, an inert crucible is used to contain solid or liquid source material. The crucible is heated by radiation from a heater, and a thermocouple is used to provide temperature feedback. The heater can either be a filament wound around the crucible, or a foil covering the entire crucible.

For Knudsen effusion cells, beams are generated thermally. In most Knudsen cells, the only factor that can determine the flux rate is the cell temperature. Under ideal conditions, the flux rate from a Knudsen cell can be calculated accurately using following equation [51].

$$J = 1.118\times10^{22}\frac{pA}{l^2\left(MT\right)^{1/2}}\ \text{molecules}\cdot\text{cm}^{-2}\cdot\text{s}^{-1} \tag{2.1}$$

Here, J is the flux rate, the number of molecules per second striking the substrate per unit area, p is the pressure in the cell, A is the area of the aperture of the cell, l is the distance from the aperture to the substrate, M is the molecular weight, and T is the absolute temperature of the cell.

A dissociation cell is a modified version of a Knudsen cell. The effusion beam is evaporated directly from a conventional Knudsen crucible, but a dissociation part with higher temperature covers the channel between beam source and substrate as a 'cracker' to break molecules into smaller parts. These sources are used for the group V materials, including arsenic and phosphorus. In our machine, a dissociation cell is used as an arsenic cracker.

The temperatures for efficient cracking of arsenic tetramers to dimers have been calibrated using mass spectroscopy in [51] (see Figure 2.4). The typical temperature for 100% cracking is between 800-1000 °C. In reality, the cracking temperature varies depending on the conditions in the machine. In our lab, 1000 °C is used to break As_4 into As_2, and 650 °C is the temperature to maintain As_4 without cracking.

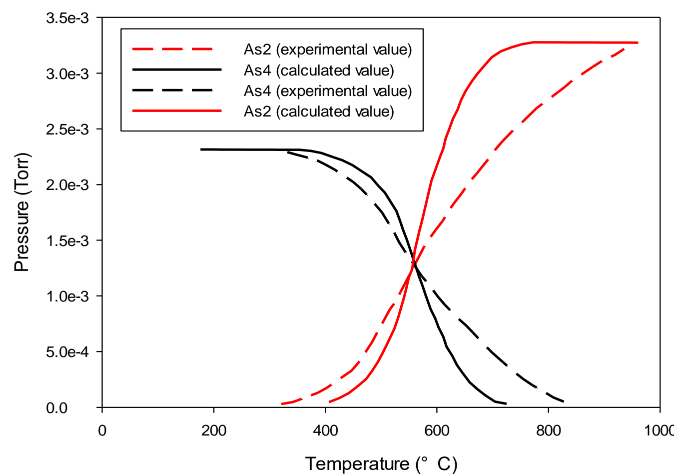

Figure 2.4. As_2 and As_4 composition with Arsenic cracker temperature, adapted from [51]

Usually, beam interrupters are only used to allow or block the beams passing through to the substrate surface. As such the flux rate of beams cannot be tuned by most beam interrupters. However, for precise control of the arsenic flux rate, an adjustable arsenic cracker valve is used in our machine.

Though the ideal flux rate as a function of temperature can be obtained from Equation 2.1, real Knudsen cells don't obey the ideal case in practise. In order to monitor the environment and growth situation, the movable ion gauge (MIG) is used to measure the chamber pressure. Besides, ion gauges are also frequently used as a beam monitor to observe and measure the real beam flux rate.

2.5. RHEED

Besides ion gauge, Reflection high-energy electron diffraction (RHEED) is another part of the monitor system in MBE. RHEED is commonly used in MBE system to observe the atomic

reconstructions of substrate surfaces [62], and it can also indirectly reflects the growth conditions on the surface of substrates. On an ultra-clean and smooth substrate surface, atoms reorder themselves to produce a periodicity different from that of the underlying crystal, which is known as a surface reconstruction. During growth, substrate surface structure due to reconstruction varies with flux rates of different material species and substrate temperature. Observing and understanding the surface structure variations based on surface physics is the most important part of MBE research and can considerably help to prepare high-quality thin films, and this can be done by RHEED. Due to the importance of RHEED, an independent part in this thesis is consumed to introduce this unique technique.

In RHEED, an electron beam is generated and accelerated in a strong electric field to an energy in the scale of 10-30 keV [63], and then strikes the crystal surface at a glancing angle of 1-2°. In this case, the electrons in the beam only have sufficient momentum to penetrate the substrate for 1-2 atomic layers below the surface. The electrons are then diffracted by the surface, and interfere with each other to form a diffraction pattern. The reconstruction pattern is usually observed using a camera.

In RHEED, electrons can be scattered elastically (without losing any energy). The elastic scattering leads to high intensity spots in the RHEED pattern at points where the diffracted electrons are in phase, in accordance with the Bragg's law [64]. At these points, the following relationship in reciprocal space is satisfied:

$$\vec{k}_f = \vec{k}_i + \vec{G} \tag{2.2}$$

Where $\boldsymbol{k}_i$ is the wave-vector of the incident beam, $\boldsymbol{k}_f$ is the wave-vector of the diffracted beam. $\boldsymbol{G}$ is a reciprocal lattice vector. With elastic scattering:

$$\left|\vec{k}_i\right| = \left|\vec{k}_f\right| = \frac{2\pi}{\lambda} \tag{2.3}$$

We define $\boldsymbol{G}=a\boldsymbol{i}+b\boldsymbol{j}+c\boldsymbol{k}$, where $\boldsymbol{i}, \boldsymbol{j}, \boldsymbol{k}$ are primitive vectors of the reciprocal lattice. If we assume that $\boldsymbol{k}$ is perpendicular to the surface, a, b should be integers, but c can be any real number. The component of diffraction perpendicular to the surface is barely influenced by the lattice since the scattering happens only in the first atomic layers of the surface.

If we consider all the possible values of $\boldsymbol{G}$, they form an orderly set of rods in reciprocal space. According to Equation 2.2, the possible values of $\boldsymbol{k}_f$ should also form a set of rods offset from $\boldsymbol{G}$ by $\boldsymbol{k}_i$.

Within the condition of Equation 2.3, the possible values of $\boldsymbol{k}_f$ form a sphere with the radius $2\pi/\lambda$, which was first proposed by Ewald [65]. In this case, the wave-vector of the diffracted beam is constrained both by the Ewald Sphere and the reciprocal rods. Figure 2.5 shows one set of rods with different a values (x-axis) and the same b values (y-axis). The spots on the RHEED screen form an

arc. Since there are also rods with different values of *b*, in reality, we must see several arcs on the screen.

When *a*, *b* are both 0, the beam is reflected by the surface, and the corresponding spot on the RHEED screen is defined as the specular spot or 0-order spot.

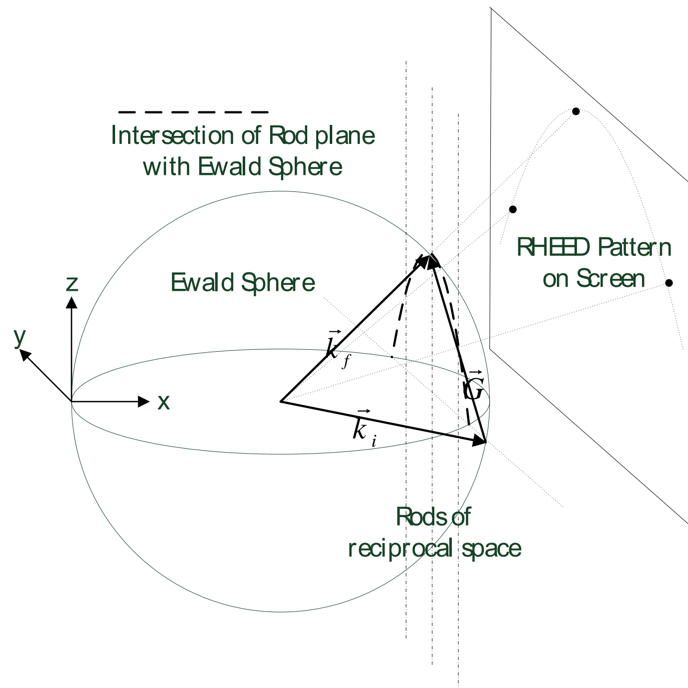

Figure 2.5. The working principle of RHEED

The wavelength of the electrons in RHEED can be calculated with the following steps. It is well known that $\lambda=h/p$. Here λ is the wavelength, h is Planck's constant, and p is the momentum of the electrons. The momentum is given by $p=(2mE)^{1/2}$, m is electron mass, and E is electron energy. Since the electron energy of RHEED is around 20keV, the wavelength is around 0.085 Å. The lattice constant of GaAs is 5.6533 Å [66], so in reciprocal space, the length of the wave-vector of the incident beam is 50-100 times longer than the reciprocal lattice constant. A simulated RHEED pattern of a simple cubic lattice structure is shown in Figure 2.6 with rotations of the sample surface. A typical RHEED image in our lab which presents the 4× part of a (2×4) pattern of GaAs surface reconstruction is shown in Figure 2.7. The surface reconstruction of GaAs will be discussed in 4.2 of this chapter.

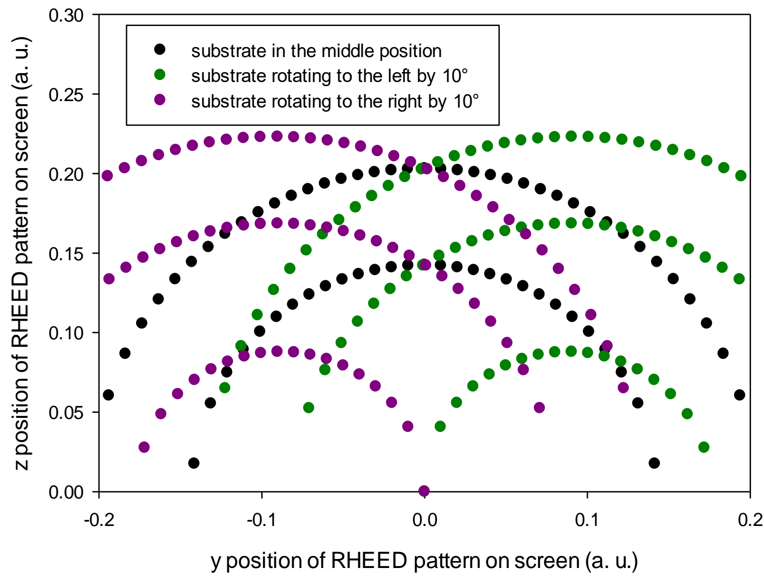

Figure 2.6. Simulation of RHEED patterns of a simple cubic lattice structure at different sample angles

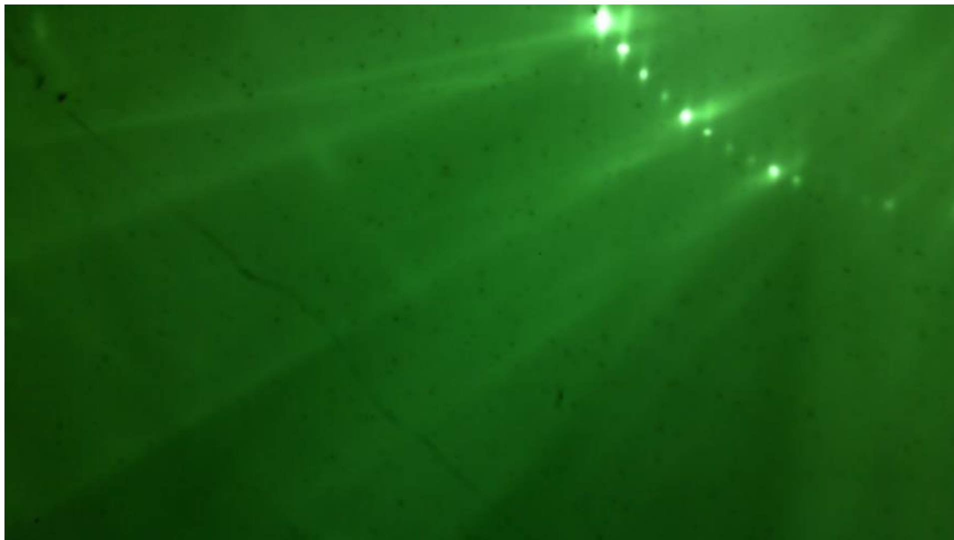

Figure 2.7. An image of RHEED pattern illustrating 4× part of (2×4) pattern of GaAs surface

RHEED is very important in MBE because it yields information about the substrate surface. Typically RHEED can be used to monitor the thermal cleaning of a substrate surface before growth. It can also tell us about the growth conditions such as the growth rate and the growth temperature, which will be introduced later. Furthermore, it can monitor changes on the substrate surface during growth if the growth environment changes, and the quality of the substrate surface can also be inferred.

2.6. System maintenance

An ultra-clean growth environment is the only prerequisite for MBE before sample growth. To realize this requirement, an MBE system should be baked rigorously after it is exposed to atmosphere to maintain a good vacuum in the chamber, and material sources should be outgassed thoroughly to make sure that the source materials are ultra-clean.

Baking procedures vary from laboratory to laboratory [67–69]. The goal of baking is to reduce the amount of residual gases, which comprise mainly H_2O, N_2, CO, CO_2 and H_2 [70]. A typical baking temperature for the system is about 150 °C - 250 °C. In this case, all system components should be manufactured with refractory materials to withstand at least 200 °C. Pressures of lower than 5×10^{-11} mBar can be routinely achieved after bake-out, and system pressures can often be below the x-ray limit of the ion gauge ($\leq 3\times10^{-11}$ mBar). Extensive baking of the system (72 hours at 200 °C) is essential for the growth of high-purity GaAs ($N_A - N_D < 10^{14}$ cm^{-3}) [67]. However, it is better not to bake the system longer than 5 days for routine maintenance, in order to prolong the lifetime of the system [70]. Our machine is usually baked for 2-3 days at 150 °C, and a background pressure below 10^{-9} mBar is achieved.

Knudsen crucibles are designed to work at the temperature at least up to 1400 °C, and it is possible to outgas the crucibles shortly at a temperature as high as 1600 °C [51]. If the material in a crucible is depleted, the crucible should be outgassed at a temperature of 1400 °C - 1600 °C before being refilled and reinstalled to the chamber. For regular use of cells, when they have been cooled down and brought back to operating, they should first be outgassed at a temperature at least 25 °C higher than the operating temperature (usually 50-100 °C) for half an hour. However, it is not suitable for the Group V cells (e.g., Arsenic), since they deplete rapidly at high temperatures.

3. Substrate preparation

Substrate preparation is an essential part of successful MBE growth. It can usually be divided into 3 processes: chemical treatment, layer outgas, and oxide removal.

Chemical treatment

Ex-situ chemical treatments are used to produce a metallic and organic free surface protected by oxide before the substrate is loaded into the chamber [51]. Usually the sample is first polished by acetone, propan-2-ol and methanol. Then the substrate is etched by a mixture of H_2SO_4:H_2O_2:H_2O to oxidize the surface, which can also help to eliminate damage caused by polishing [71]. The oxide layer has a very low carbon sticking coefficient, and can be easily desorbed in-situ [72].

In our lab, we buy pre-treated GaAs (001) substrates, and cleave them into 11.4 mm × 11.8 mm pieces to fit the sample holder. N-butyl acetate is used to clean the surface again after cleaving to

remove any dust on it. The vendor of the substrates is wafer technology, a UK based producer of III-V materials and epitaxy-ready substrates.

Outgas layer

After chemical treatment, the substrate is loaded into the MBE system via the FEL. The substrate is then heated to ~400 °C for 10-15 mins. This initial outgassing of sample (and also the sample holder) is done to evaporate water and other volatile contaminants.

Oxide Removal

For silicon, Ion sputtering is used to remove the oxide from surfaces in combination with annealing. However, this method is not used in III-V compounds, first because the oxide is easier to remove than on silicon surfaces, and also this time-consuming procedure causes surface damage, and can even introduce impurities if it is not conducted properly.

For GaAs, the substrates are heated between 580 and 600 °C in a vacuum to desorb the surface oxide [73], with an arsenic flux incident on the surface. The flux rate is usually chosen to be the rate for GaAs growth. During the heating, the surface conditions are observed using RHEED in real-time. When the oxide removal is complete, the 0-order spots are elongated and broadened. The brighter signal shows that GaAs layer is exposed, however the pattern means that the surface is quite rough. When the surface temperature is higher than 600 °C, GaAs becomes unstable (this will be discussed in detail in 5.2 in this chapter). In this case, after GaAs is exposed to vacuum at the end of oxide removal, a lower temperature would be provided to prevent its potential decomposition. A temperature around 550 °C~580 °C is usually adopted in our lab to grow a thick buffer layer to obtain a smooth surface. After the deposition of the buffer layer, usually a (2×4) or *c*(2×8) pattern will be observed on the RHEED screen.

4. Static phase investigation of GaAs surface

In this and the next section, the surface reconstructions of GaAs during growth will be introduced. A clean GaAs buffer layer is the prerequisite of growing GaAsBi, and investigating GaAs helps to give a deep understanding of MBE growth. This section is mainly focussed on non-growing conditions. Under non-growing (static) conditions, the GaAs surface structure can be changed into different reconstructions with different temperatures and arsenic flux rates. Static phase investigation can give a deep understanding of the GaAs surface reconstructions. It is also used in our lab to measure the substrate temperature.

4.1. GaAs lattice structure

The GaAs lattice structure is the foundational knowledge to understand its surface reconstruction. The lattice of GaAs is a zinc-blende structure [74]. Atoms of each element form a face-centred cubic

(FCC) structure, with the gallium cubic offset by [1/2, 1/2, 1/2]a from the arsenic cubic (see Figure 2.8), where a is the lattice constant.

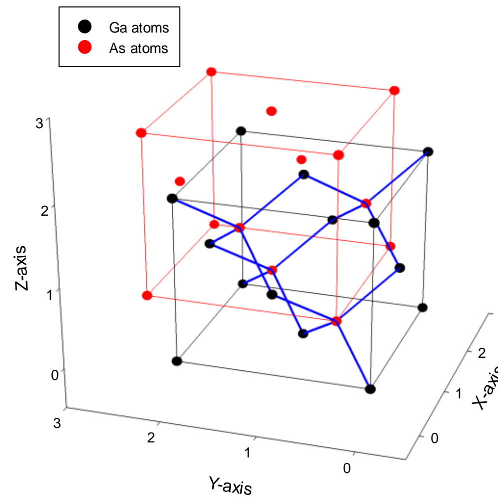

Figure 2.8. The lattice structure of GaAs

Many interests have been shown into the (001) and (111) surfaces of GaAs in MBE growth, and the (001) surface is used in our lab. (001) means that a GaAs crystal is orientated with the [001] direction normal to the surface. Samples are cleaved into a 11.8 mm × 11.4 mm rectangle to fit the sample holder. The longer side is along the (110) direction. Since the sample holder does not allow the sample to be rotated, RHEED can only show the pattern of long side.

4.2. Surface structure at different RHEED patterns

GaAs surface reconstructions are denoted by GaAs(001)-(m×n), which means that the unit cell of a GaAs surface structure is m×n times larger than the underlying bulk structure. Such surface meshes may be centred, in which case the notation would be GaAs(001)-c(m×n). If the mesh is rotated so that its principal axes are not aligned with those of the underlying bulk then the rotation angle is also included, e.g., GaAs(111)-(√19×√19)R23.4°[75].

With a sufficient arsenic flux incident on a cold surface (lower than room temperature), arsenic atoms are frozen and accumulated on the surface to form an amorphous layer. No RHEED pattern will be observed except for a haze. This technique has been used to protect the surface against contaminations from the atmosphere [76]. As the temperature increases, arsenic atoms are desorbed, leaving an arsenic terminated surface. A c(4×4) pattern is then observed with RHEED, and STM gives a possible surface reconstruction [77][78]. In a c(4×4) reconstruction, additional arsenic atoms stack on a fully-occupied arsenic layer. Figure 2.9(a) shows a possible c(4×4) surface reconstruction.

The arsenic atoms from the top layer (Figure 2.9(a)) tend to be desorbed along with some of the arsenic atoms from the bottom layer to form a (2×4) pattern or a c(2×8) pattern when the temperature is increased past the transition temperature. From STM, the surface structure has been shown to be an

arsenic layer on a gallium layer [76]. Figure 2.9(b) shows the surface structure of one possible variant of a (2×4) pattern (β structure). When arsenic atoms are exposed to a vacuum, two of them can bond covalently to form a dimer to satisfy atomic stability, and the strength pulls them to deviate slightly from the bulk atom occupation sites. This deviation forms the 2× side. The 4× side is caused by arsenic vacancies in every 4 lines. There are other possible atomic arrangements (α, β_2, γ) which also lead to (2×4) pattern [79]. However the hypothesis of 3 dimers in a cell has been subverted in further STM research, and only α and β_2 have been proved to be stable [80].

As the temperature increases further, the arsenic atoms are fully-desorbed, leaving a gallium terminated surface, which forms a *c*(8×2) pattern [81]. The most convincing structure model of *c*(8×2) pattern seems to be ζ model according to the review paper [81], which is illustrated in Figure 2.9(c).

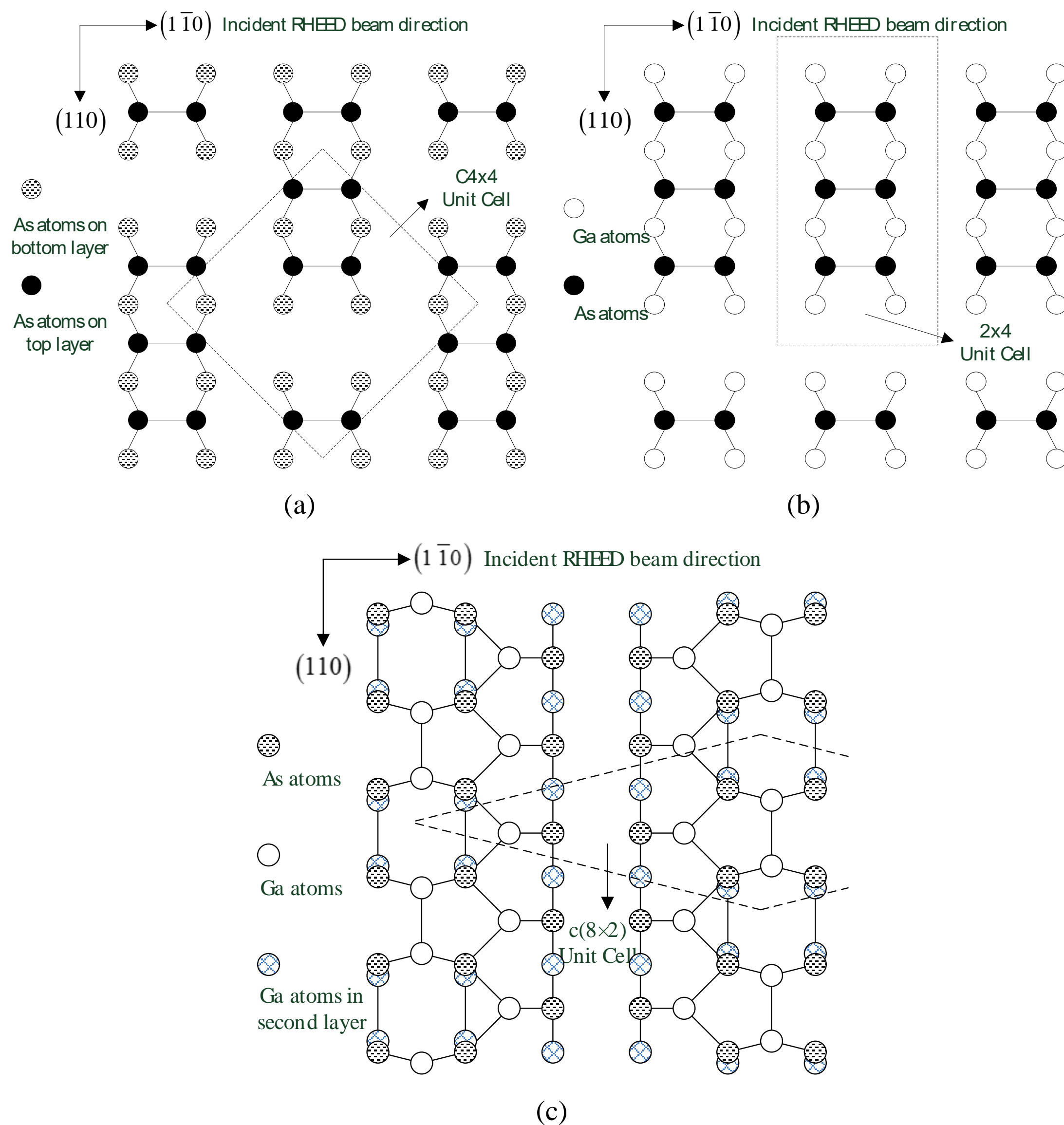

Figure 2.9. GaAs surface structure under (a) *c*(4×4) RHEED pattern, (b) *β*(2×4) RHEED pattern, (c) *c*(8×2) RHEED pattern

Surface structures of the three most common RHEED patterns have been introduced above. However, more possible RHEED patterns might exist for GaAs surfaces [82]. The temperature of pattern transition changes with arsenic flux rate, since adsorption of arsenic atoms on the surface will increase as the arsenic flux rate increases. In this case, a static phase diagram can be made to show RHEED patterns in different surface temperatures and different arsenic fluxes.

4.3. Substrate surface temperature calibration

In order to get the substrate surface temperature, several methods can be utilised such as using a thermocouple or an optical pyrometer [83]. In our system, the thermocouple is far away from the substrate, so there is a big difference between the real surface temperature and the value measured by the thermocouple. In addition, the beam flux temperature can also affect the measurement from thermocouple, leading to a large uncertainty.

GaAs substrate surface temperature is calibrated in our lab using a static phase diagram when no arsenic flux is incident to the surface. For a GaAs substrate, the oxide removal temperature is between 580 and 600 °C [73]. In addition, the Arsenic cap removal temperature is around 300 °C [76], and the $c(4\times4)$ to (2×4) transition temperature is 400 °C [84]. Assuming that the power of the substrate heater has a fixed relationship with the surface temperature, by recording the electric current passing through the heater at the three transition points, the temperature can be calibrated using the heater current.

The relationship between heating power and surface temperature varies with substrate type. The thicker the sample is, the more energy it requires to get a certain temperature. In addition, doped GaAs samples need less energy than undoped samples to reach a given temperature, since the electron density is larger. Figure 2.10 shows the different heating profiles of different doping type samples. Furthermore, experimental results show the incorporation of Bi into GaAs decreases the required heating current to reach a given temperature, due to the dramatic bandgap reduction of the material. However, for the same type of substrates, the results must be and are repeatable.

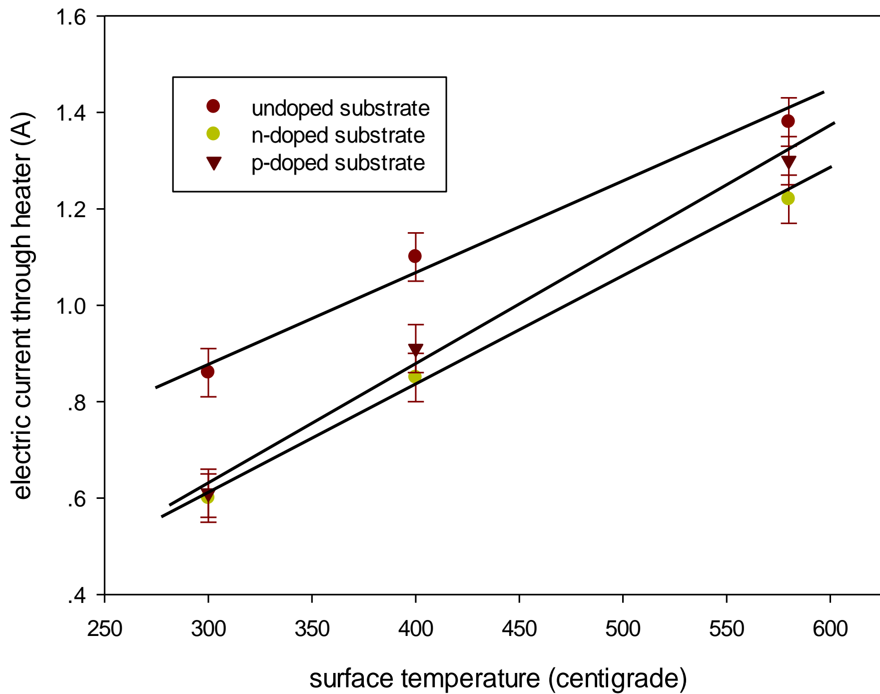

Figure 2.10. Heater current with surface temperature in undoped and doped samples

5. GaAs growth conditions

Cho [85][86] was the first person using MBE to prepare GaAs surfaces under well-defined conditions. He also used RHEED to investigate reconstructions occurring on the (111) and (001) surfaces, and how they related to growth conditions and subsequent processing. During GaAs layer growth, three important parameters should be determined: growth rate, growth temperature and As:Ga flux ratio.

5.1. Growth rate

It is important to know the growth rate in order to calculate the time needed to achieve a certain layer thickness. One way to measure growth rate is to measure the thickness of a layer after growth. However, since this is a time-consuming ex-situ measurement, the growth rate cannot be adjusted easily.

In 1981, the intensity oscillation of the RHEED pattern during growth was discovered and used to directly measure the growth rate [87–89]. The intensity oscillation is related to the surface roughness. The surface alternates between smooth and rough, as a monolayer is deposited. This allows the growth rate to be measured by monitoring the change of the reflected electron beam intensity from RHEED. Figure 2.11 shows the relationship between sample roughness and pattern intensity.

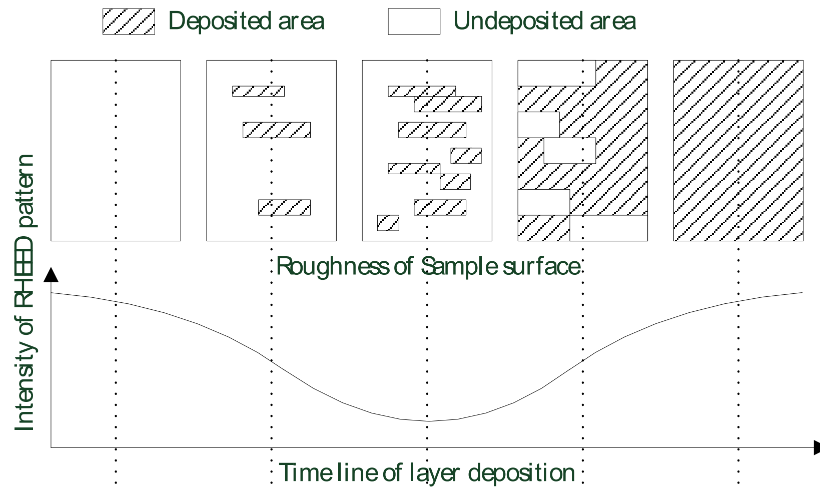

Figure 2.11. The intensity of the RHEED pattern during the deposition of a monolayer

5.2. Growth temperature range

Studies have shown that the growth rate of GaAs drops when the surface temperature is above 650 °C [90]. Above 650 °C, desorption of gallium from the surface is increased since the temperature reaches the GaAs congruent gallium sublimation temperature of Langmuir evaporation (T_c). All III-V materials are unstable above the congruent evaporation temperature, since the group V element is preferentially desorbed, and evaporation of the group III element becomes significant at even higher temperatures. Leaving the surface at such a high temperature is destructive to the surface, and can be irreversible. This means that the growth temperature should always be set below T_c. Different values of T_c were reported over years, and the lowest seems to be 625 °C [91].

On the other hand, an increased surface temperature provides atoms on the surface with sufficient energy to migrate and find the optimized place to incorporate. The Ga migration temperature is above 250 °C on the (111) surface [92]. RHEED investigation confirms that at a low growth temperature gives an amorphous haze pattern [93]. In addition, growth temperatures below 480 °C can create layers with high resistivity [94]. Though MBE is capable of depositing single-crystal GaAs at very low growth temperatures, obtaining semiconducting material of device quality requires a high epitaxial temperature. The ideal growth temperature is just below the congruent sublimation temperature. Since the temperature measurement in our lab is not direct (the method is introduced in 4.3 in this Chapter), and T_c is to some extent undetermined (we would assume that above 600 °C becomes not suitable for growth), 550 °C - 580 °C is used to secure the success of growth.

5.3. Ga flux rate

The measurement in [90] reveals an important fact: desorption of gallium from the sample surface is negligible at the growth temperature range, and thus it is reasonable to assume that gallium has a unity sticking coefficient. Other evidence shows that on the [111] surface, gallium always has a

unity sticking coefficient below 480 °C, and can still maintain a long surface lifetime (10 seconds) at 612 °C [95]. Besides, the influence of arsenic flux on the growth rate is negligible if the arsenic flux is large enough. In this case the gallium absolute atomic flux rate can be directly obtained from the growth rate measurement. This rule can also be used in other group III materials, since in most situations they have a unity sticking coefficient at the growth temperature range.

5.4. As flux rate calibration and adjustment

As mentioned above, the only important factor of influencing the sticking behaviour of gallium is substrate surface temperature, but the sticking behaviour of arsenic is trickier. Without gallium flux, adsorption of arsenic is nearly 0 above 230 °C [73]. When Ga flux is provided, one of dissociative chemisorption of As_2 molecules reacts on single Ga atoms. The sticking coefficient of As_2 is proportional to the Ga flux. In practice an excess of arsenic flux is provided during MBE in order to avoid nonstoichiometric growth, and excess arsenic atoms will be desorbed. For GaAs grown with Ga and As_4, the process is more complex. Pairs of As_4 molecules react on adjacent Ga sites. Even when excess Ga is present there is a desorbed As_4 flux. The maximum sticking coefficient for As_4 is 0.5 [96]. Therefore, it is impossible to get the absolute flux rate in the same way as for gallium.

The atomic arsenic flux rate can be determined from observation of the RHEED pattern during growth [97]. Similar to static phase mapping, a growth phase diagram was established in [82]. With different As:Ga flux ratio, two kinds of RHEED pattern can be obtained in a relatively high temperature. A (2×4) or *c*(2×8) pattern at high As:Ga flux ratios shows an As-stabilized surface, and a (4×2) or *c*(8×2) pattern at low As:Ga flux ratios shows a Ga-stabilized surface. Since a Ga-stabilized surface means Ga-rich, and vice versa, the transition point implies that the As:Ga flux ratio is almost stoichiometry.

After a stoichiometric As:Ga flux ratio is obtained, the arsenic flux rate can be adjusted using the beam equivalent pressure (BEP) near the sample surface from the movable ion gauge (MIG). Before measuring BEP, the sample is moved out from the growth place while the ion gauge is moved in. Then the pressure is recorded with the beam on and off, and the difference between them is regarded as the BEP.

Relative flux rates can be estimated from the BEP [51][98]. Derived from Equation 2.1, the relative fluxes can be calculated by

$$\frac{J_X}{J_Y} = \frac{P_X}{P_Y}\frac{\eta_Y}{\eta_X}\sqrt{\frac{T_X M_Y}{T_Y M_X}} \tag{2.4}$$

Where J_X is the flux of species X, P_X is its BEP, and T_X and M_X are the absolute temperature and molecular weight, respectively. η is the ionization efficiency varied with different atom species. According to Equation 2.4, the arsenic atomic flux is proportional to its BEP since a modulated valve is used to control the flux rate.

5.5. Dopants

Dopants have a lower flux rate than the film materials and as such generally have a unity sticking coefficient. The commonly used n-type dopants for III-V compounds are Sn, Si, and Ge. The best p-type dopant is Be, but Mg, Mn and Ge can also be used. In our lab, Si and Be are used in GaAs growth as the n-type and p-type dopants respectively.

6. Summary

In this chapter, the basic concept of molecular beam epitaxy (MBE) was introduced. The structure of MBE system was shown, and the functions of the important parts of the system were explained. One of the most important techniques in MBE is RHEED, which is used to observe the surface situation before, during and after growth. The working mechanism of RHEED was carefully introduced in this chapter. Furthermore, the growth of GaAs was also investigated especially including the surface morphology. The knowledge presented in this chapter is fundamental for the growth of GaAsBi.

Chapter 3: Technologies for investigating GaAsBi

1. X-ray Diffraction

X-ray diffraction (XRD) is a non-destructive structural characterisation technology which can be used to investigate the properties of crystal such as the layer thickness, the lattice constant and crystal quality of the layers [99]. During the experiment, an incident x-ray is diffracted by the sample surface, and photons in the diffracted beam interfere with each other to enhance or diminish the beam intensity. X-rays can be regarded as both electromagnetic waves and particles, and have wavelengths in the range of 0.01-10 nm.

X-rays can be generated in two ways. A continuously oscillating charge can emit x-rays with the same frequency as the oscillation. X-rays can also be produced when electrically charged particles (usually electrons) with sufficient kinetic energy are rapidly decelerated. In XRD, the latter is usually adopted. An x-ray tube consisting of a source of electrons and two metal electrodes is used to produce the radiation. A high voltage (usually >10 kV) is applied to the electrodes, and the resulting electric field accelerates the electrons. X-rays are produced when the electrons strike the anode.

If the applied voltage is lower than a critical value, the spectrum of x-rays will be continuous which is not suitable for the experiment. If the voltage is high enough, sharp intensity peaks appear at certain wavelengths superimposed on the continuous spectrum. The peaks are classified to several sets as K, L, M, etc. The continuous spectrum is caused by the rapid deceleration of electrons by the anode, while the wavelengths of the characteristic peaks depend on the anode material itself. The transmitted energy from decelerated free electrons excites electrons bound on orbits of atoms of the anode material to higher energy orbits. When they fall back to lower energy orbits, x-ray with a certain energy comes out. For example, the K-peak is due to the falling of electrons to orbits on K-shell. XRD measurements in this thesis were done using Cu $K\alpha_1$ radiation.

A triple axis setup is used for XRD in this thesis [100]. The setup comprises a beam conditioning section, a wide aperture detector, and a selector between the diffracted beam and the detector which only allows the beam in a very narrow angle range to pass. When taking the measurements, the sample is tilted and rotated to obtain different incident x-ray angles. The detector with narrow angle selector should also be rotated to satisfy that the incident x-ray angle be equal to the diffracted beam angle.

The diffracted beam can be observed by a fluorescent screen, a photographic film, or a counter (e.g. photo-detector). The fluorescent screen is made with zinc sulphide, which fluoresces in the visible part of the spectrum when absorbing x-rays. The photographic film uses emulsion to show the intensity of the x-rays. The counter is a device that can change x-ray into electric current.

The working principle of x-ray diffraction (XRD) is similar to RHEED since it is based on the Bragg's law [64], which describes the relation between the wavelength and reflected angle if a radiation or particle beam is reflected elastically by a crystalline structure (see Figure 3.1).

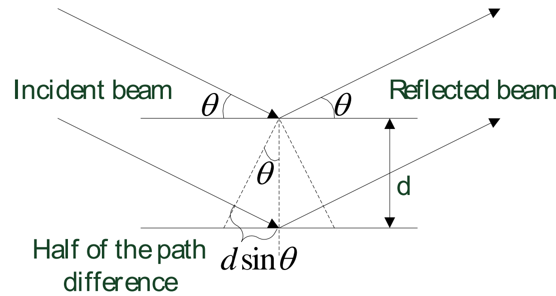

Figure 3.1. The path difference between incident beam and reflected beam

In the case of constructive interference, the phase difference between the reflected beams is zero, which means that the path difference should be a multiple of the beam's wavelength. In this case, the following equation should be satisfied (the Bragg's Law):

$$2d\sin\theta = n\lambda \tag{3.1}$$

where d is the distance between two adjacent layers, or lattice constant, θ is the incident angle of the beam, and λ is the wavelength of the beam. In this case, GaAsBi would have a different intensity peak from GaAs as their lattice constants are different. Increasing the Bi content of the epi-layer increases the lattice constant, which leads to the shift of the diffraction peak to lower diffraction angles in XRD results [2].

For a double-crystal XRD rocking curve, small peak oscillations called Pendellösung fringes might exist between two major intensity peaks directly related to the two different material. The small peaks reflect the constructive interference of diffractions from the two interfaces of a hetero-epitaxial layer, in which case the layer thickness can be obtained from investigating the fringes. The interface of epi-layer The epi-layer thickness of samples with clear Pendellösung fringes can be obtained using the following equation [101]:

$$t = \frac{\lambda}{\delta\theta \cdot 2\cos\theta_B} \tag{3.2}$$

where λ is the X-ray wavelength, $\delta\theta$ is the fringe separation and θ_B is the Bragg angle of the epi-layer peak. This assumes that the angle between the (004) plane and the sample surface is 0.

2. Nomarski

Nomarski microscopy, also called differential interference contrast (DIC) microscopy, is an optical microscopy technique [102]. Traditional transmitted light DIC is used to enhance the contrast in unstained, transparent samples. The working principle of traditional DIC is shown in Figure 3.2.

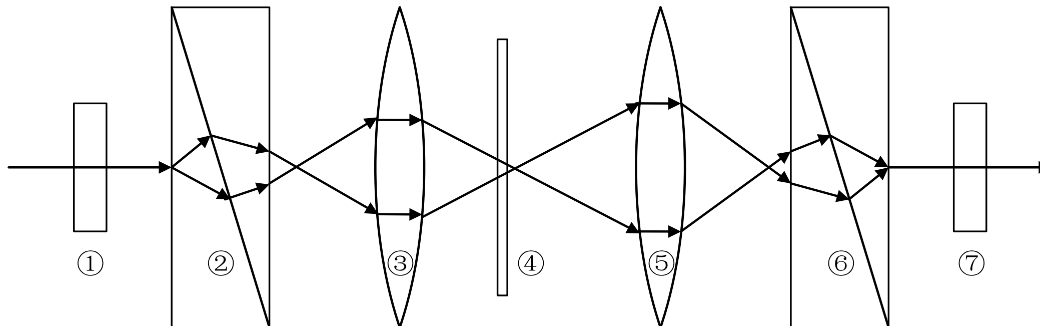

Figure 3.2. The working process of Nomarski microscopy

The arrows in Figure 3.2 represent the light passing through the system. The unpolarised light is first polarised at 45° by a polarising filter (part 1 in Figure 3.2). This light is then passed through a Nomarski-modified Wollaston prism (part 2), and separated into two rays polarised at 90° to each other. The two rays are focused by a condenser (part 3) and pass through two adjacent points (~ 0.2 μm) in the sample (part 4). If the optical paths of these two beams differ in refractive index or thickness, the lengths will be different. The two beams are then focused again by objective lens (part 5), and recombined by the second Wollaston prism (part 6). These two beams will interfere with each other to finally brighten or darken the image at that point according to the optical path difference.

The reflected light DIC microscopy is used for sample surface examination in this thesis, as the sample is opaque. Its working principle is similar to transmitted light DIC, other than that the light is reflected from sample surface, and goes back following the original path. The critical instrument parameters are simpler because only one Wollaston prism is required, and the objective lens serves as both the condenser and image forming optical system.

3. Photoluminescence

2.1. Principle

When recombination of an electron and a hole occurs, it can be either radiative or non-radiative. Radiative recombination occurs when a photon is emitted through the recombination, with the energy of the photon equal to the energy lost by the electron. Radiative recombination can also be regarded as luminescence. This process usually exists in direct band-gap materials.

Luminescence can be spontaneous. Usually we assume that the lifetime of carriers τ_r is independent of the temperature, and that the luminescence intensity as a function of temperature

should therefore be dominated by the density of carriers. The distribution of carriers obeys the Boltzmann distribution:

$$n(E) = N_0 \exp\left(-\frac{E-E_f}{kT}\right) \tag{3.3}$$

where N_0 is the number of available states in the energy level E, E_f is the Fermi energy, k is Boltzmann constant, and T is the absolute temperature. In this case, as the temperature increases, the intensity of spontaneous luminescence should increase.

Luminescence can also be stimulated. Depending on the source of excitons, the luminescence can be photoluminescence (PL) or electroluminescence (EL). PL uses a light beam (usually a laser) to excite electrons in the valence band to the conduction band [103], and EL usually uses an electric current to inject electrons directly into the conduction band.

In order to be capable of exciting electrons, the photons contained in the light beam require a greater energy than the band-gap during PL. When an electron is excited, it usually loses its energy thermally to the edge of the conduction band before recombining with a hole at the edge of the valence band. Accordingly, the emitted photon must have the same energy as the band-gap. This process is shown in Figure 3.3.

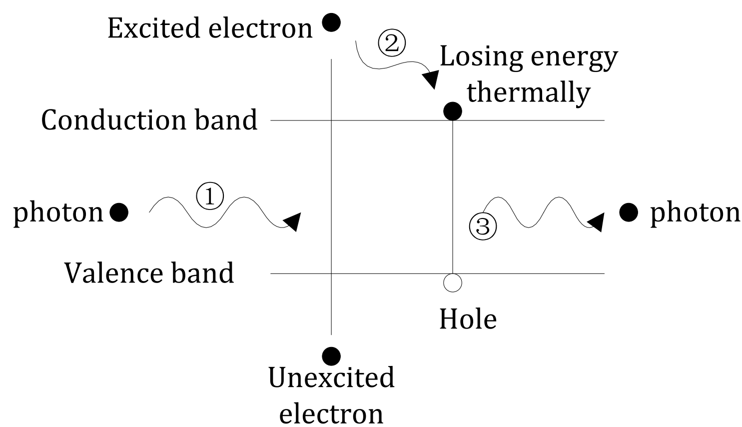

Figure 3.3. The PL process: (1) an electron is excited to the conduction band by an incident photon, (2) the electron loses its energy thermally to the edge of the conduction band, (3) the electron recombines with a hole to generate a photon

In theory, the excited electron can relax back to its original state immediately and emit a photon with the same energy as the incident photon. However, the energy lost thermally due to the interaction with the lattice happens much faster than recombination with a hole. In this case the generated photons normally have a longer wavelength than the incident photon, and this phenomenon is called Stokes shift.

If the absorption coefficient of a material is α, the intensity of light will decrease through penetrating the surface following the Beer-Lambert law:

$$I = I_0 \exp(-\alpha x) \tag{3.4}$$

In direct band-gap semiconductors the penetration depth of photons with energy above the band gap is of the order 1 μm. The diffusion length of photo-excited carriers through the material can vary widely but is typically in the range of 1-10 μm. In indirect band-gap semiconductors, or direct-gap semiconductors with sub-band excitation, absorption is weaker and the light penetrates deeper into the sample. Depending on the absorption properties of the material, PL can be dominated by surface recombination or bulk recombination.

The energy distribution and density of interface states can be ascertained by studying the power dependent PL. If there are interface traps or deep levels which can cause radiative recombination, electrons are likely to occupy these low energy states. However, since the number of these states is limited, as the incident light intensity increases they will become saturated, and the recombination will proceed as normal. If the PL spectrum is power independent, it means that the layer has few defect levels.

2.2. Setup

The PL setup in our lab is composed of a laser, a chopper, a monochromator, a germanium detector, and a lock-in amplifier. A schematic plot of the setup is shown in Figure 3.4.

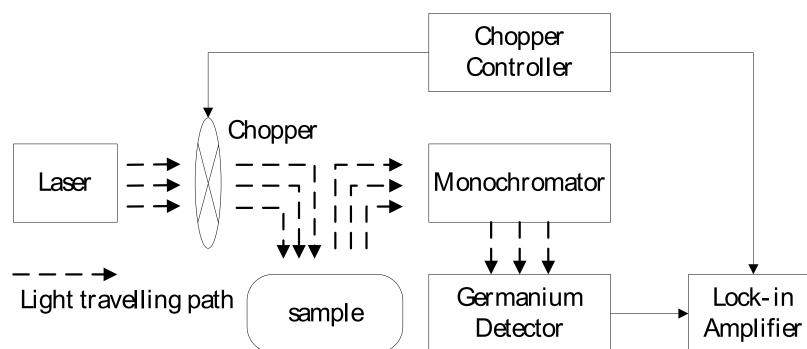

Figure 3.4. The photoluminescence setup

The laser has a wavelength of 512 nm. A laser component with a wavelength of 1024 nm is also generated, so a band-pass filter in the range of 328-600 nm is used to eliminate this component. The chopper is used to produce an alternating laser signal, and the frequency is set to around 182 Hz.

The photoluminescence from the sample is collected by a big focusing lens and transmitted to the monochromator. The monochromator extracts a single wavelength component from the luminescence, and the intensity is translated into an electric signal by the germanium detector, and reflected digitally on the lock-in amplifier.

The temperature dependence of the band gap can be calibrated by low-temperature photoluminescence (LTPL) measurements. LTPL can be realized by using a sample holder cooled with liquid helium, and the temperature of the sample holder can be adjusted by a heating element.

4. Capacitance-Voltage and Current-Voltage measurement

Capacitance-Voltage (CV) and Current-Voltage (IV) measurements can provide sufficient information about the device quality after fabrications. Figure 3.5 illustrates a typical probe station setup for both IV and CV.

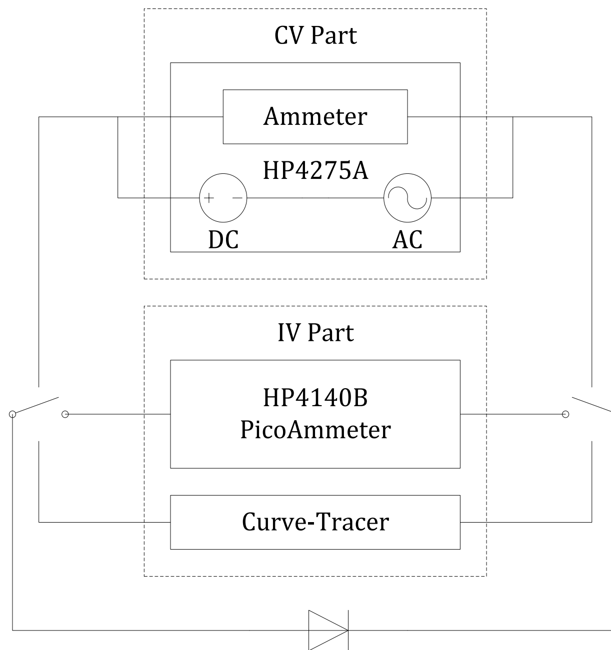

Figure 3.5. The diagram of IVCV setup

3.1. Capacitance-Voltage

CV measurements were taken on a Hewlett-Packard 4275A multi-frequency LCR meter. During a measurement, a DC voltage is added to the device first as the bias voltage. An AC voltage signal with small amplitude is added afterwards, and the amplitude and phase of the AC current is recorded as well as the AC voltage. Through comparing the amplitude and phase difference between AC voltage and current, the impedance of the device is obtained.

Since the imaginary part of the impedance (reactance) is a function of frequency, the frequency of the AC voltage signal should be chosen properly to match the measuring requirement of devices. Smaller capacitors (lower than micro-Farad) tend to be used at higher frequencies, so should be tested at 1 kHz or more. In this work, 1 MHz was used in all the CV tests as the frequency.

The impedance of the device can be modelled as either a series or a parallel connection of reactance and resistance, and the equivalent circuits are shown in Figure 3.6. If the reactance is large, the series resistance may be negligible, so the parallel model might be a better fit. Conversely, if the reactance is small, the parallel resistance may be negligible, so the series model might be better. In this thesis, the parallel model was adopted in the CV measurements, as the capacitive reactance of the devices was large enough (the capacitance of the devices are in the range of nano-Farad).

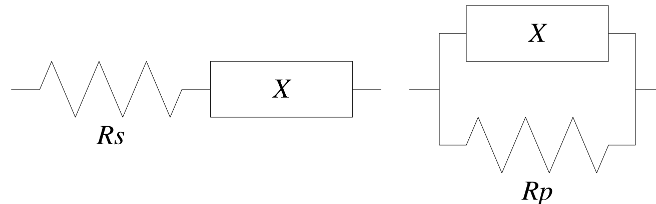

Figure 3.6. Two equivalent circuits to model impedance. R_s is the series resistance, R_p is the parallel resistance, and X is the reactance.

The quality of CV measurements can be indicated by the quality factor, Q, which is the inverse of the dissipation factor, D. D is the ratio of the real (R) to imaginary (X_C) parts of the impedance as shown in the below equation.

$$Q = \frac{1}{D} = \tan\delta = \frac{|X_C|}{R} \tag{3.5}$$

where δ is the phase angle. In physics, D illustrates the energy loss-rate during a mode of oscillation; whereas Q represents the quality of durability of that oscillation. A large Q or small D indicates a low-loss capacitance. In the ideal situation (no loss), Q is infinity and D is 0. In consequence, the phase angle between V_{AC} and I_{AC} is 90°.

When measuring small capacitances, especially in the order of pico-farads (pF), any small parasitic capacitances can make a noise which cannot be ignored. In this case, before taking CV measurements, any parasitic capacitances should be compensated to 0, such as those between the test leads, probes and device contacts. That can be done by pressing the 0-open button before probing a real device. The impedance of the test leads can be minimised by reducing the cable length to shorter than the wavelength of the AC signal. Given that most coaxial cables have a velocity factor of about 0.7 (i.e. the electrical signal travels at ~70% of the speed of light through the cable), the length of each test lead must be kept shorter than 20 m with frequencies up to 10 MHz.

High leakage current can pose a problem for CV measurements as well. If the mesa diode has a low shunt resistance (usually due to dislocations in the bulk epi-layer), or leaky etched surface surrounding the device active region, the accuracy and quality factor of the measured capacitance will be degraded, reducing the phase angle between AC voltage and current. The problem can be

overcome to some extent by increasing the frequency of the test signal to reduce the capacitive impedance and thus increase the magnitude of the measured current.

In our equipment, the frequency of AC voltage signal is between 10 kHz and 10 MHz, and the amplitude is around 50 mV. The majority of the CV measurements in this thesis were performed at room temperature with the purpose of determining the epi-layer parameters. The majority of the CV data were collected at a phase angle between 80 and 90, which means a relatively large reactance to resistance ratio. Different sizes of devices are measured, and good area scaling of the CV curves helps to indicate bulk capacitance with negligible parasitic effects.

CV measurements are mainly used to determine the doping profile and the i-region thicknesses for p-i-n structure samples. If we consider the thermal effect, the expression of capacitance per area can be [104]:

$$C_D = \frac{\varepsilon_s}{W_D} = \sqrt{\frac{q\varepsilon_s N}{2}}\left(\psi_{bi} - V - \frac{2kT}{q}\right)^{-1/2} \tag{3.6}$$

Here, C_D is the capacitance per area, ε_s is the dielectric constant of the material, N is the doping density, ψ_{bi} is the built-in self-potential, and V is the bias voltage. Equation 3.5 is obtained by solving the basic Poisson Equation. A typical CV measurement result can be found in Figure 5.3.

Rearrange Equation 3.6, Equation 3.7 is obtained:

$$\frac{1}{C_D^2} = \frac{2}{q\varepsilon_s N}\left(\psi_{bi} - V - \frac{2kT}{q}\right) \tag{3.7}$$

From Equation 3.7, $1/C_D^2$ is a linear function of bias voltage. In this case, if the thermal part $2kT/q$ is ignored, the intersection of the plot based on Equation 3.6 with the x-axis is the built-in self-potential. As an example, Figure 5.4 shows $1/C_D^2$ as a function of bias voltage.

Equation 3.8 is obtained from differentiating Equation 3.7:

$$N = -\frac{2}{q\varepsilon_s} \Big/ \frac{d\left(1/C_D^2\right)}{dV} \tag{3.8}$$

The doping situation in p-n junction can therefore be obtained from CV measurement, if we plot the doping with depletion width (see Appendix 3 to get the calculation of depletion width). If it is a p-i-n structure, a more accurate measure of the i-region thickness can also be obtained (the position where doping changes abruptly, see Figure 5.5 as an example).

Another purpose of CV can be observing the charging and discharging of deep-level traps, which are manifested in the form of dispersion in CV at low temperature and test frequencies below 1 MHz.

3.2. Current-Voltage

During IV measurements, a bias voltage (either forward or reverse) is added on the device and the corresponding current is recorded. The measurements are typically implemented under a dark environment. Either a HP4140B picoammeter or a Keithley 236/237 source-measure unit (SMU) is used in the measurements.

The IV equation can help us to understand the ideal case and non-ideal effects on IV curve. The ideal current density equation is [104]:

$$J = J_0\left[\exp\left(\frac{qV}{kT}\right) - 1\right] \tag{3.9}$$

$$J_0 \equiv \frac{qD_p p_{n0}}{L_p} + \frac{qD_n n_{p0}}{L_n} \equiv \frac{qD_p n_i^2}{L_p N_D} + \frac{qD_n n_i^2}{L_n N_A} \tag{3.9a}$$

Here, k is the Boltzmann constant, T is the absolute temperature, and q is the elementary electric charge. J_0 is the saturation current, D_p and D_n are the diffusion constants which are related to the mobility of minority carrier, p_{n0} and n_{p0} are the minority carrier densities in the neutral zone far away from the diffusion region, and L_p and L_n are the diffusion lengths of minority carriers in the n-region and the p-region respectively. The definition of diffusion lengths is:

$$L = \sqrt{D\tau} \tag{3.10}$$

$$\tau = 1/(rN) \tag{3.10a}$$

where τ is the lifetime of minority carriers which can be given by time-resolving photoluminescence measurements, r is the recombination rate in the diffusion regions, and N is the doping density. So a larger doping profile leads to a smaller lifetime, and a larger diffusion length can increase the dark current.

$V = (E_{Fp}\text{-}E_{Fn})/q$ is the quasi-Fermi potential in the depletion region if the quasi-equilibrium approximation is considered [105]. E_{Fp} and E_{Fn} are the quasi-Fermi energies of holes and electrons respectively. There are several different factors that can lead to a variation of the quasi-Fermi potential [106]. Recombination in the depletion region is the dominant factor when carrier injection or generation is small. When the bias voltage is small enough, the current due to the generation-recombination process in depletion region cannot be ignored anymore. If a large forward bias is implemented, high injection (minority carrier density is comparable to the majority concentration) happens, and both drift and diffusion current components must be considered. When the bias is even higher, the diode works as a resistor, so the serial resistance should be taken into account. All these effects would lead to the deviation of current-voltage shape from ideal case. Ideality factor has been introduced to describe the non-ideal case, and current-voltage equation is changed to:

$$J = J_0\left[\exp\left(\frac{qV - JR_s}{nkT}\right) - 1\right] \tag{3.11}$$

where R_S is the series resistance, and n is the ideality factor.

At reverse bias voltage, in the ideal case, it should be nearly a constant. If we add a reverse bias of -1 V to the device at room temperature, $\exp(qV/kT) \approx 1.59 \times 10^{-17}$, which means that a very small reverse bias can lead to the saturation of the reverse current.

However, the behaviour of current in reverse bias is much more complicated in reality. Usually we need to consider the leakage current through the mesa periphery, and it can be very large depending on the fabrication process.

Breakdown of current happens when the reverse bias is high enough. Tunnelling breakdown happens when the electric field in depletion region reaches a high value that gives electrons sufficient energy to travel through the barrier. Avalanche breakdown is when an electron gets sufficient energy during its free-path without scattering with phonons or carriers, and during the scattering, energy transition creates another electron. These two breakdown mechanisms can both lead to a dramatic increase of reverse current, and they exist simultaneously in devices. But tunnelling breakdown often happens before avalanche in high doping concentration devices, and in low doping devices, avalanche breakdown is more important. Besides, the amplitude of electric field in depletion region can be used to determine the dominant breakdown type. Tunnelling breakdown is found to occur at electric field of above 10^6 V/m in Silicon, while avalanche breakdown usually happens in a lower electrical field.

5. Photocurrent

When a beam of photons is incident on a semiconductor material with energy larger than the band-gap of the material, electrons will be excited from valence band to conduction band. Photoluminescence is based on this excitation and radiative recombination afterwards. In the depletion region of a p-n junction, when an electron is excited, it might be swept out of the depletion region by an electric field before it finds a hole to recombine. In this case, the electron contributes to the drift current. The current corresponding to the excitation is called photocurrent. Not only the electrons generated in depletion region have the chance to be a part of current, but the ones in neutral zone also have the possibility due to carrier diffusion.

Photocurrent measurement in our lab is based on the alternative signal detect with Lock-in amplifier. The structure plot of the setup is shown in Figure 3.7.

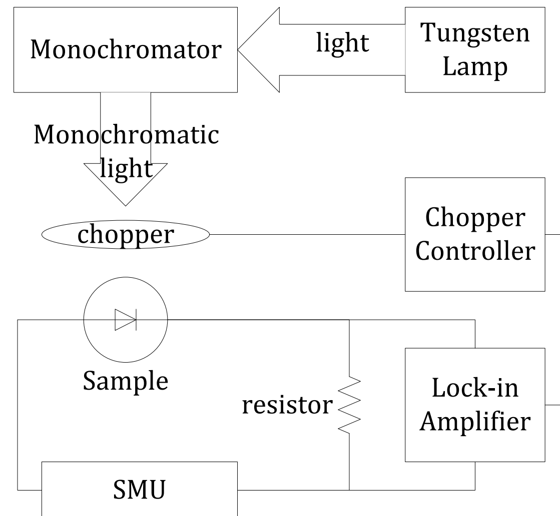

Figure 3.7. The schematic plot of photocurrent setup

A tungsten light is used to provide the light source. It's reasonable to regard the light as a radiation which obeys the Planck's law. Then a monochromator selects the specific wavelength of the light to produce a monochromatic light beam. A chopper is used to transfer the light beam into alternative signal, so the current generated from light will become alternative as well. We use a resistor with 10 kΩ resistance as a collector of current, and the voltage on the resistor is measured by a lock-in amplifier.

6. Impact ionisation and avalanche multiplication

6.1. Impact ionisation

In solid state material, carriers (electrons and holes) will be accelerated if an electrical field is added [107]. In this accelerating process, carriers would interact with the lattice vibrations of the crystal by emitting or absorbing phonons, in such a way acting as a resistive or frictional force against the accelerating field. However, in a sufficiently high field, electrons and holes may have a great chance to gain enough energy before interacting with phonons. When the carriers with excess energy even larger than the bandgap, they can pass the energy to electrons in the valence band and then excite them into the conduction band. In this case, extra free electron-hole pairs are generated, and the process is called impact ionisation.

In order to have impact ionisation happen before carrier-phonon interaction, carriers should have a smaller mean free path for hole-electron pair production compared to that for carrier-phonon interaction. Impact ionisation coefficients (α for electrons and β for holes) are used to represent the impact ionisation rate, which are defined as the inverse of the mean free path travelled by the carriers before impact ionisation. Both of the parameters increase strongly with the magnitude of the electric field after reaching a threshold (normally in the range of $10^5 \sim 10^6$ V/cm).

A "lucky electron" theory was proposed by Shockley to explain how carriers achieve high enough energy to cause impact ionisation [108], in which the impact ionisation coefficient can be expressed as:

$$\alpha = \frac{qE}{\varepsilon_{th}} \exp\left(-\frac{\varepsilon_{th}}{qE\ell} \right) \tag{3.12}$$

where ε_{th} is the ionization threshold energy, q is the electron charge, E is the electric field, and ℓ is the mean free path between collisions. The parameters are only related to the properties of the material other than electric field.

6.2. Avalanche multiplication

Both the original and the generated electron-hole pairs can subsequently gain energy and undergo further impact ionisation events. In that situation, avalanche multiplication happens as a chain reaction of impact ionisation which produces an internal current gain.

Considering a p-i-n structure which i-region thickness is w, the position of p-i interface is set to 0, and the position of i-n interface is set to w. If an electron-hole pair is generated in position x, an average $\langle M(x) \rangle$ pairs would be collected at the edge of i-region through multiplication, which is presented in the following expression based on McIntyre's local model [109][110]. Obviously, $\langle M(x) \rangle$ is the mean internal avalanche gain.

$$\langle M(x) \rangle = 1 + \int_0^x dx' \beta(x') \langle M(x') \rangle + \int_x^w dx' \alpha(x') \langle M(x') \rangle \tag{3.13}$$

where α and β are electron-initiated and hole-initiated impact ionisation coefficient respectively.

If we define γ as:

$$\gamma(x) \equiv \alpha(x) - \beta(x) \tag{3.14}$$

Solve Equation 3.13, we can get:

$$\langle M(x) \rangle = \frac{\exp\left(-\int_0^x dx' \gamma(x') \right)}{1 - \int_0^w dx' \alpha(x') \exp\left(-\int_0^{x'} dx'' \gamma(x'') \right)} \tag{3.15}$$

According to Equation 3.12, impact ionisation coefficients are functions of local electric field which distribution can be expressed as a function of position. In a p-i-n diode, the electric field distribution in the i-region is strongly dependent of doping density. A small enough doping density would cause a relatively flat field distribution, which can be regarded as irrelevant to the position. If the ionisation coefficients are assumed to have no relation with the position, then:

$$\langle M(x) \rangle = \frac{\gamma \exp(-\gamma x)}{\alpha \exp(-\gamma w) - \beta} \tag{3.16}$$

$$M_e = \frac{\gamma}{\alpha \exp(-\gamma w) - \beta} \tag{3.16a}$$

$$M_h = \frac{\gamma \exp(-\gamma w)}{\alpha \exp(-\gamma w) - \beta} \tag{3.16b}$$

where M_e is the multiplication factor when the initial impact ionisation happens at the p-i interface, which is induced by incident electrons, and M_h is the factor when the initial impact ionisation happens at the i-n interface, which is induced by incident holes.

Combining Equations 3.16a and 3.16b, the following equations are deduced:

$$\alpha = \frac{1}{w}\left(\frac{M_e - 1}{M_e - M_h}\right)\ln\left(\frac{M_e}{M_h}\right) \tag{3.17a}$$

$$\beta = \frac{1}{w}\left(\frac{M_h - 1}{M_h - M_e}\right)\ln\left(\frac{M_h}{M_e}\right) \tag{3.17b}$$

Therefore, the impact ionization coefficients can be obtained by measuring electron-initiated and hole-initiated avalanche gains in photo-multiplication measurements. Besides, avalanche breakdown happens when the gain goes infinite, and hence the breakdown voltage is when the denominator of equation 3.16 equals 0.

6.3. Photo-multiplication measurement

Photo-multiplication measurement can be used to measure the avalanche gain. The working mechanism is similar to photocurrent measurement, except that a laser is used as the light source instead of using a monochromator. Lasers can provide much stronger light intensity than the light from monochromator, and the wavelength range of laser is much narrower. The reason of using monochromator in photocurrent measurements instead of laser is that the wavelength of laser cannot be easily changed, which makes the laser not suitable for rapid wide range spectrum measurements.

The same as photocurrent measurement, when the laser is incident on the sample, electron-hole pairs are generated and collected by the electrical field when adding a reverse bias. By increasing the reverse bias, avalanche multiplication would happen, and the photocurrents at different biases can be used to extract the avalanche gain.

7. Summary

XRD, PL, IV, CV and photocurrent measurements are introduced as techniques of measuring electrical and optical properties of GaAsBi samples in this chapter. X-ray diffraction combining with PL can be used to examine sample properties before fabrication. The lattice constant can be obtained from x-ray measurements, and information such as the bismuth content and the sample quality can be inferred from the results. For room temperature PL, we often rely on it to determine the quality of the samples, and to find the bismuth incorporation. After fabricating samples into devices, IV, CV and photocurrent measurements can be used to find the electrical and optical properties of the devices. The doping profile can be determined by CV measurements, and the dark current properties can be found by IV measurements. Photocurrent measurements can reflect the sensitivity and responsivity of the device. For solar cells it is useful to calculate the power generation efficiency from the photocurrent measurements. The impact ionisation and avalanche gain can be obtained from photo-multiplication measurements. These techniques are keys to unveil the characteristics of GaAsBi.

Chapter 4: Analysis for the MBE growth of GaAsBi material

1. Background study of Bismuth growth

The first GaAsBi sample was grown by MOVPE in 1998 [1] using a growth temperature as low as 365 °C. Secondary ion mass spectrometry (SIMS) measurements showed that the Bi content was nearly 2%. The band-gap reduction and the improved temperature insensitivity of this material were first discovered from this sample. After that, GaAsBi samples were first obtained by MBE in 2003 [2]. Up to 3.1% Bi was managed to be incorporated into GaAs in those samples, and Rutherford back-scattering (RBS) was used to determine the Bi content.

One of the challenges for the growth of GaAsBi is that the Bi flux may cause surface segregation due to surfactant effects. In this case, a low growth temperature (usually lower than 400 °C) is required in order to incorporate a significant fraction of Bi into GaAs to extend the emission wavelength. In addition, the As:Ga flux ratio needs to be close to the stoichiometric value in order to incorporate Bi significantly. This is because that the Bi incorporation will be reduced dramatically by an excess As flux [111][112], while in the contrary, Ga or Bi droplets can be formed on the surface due to an insufficient As flux.

In addition to the (001) surface, GaAsBi has also been grown on (311)B GaAs substrates [113], and it is claimed that Bi incorporates more easily on this surface. In-situ UV light has been used in [114] to indicate the surface quality during growth. The intensity of light scattering can be used to determine the roughness of the layer, especially since the Ga-Ga and Bi-Bi droplets can reflect light very efficiently. In that case, the brighter the light scattering is, the more Ga droplets exist. Before 2008, the highest Bi incorporation content was 8% [17][31].

2. Growth conditions for GaAsBi

In order to improve the quality of GaAsBi layers, different growth conditions have been discussed through these years of study. In addition to the three important parameters mentioned in Chapter 2: growth temperature, growth rate and As:Ga flux ratio, Bi flux rate is the fourth key parameter for GaAsBi growth. From investigating GaAs growth, it is well known that Ga has a unity sticking coefficient when the substrate temperature is lower than 650 °C [90]. Since the behaviour of As atoms on the surface relate to Ga atoms, and Bi atoms are even harder to incorporate, it is obvious that the Ga flux determines the growth rate. To make Bi incorporation happen, as discussed in the above section, growth temperature should usually be lower than 400 °C, and the As:Ga flux ratio should be near stoichiometry. However, growing a high quality GaAsBi layer requires much deeper investigation other than only considering those two key prerequisites. Many researchers devote their

time to getting a smoother surface without forming Ga or Bi droplets on the surface, which may lead to lower doping density, lower dark current and better optical behaviours.

A concept of kinetic-limited growth regime has been proposed in 2012 [111]. This paper claimed that with sufficiently low growth temperature (315 °C ± 5 °C was chosen in the paper) and relatively low Bi flux, GaAsBi growth is kinetically limited, which leads to a Bi incorporation which content is proportional to the Bi flux. In this growth regime, Bi atoms don't have enough kinetic energy (kinetically limited) to escape the accumulated monolayers and segregate on the surface, and therefore are completely incorporated into the layers. Besides, the bismide layer can be smoother with the kinetic movement of Bi atoms in it, where Bi acts as a surfactant.

The most important conclusion from [111] is that the growth rate is playing a very important role in Bi incorporation, since the higher the growth rate is, the more kinetic energy the Bi atoms need to exceed the deposition rate. Thus a growth with low growth rate and high Bi:Ga flux ratio would be easier to form Bi droplets. In the contrary, a growth with high growth rate and low Bi:Ga flux ratio would make the surface rough due to insufficient surfactant effect. Figure 4.1 from [111] shows the relationship between Bi content and sample roughness at different growth rates which is obtained from atomic-force microscope (AFM) measurements.

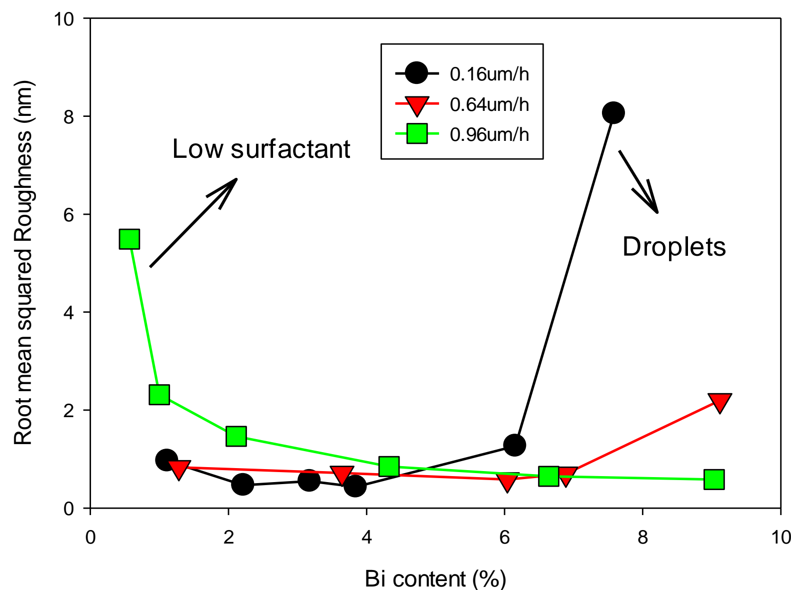

Figure 4.1. The root mean squared roughness obtained from AFM scans for different growth rates and Bi compositions, which is adapted from [111]

Under a certain growth temperature and growth rate, GaAsBi growth will eventually come up with a temperature limited growth regime instead of a kinetic limited regime when keeping increasing Bi flux. In this temperature limited growth regime, the amount of incorporated Bi atoms is no longer

proportional to the Bi flux, but seems to become unchanging. Lattice would have no more space for all the atoms when supplying excess Bi, and the excessive Bi atoms would segregate on the surface. Besides, a higher temperature would lead to less Bi incorporation, since Bi atoms would have more kinetic energy to escape the accumulated layers. A set of samples called STE2 series are grown in our lab which are able to give an obvious evidence to this transition. The bismuth cell temperatures used in the STE2 series are from 450 °C to 530 °C.

From investigating the STE2 series, it was found that the incorporation of bismuth saturates with a certain threshold bismuth flux (Figure 4.2). As the bismuth flux increases, the GaAsBi PL peak intensity increases at first, and then drops when the bismuth flux exceeds a certain value (Figure 4.3). Several papers claimed that this is due to the Bi_{Ga} antisite defects [115][46]. However it is hard to tell if it is true, since evidence shows little Bi_{Ga} exists in GaAsBi layers [47]. Another explanation can be from [111], which is that the surface Bi droplets diminish the PL intensity. Besides the intensity peak position and the incorporation saturation transition point are at different wavelengths. Since the Bi droplets form before the growth reaches temperature limited regime, this phenomenon matches quite well with the description in paper [111].

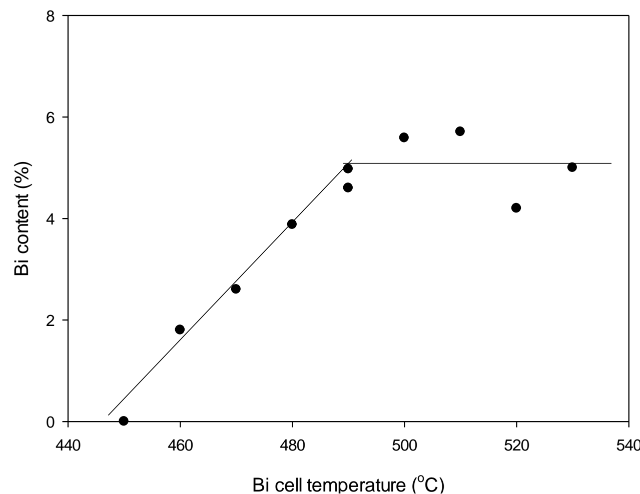

Figure 4.2. Bismuth incorporation with bismuth flux (Bi contents are obtained from PL measurements)

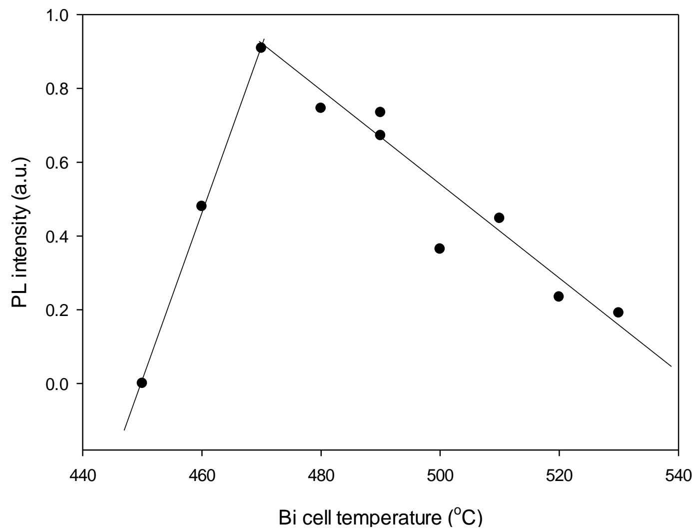

Figure 4.3. Photoluminescence intensity of GaAsBi peak with bismuth flux

3. Surface reconstructions of GaAsBi growth

During growth, surface reconstruction is a very important indication of the growth environment. It provides significant information of growth temperature and atomic flux ratio of each source material. It needs quite a deep knowledge of surface structural chemistry to understand the formation mechanism of surface reconstruction. Two basic concepts are the key to explain surface reconstruction: chemical bonding and charge neutrality [79]. Three principles based on the two concepts are summarized in paper [79] to explain the different reconstruction patterns under different preparation conditions. First is about the charge neutrality on surfaces: surfaces tend to be auto-compensated. For instance, GaAs surface can be As-rich (As:Ga atomic ratio on the surface is larger than 1) at lower temperature, which still satisfies charge neutrality. Second, at a certain auto-compensated surface situation, the bonds of atoms will be rehybridized to form lower surface state bands. In this case, semiconducting bands are with higher probability to form instead of metallic ones (sometimes the atom bonds on the surface will be tilted to satisfy that), and electrons tend to occupy valence bands with lower energy. Consequently, the dangling bonds are removed. The third is based on the kinetic accessibility of surface reconstructions under different preparation conditions.

Bi-related surface reconstruction investigation was first focused on the static situation. As mentioned in Chapter 2, static situation is when no new atomic layer deposits on the surface. Usually for III-V Group material on (001) surface, (2×4) and (4×2) unit cells are the smallest ones on V- and III- stabilized surfaces respectively with part of paired surface atoms missing, based on electron counting model (ECM) developed from the basic principles mentioned in the above paragraph [116]. However, a Bi-induced (2×1) surface without any dimer vacancies has a high probability to be metallic which seems to disobey the second principle, since such a small unit cell should include a

half-filled dangling bond [116][44]. This pattern appears when Bi atoms sit on prepared Ga-rich surface (Figure 4.4). In this case, the surfactant function of Bi during growth can be explained by this metallic surface behavior, since the III atom diffusion should increase on metallic surface. Furthermore, STM I-V curve shows that the (2×1) surface at low temperature (270 °C) behave metallically, but at high temperature (> 300 °C) with mixed pattern (2×1) and (2×4), the surface has a semiconducting behavior, which suggests the existence of BiBi and sBiAs structure respectively. A stable static (4×3) pattern was presented in [117] at even higher temperature (350 °C ~ 450 °C) after depositing Bi atoms on GaAs surface. The (4×3) reconstruction is a semiconducting layer, presumably inherited from the initial *c*(4×4) reconstruction, which consists of a full atomic layer of a group V species with additional group V dimers rotated 90° and back bonded onto the underlying group V (see Figure 4.5).

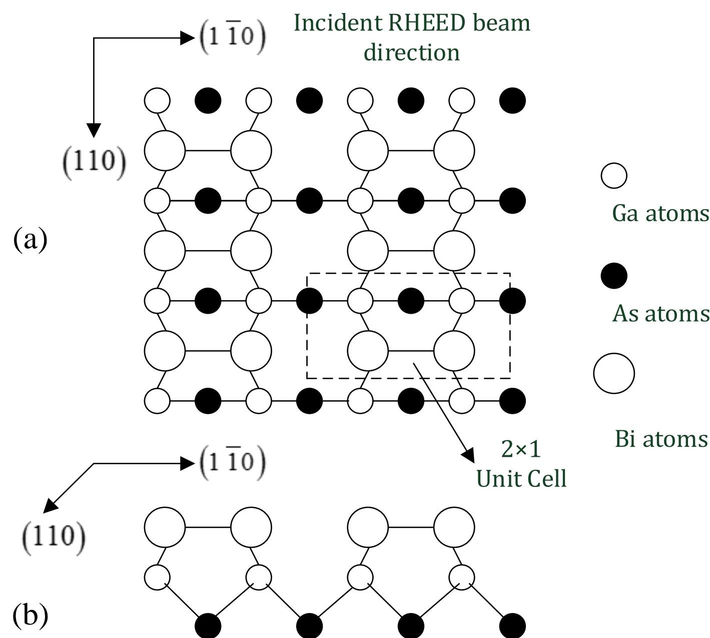

Figure 4.4. Surface reconstruction of GaAsBi layer with (2×1) RHEED pattern, (a) top view, (b) view along (110)

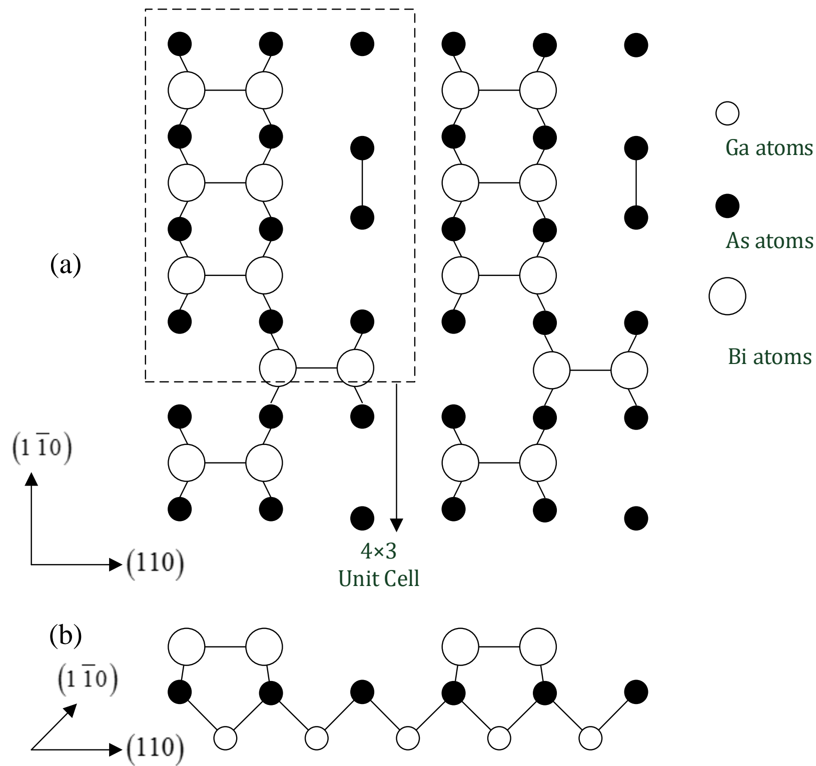

Figure 4.5. A possible surface reconstruction of GaAsBi layer with (4×3) RHEED pattern, (a) top view, (b) view along $(1\bar{1}0)$

The dynamic surface reconstruction studies of GaAsBi were majorly focused on (2×1) RHEED pattern [117]. As discussed in the above paragraph, the (2×1) surface is metallic. During growth, (2×1) unit cells are disrupted by (4×3)-type unit cells. These two reconstructions show two different situations: Bi dimers landing on As-sites, and Bi dimers landing on Ga-sites. Possible incorporation processes could exist as following:

1. As atoms break Ga-Bi bonds, and the reconstruction change from (2×1) to (4×3), in this case, the Bi atoms on the surface behave as a surfactant.
2. Ga atoms break As-Bi weak bonds, and the reconstruction change from (4×3) to (2×1).
3. Bi atoms are buried by Ga atoms when Ga atoms landing on (2×1) unit cells.

Besides, an interesting assumption without verification is made based on the above discussion: Bi incorporates as dimers within the GaAs matrix. Further discussion of the incorporation processes is presented in the next section of this chapter: the modeling of Bi incorporation into GaAs.

4. The GaAsBi growth models

4.1. Lu's model

Many researches focused on improving the bismuth content in GaAsBi layer and growing better layer quality, but there are only two papers [118][119] having discussed quantitatively about the effect of growth conditions on the incorporation of bismuth.

The first growth model for GaAsBi was proposed in 2008 [118]. In [118], up to 10% of Bi was incorporated. The Bi flux consists of monomers and dimers. In this model, Bi is supposed to adhere to the surface first and form an amorphous metallic Bi layer, and the layer is the source of the incorporated Bi. Three Bi incorporation processes are shown in Figure 4.6. Among them, the author claimed that process 2 is impossible as Bi is too large to form Bi-Ga-Bi.

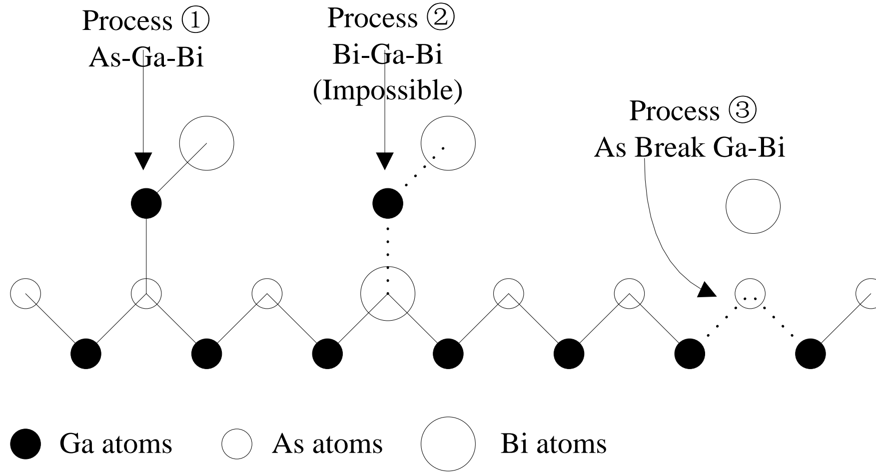

Figure 4.6. Three processes during Bi incorporation in [118]

If the coverage of the metallic Bi layer on the surface is θ_{Bi}, Ga and As flux rates are F_{Ga} and F_{As} respectively, and the Bi incorporation percentage is x, the following expression is obtained.

$$\frac{dx}{dt} \propto \theta_{Bi} F_{Ga} (1-x) - aF_{As} x \exp\left(-\frac{U_1}{kT}\right) \tag{4.1}$$

Here a is a dimensionless fitting parameter. Since a Ga-Bi bond is broken during process 3, it is believed that process 3 is caused by thermal activation, and U_1 is the activation energy of bismuth knocked out from surface layer. In the equilibrium state, dx/dt should be 0.

Considering the formation of the metallic Bi layer, the adsorption of Bi from the area 1-θ_{Bi} should be equal to the desorption of Bi from the area θ_{Bi}. This idea was first used to explain the static behaviour of atoms on surface at a certain surface conditions, which is called Langmuir Theorem. Desorption of Bi is a process of thermal evaporation, and U_0 is the activation energy for bismuth desorption. b here is a pre-exponential factor. The author claimed that since some of the Bi is

incorporated instead of contributing to the metallic layer, the equivalent flux rate of the adsorbed Bi should be F_{Bi}-xF_{Ga}. Then a second expression is obtained.

$$b\left(1-\theta_{Bi}\right)\left(F_{Bi}-xF_{Ga}\right)=\theta_{Bi}\exp\left(-\frac{U_0}{kT}\right) \tag{4.2}$$

So in equilibrium, θ_{Bi} is:

$$\theta_{Bi}=\frac{b\left(F_{Bi}-xF_{Ga}\right)\exp\left(\frac{U_0}{kT}\right)}{1+b\left(F_{Bi}-xF_{Ga}\right)\exp\left(\frac{U_0}{kT}\right)} \tag{4.3}$$

The variables are surface temperature and Ga, As and Bi flux rate. The values of constant parameters are given as $b = 8.5\times10^{-11}$ nm^2·s, $a = 2.5\times10^8$, $U_0 = 1.3$ eV, and $U_1 = 0.8$ eV.

4.2. Lewis's model

Another growth model was proposed by Lewis in 2012 [119]. Bi incorporation in GaAsBi alloys is limited by weak Ga-Bi reactivity and the strong tendency for Bi to surface segregate. Substrate temperature was measured using optical bandgap thermometry with an accuracy of ±5 ^{o}C.

The author claimed that during growth, a Ga-terminated surface exists, and the coverage is θ_{Ga}. If the coverage of the As-terminated surface is θ_{As}, then $\theta_{Ga}+\theta_{As}+x=1$. Figure 4.7 shows the incorporation processes considered in this model. Bi will be incorporated into the surface layer when As-Ga-Bi bonds form. The Bi-Ga bonds will bury Bi into the lower layer, and decrease the amount of Bi on the surface. Ga-Bi bonds can be broken thermally, or the bismuth atoms can be replaced by As atoms.

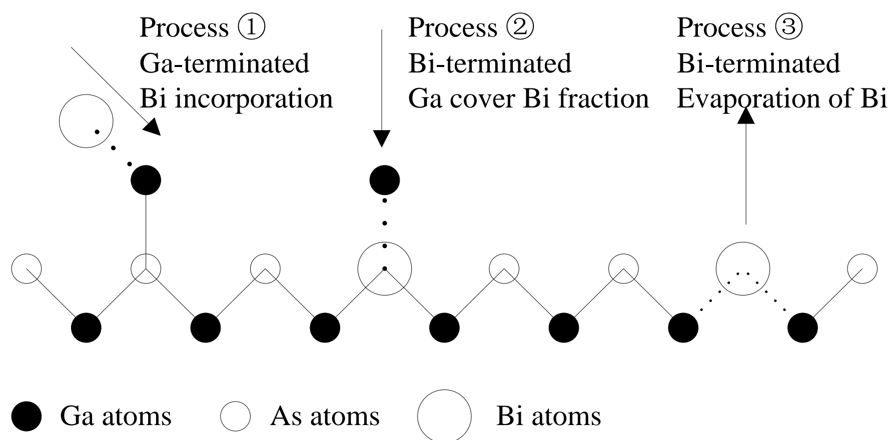

Figure 4.7. The processes of Bi incorporation in [119]

Equation 4.4 has been given based on the three processes. a_1 is a constant which represents the combination rate of Ga atoms from Ga flux with Bi-terminated sites. a_2 is a pre-exponential factor.

$$\frac{dx}{dt} \propto \theta_{Ga}\theta_{Bi} - a_1 x F_{Ga} - a_2 x \exp\left(-\frac{U_1}{kT}\right) \tag{4.4}$$

The author adopted equation 4.3 from Lu's Model as the second component of his model. Since there are 3 unknowns in this model, while only 2 exists in Lu's Model, the author proposed a third equation.

$$\frac{d\theta_{As}}{dt} = F_{As}\theta_{Ga}\sum_{n=0}^{\infty}\left[(1-\theta_{Ga})(1-P_{As})\right]^n - F_{Ga}\theta_{As}\sum_{n=0}^{\infty}\left[(1-\theta_{As})(1-P_{Ga})\right]^n \tag{4.5}$$

The equation is based on a hopping hypothesis. Ga atoms will stick to the As-terminated area θ_{As} with a unity coefficient, and As atoms will stick to the Ga-terminated area θ_{Ga} with a unity coefficient. However, when As atoms land on the As-terminated surface, they either are desorbed with probability P_{As}, or hop to a new site with probability 1-P_{As}. When Ga atoms land on a Ga-terminated surface, they can form Ga-Ga droplets with probability P_{Ga}, or hop to a new site with probability 1-P_{Ga}. In paper [119], the values of the parameters are $a_1 = 0$, $P_{As} = 0.12$, $P_{Ga} = 0.001$, $U_1 = 0.28$ eV, $a_2 = 3300$. $U_0 = 1.8$ eV. $b = 2\pi\sigma_0/\omega_0$, $\sigma_0 = 0.2$ nm^2, $\omega_0/2\pi = 10^{12}$ s^{-1}, so $b = 2\times10^{-13}$ nm$^2\cdot$s.

Figure 4.8 shows the comparison between Lewis's model and Lu's model. The experimental data of Bi contents are obtained from PL measurements. The data matches the trend of Lewis's model, but there is some experimental scatter. As pointed out in [119], the desorption probability of arsenic atoms when landing on Ga-terminated sites, P_{As}, is temperature dependent, but it is regarded as a constant since the temperature is relatively low in GaAsBi growth regime. From Figure 4.8, a much better fit of Lewis's model with experimental data is observed compared to Lu's model. All the parameters in both models used to get the curves are from the papers [118][119]. This great mismatch of Lu's model with real data can be that either some of the parameters provided in [118] are not quite right, or Lu's model can only match the situation in a certain range. In [118], only the result of Bi content as a function of Bi/As was provided.

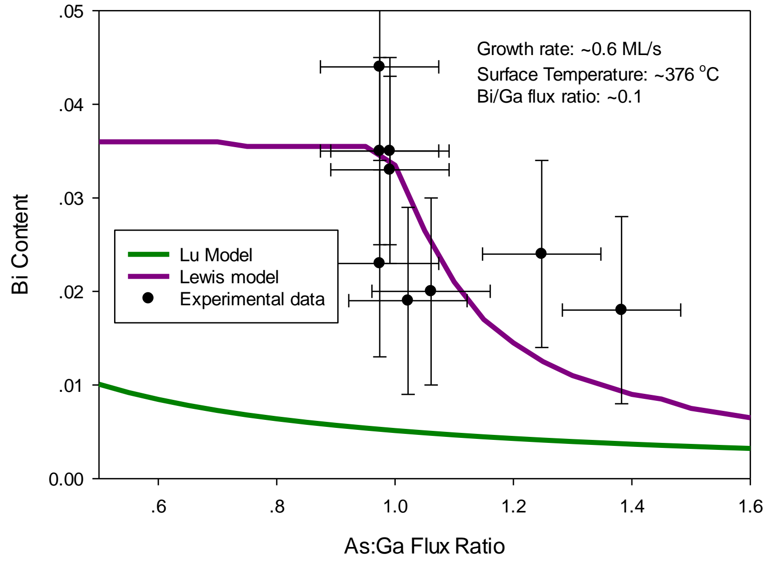

Figure 4.8. Bi Content as a function of As:Ga Flux ratio compared with simulation results of Lewis's model and Lu's model

4.3. Analysis of previous models

Both of the two models claimed the existence of an amorphous Bi metallic layer on top of the GaAsBi surface, though there is no strong evidence to prove this idea. This idea is based on the surfactant function of Bi during growth of different materials such as GaAs, InGaAs, GaAsN, etc. When supplying a certain amount of Bi flux, they tend to stick on the surface and change the surface reconstruction. At typical GaAs growth temperature, RHEED shows that the (2×4) pattern is changed to (n×3) which might be due to Bi atoms sitting on As-terminated sites [41]. However, the Bi atoms on the surface tend to move upwards staying at the surface during growth, and thus nearly no Bi atoms are incorporated. Though from the behaviour of Bi atoms on surface, the situation is more complicated (e.g. Bi atoms on Ga-terminated sites and Bi atoms on As-terminated sites must have different behaviours), the simplified treatment of regarding Bi atoms on surface as an amorphous layer is, to some extent, reasonable.

From both Equations 4.1 and 4.3, and Figures 4.4 and 4.5, it is clear that both models assumed that the only source of incorporated Bi atoms to the 'real' surface is the amorphous metallic layer. It is not hard to deduce that the whole Bi flux only contributes to the metallic layer instead of partly to the lower 'real' surface based on the assumption. In this case, the net flux should be F_{Bi} instead of F_{Bi}-xF_{Ga}. In addition, the Bi atoms in the metallic layer will decrease not only by desorption, but also by incorporation into the lower surface. Under the above considerations, Equation 4.2 should be changed as following:

$$\frac{d\theta_{Bi}}{dt} \propto (1-\theta_{Bi})C_{Bi}F_{Bi} - \theta_{Bi} \cdot \frac{1}{b}\exp\left(-\frac{U_0}{kT}\right) - \Delta \tag{4.6}$$

C_{Bi} is the probability that an incident Bi atom will form part of the metallic layer rather than instantly desorbing. At low temperature, it has a high probability to be unity. b is a pre-exponential factor (attempt frequency depending on the desorption barrier). The third part at the right side of Equation 4.6 (Δ) represents the amount of Bi atoms incorporated into lower surface from metallic layer. In the steady state, the left side of the equation should be 0.

As described in Lu's Model, Figure 4.6 implies that in steady state, Bi atoms bonded by Ga atoms should be the same as Bi atoms knocked out by As atoms. If that is the case, no Bi will be incorporated into the bulk. In Lewis's Model, besides the two processes, Bi atoms will be buried into the lower layer when Ga atoms land on Bi atoms, and decrease the amount of Bi on the surface. Therefore, in my view, Lewis Model considers more comprehensively than Lu's Model, since it includes Bi incorporation into the bulk.

However, Lewis assumed that when Ga atoms land on Bi-terminated sites, the behaviour is the same as on Ga-terminated sites. Based on this assumption, the author said that the second part of Equation 4.4 can be neglected ($a_1 \approx 0$ in Equation 4.4), since Ga-Ga bonds are almost impossible to form (which means that Ga-Bi bonds are in the same situation). If that is the case, Bi is rarely buried into the material, which leads to no incorporation of Bi.

If Ga atoms land on Bi-terminated sites, it is with high probability that As-Bi-Ga bonds can be formed with unity probability (similar to Ga atoms on As-terminated sites), as shown in process 1 in Figure 4.9.

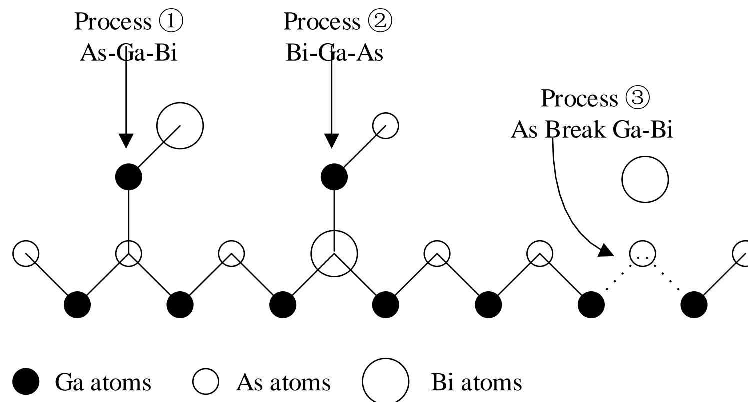

Figure 4.9. A possible revision of Lu's Model

So one possible revised version of Equation 4.1 in Lu's Model can be as following which only considers As-terminated sites and Bi-terminated sites:

$$\frac{dx}{dt} \propto \theta_{Bi} F_{Ga} (1-x) - xF_{Ga} - \left[F_{As} - (1-x) F_{Ga} \right] x \cdot a \exp\left(-\frac{U_1}{kT} \right) \tag{4.7}$$

The first part of the right side of the equation is the Bi incorporated into the surface layer when Ga atoms land on As-terminated sites and Bi atoms are in the meantime provided by the metallic layer to form As-Ga-Bi bonds (process 1 in Figure 4.9). The second part represents the Bi atoms buried into the lower layer by Ga atoms when Ga atoms land on Bi-terminated sites to form Bi-Ga-As bonds (process 2 in Figure 4.9), if we assume a unity sticking coefficient of Ga atoms on Bi-terminated sites. The third part is the Bi atoms knocked out from the surface layer to the metallic layer by excess As atoms (process 3 in Figure 4.9). If we consider that a part of As atoms in the incident flux contributes to GaAs before them act on Bi atoms, the net flux should be changed from F_{As} to F_{As}-(1-x)F_{Ga}.

From Equation 4.7, the first part and the third part of the right side is related to the change of Bi atoms between metallic layer and surface layer, and the second part is the incorporation of Bi atoms into the bulk. In steady state, the left side of Equation 4.6 should be 0, which means that the increase rate of Bi atoms from metallic layer to surface layer is equal to the rate of Bi atoms into the bulk. In this case, the third part of Equation 4.6 here is $\Delta = xF_{Ga}$.

A complete model is thus established based on Equations 4.6 and 4.7. A comparison of this model, Lu's [118] and Lewis's [119] is shown in Figures 4.10 and 4.11. The model displays the transition from Bi flux limited to temperature limited incorporation accurately.

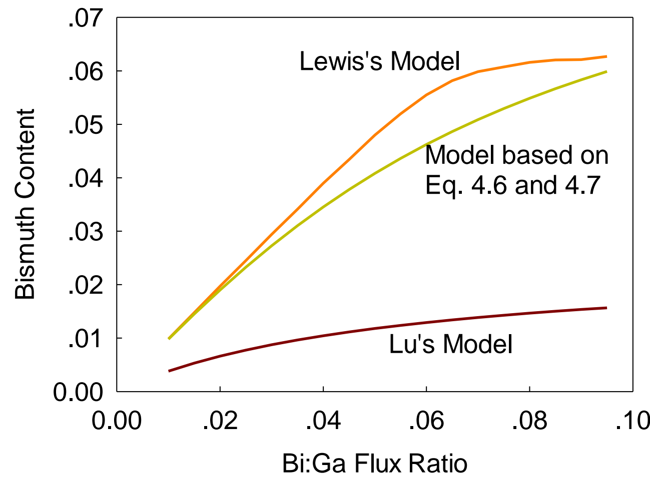

Figure 4.10. Comparison of three models where the growth rate is 0.55 ML/s, the surface temperature is ~ 320 °C, and the As:Ga atomic flux ratio is 1 (assuming As_2 is used).

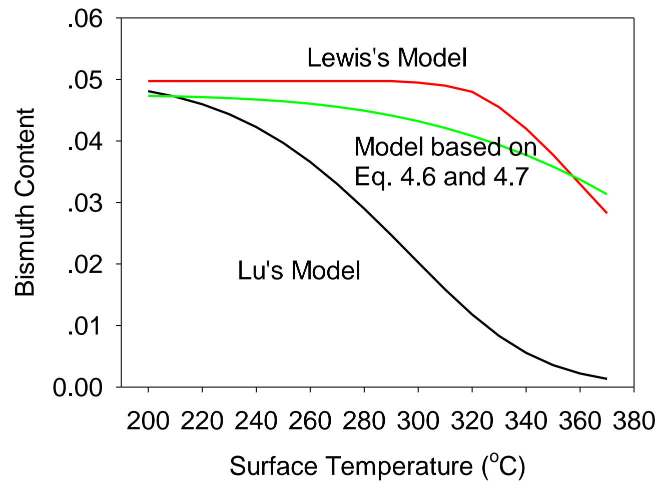

Figure 4.11. Comparison of the models where the growth rate is 0.55 ML/s, the Bi:Ga atomic flux ratio is 0.05, and the As:Ga atomic flux ratio is 1 (assuming As_2 is used).

However, there are still some issues yet to be discussed. The first is that: is it fair to regard that only As-terminated sites and Bi-terminated sites exist during growth? Although it is possible that when a site is Ga-terminated, it will soon be occupied by As or Bi atoms. The second is that: it is hard to tell if the desorption of Bi atoms from the surface layer to the metallic layer is related to As flux or not. The third is about the value of the As net flux even if the Bi desorption is related to As flux. When $F_{As} < (1\text{-}x)F_{Ga}$, the As net flux becomes 0, which is clear that it does not quite reflect the truth, since there should still be some As atoms moving around the surface.

In this case, the way of considering atom behaviours in Lewis's model seems to be more comprehensive. Lewis's model assumes that there are a considerable number of Ga-terminated sites on the surface. The changing of GaAsBi RHEED pattern from (n×3) in the static state to (2×1) during growth [120] provided an indirect evidence of the assumption. However, as mentioned above, the model assumes that when Ga atoms land on Bi-terminated sites, their behaviour is the same as landing on Ga-terminated sites, which leads no Bi incorporation into bulk. The better assumption should be regarding Bi-terminated sites as As-terminated sites.

In order to consider the problem in a more comprehensive way, a diagram of different atoms moving on the surface is drawn, which is shown in Figure 4.12. The top Ga and As atoms are directly from Ga flux and As flux respectively, and the top Bi atoms are from the amorphous metallic layer. Each atom has the possibility to land on three different types of sites, as shown from process 1 to 9 in Figure 4.12. When Ga atoms land on Ga-terminated sites, it has the probability $1\text{-}P_{Ga}$ to hop to other sites, as discussed before, and this hopping process is as shown in process 11 and 12. The similar hopping behaviour of As atoms is shown in process 13 and 14. The Bi atoms here are considered to be slightly different. There are seldom Bi atoms to land on Bi-terminated or As-terminated sites, since the Bi atoms are from amorphous layer, which already covers the whole surface area. Therefore,

process 7 and 9 can be ignored. Besides, the Bi atoms have the possibility to be desorbed back into the metallic layer, which is shown as process 10 in Figure 4.12.

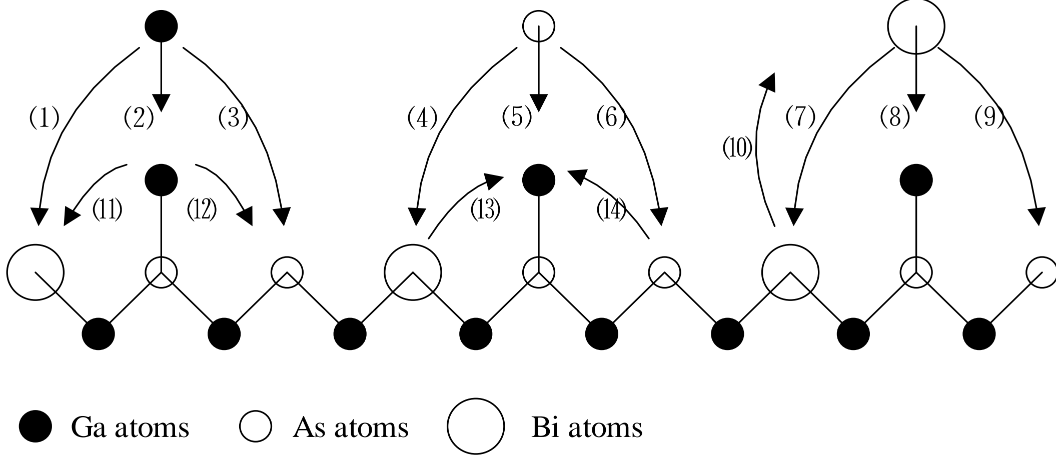

Figure 4.12. The behaviours of different atoms on GaAsBi surface

In Figure 4.12, a complete diagram about all the atoms moving around the growth surface is thus established. Before further discussing, it is better to clarify the notations that would be used. Previously, θ_{Bi} was used in Lu's and Lewis's models as the coverage of Bi amorphous layer. However, it is not consistent with the definitions of θ_{Ga} and θ_{As}. In this case, φ_{Bi} is chosen to replace θ_{Bi}, and θ_{Bi} will be the percentage of Bi-terminated sites on the surface.

If we only consider about the processes related to the increase and decrease of As atoms on the surface, processes 3 and 12 are responsible for the decrease of As atoms, and processes 5, 13 and 14 are for the increase of As atoms. The chance of Ga atoms landing on Ga terminated sites (process 2) would be proportional to θ_{Ga}. There is little chance for Ga atoms to stay on and form Ga droplets with a probability of P_{Ga} which is near 0. The Ga atoms would then hop around to find new sites (process 11 or 12, or repeat process 2). In this case, the chance for Ga atoms to land on As-terminated sites at the first time would be proportional to θ_{As}, and to land on Ga-terminated sites first, and then land on As-terminated sites would be proportional to $\theta_{\mathrm{Ga}}(1- P_{\mathrm{Ga}})\theta_{\mathrm{As}}$, to land on As-terminated sites at the third time would be proportional to $\theta_{\mathrm{Ga}}(1- P_{\mathrm{Ga}})\theta_{\mathrm{Ga}}(1- P_{\mathrm{Ga}})\theta_{\mathrm{As}}$, and so on. Thus the probability that Ga atoms finally land on As-terminated sites would be the sum of the above probabilities, which is proportional to the following:

$$\theta_{As} + \theta_{Ga}\left(1-P_{Ga}\right)\theta_{As} + \cdots + \left[\theta_{Ga}\left(1-P_{Ga}\right)\right]^n \theta_{As} + \cdots = \theta_{As}\sum_{n=0}^{\infty}\left[\theta_{Ga}\left(1-P_{Ga}\right)\right]^n \tag{4.8}$$

Similarly, the behaviour of As atoms can also be deduced in the same way. Therefore, Equation 4.9 is obtained to describe the increase and decrease of As atoms on the surface:

$$\frac{d\theta_{As}}{dt} \propto F_{As}\theta_{Ga}\sum_{n=0}^{\infty}\left[\left(1-\theta_{Ga}\right)\left(1-P_{As}\right)\right]^n - F_{Ga}\theta_{As}\sum_{n=0}^{\infty}\left[\theta_{Ga}\left(1-P_{Ga}\right)\right]^n \tag{4.9}$$

In steady state, the left side of the equation should be 0.

If we consider about the processes related to the changing of Bi atoms on the surface, process 8 is to increase Bi atoms, process 10 is to desorb Bi atoms to metallic layer, and processes 1 and 11 are to bury Bi atoms to bulk. Based on this analysis, the following equation is obtained:

$$\frac{d\theta_{Bi}}{dt} \propto c\theta_{Ga}\varphi_{Bi} - \theta_{Bi} a \exp\left(-\frac{U_1}{kT}\right) - \theta_{Bi} F_{Ga} \sum_{n=0}^{\infty} \left[\theta_{Ga}\left(1-P_{Ga}\right)\right]^n \tag{4.10}$$

where a is a pre-exponential factor, and U_1 is the activation energy for Bi atoms to be thermally desorbed to the metallic layer. c here is a constant which represents the combination rate of Bi atoms from metallic layer with Ga-terminated sites.

A simple diagram (Figure 4.13) shows the detailed behaviour of the amorphous Bi metallic monolayer. Process 1 in Figure 4.13 is to desorb Bi atoms from the metallic layer, and process 2 is to adsorb Bi atoms from Bi flux. Processes 3 and 4 in Figure 4.13 are corresponding to processes 8 and 10 in Figure 4.12 respectively.

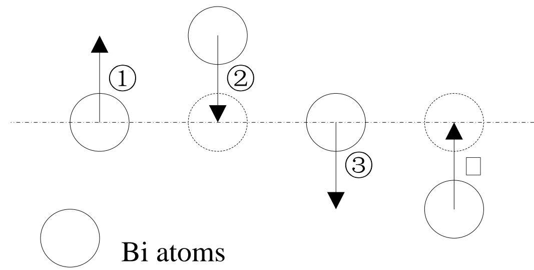

Figure 4.13. The behaviour of Bi atoms in the metallic layer

According to Equation 4.9, in Figure 4.12, the combination of processes 8 and 10 should be equal to the combination of processes 1 and 11. In this case, the following equation is obtained which is from Equation 4.6 if we assume $C_{Bi} = 1$.

$$\frac{d\varphi_{Bi}}{dt} \propto -c\theta_{Ga}\varphi_{Bi} + \theta_{Bi} a \exp\left(-\frac{U_1}{kT}\right) + \left(1-\varphi_{Bi}\right)F_{Bi} - \varphi_{Bi} \cdot b \exp\left(-\frac{U_0}{kT}\right) \tag{4.11}$$

where b is a pre-exponential factor, and U_0 is the activation energy for Bi atoms to be desorbed from the metallic layer. Combining Equations 4.8-4.10, θ_{Bi} can be solved out. Since the surface is in a dynamically balanced situation, the percentage of Bi-terminated sites on the surface would maintain a constant during growth, and the Bi incorporation rate x is then equal to $\theta_{Bi}/(\theta_{Bi}+\theta_{As})$.

The modelling results compared with experimental data in the aspect of Bi content vs. growth temperature and Bi content vs. Bi:Ga flux ratio are shown in Figure 4.14 and Figure 4.15 respectively. The experimental results are from a recent sample set STF9 grown by Thomas Rockett. However, the change of the parameter As:Ga flux ratio was not included in that set, and thus the comparison

between modelling results and experimental data cannot be provided. To fit the data, the parameters are selected as following: P_{Ga} = 0.001, P_{As} = 0.02, U_0 = 1.8 eV, U_1 = 0.9 eV, $a = 3\times10^8$ nm^{-2}s^{-1}, $b = 5\times10^{13}$ nm^{-2}s^{-1}, and c = 15 nm^{-2}s^{-1}.

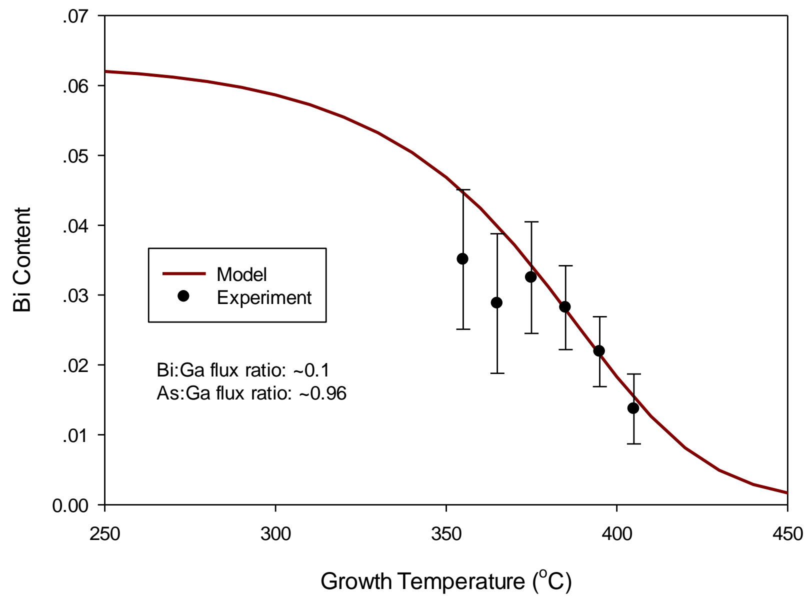

Figure 4.14. Modelling results compared with experimental data. Bi:Ga flux ratio is around 0.1, and As:Ga flux ratio is around 0.96.

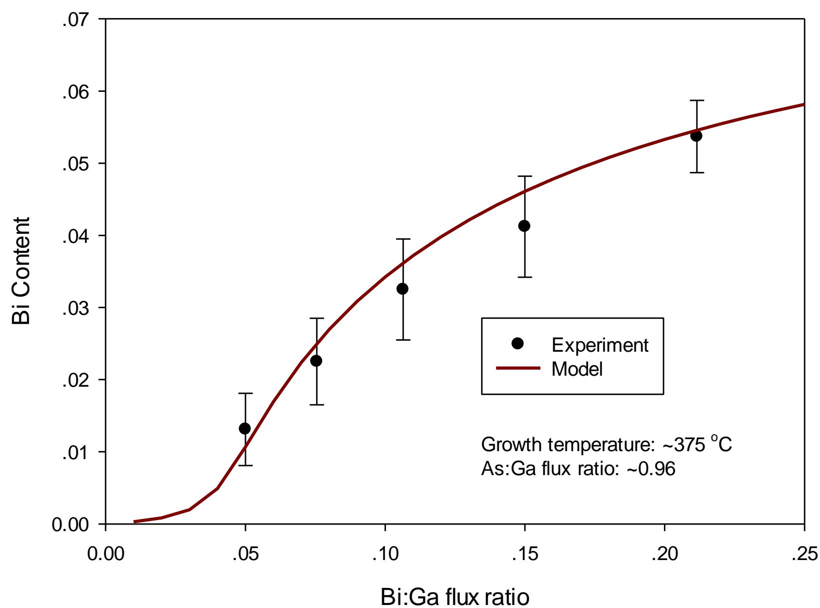

Figure 4.15. Modelling results compared with experimental data. Growth temperature is around 375 °C, and As:Ga flux ratio is around 0.96.

Further discussion can be made to consider that there is no such metallic Bi amorphous monolayer on top of the surface, since during growth, the RHEED pattern changes from (n×3) to (2×1), which means Bi dimers sitting on Ga-terminated sites. In this case, the source of Bi atoms becomes directly from Bi flux. Besides, the processes related to the change of Bi atoms on the surface are still 1, 11, 8 and 10. However, considering that Bi atoms might move around the surface, it is reasonable to assume a similar hopping behaviour of Bi atoms as Ga and As atoms. If we define that the desorption probability of Bi atoms landing on Bi-terminated or As-terminated sites is P_{Bi}, the following equation can be established:

$$\frac{d\theta_{Bi}}{dt} = F_{Bi}\theta_{Ga}\sum_{n=0}^{\infty}\left[(1-\theta_{Ga})(1-P_{Bi})\right]^n - F_{Ga}\theta_{Bi}\sum_{n=0}^{\infty}\left[\theta_{Ga}(1-P_{Ga})\right]^n - a\theta_{Bi}\exp\left(\frac{-U_0}{kT}\right) \quad (4.12)$$

Based on Equations 4.9 and 4.12, the Bi content can also be calculated, and modelling results compared with experimental data can be shown in Figure 4.16 and 4.17. The experimental data is provided by Robert Richards according to previous growth records. However, it seems that the hopping assumption cannot explain Bi sticking on As-terminated sites quite well. Besides, this model does not have the scope to describe effects such as the surfactant function of Bi atoms.

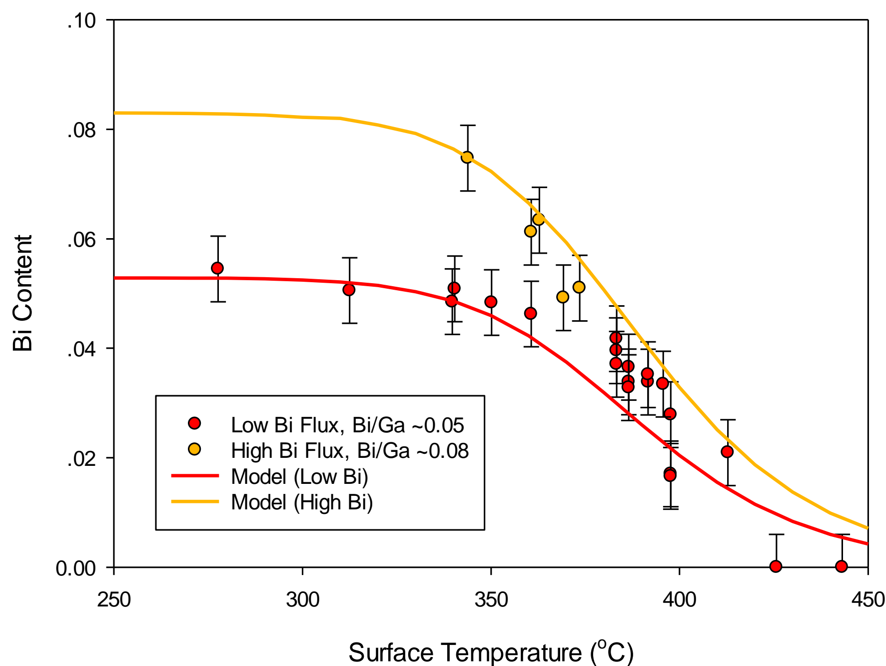

Figure 4.16. Bi content vs. surface temperature. As:Ga atomic flux ratio is around 1, growth rate is around 1ML/ss.

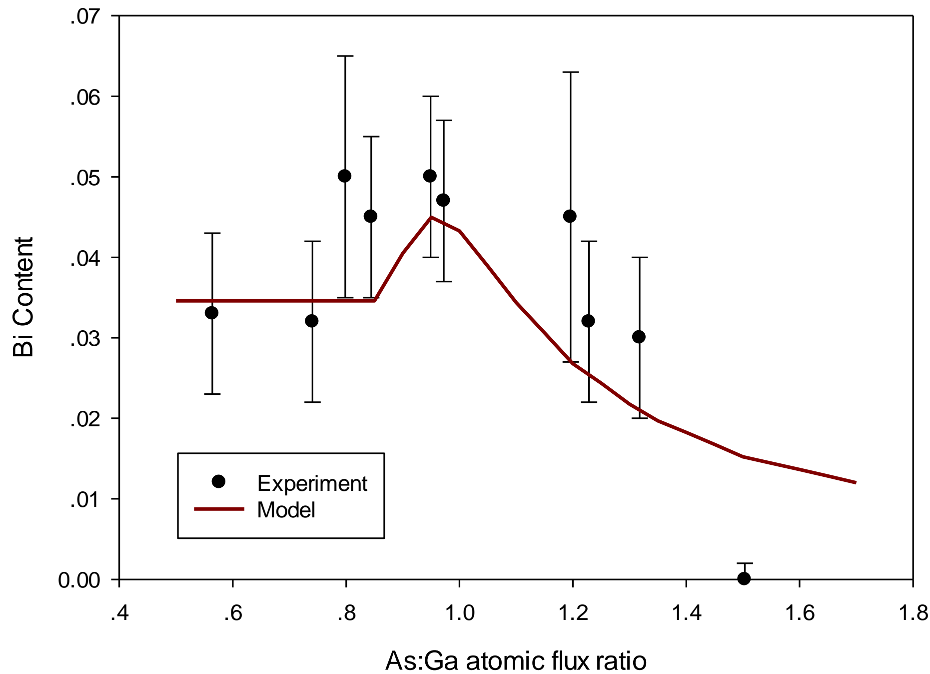

Figure 4.17. Bi content vs. As:Ga atomic flux ratio. Surface temperature during growth is around 365 °C, growth rate is around 1ML/s.

Nonetheless, the thought of non-existence of Bi amorphous layer provides a different angle to see the problem. To think about this problem completely, different types of atoms should have similar behaviours; only the extent of each behaviour in different atoms would be different. For example, Bi might be able to stick on As-terminated sites, so as that As atoms sticking on Bi-terminated or As-terminated sites. The behaviours are depending on the binding energy of different bonds (e.g. Bi-Ga, Bi-Bi, As-Ga, As-Bi).

5. Summary

This chapter investigated the growth of GaAsBi. There are four important growth parameters for bismide growth: the growth temperature, the As:Ga flux ratio, the growth rate, and the Bi flux. During bismide growth, the growth temperature should be low enough, and the As:Ga flux ratio should be stoichiometric to get Bi incorporated. When the Bi flux is low, the growth would be in the kinetic limited regime, in which Bi incorporation is proportional to Bi flux. With increasing Bi flux, the growth would reach the temperature limited regime, and the incorporation would no longer be related to Bi flux. Besides, the growth rate would affect the quality of the surface, since the increasing amount of Ga atoms would make Bi atoms harder to behave as a surfactant.

The surface reconstruction was discussed in Section 3 of this chapter. In static state, the surface reconstruction pattern of GaAsBi is usually ($n\times3$), in which case the Bi atoms are landing on Ga-

terminated sites. During growth, the (2×1) pattern appears, which shows that Bi atoms have the chance to form Bi-Ga bonds. Besides, the metallic property of (2×1) surface can be used to explain the surfactant function of Bi during growth.

Previous growth models (Lu's and Lewis's) were discussed in detail in Section 4. Based on their work, a more comprehensive model was proposed considering more complete atom behaviours. The Bi metallic layer assumption was adopted as the source of incorporated Bi atoms. Langmuir equation was adapted to describe the behaviour of the metallic layer. When discussing the behaviour of the real surface, three different terminated sites were considered, and 13 processes were proposed to cover all the atom moving possibilities. A hopping assumption was adopted to describe the Ga and As atoms when they land on Ga- and As-terminated sites respectively. The differences between this model and the previous models are mainly about two points: 1, it considered the Bi incorporation into bulk, and 2, Bi-terminated sites are more to behave as As-terminated sites, rather than Ga-terminated sites. Besides, a different model without considering an amorphous metallic layer was also discussed. The discussion gives an insight into how incorporation works, which can help people to understand the growth mechanism better, and to improve the incorporation rate and growth quality.

Chapter 5: Absorption Properties of GaAsBi Based p-i-n Heterojunction Diodes

1. Growth structure of GaAsBi samples

A set of samples named STD5 series were grown with our Omicron STM-MBE system by Danuta F Mendes (with sample structures as shown in Figure 5.1) to investigate the absorption properties of GaAsBi material in this work. After oxide removal, an n-doped GaAs buffer layer > 100 nm was grown at ~ 580 °C with As_2. The growth temperature used for the bismide layers was around 375 °C, while the growth rate was 0.55 ML/s. As_4 was used during bismide growth [121]. The bismuth flux was varied throughout the series to obtain different bismuth contents. The p+ GaAs region was grown at ~ 525 °C with As_2. The doping of the p+ region was around 2.8×10^{18} cm^{-3}.

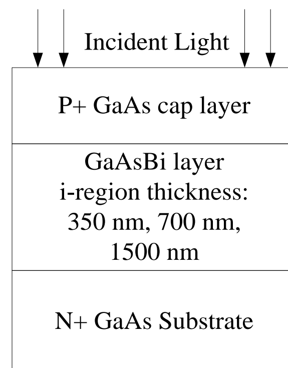

Figure 5.1. Sample structure of STD5 series

An interrupt technique was used in an attempt to prevent the formation of Bi droplets due to the accumulation of excess bismuth on the growth surface with high Bi:As flux ratio [112]. This technique involves a technique which is about growing inverted quantum well (GaAsBi/GaAs/GaAsBi) during GaAsBi layer growth (growing very thin GaAs layers inside the bismide layer). When growing a thick GaAsBi layer, if growth time is considered long enough, we would shut the Bi cell off for a very small period, and then turn it on again. The purpose of this technique is as an attempt to consume the segregated Bi atoms on the surface, and hope the segregated Bi atoms would be incorporated again. However, no evidence is very clear to show that this technique can reduce the chance of forming Bi droplets and improve the layer quality. This method was tested on two groups of samples, STE5 and STE8. The inverted quantum wells on STE5 are relatively broad (5 nm), and on STE8 are narrower (2.5 nm). It seemed that the growth interrupt technique gave small increases in layer quality with an oversupply of the bismuth flux, however more data is needed.

The samples were divided into 3 groups based on their i-region thicknesses. Brief information of each sample in STD5 series is provided in Table 5.1.

Table 5.1. Brief information of STD5 series samples

i-region thickness	350 nm	700 nm	1500 nm
Bi: ~ 2.3 %	STD51, STD52, STD55, STD56	STD57	STD5A
Bi: ~ 3.5 %		STD58, STD59	STD5B

Room temperature PL of STD5 series as shown in Figure 5.2 is sufficient to measure the band-gap of a direct band-gap material such as GaAsBi. From PL measurements it is clear that the different bismuth fluxes give rise to two different band gaps throughout the series: 1.24 ± 0.02 eV and 1.16 ± 0.01 eV (see Figure 5.2).

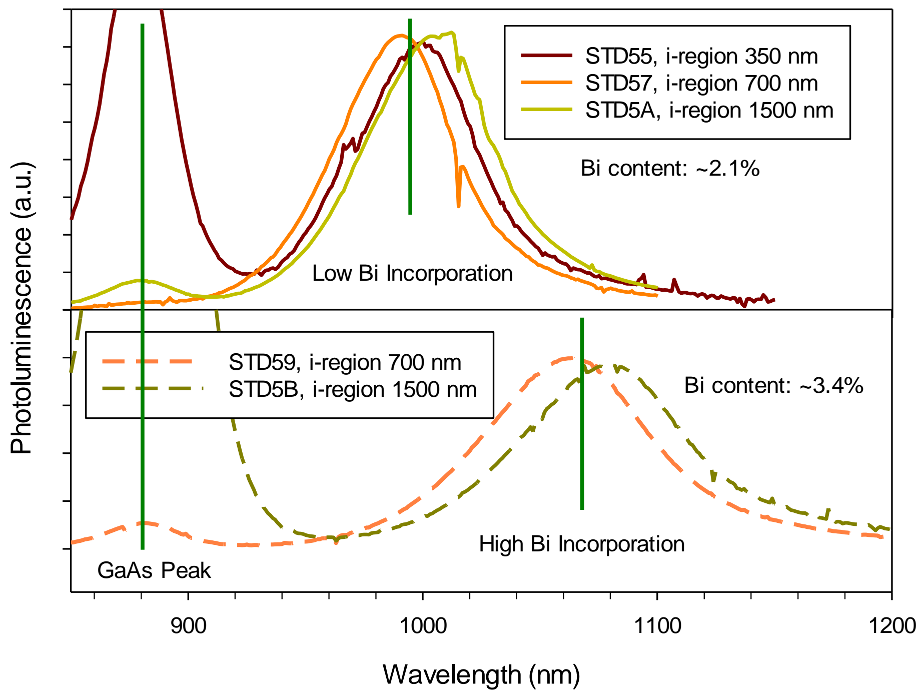

Figure 5.2. Normalized PL spectra from the samples grown in this work. Bi:Ga atomic flux ratio at top: ~ 0.05, at bottom: > 0.1

Combining with the VBAC model, the Bi contents in these samples can be calculated. The Bi contents are estimated to be around 2.1 % ± 0.3 % and 3.4 % ± 0.1 % from the valence band anti-crossing model [17][20]. Detailed results are shown in Table 5.2.

Table 5.2. The band-gap and bismuth incorporation information from PL peak position

Device	Peak (nm)	Band gap (eV)	Bi content (%)
STD51	985	1.26	1.8
STD52	1073	1.15	3.5
STD55	1000	1.24	2
STD56	1015	1.22	2.4
STD57	991	1.25	1.9
STD59	1064	1.16	3.3
STD5A	1012	1.23	2.3
STD5B	1079	1.15	3.5

2. IVCV measurements

2.1. Capacitance-Voltage

Even though bismuth can enhance the surface migration of the constituent atoms during growth and lead to a lower density of As and / or Ga related defects [45], there will still be some defects caused by the low growth temperature. Besides Bi can unintentionally increase background doping (as discussed in Chapter 1) possibly due to its isoelectric donor behaviour, Bi clusters and antisite defects [46]–[48]. The unintentional doping in the i-region and the i-region thickness can be obtained from CV measurements. Figure 5.3 shows the capacitance per unit area of the samples against reverse bias voltage from CV measurements. A test signal with ~60 mV amplitude and 1 MHz frequency was used for the measurements.

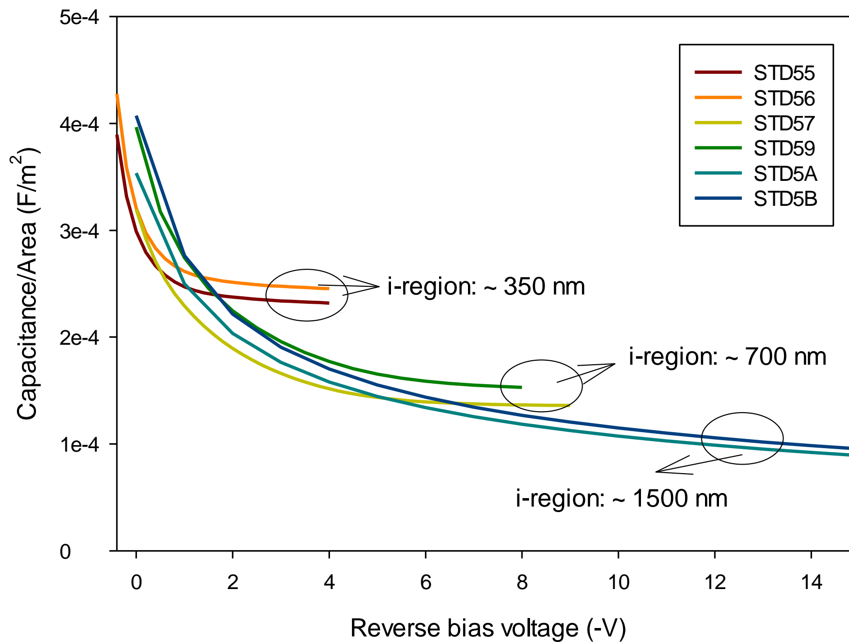

Figure 5.3. Capacitance-Voltage results of STD5 series

Figure 5.4 shows the plot of $1/C_D^2$ with bias voltage in the samples, where built-in self-voltages can be estimated. The 'saturation' shape at higher bias voltage in Figure 5.4 (e.g. $1/C_D^2$ of STD57 linearly goes up with reverse bias until ~ 5 V, and becomes flat) is due to the fully-depletion of i-region. When the device reaches a fully-depleted i-region, the doping density at the edge of depletion region increases dramatically, which makes the value of $1/C_D^2$ increase slowly with the bias voltage.

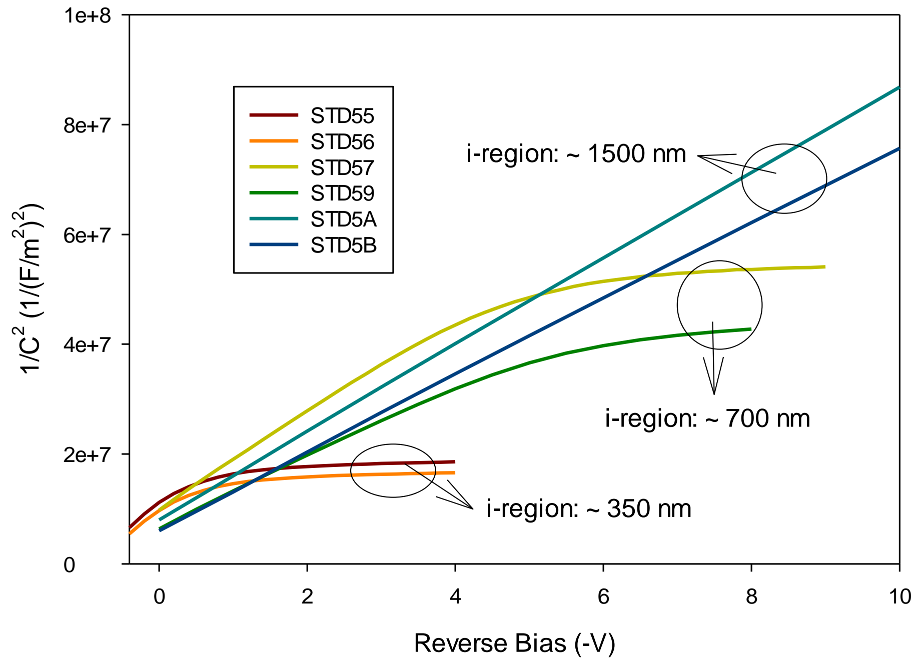

Figure 5.4. $1/C_D^2$ with bias voltage on STD51-STD5B

Based on the direct relationship between depletion width in the i-region and bias voltage (recorded in Appendix 3), the doping density of each sample as a function of depletion width was obtained, which is shown in Figure 5.5. In Figure 5.5, the doping density at first maintains a nearly constant value when the depletion width is small, which means that the depletion region extends in the i-region (i.e. the i-region is partially depleted), and the value can be regarded as the doping density in the i-region. The doping density would then go up dramatically at a certain depletion width, indicating that the edge of depletion region meets a much higher doping region (i.e. the i-region is fully-depleted), and the certain depletion width can be regarded as the i-region thickness. The doping densities of all the samples are approximately $1.2 - 2 \times 10^{16}\,cm^{-3}$ from Figure 5.5. The estimated i-region thicknesses of the samples are recorded in Table 5.3.

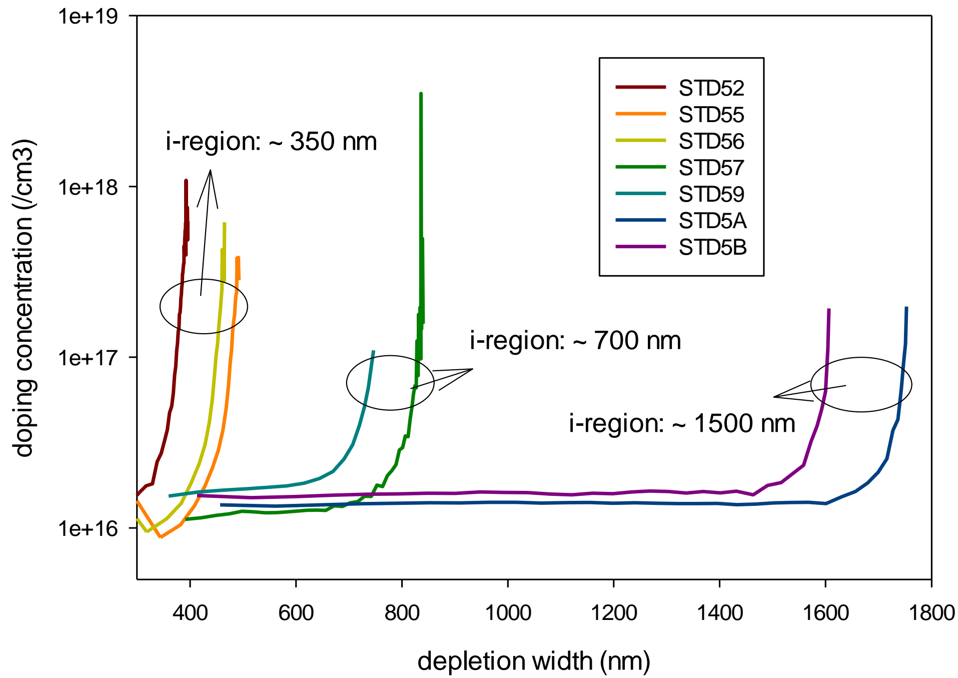

Figure 5.5. Doping profile of STD5 series

Table 5.3. i-region thicknesses of STD5 series

sample	Intended i-region thickness	i-region thickness from CV
STD52	350 nm	360 nm
STD55	350 nm	460 nm
STD56	350 nm	440 nm
STD57	700 nm	820 nm
STD59	700 nm	730 nm
STD5A	1500 nm	1740 nm
STD5B	1500 nm	1600 nm

2.2. Current-Voltage

Current-voltage (IV) characterisation of STD5 series devices shows clear diode-like characteristics (shown in Figure 5.6). The forward IV scales with area in all the samples. Since current-voltage equation has an exponential form, the logarithmic plot has the shape of a straight line. The saturated current J_0 and ideality factor n can be obtained by fitting the curve. The ideality factor of these devices in forward bias is nearly 2, which indicates that there is significant recombination in the depletion region. The forward curve is only shown up to 0.8V, above which the series resistance effect becomes significant. The reverse leakage currents were below 0.1 A/m^2 at -1 V at all samples except STD59. The high reverse leakage current may be due to the presence of dislocations caused by

strain relaxation, since the samples are all thicker than the Matthews-Blakeslee critical layer limit [122].

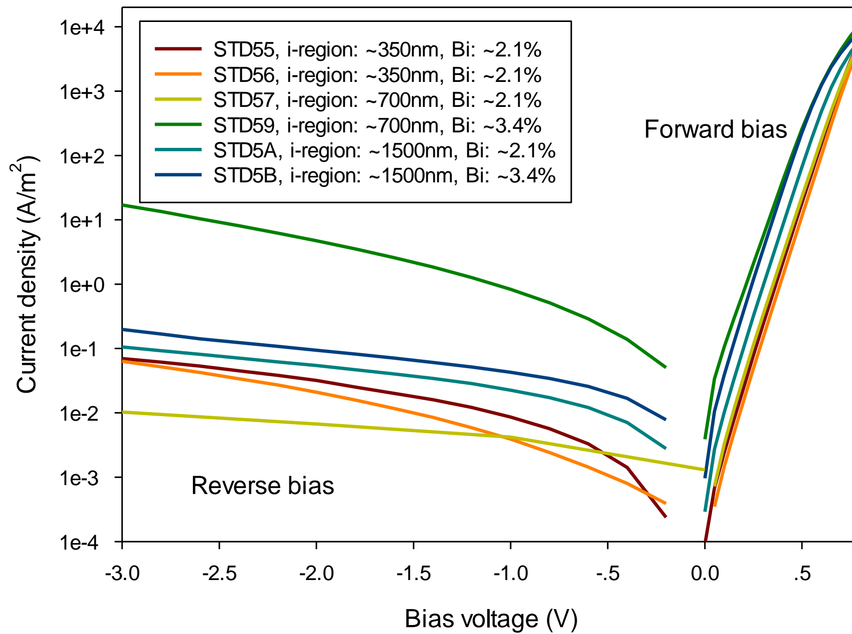

Figure 5.6. Current-Voltage results of STD5 series in forward bias and low reverse bias

The reverse currents of STD5 series up to breakdown are shown in Figure 5.7. Current-Voltage (IV) measurements in reverse bias show the breakdown voltages are roughly -17V, -28V and -43V for the three different thickness samples, STD51, STD57 and STD5A respectively. If we scale the dark current densities with the electric field, it is clear that the currents show similar behaviour as a function of electric field from Figure 5.7(b), which indicate that the breakdown field for these samples is 4 - 5 $\times$ 10^5 V/cm, which is almost the same as GaAs [123].

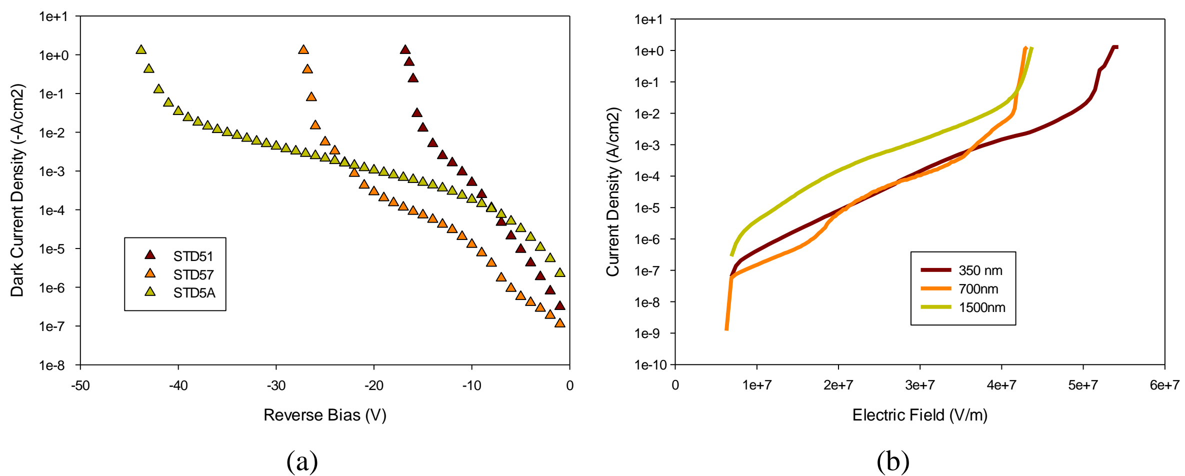

(a) (b)

Figure 5.7. (a) Current density with reverse bias, (b) Current density with electric field

3. Photocurrent measurements

3.1. Photoresponsivity and quantum efficiency

In order to investigate the absorption coefficient and its related characteristics, photocurrent measurements were first taken only on the fully-depleted thinner devices (350nm and 700nm), since the thickest i-region (1500nm) devices require a relatively high reverse bias to be fully-depleted and the Franz-Keldysh effect [124] might become significant. According to the CV measurements, the highest reverse bias voltage necessary to fully-deplete the thinner devices was -6V, only producing a peak electric field of less than 10^5 V/cm across the i-region. Figure 5.8 shows a photocurrent spectrum with wavelength for part of thinner samples in STD5 series directly from the lock-in amplifier (LIA).

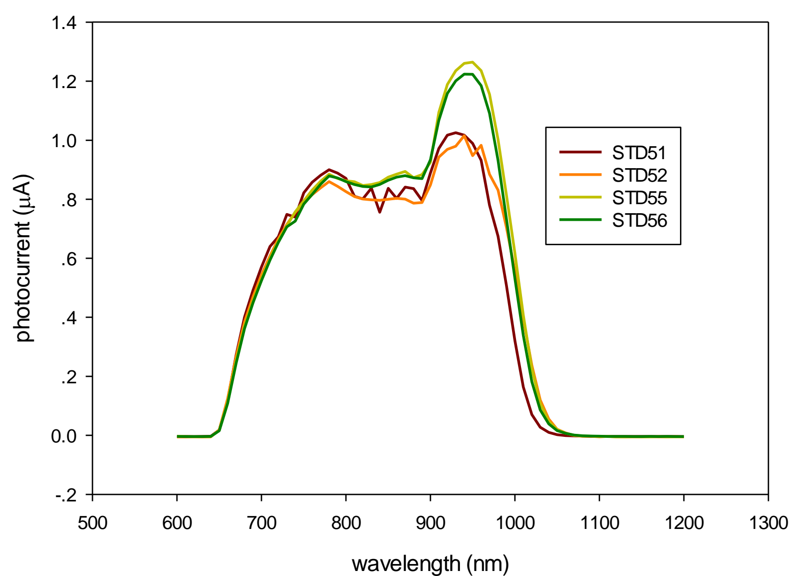

Figure 5.8. Raw photocurrent data from the setup

The photoresponsivity is the ratio of photocurrent with incident light intensity. Since the intensity of the light source is distributed following Planck's law, and through the monochromator and lenses, the intensity has been further attenuated with different degrees in different wavelengths, the light source intensity distribution needs to be determined. Two commercial devices have been used to detect the intensity of the light: one is silicon, and another is InGaAs. The reason of using two devices is to cover the whole range of desired wavelength (600nm-1300nm). Through measuring the photocurrent and comparing the data with the photoresponsivities of these two commercial photodiodes (from the datasheet of these devices), the intensity distribution of light source is determined. Figure 5.9 shows the light source intensity distribution in our setup.

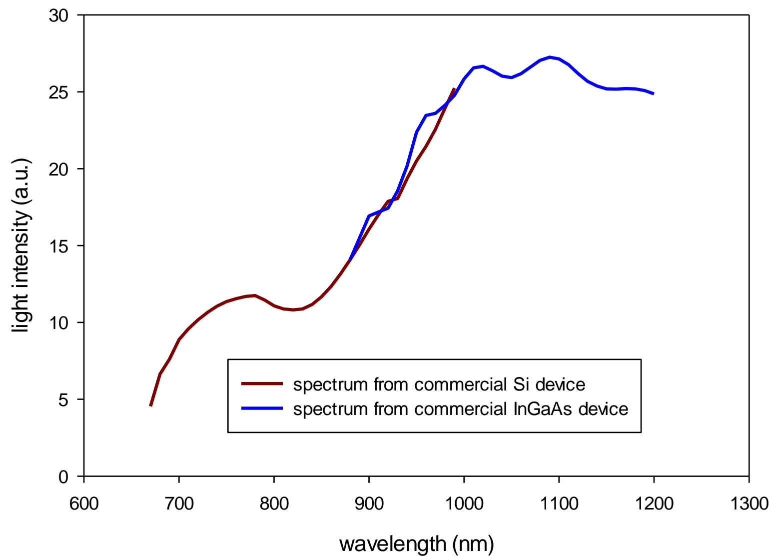

Figure 5.9. The intensity spectrum of light source in the photocurrent measurement setup

Another photocurrent setup with a laser as the light source is used to measure the real photoresponsivity in a specific wavelength. Combining the absolute responsivity, the intensity distribution of light source, and the photocurrent spectrum, the photoresponsivity spectrum of STD5 series was obtained (see Figure 5.10).

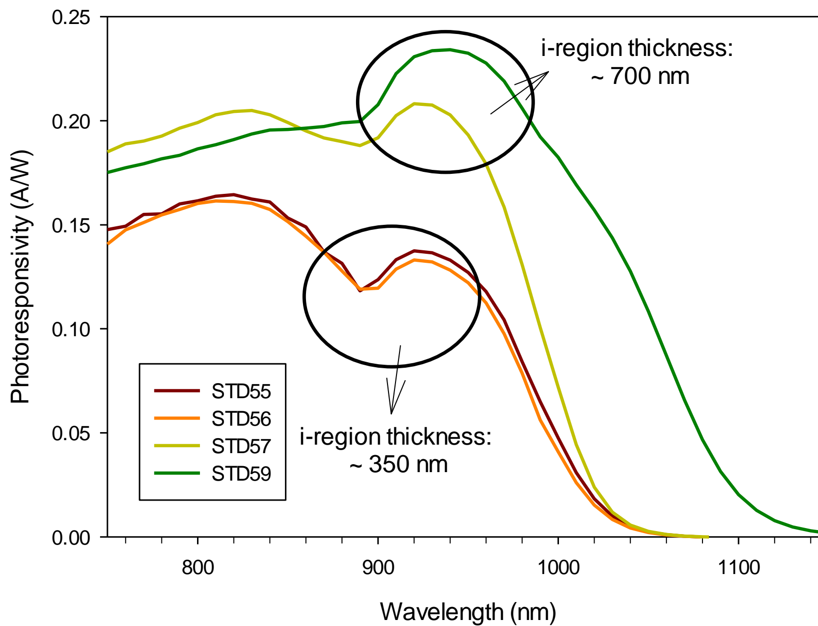

Figure 5.10. Photoresponsivity spectrum at a certain reverse bias (-2V)

Quantum efficiency is another very important concept in photocurrent measurement. It is the possibility that a photon can excite an electron to conduction band and contribute to the photocurrent.

A lot of things are needed to be considered during analysing quantum efficiency, since when an electron is generated, it has the chance to diminish by other ways such as recombination instead of being part of photocurrent. However, if we simply define the ratio of electron density in photocurrent with photon density in incident light as the external quantum efficiency, a direct relationship of quantum efficiency with photoresponsivity can be obtained:

$$Q_E = \frac{Rhc}{q\lambda} \tag{5.1}$$

Where R is the photoresponsivity, h is Planck's constant, c is the speed of light, q is the elementary electric charge, and λ is the wavelength of the incident photons. Figure 5.11 shows the calculated external quantum efficiency for the thinner samples in STD5 series.

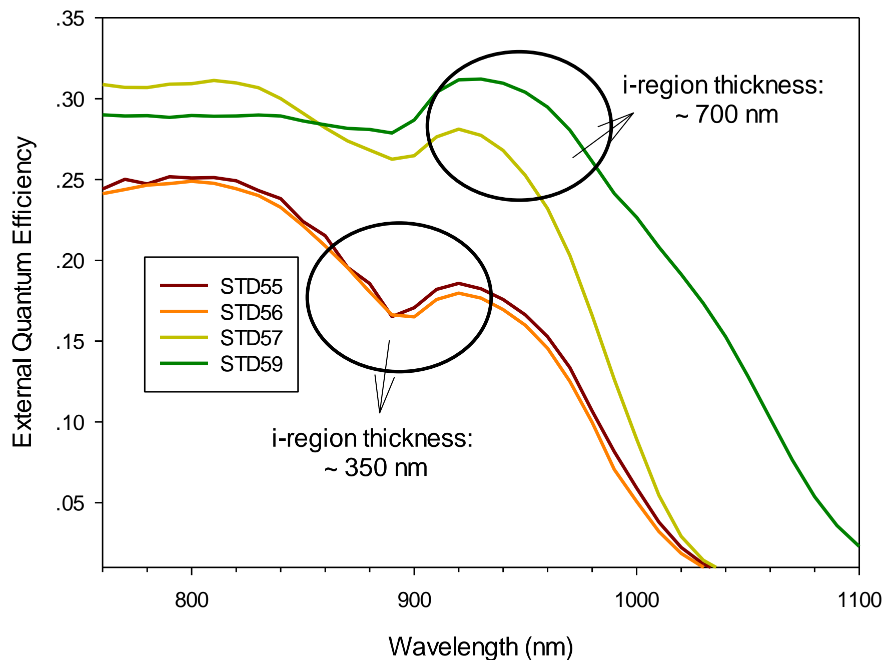

Figure 5.11. External quantum efficiency of samples in STD5 series calculated from photoresponsivity

3.2. Absorption coefficient

The photocurrent has already been deeply investigated through these years. The current has usually been regarded as the combination of drift current in depletion region and diffusion current in neutral zone, which is simple and accurate enough [104].

Any light of wavelength longer than 870 nm will only be weakly absorbed in the GaAs layer, so it is fair to assume that it is essentially only absorbed in the GaAsBi layer. If the GaAsBi layer is also

fully-depleted, all the generated carriers are collected as drift current. If a reverse bias is added to make i-region fully-depleted, the photocurrent can be expressed as:

$$J_{photo} = q\phi_0\left[1-\exp\left(-\alpha W_I\right)\right] \tag{5.2}$$

Here, q is elementary electric charge, ϕ_0 is the density of incident photons at the above edge of I-region, W_I is the thickness of i-region, α is the absorption coefficient. Therefore, absorption coefficients of GaAsBi layers for incident photon energies lower than 1.42 eV (GaAs band gap) can be obtained based on the absorption expression in [25]:

$$\alpha = -\frac{1}{W_I}\ln\left(1-\frac{R}{1-R_p}\frac{hc}{q\lambda}\right) \tag{5.3}$$

where R_p is the reflection coefficient of GaAs (~0.32 at the band-gap energy), and $hv = hc/\lambda$ is the incident photon energy. Since the band-gap of GaAs is 1.42eV, Equation 5.3 can only be used when incident photon energy is lower than 1.42eV. The absorption coefficients of the devices as a function of the incident photon energy are plotted logarithmically in Figure 5.12. There is a big difference of photoresponsivity between thick layer and thin layer (see Figure 5.11); whereas we can see the difference is diminished in the absorption coefficient spectrum in Figure 5.12. It is easy to find that the absorption coefficient is independent of the i-region thickness. The results are in an excellent agreement with previous measurements [25] from Figure 5.12.

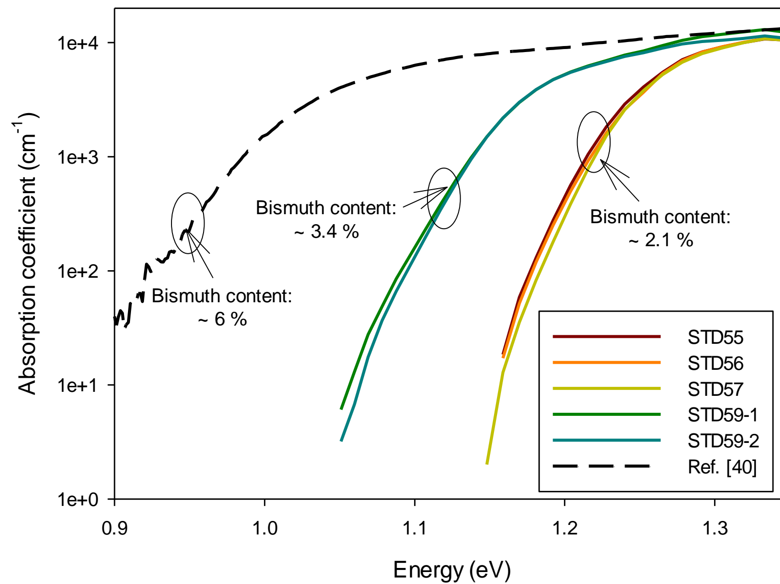

Figure 5.12. Absorption coefficient spectrum with incident photon energy, the 6% Bi content result is from [25]

The absorption coefficient for incident photons with energies greater than the band gap can be described by the Tauc relation [125], in which if the material is direct band gap, the absorption coefficient should satisfy:

$$\alpha(h\nu) \propto (h\nu - E_g)^{1/2} \tag{5.4}$$

where h is the Planck's constant, v is the frequency of incident photons, and hv is the energy. E_g is the band-gap energy.

From plotting the square of the absorption coefficient (Figure 5.13) against incident photon energy, straight lines are obtained, and the results agree with Equation 5.4, confirming that GaAsBi is a direct band gap material. The band gap can be estimated by extrapolating the plot to the intercept of the x-axis.

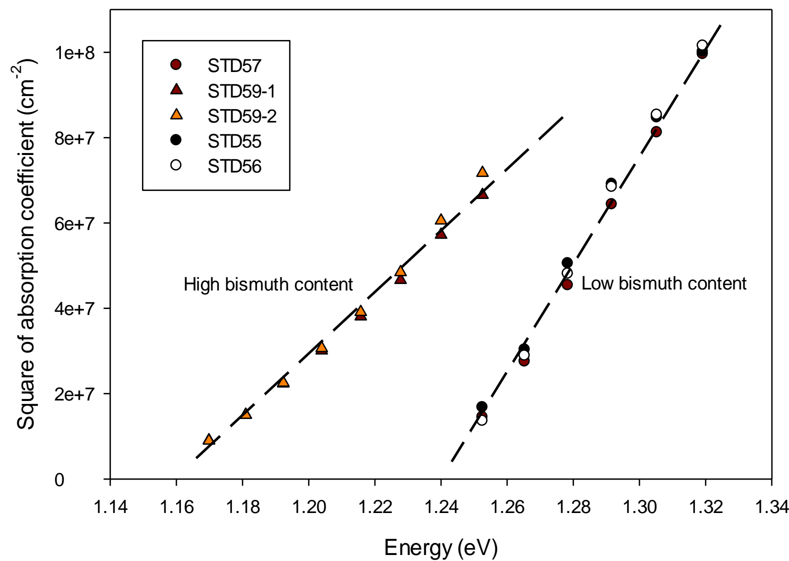

Figure 5.13. The square of absorption coefficient with incident photon energy

The band-gap of STD51, 52, 55, 56 and 57 is estimated as 1.24 eV ± 0.01 eV, and the band-gap of STD58 and 59 is estimated as 1.16 eV ± 0.01 eV (some of the results are not shown in this thesis). Comparing the result with Table 5.2, they match quite well. To some extent, absorption measurement is a more accurate method to estimate the band gap.

When the incident photon energy is below the band-gap, the absorption drops dramatically in an exponential way, and this exponential decay is named after Urbach [126]. An equation is proposed to describe this behaviour [127]:

$$\alpha(h\nu) = \alpha_g \exp\left(\frac{h\nu - E_g}{E_0}\right) \tag{5.5}$$

Here α_g is the absorption coefficient when the incident photon energy is equal to the band-gap. E_0 is a characteristic indicator that reflects the distribution of states due to lattice vibration, structural disorder and impurities [128]. From Figure 5.12, we can obviously observe the Urbach tail, and E_0 of each sample can be estimated by fitting the curve. E_0 is estimated as 17 ± 1 meV and 20 ± 0.5 meV for samples with low bismuth content and high bismuth content respectively. The results from [25] show that E_0 at 6 % bismuth content is approximately 24 meV. This suggests that E_0 increases with bismuth content and this matches with the bismide PL peak broadening due to localized states, probably caused by Bi-based defects [20], [46–48].

3.3. Investigation of diffusion length at samples with thick i-region thickness

Usually all the generated electron-hole pairs in depletion region are regarded as being entirely collected by the electric field. On the contrary, the electron-hole pairs generated in neutral zone, or diffusion zone, are assumed to be only partially collected by the diffusion current. For a GaAs/GaAsBi/GaAs p-i-n heterojunction, if the i-region is fully-depleted, there will only be drift photocurrent if only longer wavelength photon is absorbed, and that is how we get the absorption coefficient. However, if the i-region is partially-depleted, we need to consider the diffusion current. A large diffusion length of minority carriers can help to improve collection, as carriers created outside the depletion region can still be collected. This property is useful especially when the absorption region of devices is thick.

The diffusion current is caused by the variation of split quasi-Fermi levels. It has been argued that several cases can lead to the change of quasi-Fermi level in depletion region: recombination current at the interface of heterojunction, and electron-hole pairs generated by the incident light through the device [106]. But from the results mentioned in [106], those effects are small enough. So it is fair to use quasi-equilibrium approximation [105], which means flat quasi-Fermi levels in depletion region. Besides, GaAsBi would reduce the band-gap by rising up valence band instead of lower down conduction band [17]. In this case, the flow of electrons would not be affected much by heterojunction barrier.

Doping type determination

When shining a short wavelength light (850 nm) on the samples with larger i-region thicknesses, the photoresponse as a function of depletion width when the i-region is partially-depleted is investigated. The purpose of using incident light with a short wavelength is to make sure that most of photons are absorbed in the p^+ GaAs region and most of the generated carriers diffuse to the i-region. In a p-n homojunction, the drift photocurrent in the depletion region caused by the electric field can be calculated using the Beer-Lambert law as:

$$J_{drift} = q\phi\left(e^{\alpha W_{Dp}} - e^{-\alpha W_{Dn}}\right) \tag{5.6}$$

$$\phi = \phi_0 \exp\left(-\alpha W_P\right) \tag{5.6a}$$

where W_{Dp} and W_{Dn} are the depletion widths in the p and n-region respectively, which are determined by the doping density. ϕ is the photon flux at the p-n junction interface, whereas ϕ_0 is the incident photon flux incident on the device (see Figure 5.1) and W_P is the thickness of the p-region. W_{Dp} and W_{Dn} are determined by the doping in p and n region respectively, so for example, if the structure is p$^+$-n, then we can fairly regard W_{Dp} as 0.

When the diffusion current is considered, the following equations can be obtained from solving the continuity equation [104] with the correct boundary conditions:

$$J_{diff-n} = \frac{qD_p p_{n0}}{L_p}\left[\exp\left(\frac{qV_b}{kT}\right)-1\right] - q\phi\frac{\alpha L_p}{1+\alpha L_p}\exp\left(-\alpha W_{Dn}\right) \tag{5.7}$$

$$J_{diff-p} = \frac{qD_n n_{p0}}{L_n}\left[\exp\left(\frac{qV_b}{kT}\right)-1\right] - q\phi\frac{\alpha L_n}{\left(1-\alpha L_n\right)}\exp\left(\alpha W_{Dp}\right) \tag{5.8}$$

D_p and D_n are diffusion constant of p and n carriers, L_p and L_n are diffusion lengths, p_{n0} and n_{p0} are minority carrier densities in neutral zone far away from diffusion region. V_b is the built-in self-potential which is proportional to the quasi-Fermi level, k is Boltzmann constant, T is the absolute temperature.

In the meantime, the dark current density is (Equation 3.8):

$$J_{dark} = \left(\frac{qD_n n_{p0}}{L_n} + \frac{qD_p p_{n0}}{L_p}\right)\left[\exp\left(\frac{qV_b}{kT}\right)-1\right] \tag{5.9}$$

So the photocurrent is:

$$J_{photo} = J_{drift} + J_{diff-p} + J_{diff-n} - J_{dark} = q\phi\left(\frac{e^{\alpha W_{Dp}}}{1-\alpha L_n} - \frac{e^{-\alpha W_{Dn}}}{1+\alpha L_p}\right) \tag{5.10}$$

From Equation 5.10, it can be verified that the expression has the same trend as Equation 5.6. It is amazing that Equation 5.10 is so concise; only the incident light intensity (ϕ), the depletion widths (W_{Dp} and W_{Dn}) and the diffusion lengths (L_p and L_n) are included. In addition, any uncertainty of the quasi-Fermi potential is eliminated.

In a p-i-n diode with a slightly doped i-region, if the i-region is partially depleted, the photocurrent behaviour is almost the same as a p$^+$-n$^-$ or p$^-$-n$^+$ junction if the i-region is n-doped or p-doped respectively. If the i-region is p-doped, the light will be absorbed in both p and i-regions before it reaches the p$^-$-n$^+$ junction interface. This means that the term ϕ in Equation 5.6a should be changed from $\phi_0\times\exp(-\alpha W_P)$ to $\phi_0\times\exp[-\alpha(W_P+W_I)]$, where W_I is the thickness of i-region.

Since the p-region doping in the samples is around 2×10^{18} cm^{-3}, the diffusion length of electrons is approximately 0.8 μm [129], which is larger than the p-region thickness (~ 0.4 μm). In this case, surface recombination may become significant. The surface recombination velocity, S_n, can be larger than 10^7 cm/s in p-type GaAs [130]. The diffusion coefficient D_n in GaAs is less than 200 cm^2/s when the electric field is low [131]. If we define $K_n = D_n/S_n$, when considering the surface recombination in the p-region, the photocurrent is:

$$\frac{J_{photo}}{q\phi_0} = e^{-\alpha W_P}\left[\frac{e^{\alpha W_{Dp}}}{1-\alpha L_n} - \frac{e^{-\alpha W_{Dn}}}{1+\alpha L_p} - \frac{2\alpha L_n e^{\alpha W_{Dp}}}{\left(1-\alpha^2 L_n^2\right)} \frac{1-\frac{\left(1+\alpha K_n\right)L_n}{L_n - K_n} e^{\left(\frac{1+\alpha L_n}{L_n}\right)\left(W_P - W_{Dp}\right)}}{1-\frac{L_n + K_n}{L_n - K_n} e^{\frac{2\left(W_P - W_{Dp}\right)}{L_n}}}\right] \quad (5.11)$$

Figure 5.14 shows the ideal photocurrent as a function of depletion width in a p-i-n diode with different doping types in the i-region. The doping type can be determined from the slope of the curve according to Figure 5.14, and it has a strong influence on the photocurrent if the diffusion length is sufficiently long. Surface recombination does not change the shape of the curve (see Figure 5.14), but it diminishes the photocurrent dramatically.

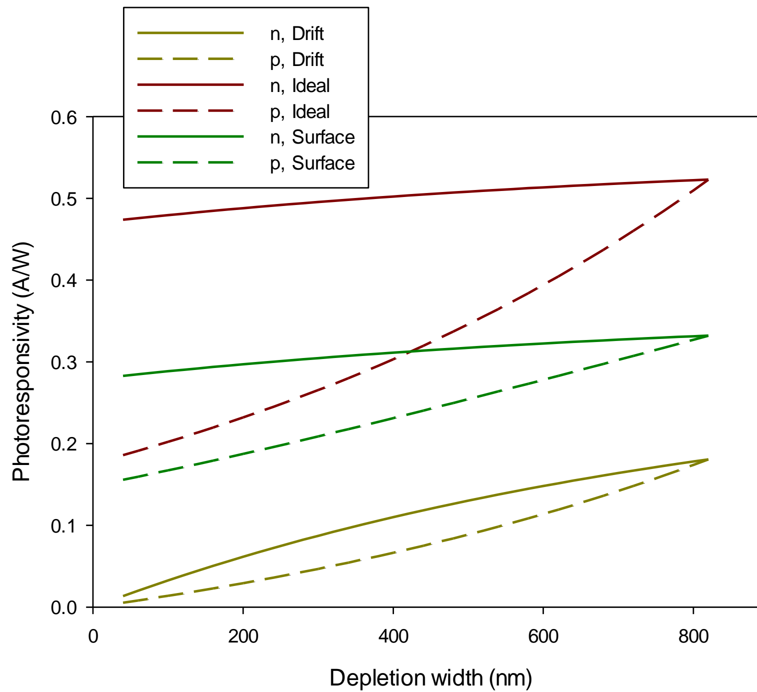

Figure 5.14. The ideal photoresponsivity in a p-i-n junction as a function of depletion width, p and n indicate the i-region doping type, Drift is the drift photocurrent—Equation 5.6, Ideal is the total photocurrent—Equation 5.10, and Surface is the photocurrent considering surface recombination—Equation 5.11

The above analysis ignores the difference in the diffusion lengths of a p^+ / n^+ GaAs region and an unintentionally p / n doped i-region, and the difference in the absorption coefficients of the p, i and n regions is not considered. However, it is still able to give the right trend, and to yield the doping type of the i-region. From Figure 5.15, it seems that the i-regions of the 4 samples are all n-type doped. Since the Bi atom is much larger than As it is more likely to behave as an isoelectronic donor [50], just as nitrogen is likely to act as an isoelectronic acceptor in GaAsN, which leads to an unintentional p-type doping of the material [132].

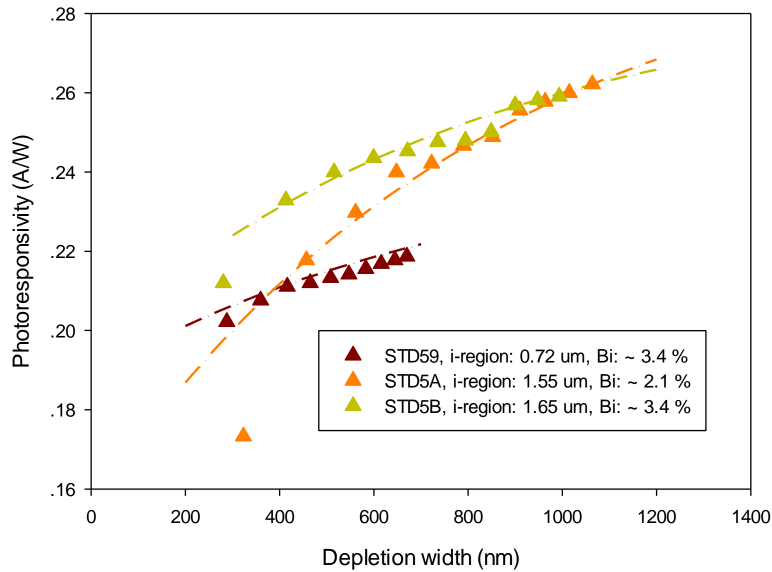

Figure 5.15. Photoresponsivities of 4 samples, the incident light wavelength is 850 nm, dashed lines are fitting curves from Equation 5.11

Photocurrent of partially-depleted i-region devices

In order to find the actual diffusion length of GaAsBi, two prerequisites are proposed here. First, the wavelength of the light is long enough that the light would only be absorbed in i-region. Here a 980 nm laser was used for the measurements. Second, different diffusion lengths in p, i, and n are considered.

The formula of photoresponsivity is obtained as shown in Equation 5.12 if the i-region is slightly p-doped, in which the dark current has already been eliminated:

$$R=\frac{q\lambda}{hc}\left(1-R_p\right)e^{-\alpha(W_I-W_D)}\left[\frac{1}{1-\alpha L_n}-e^{-\alpha W_D}-\frac{2\alpha L_n}{1-\alpha^2 L_n^2}\frac{1-\frac{\left(1+\alpha L_{n2}\right)L_n}{L_n-L_{n2}}e^{\frac{1+\alpha L_n}{L_n}(W_I-W_D)}}{1-\frac{L_n+L_{n2}}{L_n-L_{n2}}e^{\frac{2(W_I-W_D)}{L_n}}}\right] \tag{5.12}$$

If the i-region is n-doped, the photoresponsivity is:

$$R=\frac{q\lambda}{hc}\left(1-R_p\right)\exp\left(-\alpha W_D\right)\left[e^{\alpha W_D}-\frac{1}{1+\alpha L_p}-\frac{2\alpha L_p}{1-\alpha^2 L_p^2}\frac{1-\frac{\left(1-\alpha L_{p2}\right)L_p}{L_p-L_{p2}}e^{\frac{1-\alpha L_p}{L_p}(W_I-W_D)}}{1-\frac{L_p+L_{p2}}{L_p-L_{p2}}e^{\frac{2(W_I-W_D)}{L_p}}}\right] \quad (5.13)$$

Where λ is the wavelength of the incident light, c is the light speed, and R_p is the reflection coefficient of GaAs (~ 0.32 at the band-gap energy). Here L_n and L_p are the minority carrier diffusion lengths in the i-region when the i-region is p-doped and n-doped respectively, and L_{n2} and L_{p2} are the diffusion lengths of p-region and n-region respectively. The calculation method of Equations 5.12 and 5.13 can be seen in Appendix 4. By using the method outlined in [104], the diffusion length can be estimated by fitting the photoresponsivity as a function of the depletion width.

From the above expressions, the photoresponsivity is only dominated by the depletion width and the diffusion lengths of minority carriers. In addition, since the i-regions of the samples are assumed to be n-doped from the above analysis, the diffusion length of electrons in the GaAs p-region has no effect on the responsivity. The diffusion length of holes in the n-region is adopted from [129], which is around 4 μm. Furthermore, the contribution of photo-generated holes from the n^+ GaAs substrate to the responsivity is very small and can be ignored. Even changing the diffusion length by several orders of magnitude, the fitting curves are only changed by ~ 2 % in Figure 5.16. From Figure 5.16, a diffusion length of holes in the GaAsBi layer is obtained, which is in the range of 0.5 ~ 1 μm.

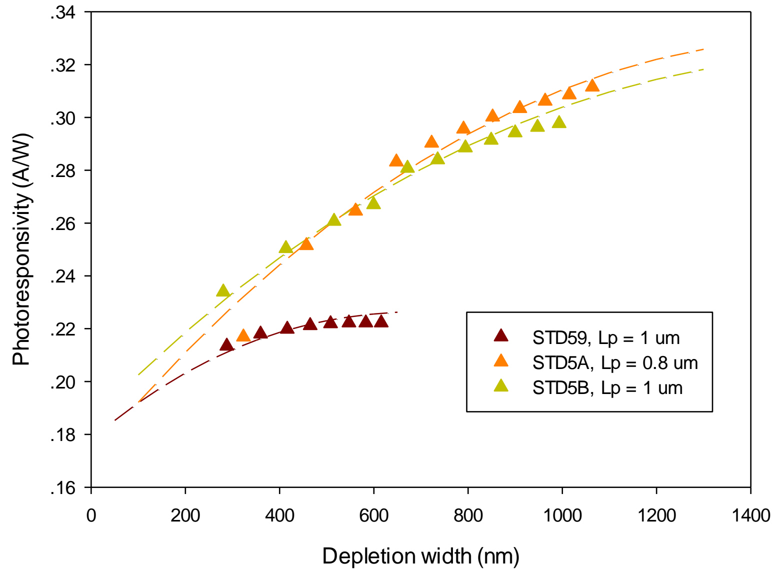

Figure 5.16. Photoresponsivity as a function of depletion width under illumination at 980nm, dashed lines are fitting curves calculated by Equation 5.13

4. Summary

In this chapter, a set of GaAsBi p-i-n samples were grown to investigate the optical properties of GaAsBi. Photoresponsivity measurements were undertaken on GaAsBi based p-i-n heterojunction diodes. The absorption properties were investigated as a function of both incident photon energy and bias voltage. The absorption behaviour of GaAsBi above the band gap shows that GaAsBi is a direct band gap material. As the incorporated bismuth increases, the absorption above modified band gap (band gap decreased by Bi incorporation) increases, which might mean that the density of Bi-related states in the forbidden band increases. GaAsBi seems to be unintentionally n-type doped from photocurrent measurements as a function of depletion width. Finally, an equation has been deduced to estimate diffusion lengths of GaAsBi samples. The minority carrier diffusion length (L_n / L_p) is the only adjustable parameter in that equation. The average diffusion length of holes in GaAsBi has been estimated at up to 1 μm from the analysis undertaken in this work.

Chapter 6: The electrical and optical properties of p-i-n and n-i-p structure diodes

1. The structure and related analysis of PINs and NIPs

Two sets of samples named as STF8 series and STFA series which structures are p-i-n and n-i-p GaAs/GaAsBi/GaAs heterojunction diodes respectively were grown and fabricated. STF8 series was grown by Thomas Rockett, and STFA series was grown by me. All the samples were fabricated by Faezah Harun. The sample structures are shown in Figure 6.1, and the brief information of the samples in these two series is recorded in Table 6.1.

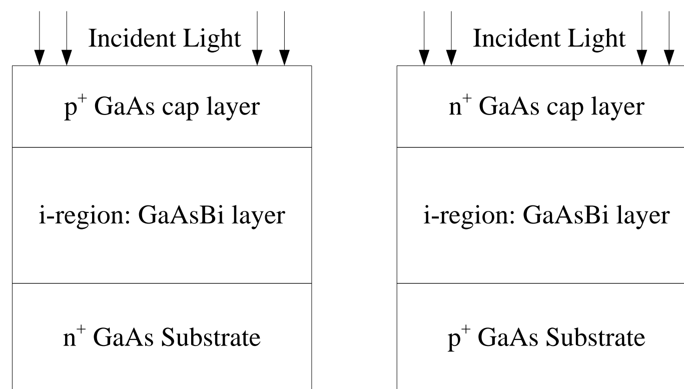

Figure 6.1. Sample structure of STF8 and STFA series: left is STF8, and right is STFA

Table 6.1. Brief information of STF8 series and STFA series

i-region thickness	p-i-n structure	n-i-p structure
100 nm	STF85	STFA7
200 nm	STF81	STFAD
400 nm	STF84	STFAE
800 nm	STF83	STFAB
1600 nm	STF82	STFAC

For each sample in STF8 and STFA series, a GaAs buffer layer which thickness is ~ 100 nm was grown at ~ 580 °C with As_2 after oxide removal. The As:Ga flux atomic ratio used to grow STF8 buffer layer was ~ 1.5. The growth temperature used for the bismide layers of all the STF8 samples was around 375 °C, while the growth rate was ~ 0.6 ML/s. The bismuth flux was fixed throughout the series to obtain a constant bismuth content, and the Bi:Ga flux ratio based on beam equivalent pressure (BEP) was ~ 0.11. The p+ GaAs region with a thickness of 450 nm was grown at ~ 580 °C with As_2, which means that the bismide layers in these samples were annealed at a higher temperature than in STD5 series. The doping of the p^+ region was ~ 5×10^{18} cm^{-3}.

As_4 was used during p-i-n GaAsBi layer growth. The As:Ga atomic flux ratio was ~ 1.3. Previous research shows that when As_4 is used as the As source, only half of the atoms in As_4 molecule would be effectively used during the growth of the bismide layer [121]. In this case, the stoichiometric growth should happen when the As:Ga flux ratio is ~ 2. An As:Ga flux ratio of ~ 1.3 may thereby lead to insufficient As flux supply and form Ga droplets on the surface. However, it seems that at a very low As_4 flux a good surface with sufficient amount of Bi incorporated is still able to obtain according to the results.

The p-type substrates for the n-i-p growth were Zinc doped, whereas Be was used for the p-type buffer layer during growth. The growth rate was ~ 0.41 ML/s for all the STFA series samples. The As:Ga flux ratio used for the growth of GaAs buffer layer and top n^+ layer was ~ 1.45, and the growth temperature for the two layers was ~ 580 °C. The As:Ga atomic flux ratio used for the bismide layer was ~ 1.9. Using the method mentioned in Chapter 2 to estimate our growth temperature, the growth temperature for STFA series was ~ 360 °C. The Bi:Ga flux ratio depending on the BEP was ~ 0.04. Though the growth temperature and Bi:Ga flux ratio for STF8 and STFA series were quite different, almost the same Bi content in both series was obtained. STF8 series was grown at a higher temperature and Bi:Ga flux ratio than STFA series. From the previous analysis in Chapter 4, STF8 series was probably grown in the temperature limited regime, whereas STFA series was in the bismuth kinetic limited regime.

1.1. The analysis of the surface profile

The strain and related issues such as strain relaxation and generated dislocations should be considered when producing high performance detectors. If the misfit between the substrate and the growing epi-layer is sufficiently small, the first few atomic layers which are deposited will be strained to match the substrate [133]. However, the strain relaxation would happen when exceeding Matthews-Blakeslee critical thickness [122], where both elastic strain and misfit dislocations exist for the lattice mismatch. The knowledge of the critical thickness is very important since dislocations cause a strong degradation of optoelectronic properties of materials [133]. The strain in a hetero-structure is given by:

$$f_s = \frac{a_l - a_s}{a_s} \tag{6.1}$$

where a_l is the lattice constant of the free standing epitaxial layer on top of the substrate, and a_s is the substrate lattice constant. Since incorporating a small fraction of Bi can lead to a large band gap reduction, the lattice mismatch between dilute bismide and GaAs can be small for a sufficiently reduced band gap. Nomarski images are shown in Figure 6.2-6.6 for STF8 series and Figure 6.7-6.11 for STFA series. Scale bars are the same for all the images as marked in Figure 6.7. More or less sub-surface damage happened on all the samples according to the scratching lines shown on the surface images. Figures 6.2 and 6.7 show no obvious orthogonal crosshatching lines, which indicate that both

of the two samples with a ~ 100 nm i-region thickness are without strain relaxation. Seldom scratching lines are shown in Figure 6.2 different from Figure 6.7. The scratching lines in Figure 6.7 might be due to not so good substrate preparation processes such as surface cleaning and/or oxide removal. With the increase of the i-region thickness, deeper and clearer crosshatching lines appear on the surface illustrating the emergence of strain relaxation. In this case, the critical thickness for samples with this Bi content must be around 200 nm. The shiny dots existing on almost all the sample surfaces might be Ga-Ga droplets or Bi-Bi droplets. It is with higher probability to form droplets when thicker layer is grown, which matches the trend shown in the images. The STF8 samples tend to have better surfaces than STFA series in overall. A higher growth rate was used in STF8 series, which may cause a better incorporation for samples with this Bi content (see the discussion in Section 2 of Chapter 4). A higher Bi flux was used in STF8 series, so the surfactant function of Bi atoms might be stronger. If it is the case, Bi-Bi droplets would be easier to form on the surfaces of STF8 series, whereas Ga-Ga droplets tend to form on the surfaces of STFA series. Besides, relatively clean surfaces of STF8 series samples indicate that the growth is with sufficient As flux even if the As:Ga atomic flux ratio for As_4 species is so low.

Figure 6.2. Nomarski image for STF85, which i-region thickness is 100 nm

Figure 6.3. Nomarski image for STF81, which i-region thickness is 200 nm

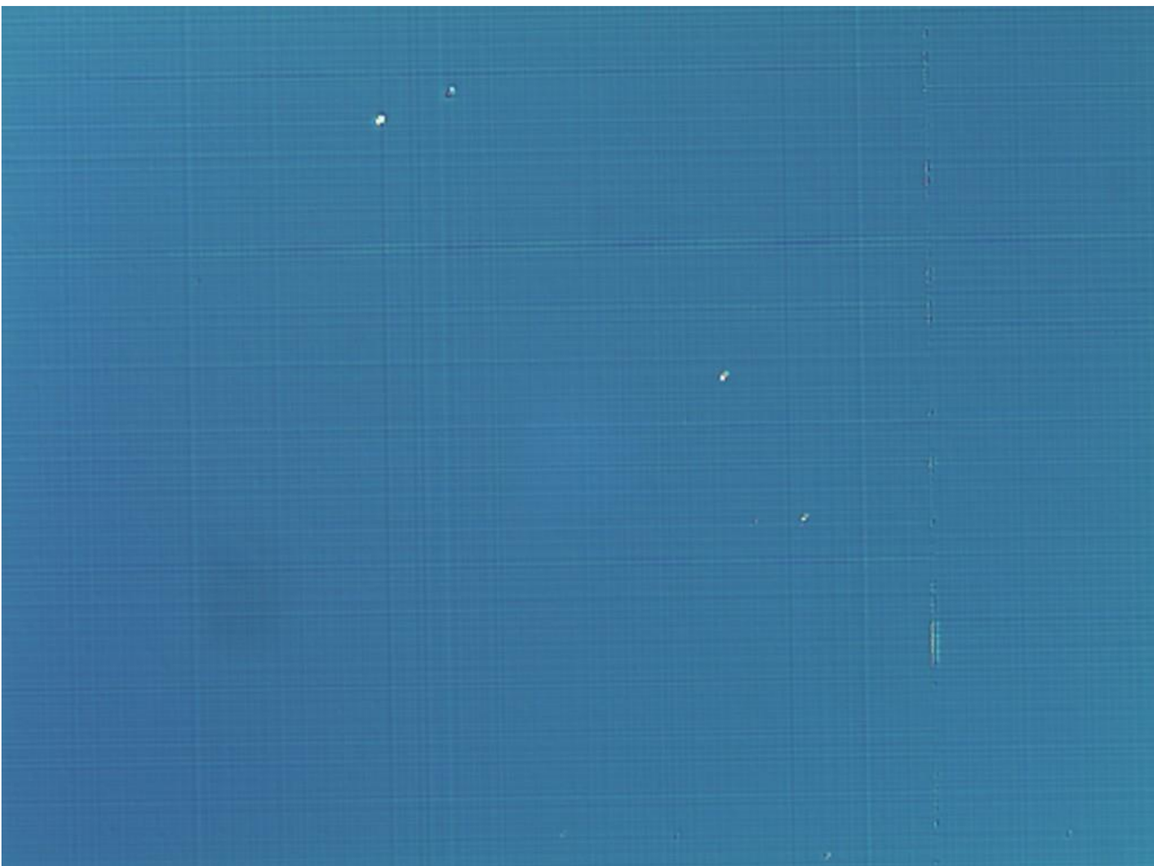
Figure 6.4. Nomarski image for STF84, which i-region thickness is 400 nm

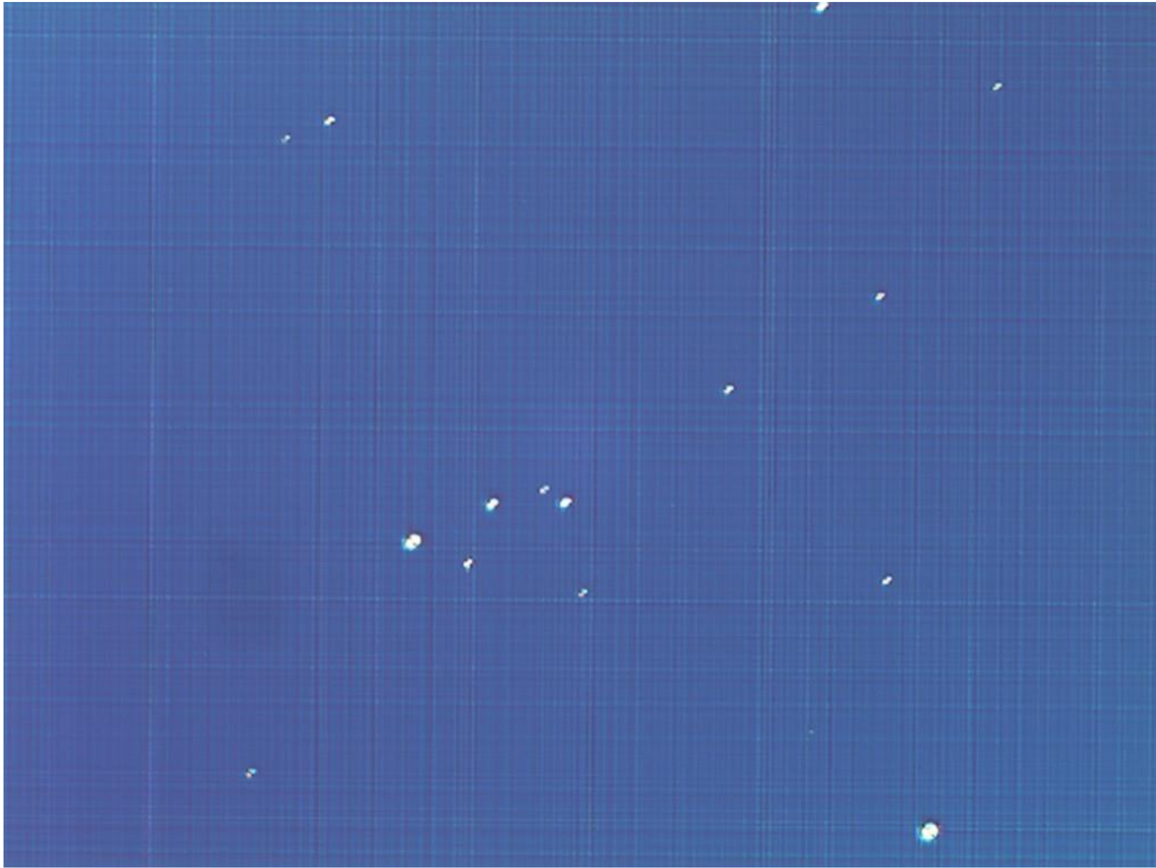
Figure 6.5. Nomarski image for STF83, which i-region thickness is 800 nm

Figure 6.6. Nomarski image for STF82, which i-region thickness is 1600 nm

Figure 6.7. Nomarski image for STFA7, which i-region thickness is 100 nm, 3 black lines are marked following 3 scratching lines on the image as illustrations.

Figure 6.8. Nomarski image for STFAD, which i-region thickness is 200 nm

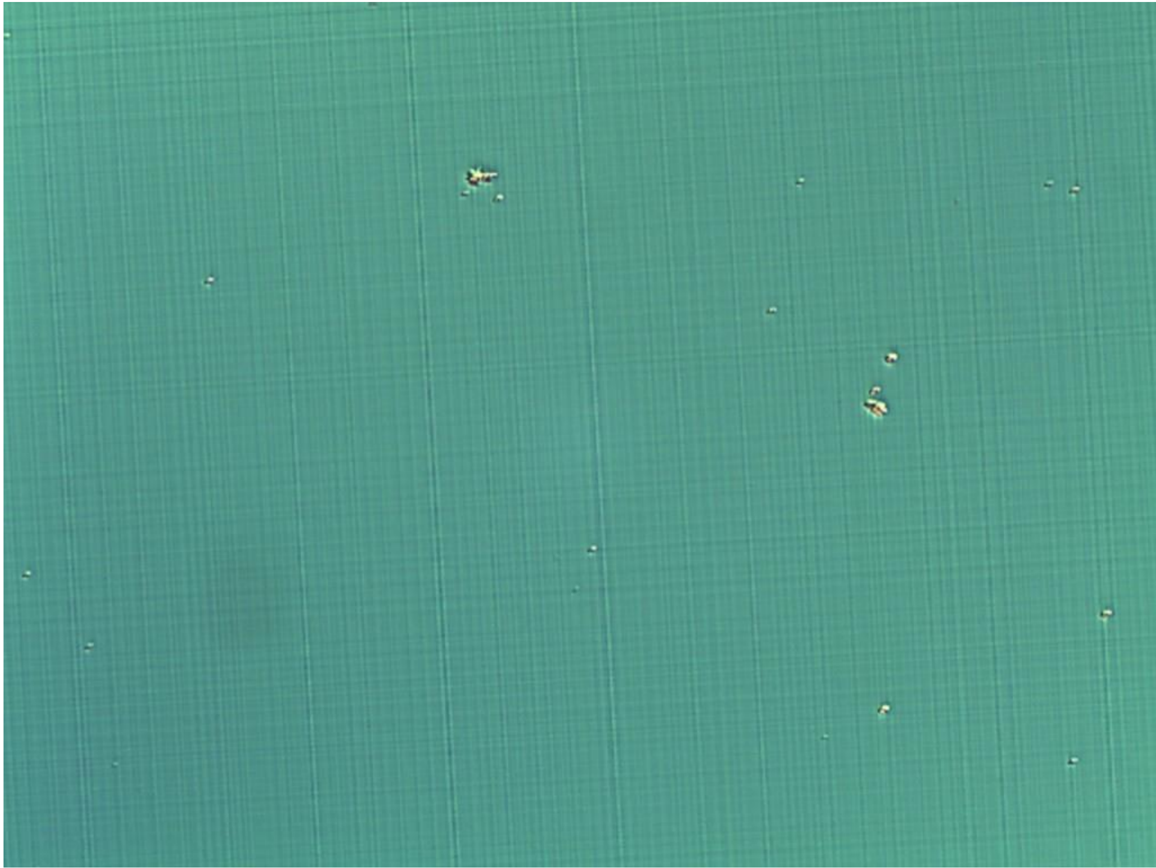

Figure 6.9. Nomarski image for STFAE, which i-region thickness is 400 nm

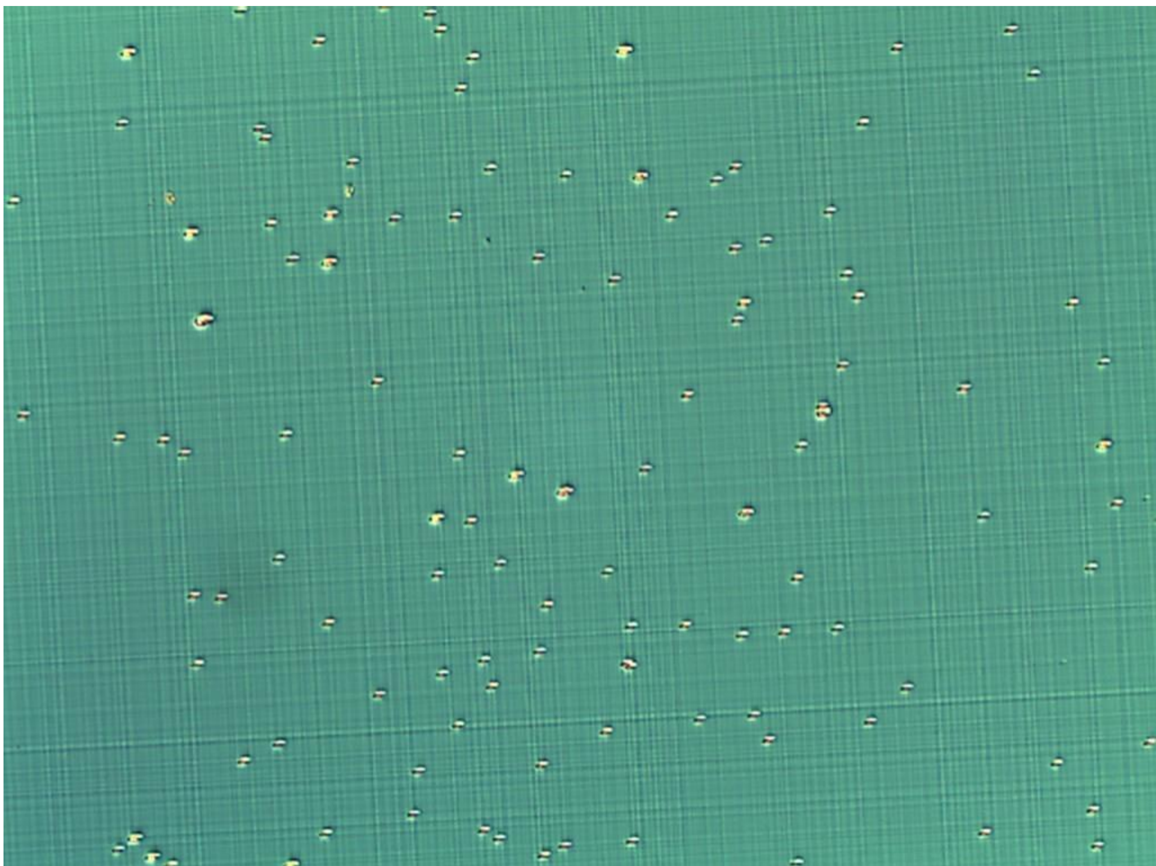

Figure 6.10. Nomarski image for STFAB, which i-region thickness is 800 nm

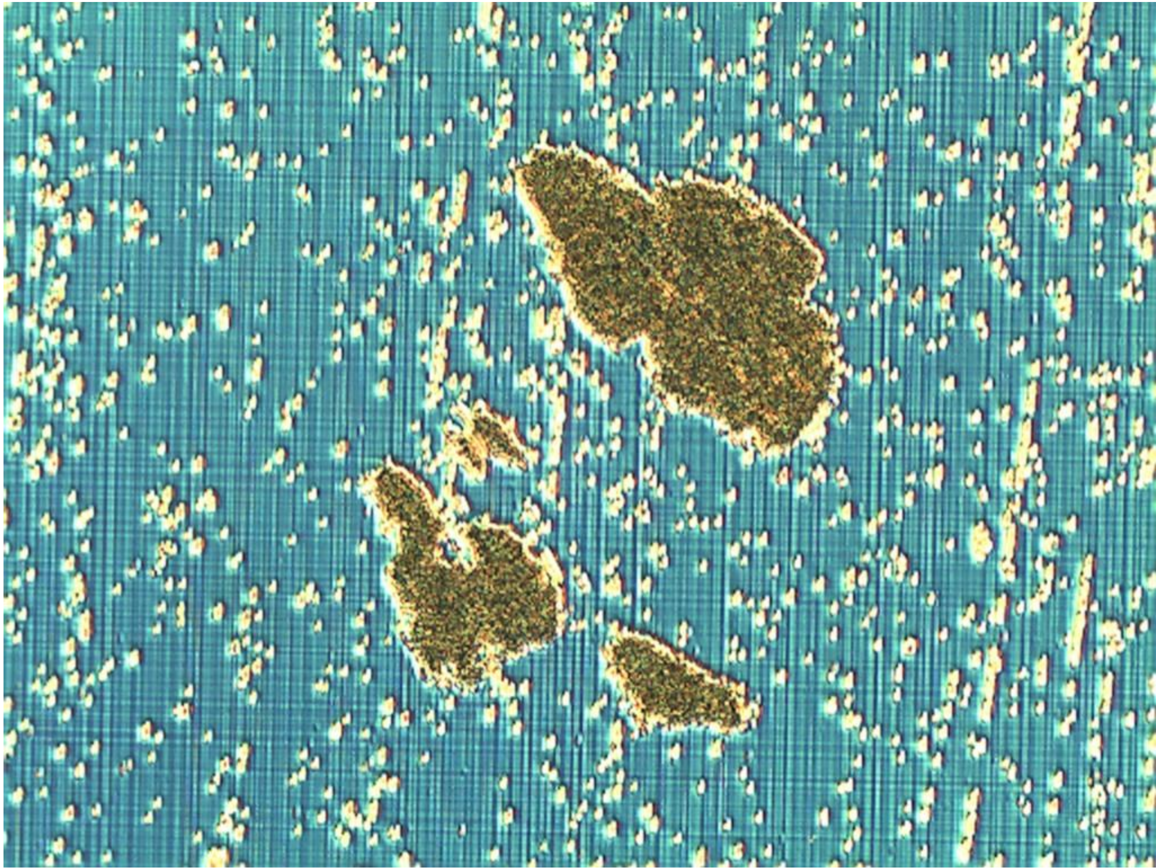

Figure 6.11. Nomarski image for STFAC, which i-region thickness is 1600 nm

1.2. X-ray diffraction results

(004) X-ray diffraction (XRD) ω-2θ scans were taken on the two sets of samples using Cu $K\alpha_1$ radiation. Results are shown in Figures 6.12 and 6.13, and clear GaAsBi lattice peaks are observed in these curves. All scans were modelled using RADS Mercury software. The structural parameters determined from the fittings are shown in Table 6.2.

Table 6.2. Structural parameters of STF8 series and STFA series from XRD results

i-region thickness	Bi content (%)		Modelled i-region thickness (nm)		GaAsBi peak FWHM (″)		GaAs peak FWHM (″)		Relaxation (%)	
	p-i-n	n-i-p	p-i-n	n-i-p	p-i-n	n-i-p	p-i-n	n-i-p	p-i-n	n-i-p
100 nm	4.79	2.32	95	94	180	194.4	14.4	43.2	0	0
200 nm	3.7	3.76	194	157	108	129.6	36	21.6	0	5
400 nm	4.1	3.8	432	402	194.4	172.8	39.6	43.2	27	25
800 nm	3.5	2.82	762	843	167.4	180	27	54	36	44
1600 nm	3.4	2.97	1504	1575	133.2	151.2	36	43.2	51	44

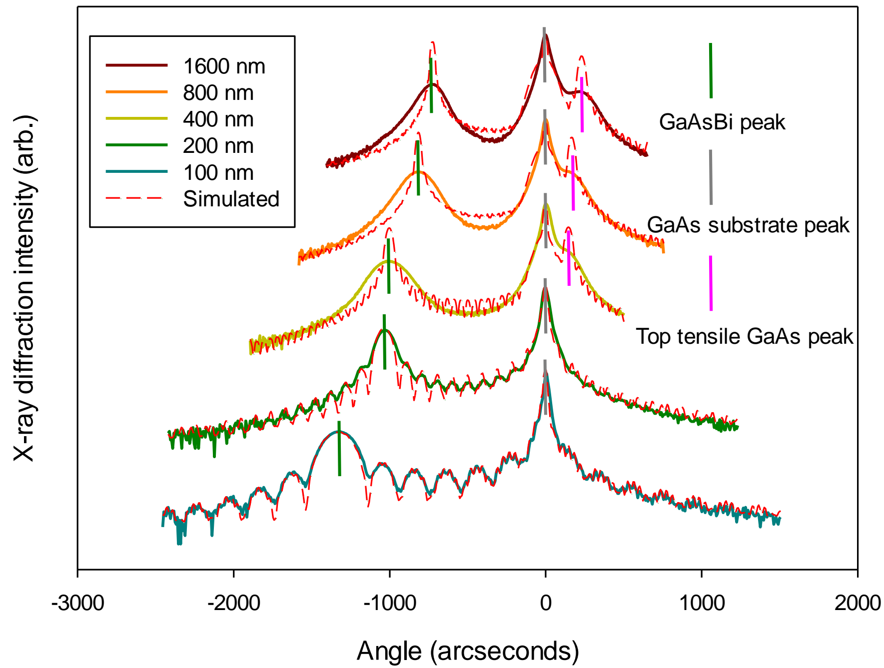

Figure 6.12. X-ray diffraction results of STF8 series. Scans are normalised and vertically offset for clarity. 0 angle is where to get GaAs peak. Peaks are interpreted as labelled in the graph

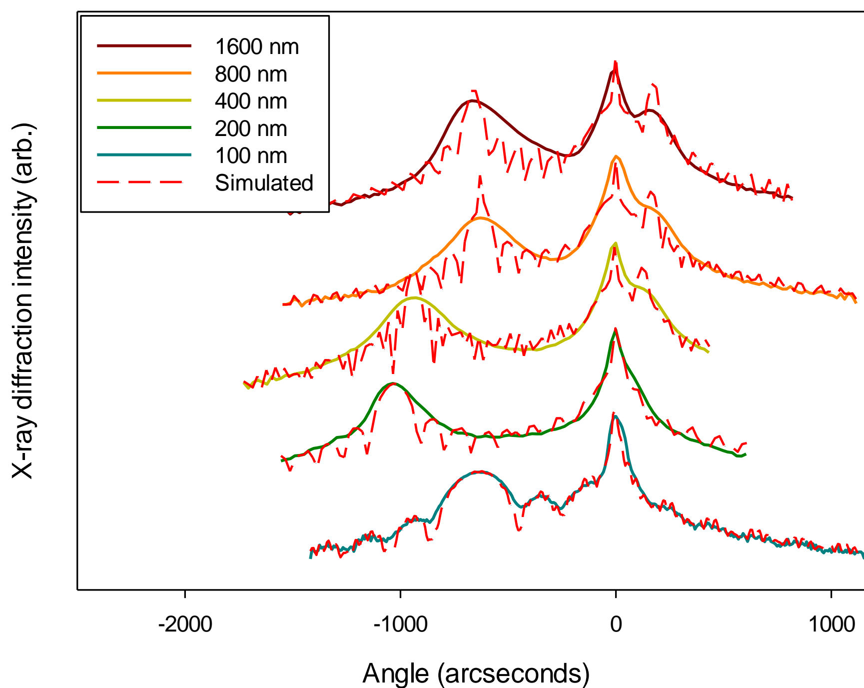

Figure 6.13. X-ray diffraction results of STFA series. Scans are normalised and vertically offset for clarity. 0 angle is where to get GaAs peak. Peaks are interpreted the same way as in Figure 6.12

From Figures 6.12 and 613, the spectra for samples STF85 (100 nm p-i-n), STF81 (200 nm p-i-n), and STFA7 (100 nm n-i-p) show Pendellösung fringes, indicating good quality GaAsBi/GaAs interfaces, whereas the spectra for other ones are unfortunately without fringes. Besides, the simulated results matched the curves with clear Pendellösung fringes (i.e. 100 nm and 200 nm PINs, and 100 nm NIP) very well. However, with the increasing of the i-region thickness, it is harder and harder to get a good fitting with the experimental data. This phenomenon is clearly related to the shoulder peaks at the right side of the GaAs peaks, which indicate strain relaxation of the material. In the meantime, the simulated GaAsBi peak is getting narrower with the increasing i-region thickness since the reciprocal space is inverse of real space. However, the real GaAsBi peaks are broadened compared to the simulated results when the i-region thickness is larger enough. Some of the possible reasons can be inhomogeneous strain due to relaxation, crystal defects caused by dislocations, etc. [101]. There is also a possibility that Bi content varied during the long growth time since the growth environment might be changed. The disappearing of Pendellösung fringes for thicker samples also reveals that the heterojunction interface might not be abrupt as well.

The samples without obvious shoulder peaks (STF85, STF81, and STFA7) are regarded as strain-balanced samples. In this case, the lattice parameter of GaAsBi epi-layer is compressed in the horizontal plane, and elongated in the vertical direction, as shown in Figure 6.14(b). No misfit dislocations would be generated if the lattice is perfectly strain balanced. GaAs epi-layer on top of the GaAsBi layer can also maintain its regular lattice parameter. This matches the observation in the Nomaski results. However, for the other samples in these two sets which have thicker GaAsBi layers, since strain builds up when the layer accumulates thicker and thicker during growth, at a certain point, the layer would be relaxed to release part of the strain as shown in Figure 6.14(c), and misfit dislocations are generated, which behave as cross-hatching lines exhibited in Nomaski results. Correspondingly, the lattice of the GaAs layer on top of GaAsBi layer will be extended in the horizontal plane, and shortened in the vertical direction, until the layer reaches a certain critical thickness and relaxes itself.

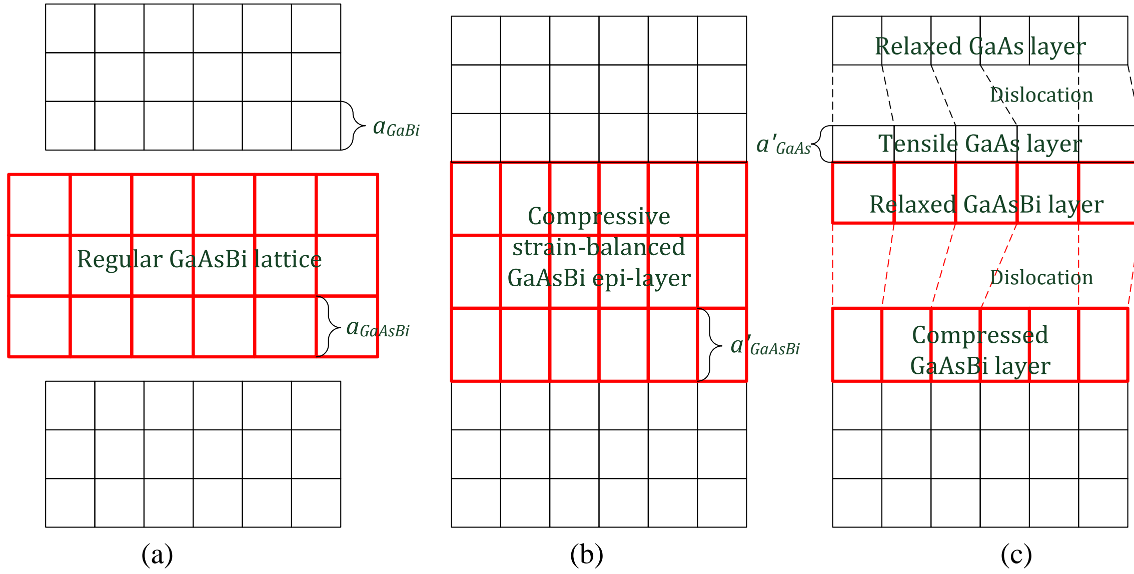

Figure 6.14. Diagrams of strain and strain relaxation: (a) regular GaAs and GaAsBi lattice structure, (b) strain balanced GaAs/GaAsBi/GaAs heterojunction lattice structure, GaAsBi layer is compressed in the horizontal plane and elongated in the vertical direction, (c) strain relaxed GaAsBi layer and top GaAs layer, top GaAs layer is tensioned at the GaAs/GaAsBi interface

Since the GaAsBi peak angles were obtained from the measurements and the wavelength of incident X-ray beam is known, (004) plane spacing can be calculated for each sample using Bragg's law, which is corresponding to the lattice parameter of GaAsBi layer. If no relaxations were happened, the lattice parameter can then be obtained assuming that the Poisson's ratio is the same as that of GaAs (0.311). Thereafter the GaAsBi content can be obtained using Vegard's law when we get the GaBi lattice constant. GaBi is expected to be semi-metallic and has never been successfully synthesised [18][134]. Over the past few years, there have been several attempts to estimate the GaBi lattice constant from theoretical side and experimental side. The lattice constant was estimated to be 6.324 Å in [134] theoretically and 6.33 Å in [2] experimentally. In this thesis, a more recent data, 6.28 Å, was adopted [135] in the simulation. Vegard's law is simply a linear relationship which can be presented as following, where x is the fraction of Bi in $GaAs_xBi_{(1-x)}$.

$$a_{GaAsBi} = (1-x)\,a_{GaAs} + x a_{GaBi} \tag{6.2}$$

Samples without Pendellösung fringes cannot get good fittings from simulation, and the thickness data in Table 6.2 of those samples are not trustable. The disappearing of Pendellösung fringes might be due to the misfit dislocations generated through relaxation. Besides, relaxation should then be included in the simulation, since the epi-layer peak position depends on both the Bi composition and relaxation. The shrinking of lattice parameter in the vertical direction due to strain relaxation would lead to the right shift of GaAsBi peak position. The tensile GaAs epi-layer with smaller lattice parameter in the vertical direction would also shift its peak to right and generate a "shoulder" peak.

Several methods have been proposed to calculate the critical thickness of a mismatched system [122], [136]–[140] based on the Matthews-Blakeslee equation expressed as:

$$h_c = \frac{b}{8\pi f} \frac{1 - v\cos^2\theta}{(1+v)\cos\lambda} \left[\ln\left(\frac{h_c}{b} \right) + 1 \right] \tag{6.3}$$

where b is the length of the Burgers vector, f is the lattice misfit, v is the Poisson ratio, θ is the angle between the dislocation line and its Burgers vector, λ is the angle between the slip direction and that direction in the film plane which is perpendicular to the line of intersection of the slip plane and the interface. The critical thickness of STF8 and STFA series is around 150 nm due to their similar bismuth content.

The effect of strain on the band structure of semiconductors is essentially a reduction of degeneracy at the top of the valence band due to the reduction in symmetry from cubic to tetragonal (for 001 oriented structures). This reduces the density of states, so tensile and compressive strain reduce the carrier density required for population inversion in laser diodes. This would improve the efficiency and reduce the temperature sensitivity of the devices. Furthermore, the heavy hole band would probably be flattened due to the splitting of the valence band (reduction of degeneracy), and the ionization coefficient of holes, β, would be suppressed, leading to an increase of the ratio k (α/β).

1.3. Room temperature photoluminescence results

Room temperature photoluminescence results of STF8 and STFA series are shown in Figures 6.15 and 6.16. The data in these two graphs are normalized, and the factors are marked on the legends. The Bismuth content of the two sample sets can be obtained from VBAC model, and the results are shown in Table 6.3.

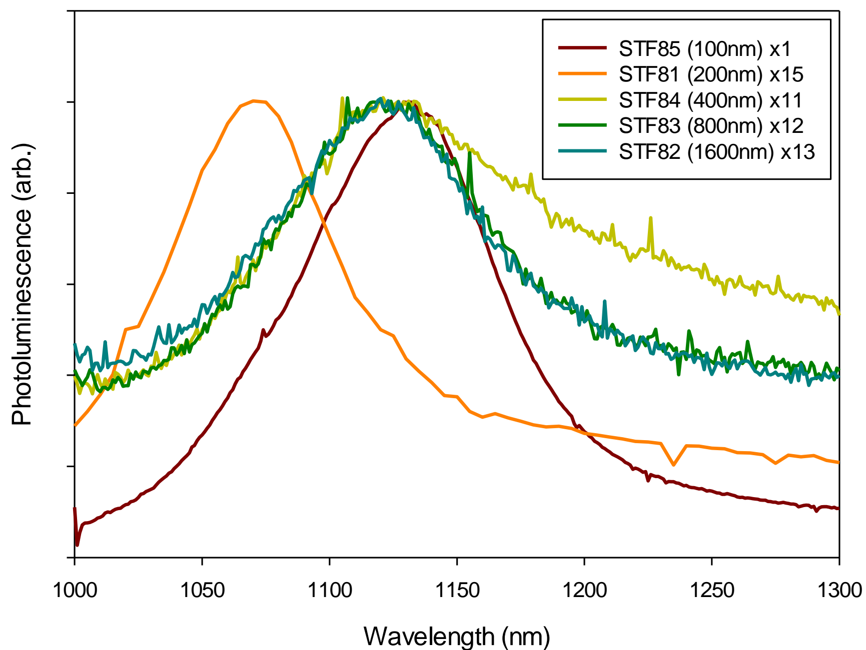

Figure 6.15. Photoluminescence of STF8 series

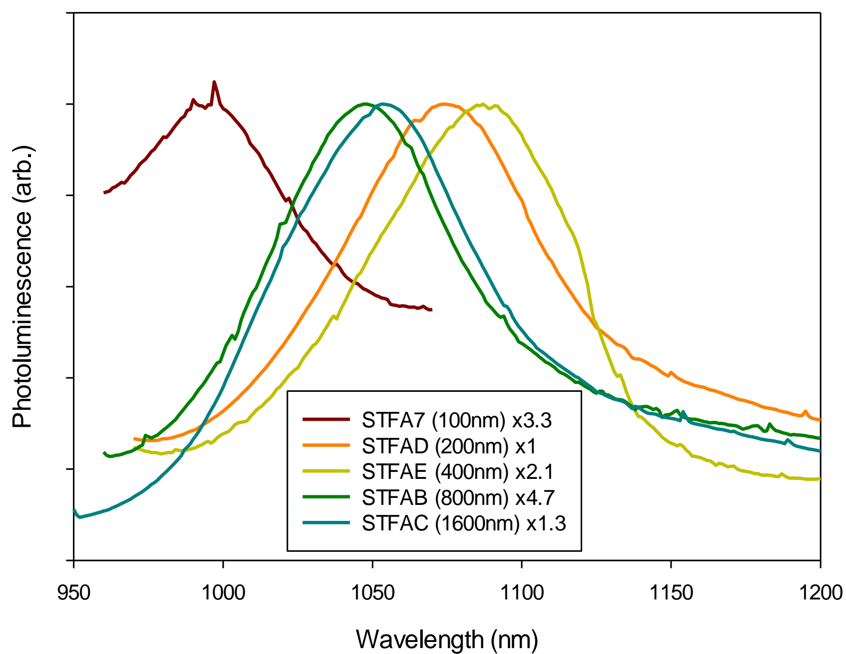

Figure 6.16. Photoluminescence of STFA series

Table 6.3. Bismuth content obtained from XRD and room temperature PL

i-region thickness	Bi content (%) from XRD		Bi content (%) from PL	
	p-i-n	n-i-p	p-i-n	n-i-p
100 nm	4.79	2.32	4.4	2
200 nm	3.7	3.76	3.5	3.5
400 nm	4.1	3.8	4.1	3.7
800 nm	3.5	2.82	4.1	3
1600 nm	3.4	2.97	4.1	3.1

The PL intensities of PINs are very weak compared to NIPs and previous grown samples (e.g. STD5 series), especially that the curves of STF84, STF83 and STF82 are very noisy. This might be possibly due to that the As:Ga ratio was low during growth, and Bi-clusters were more easily to form. As discussed previously, the Bi-clusters may introduce states in the forbidden band, and these states can be non-radiative recombination centres. Besides, the FWHM of both PIN and NIP PL curves are large, which might be due to the non-uniformity of these samples.

From the comparison of the Bi content data from XRD and PL, the measurement results of XRD and PL agrees with each other, though not all of them match quite well. The difference of the Bi content between XRD and PL results is ~ 0.2% for average, and the largest difference is ~ 0.7%. Besides, NIPs results agree better than PINs, for the largest difference is ~ 0.3%. With the increasing thicknesses of the samples, the GaAsBi peaks of XRD would be right shifted due to the relaxation, leading to a smaller value of Bi content. On the other hand, the relaxation would bring back the degeneracy of valence band, causing a red shift of PL peak and thus a larger value of Bi content. This phenomenon can be reflected from the results in Table 6.3.

1.4. Capacitance-Voltage measurements

Figure 6.17 shows the capacitance per unit area of the samples against reverse bias voltage from capacitance-voltage (CV) measurements. A test signal with ~60 mV amplitude and 1 MHz frequency has been used for the measurements. The doping profile as a function of depletion width is plotted in Figure 6.18. The estimated i-region thicknesses of STF8 and STFA series are recorded in Table 6.4.

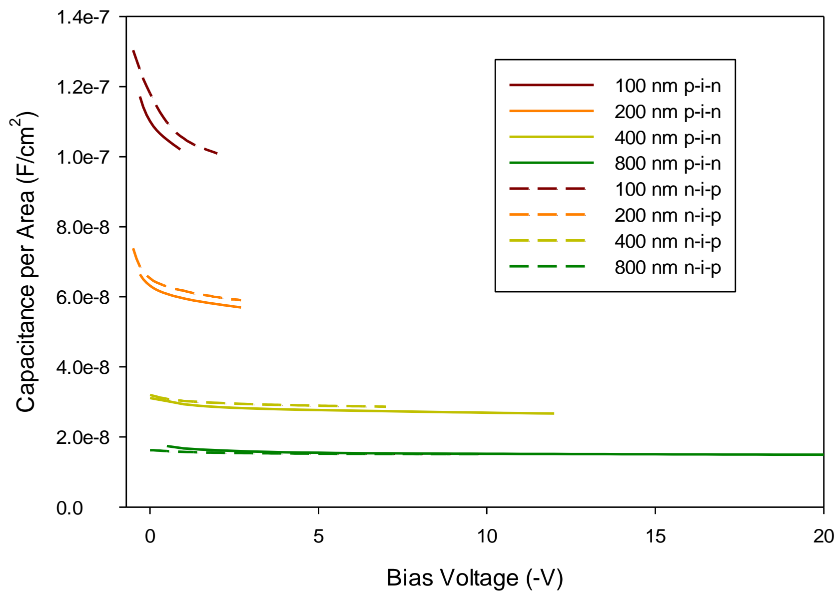

Figure 6.17. Capacitance-voltage results of STF8 and STFA series

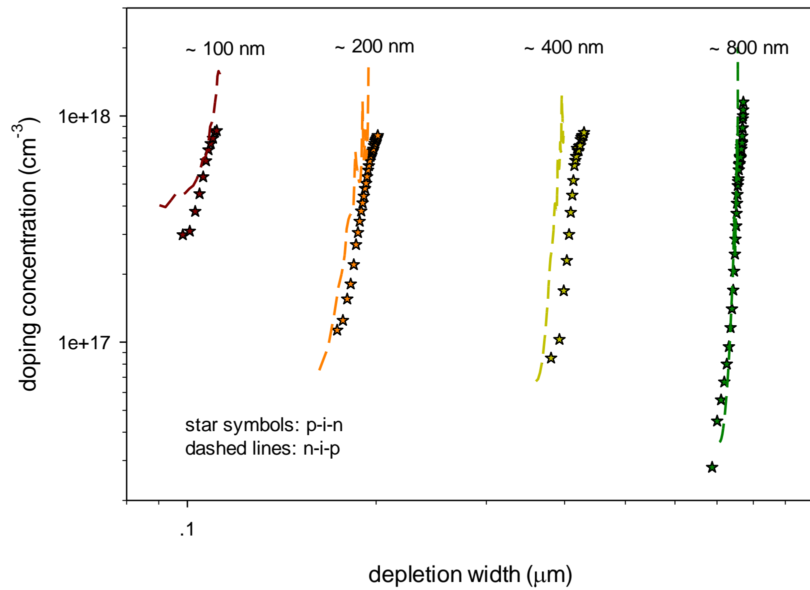

Figure 6.18. Doping concentration distribution of STF8 and STFA series

Table 6.4. The i-region thicknesses of STF8 and STFA series

p-i-n	Intended	Actual	n-i-p	Intended	Actual
STF85	100 nm	100 nm	STFA7	100 nm	100 nm
STF81	200 nm	190 nm	STFAD	200 nm	180 nm
STF84	400 nm	405 nm	STFAE	400 nm	380 nm
STF83	800 nm	745 nm	STFAB	800 nm	745 nm

1.5. Current-voltage measurements

Current-voltage (IV) characterisation of STF8 and STFA series shows clear diode-like characteristics (Figures 6.19 and 6.20). The reverse currents of these samples as a function of electrical field are plotted in Figure 6.21. The results of the thickest samples (1600 nm i-region thickness ones) are not presented in the Figures due to bad reverse IV behaviours. The reverse leakage currents of 1600 nm ones are very high, reaching 100 μA (the limit we set for protecting samples from damage) very quickly at around -10 V, whereas most 800 nm thick ones can do at more than -20V. This can be due to several reasons. First, the thicker the layer is, the worse the surface quality can be. Second, the growth condition was not set in an ideal situation, leading to a very bad surface (see Nomaski images) with loads of droplets and dislocations.

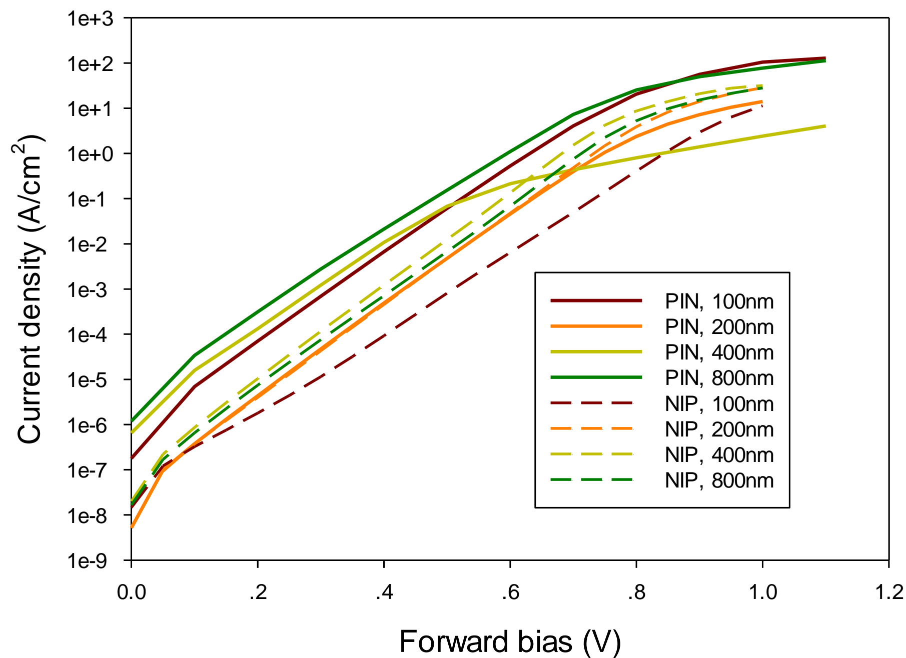

Figure 6.19. The forward current-voltage plot of STF8 and STFA series

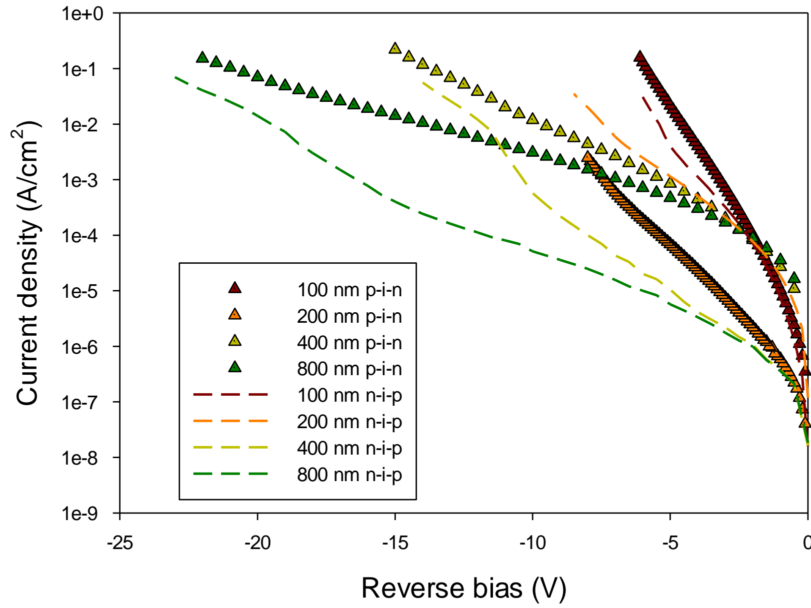

Figure 6.20. The comparison of the reverse IV between STF8 and STFA series

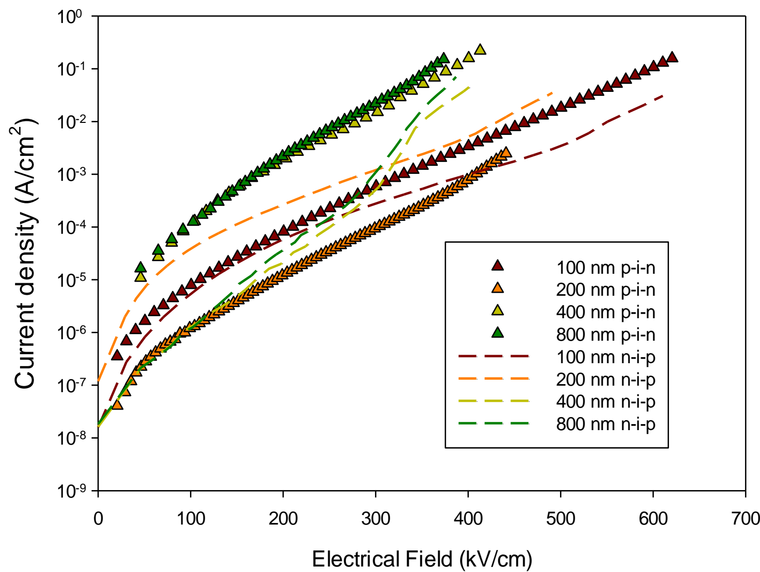

Figure 6.21. The comparison of the reverse IV between STF8 and STFA series as a function of electrical field

The forward and reverse currents of STD5, STF8 and STFA are summarized in Figure 6.22 for comparison of different GaAsBi samples. From Figure 6.22, the currents at 0.4V seems to be nearly proportional to the currents at -1V, and the ratio is roughly $2\text{-}10\times10^2$. The reverse currents are very high compared to GaAs samples. There is hard to find any trend due to the change of thickness or Bismuth content. The possible reason can be that the growth conditions are not optimized to a good level. The high leakage current would affect a lot of optical characteristics of this material, especially for the photo-multiplication.

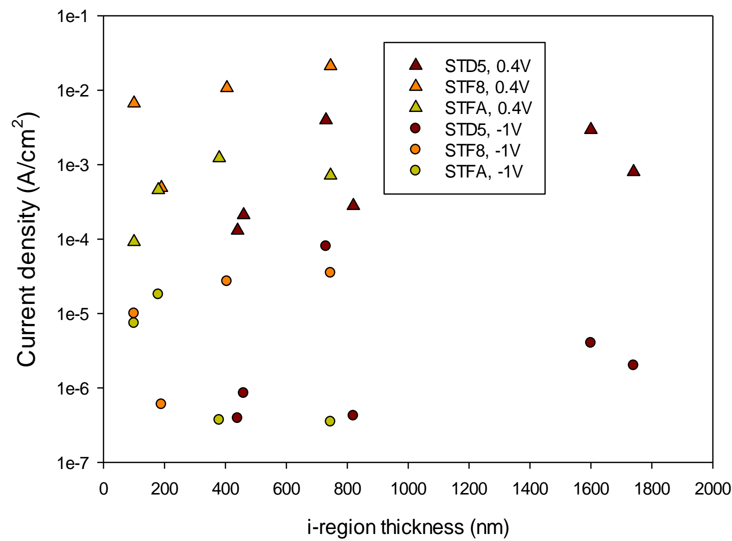

Figure 6.22. The comparison of forward and reverse currents of STD5, STF8 and STFA series samples.

1.6. Low-temperature current-voltage behaviour

Temperature dependent dark currents of STFA7 were measured which results are shown in Figure 6.23 and Figure 6.24. The dark currents as a function of the square root of reverse bias voltage are plotted in Figure 6.25. From Figure 6.25, when the reverse bias voltage is larger than 0.25 V, the IV plots seem to scale linearly with similar slopes on a semi-log scale, which suggests that the current might be determined by a kind of thermal emission process over a potential barrier which can be reduced by increasing electric field. Meanwhile, the dark currents are seriously affected by the recombination process in the i-region at lower reverse biases (0 ~ 0.25 V). At higher biases, the temperature dependence of IV becomes weaker, which might be due to band-to-band tunnelling.

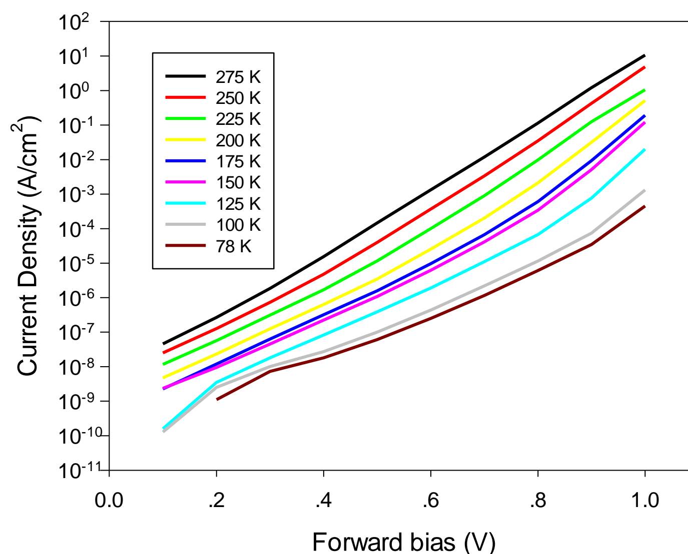

Figure 6.23. The forward temperature-dependent current voltage behaviour of STFA7

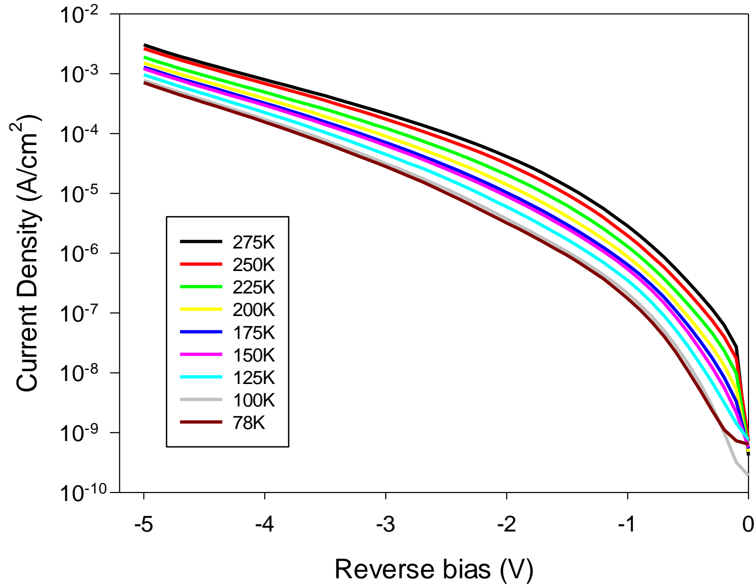

Figure 6.24. The reverse temperature-dependent current voltage behaviour of STFA7

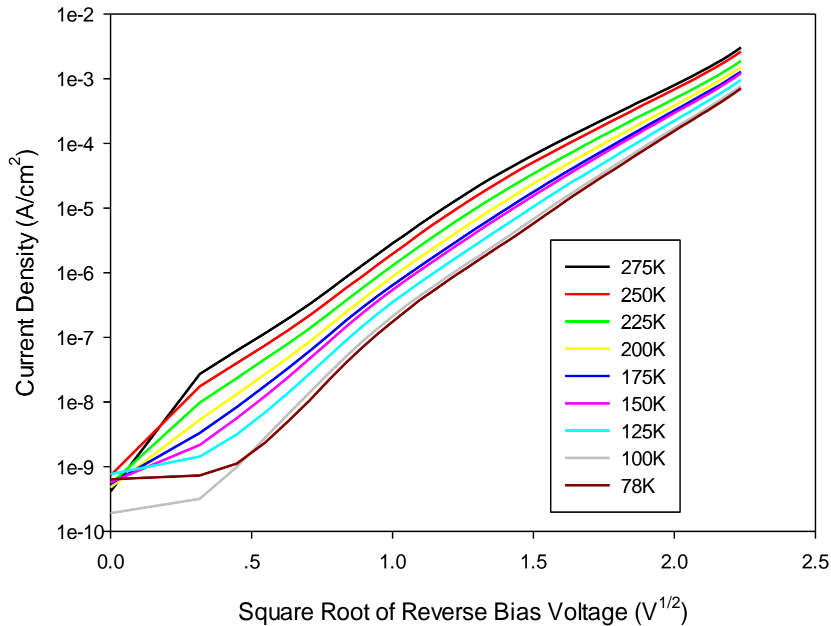

Figure 6.25. The temperature dependence of the dark current density as a function of the square root of reverse bias voltage

Through measuring current-voltage on devices with different radiuses (not shown here), it has been found that the dark currents were almost linearly scaled with the mesa area, which illustrates that the bulk-limited part must dominate the current. The behaviour of the sheet resistance as a function of the temperature is plotted in Figure 6.26. The sheet resistance was obtained when the reverse bias voltage is 0.3 V. A relationship between sheet resistance and temperature was found as following:

$$R_0 A \propto \exp\left(E_a / kT\right) \tag{6.4}$$

where R_0 is the resistance, A is the mesa area, k is Boltzmann constant, T is the absolute temperature, and E_a is called activation energy. Equation 6.4 can be deduced from Equation 3.9 if we consider the change of intrinsic carrier density with temperature. The activation energy can be extracted by fitting the curve from Figure 6.26. The E_a value above 200K is ~ 100 meV, and the one below 200K is ~ 37.5 meV. They are both much lower than the band gap. Similar phenomena with only one very small activation energy have been reported in [141]. It was claimed that this might be due to deep level defects. The finding of two unusually small activation energies matches the two possible localized states discovered from low-temperature PL (Figure 6.40). The effect of deep level defects will be discussed in Section 2 in detail.

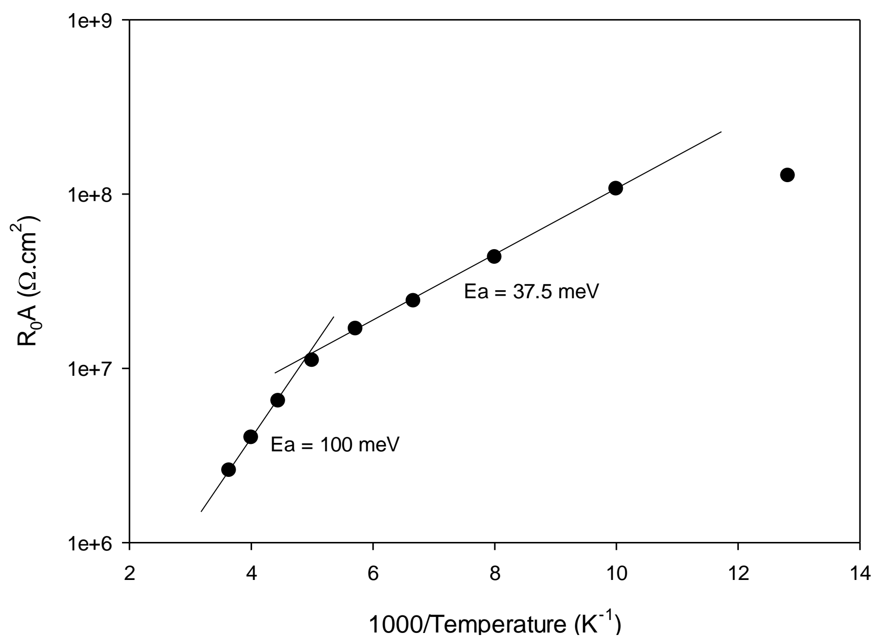

Figure 6.26. Sheet resistance of STFA7 as a function of 1000/T (Arrhenius plot)

1.7. Photocurrent

Photocurrent measurements were taken for STF8 and STFA series to investigate the absorption coefficient and its related characteristics. The reverse biases selected for these samples were based on CV measurements where the i-regions were saturated. The photoresponsivity spectrums were then obtained by the same method mentioned in Chapter 5 (shown in Figures 6.27 and 6.28).

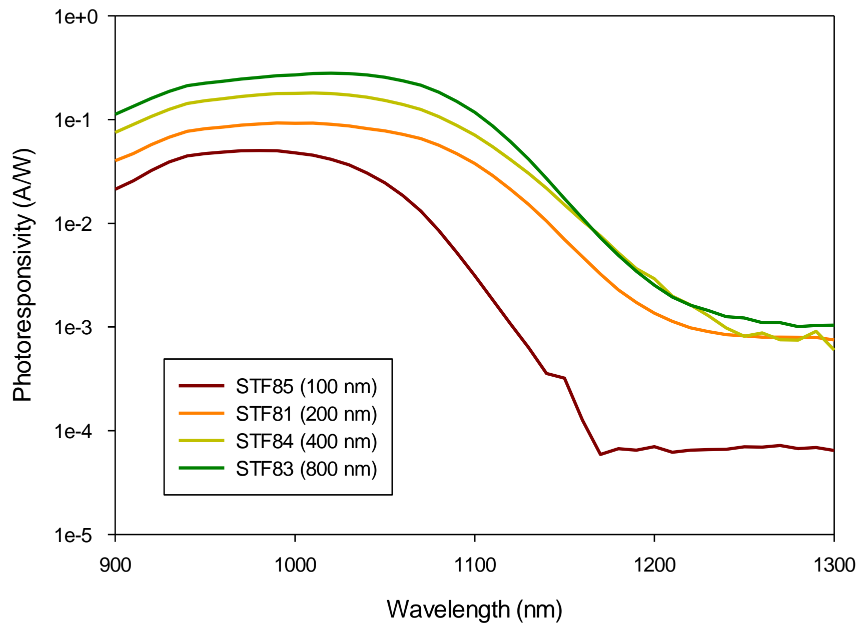

Figure 6.27. Photoresponsivity of STF8 series

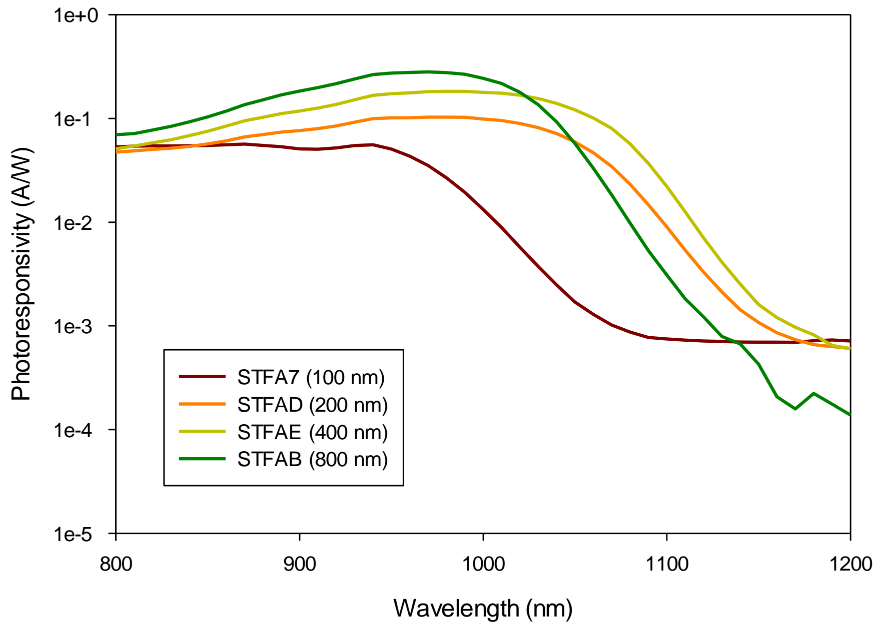

Figure 6.28. Photoresponsivity of STFA series

The absorption coefficients for STF8 and STFA series can be calculated using Equation 5.3. The absorption coefficients of the devices as a function of wavelength are plotted logarithmically in Figures 6.29 and 6.30.

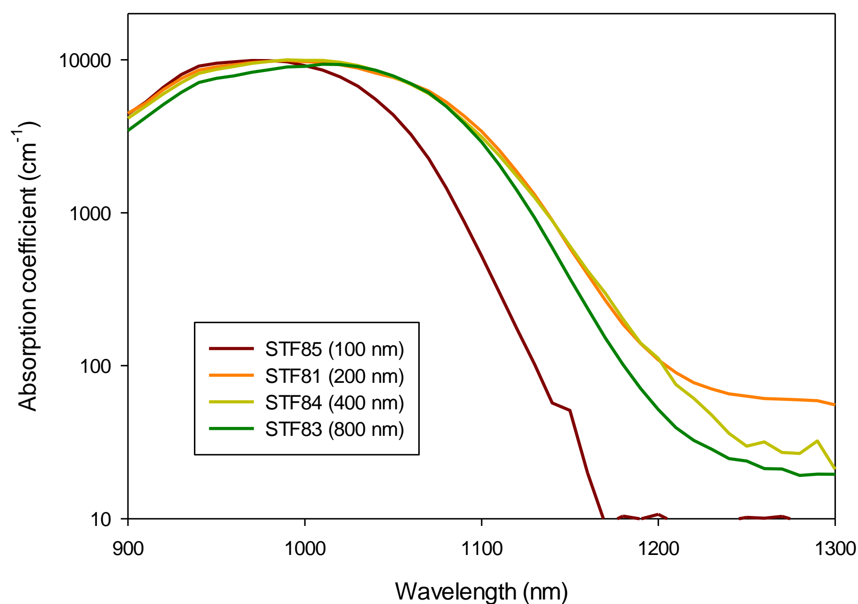

Figure 6.29. Absorption coefficient distribution of STF8 series

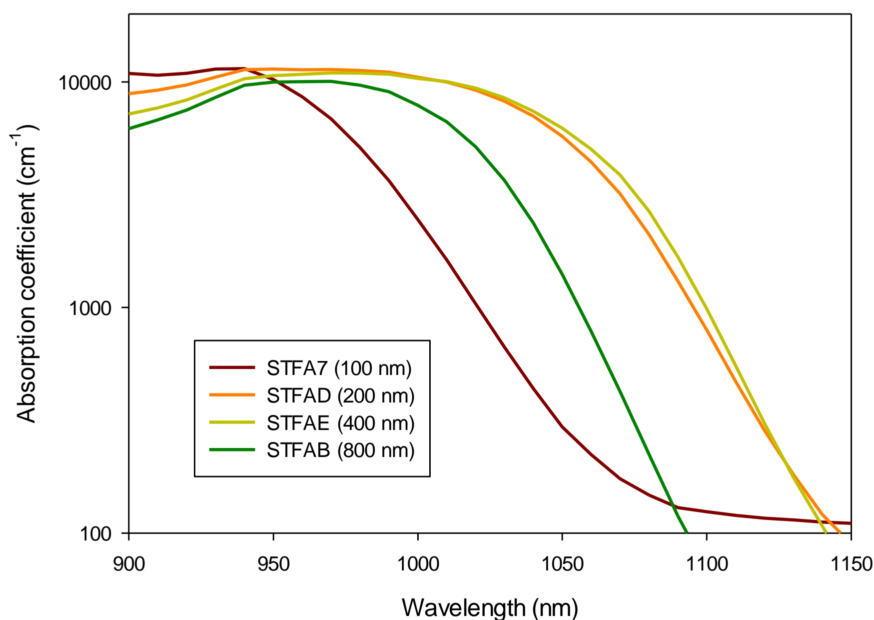

Figure 6.30. Absorption coefficient distribution of STFA series

From plotting the square of the absorption coefficients (Figures 6.31 and 6.32) against incident photon energy, straight lines are obtained. The band gap can then be estimated by extrapolating the plot to the intercept of the x-axis. The band-gaps and the corresponding estimated Bismuth contents of STF8 and STFA series are summarized in Table 6.5. The bismuth contents obtained from photocurrent measurements matched fairly well with those values from XRD and PL except for

STF85, the p-i-n with 100 nm i-region thickness. In this thesis, Bi contents obtained from PL are used most of the situations.

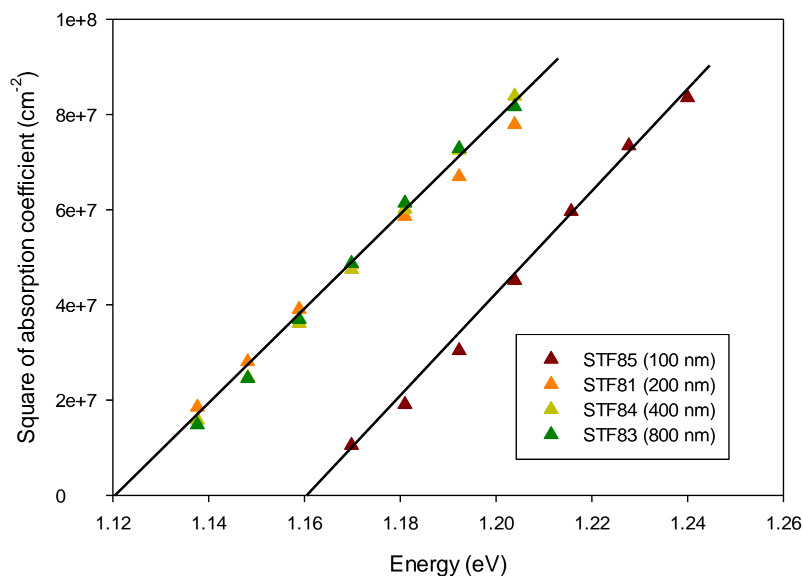

Figure 6.31. Square of absorption coefficient of STF8 series

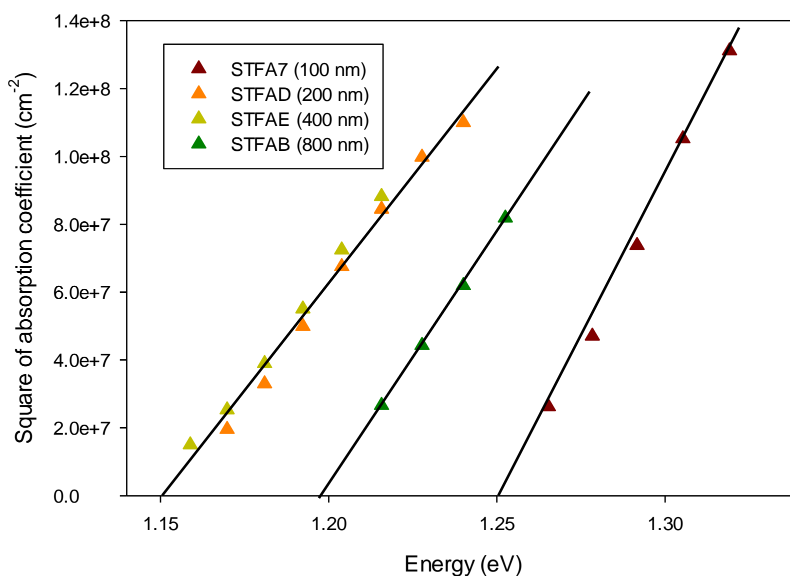

Figure 6.32. Square of absorption coefficient of STFA series

Table 6.5. Band-gaps and Bismuth contents of STF8 and STFA series

i-region thickness	Bi content (%) from XRD		Bi content (%) from PL		Band-gap energy (eV) from Photocurrent		Bi content (%) from Photocurrent	
	p-i-n	n-i-p	p-i-n	n-i-p	p-i-n	n-i-p	p-i-n	n-i-p
100 nm	4.79	2.32	4.4	2	1.16	1.25	3.5	2
200 nm	3.7	3.76	3.5	3.5	1.12	1.15	4	3.6
400 nm	4.1	3.8	4.1	3.7	1.12	1.15	4	3.6

800 nm	3.5	2.82	4.1	3	1.12	1.20	4	2.9
1600 nm	3.4	2.97	4.1	3.1				

2. Low-temperature photoluminescence

2.1. The investigation of the band-gap changing with temperature

The band-gap of the sample material would change when the sample temperature changes. There are 2 possible reasons for this change of the band-gap: the dilation of the lattice structure and the change of lattice vibration [142]. Theoretical treatments show that lattice vibration leads to a temperature dependence of band-gap as following [143]:

$$\begin{cases} \Delta E_g \propto T^2 & T \ll \theta \\ \Delta E_g \propto T & T \gg \theta \end{cases} \tag{6.5}$$

Here θ is the Debye temperature. An empirical equation was proposed by Varshni to show the change of the band gap with temperature [144]:

$$E_g = E_0 - \frac{\alpha T^2}{\beta + T} \tag{6.6}$$

Here E_g is the band-gap of the material, and E_0 is the band-gap at 0 K. α and β are fitting parameters. Various enhanced versions of the Varshni equation have since been proposed [145].

A 'band-tail' equation has also been proposed to describe the shift of PL peak position as a function of temperature in the high temperature range [146]:

$$h\nu_0 = E_g(T) - \frac{\sigma^2}{kT} \tag{6.7}$$

where $h\nu_0$ is the peak position of the PL energy spectrum, $E_g(T)$ is the band-gap energy of the material which can be described by Varshni equation, and σ is a parameter related to the deep levels. This "band-tail" model is to assume that the density of states at the band edge has a Gaussian-like temperature dependent distribution, and thus the emission peak would be influenced by the distribution. By fitting the parameter, information of deep levels can be uncovered. The problem with the 'band-tail' equation is that it does not satisfy the low temperature range.

The above equations can be used to fit the behaviours of quite a lot of materials very well, but for some materials, such as GaAsBi, new phenomenon named "S-shape" has been observed [20] which cannot be simply explained by the above equations. Figure 6.33 shows the band-gap change as a function of temperature for GaAsBi samples (the data is provided by Robert Richards).

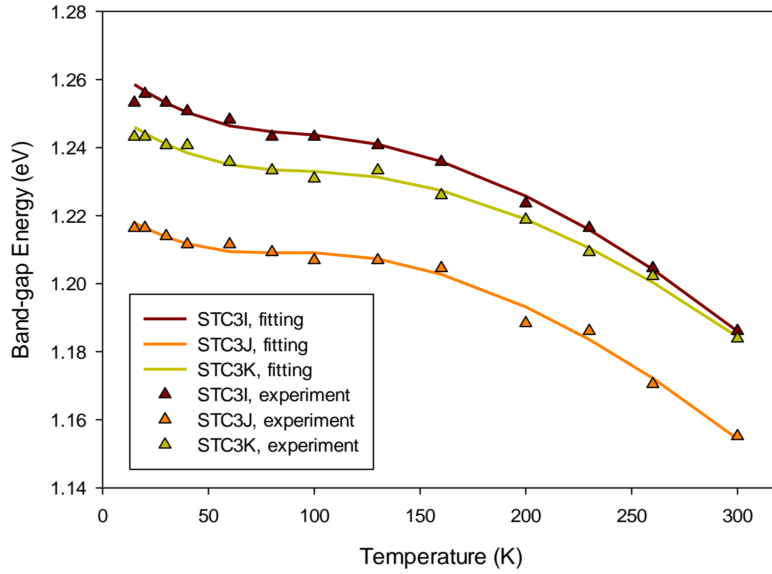

Figure 6.33. The band-gap energy as a function of temperature for GaAsBi samples

For the low temperature range a model using a numerical solution was proposed [147], and has been used in [148] and [20]. This model is based on an assumption that all the photoluminescence is generated from localized states instead of band-to-band recombination, and it can be used to explain the S-shape behaviour. The following discussion will introduce the deduction of this model, and the final equations are shown as Equations 6.17 and 6.18.

Most of the time defect states or deep levels act as long-lived traps. At relatively low temperature, carriers are still captured by the so-called 'localized' states. During the change of the temperature, the states will be delocalized thermally.

It is believed that the change of the density of localized states is the major reason for the change of PL intensity with temperature. If the states are delocalized, they act as trap centres, and Shockley-Read-Hall recombination would happen instead of radiative recombination. However, when the states are localized the recombination becomes radiative. In this case the density of localized states is almost proportional to the integrated PL intensity. The recombination rate can therefore be written as N/τ_r, where N is the density of localized states, and τ_r is the recombination lifetime which can be regarded as a constant.

When doing photoluminescence measurements, an excitation source should be used to provide incident photons to excite carriers from localized states. This generation rate, which is different from recombination lifetime, is related to a barrier energy called activation energy that electrons should overcome. Arrhenius plot has been introduced to find the activation energy of those localized states [147]. Several papers including [147] claim that the intensity should have the form:

$$I \propto \exp\left(\frac{E_a}{kT}\right) \tag{6.8}$$

where I is the PL intensity, T is the absolute temperature, k is Boltzmann constant, and E_a is the activation energy ($E_a > 0$). From plotting the logarithmic PL as a function of 1000/T (Arrhenius plot), a straight line should be obtained according to Equation 6.9. Figure 6.34 gave an Arrhenius plot of the experimental integrated electroluminescence (EL) data of a GaAsBi sample. The mechanism of EL is the same as PL, except that EL uses electrons as the excitation source. From Figure 6.34, a straight line was obtained, and the activation energy was therefore calculated.

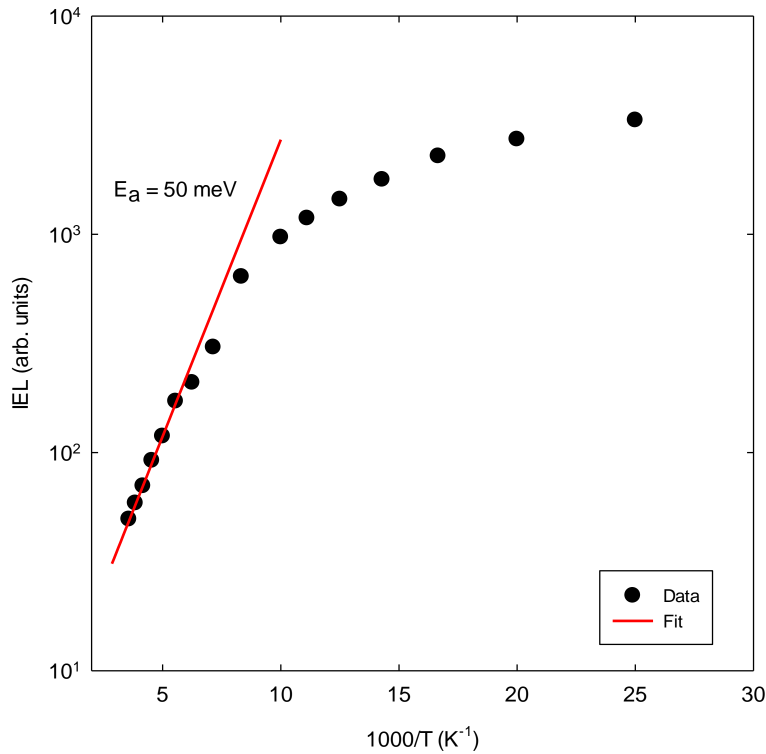

Figure 6.34. Arrhenius plot of a GaAsBi sample STB063 (adapted from [149])

Rewrite Equation 6.8, the following equation is obtained:

$$C = A\exp\left(\frac{-E_a}{kT}\right) \tag{6.9}$$

Here A is proportional to the integrated PL, or available localized states where the occupied carriers can be excited by the source, and C is just a constant which meaning would be explored in the next discussion.

If we assume that the activation energy is always a constant in different localized states, in the static state, the following equation is obtained, since the excited carriers per time should be equal to the returned carriers per time (see Figure 6.35).

$$G(E)=\frac{N}{\tau_r}+\frac{N}{\tau_{tr}}\exp\left(-\frac{E_a}{kT}\right) \tag{6.10}$$

where N is the density of localized states, $G(E)$ is the excitation rate, τ_r is the recombination lifetime (independent to the temperature), and τ_{tr} is the localized lifetime (e.g. lifetime of a hole from a deep trapped level to valence band).

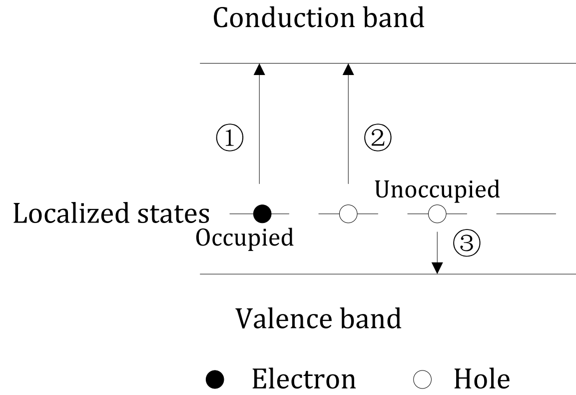

Figure 6.35. The behaviour of localized states under luminescence in the static state

If we assume N_0 is the density of localized states at 0 K, Equation 6.11 can be solved to give:

$$N=N_0\frac{1}{1+\frac{\tau_r}{\tau_{tr}}\exp\left(-\frac{E_a}{kT}\right)} \tag{6.11}$$

When the temperature is high, if τ_r/τ_{tr} is very large, then Equation 6.8 is derived from Equation 6.11. According to [148] the value of τ_r/τ_{tr} is around 104, so Equation 6.8 is quite an accurate approximation. From Equation 6.11 we can estimate not only the activation energy, but also the ratio of recombination lifetime to excitation lifetime.

In the above discussion, the localized states were assumed to have the same energy level, but in reality that is not the case. Here we use Gaussian distribution for localized states at 0 K [147] as following:

$$\rho(E)\propto\exp\left[\frac{-(E-E_0)^2}{2\sigma^2}\right] \tag{6.12}$$

Here E_0 represents the energy at the centre of localized states. The Gaussian assumption is based on the shape of LTPL measurements [150]. This 0 K localized states are assumed to be the distribution of all the available deep levels, since according to Fermi-Dirac distribution, all the electrons would be fallen into lower energy (valence band), and no carriers captured by deep levels would be thermally delocalized.

The Gaussian-like distribution of deep levels might be due to the natural distribution caused by non-uniformity. If there is only one deep level, it acts as a δ function. A luminescence quenching model has been proposed based on the δ function [151].

If we consider the equilibrium state of photo-luminescence on localized states, there are 4 possible processes (Figure 6.36).

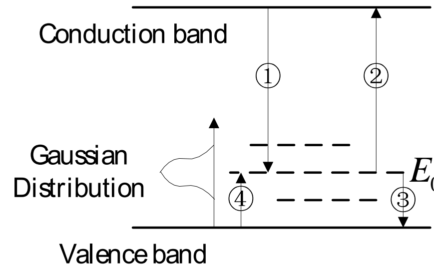

Figure 6.36. Four processes at the equilibrium state on localized states, (1) increase of holes in localized states by photon excitation (create holes) (2) recombination (3) holes excited thermally to valence band (4) holes fallen back to localized states (thermal redistribution)

If we define the density of localized states in a peculiar energy E at a certain temperature T as $N(E,T)$, the following equation can be obtained:

$$\frac{dN(E,T)}{dt}=\left\{\begin{array}{l} G(E)+\alpha\dfrac{\rho(E)}{\int_E \rho(E)dE}\int_{E'}\dfrac{N(E',T)}{\tau_{tr}}\exp\left(\dfrac{E'-E_a}{kT}\right)dE' \\ -\dfrac{N(E,T)}{\tau_{tr}}\exp\left(\dfrac{E-E_a}{kT}\right)-\dfrac{N(E,T)}{\tau_r} \end{array}\right\} \tag{6.13}$$

In equilibrium state, $dN(E,T)/dt=0$. The recombination lifetime τ_r is believed to be independent to the temperature. The 4th part on the right hand side of Equation 6.15 is the only part contributing to the photoluminescence. The 1st part represents carriers excited to deep levels, and the 3rd part is the thermal loss of carriers from localized states. The 2nd part is the re-capture of carriers from the loss. Since the distribution of deep levels is a Gaussian-like distribution, and if we assume the carriers are re-captured following this distribution, the 2nd part is obtained. In my view, the recapture of carriers should be related to the vacancies at deep levels instead of following the distribution, in which case the 2nd part should be rewritten as:

$$\alpha\left[\rho(E)-N(E,T)\right]\int_{E'}\frac{N(E',T)}{\tau_{tr}}\exp\left(\frac{E'-E_a}{kT}\right)dE' \tag{6.14}$$

This view is based on the recombination coefficient, as the recombination depends on the density of vacancies (holes) and available carrier density (electrons): $R=rpn$ [104]. The author of [147] claimed that the solution of Equation 6.13 is:

$$N(E,T) \propto \frac{\rho(E)}{1+\frac{\tau_r}{\tau_{tr}}\exp\left(\frac{E-E_a}{kT}\right)} \tag{6.15}$$

Which is exactly the same as Equation 6.11.

If we define:

$$\Lambda = \int_{E'} \frac{N(E',T)}{\tau_{tr}} \exp\left(\frac{E'-E_a}{kT}\right) dE' \tag{6.16}$$

This function should be a function of temperature. But it is treated as a constant in [147], which is not fair. We can try to calculate Equation 6.14 numerically and compare the result with the solution of Equation 6.12, to see how accurate the assumption (the recapture of carriers are negligible) is.

The maximum of $N(E,T)$ can be obtained at $\mathrm{d}N(E,T)/\mathrm{d}E=0$. If we define $x=(E_0-E)/kT$, we can get the PL spectrum peak position E_m when x satisfies the following equation:

$$xe^x = \left[\left(\frac{\sigma}{kT}\right)^2 - x\right]\frac{\tau_r}{\tau_{tr}}\exp\left(\frac{E_0-E_a}{kT}\right) \tag{6.17}$$

Furthermore, the deep level centre E_0 is believed to have the same trend as the conduction band and valence band change with temperature, which is described in Varshni equation. In this case, the peak position should have the form of:

$$E_g = E_{g0} - \frac{\alpha T^2}{\beta+T} - xkT \tag{6.18}$$

where E_{g0} is the band-gap at 0 K. The above discussion investigated the band-gap change with temperature theoretically, especially for the influence of localized states. The theory explained the "S-shape" well, and the experimental LTPL data of quantum well GaAsBi samples provided by Robert Richards (see Figure 6.33) matched the theory.

2.2. Experiment

To better understand the behaviours of GaAsBi related to band-gap and localized states, low temperature photoluminescence measurements were taken on a sample named STFA9. This sample was grown under the same growth environment as STFA7, except that the GaAs cap layer was undoped with 100 nm thick. PL was taken under different temperatures in a range from ~10 K to ~275 K with a step of 25 K. Incident 532 nm laser with different powers was used as the carrier generator. The original experimental results were recorded in Appendix 5. Figures 6.37 shows a power dependent PL at ~ 12 K. Figure 6.38 shows a temperature dependent PL with the laser power of ~ 0.1 W. The left side PL peaks in these plots are from GaAs material.

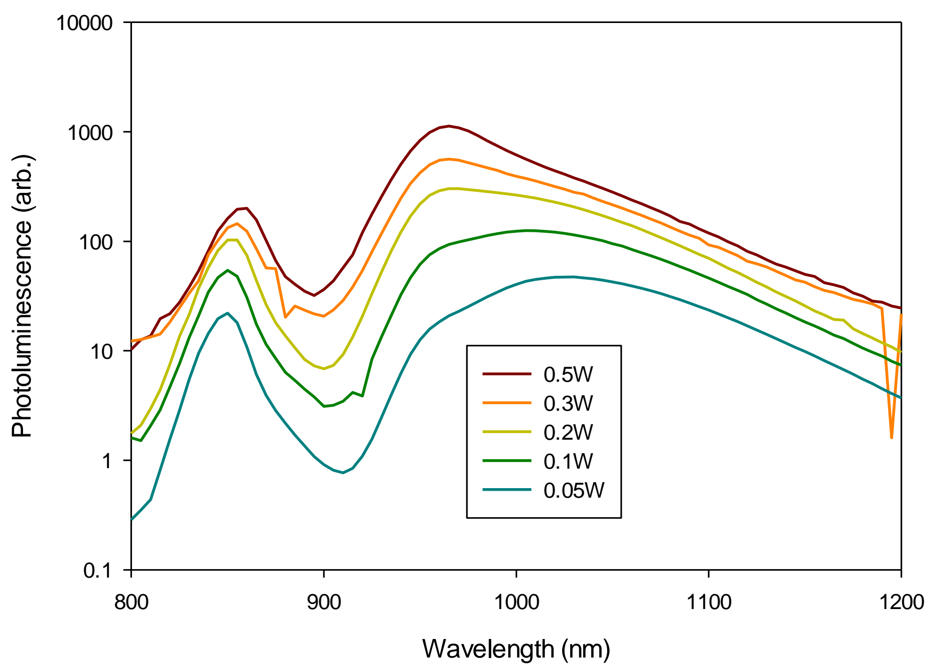

Figure 6.37. photoluminescence of STFA9 at ~12K

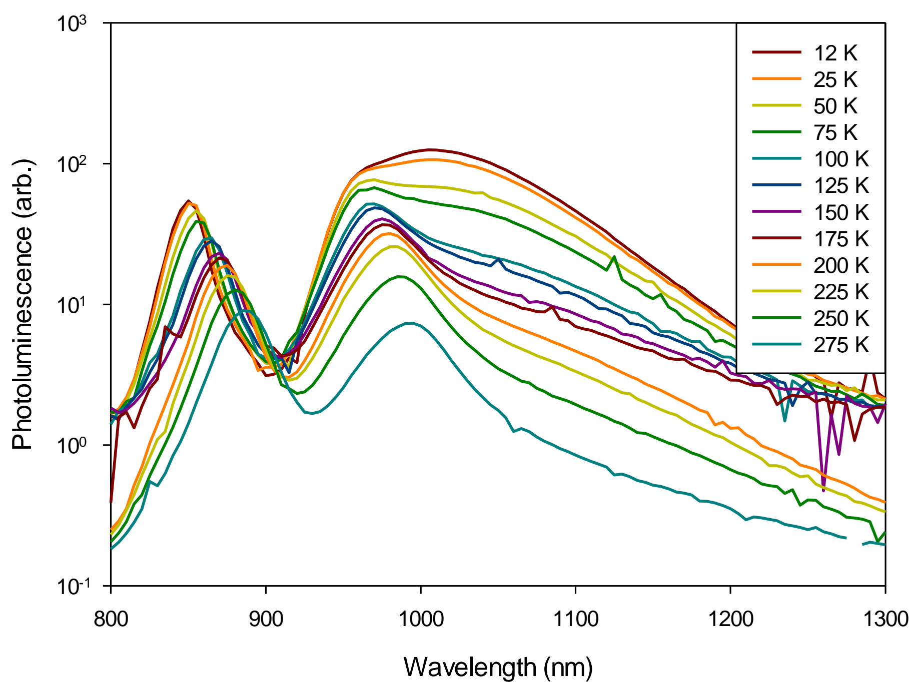

Figure 6.38. The temperature dependence of PL of STFA9 with incident laser power of ~ 0.1 W

An interesting phenomenon was found from these plots. At high temperatures, only one obvious GaAsBi peak was observed, but a distinct hump was developed in the low-energy tail of the PL band at lower temperatures. Similar phenomenon of two bismide peaks has also been observed in [152], but

in which the two peaks appear at high temperatures. A possible reason which caused the difference between the two results would be that the samples used in [152] were quantum wells. Quantum well samples naturally have a more complicated structure, and therefore the behaviours are harder to be predicted. But obviously one conclusion can be made that there is an existence of two separate PL peaks with different temperature dependences. Two peaks were also shown in [153] at a low temperature (10 K), though the peak in the low energy was not very clear.

As the analysis in the previous part, the most possible explanation of the two peaks is due to localized states from within the forbidden band. From Figure 6.37, with the increase of the incident laser intensity, the lower-energy peak got less and less significant in the plot. This is possibly because that the photons tended to excite the carriers with lower energy first (i.e. carriers trapped in the localized states). Whereas the limited amount of localized states is easily to be saturated, in which case at high intensity of photons free carriers in higher energy levels start to be excited. Another possible reason for multiple luminescence peaks could be the presence of more than one bismuth composition within the GaAsBi layer [154].

The integrated photoluminescence (IPL) over the wavelength range as a function of the incident laser power is plotted in Figure 6.39. As the temperature increases, the IPL drops down, which illustrates that more and more recombinations change gradually from radiative to non-radiative [155]. At higher temperature (> 125 K), IPL presents a linear relationship with laser power, which means that almost all the deep levels are nearly delocalized. On the contrary, the non-regular relationship between IPL and laser power at lower temperature reflects a more complicated behaviour when the traps are not thermally delocalized.

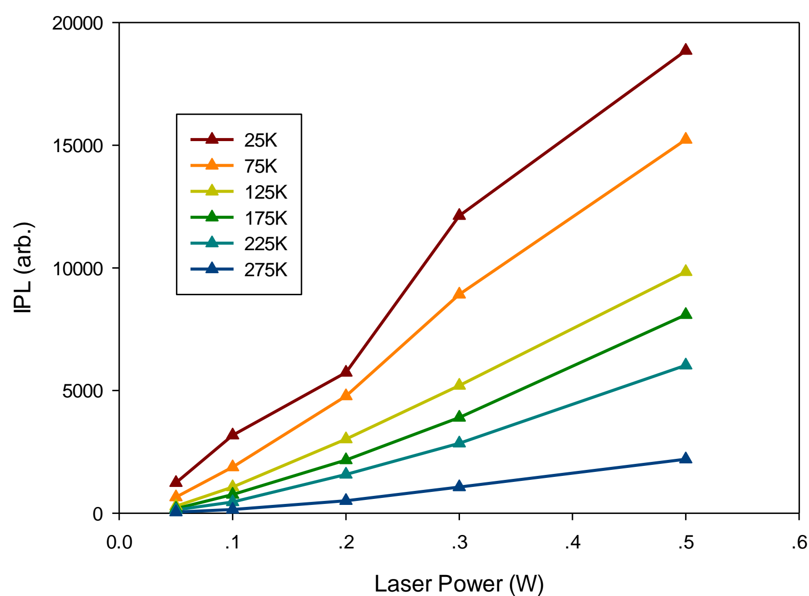

Figure 6.39. Integrated PL over the whole wavelength range plotted as a function of incident laser power and temperature

The log plot of IPL of STFA9 as a function of 1000/T (Arrhenius plot) with a laser power of 0.2 W is shown in Figure 6.40. From Figure 6.40, a similar curve to Figure 6.34 is obtained. Different from the conclusion made in Chris Hunter's thesis [149], it seems that there are at least two straight lines from the plots, which means that the activation energy is not a constant. It can be an indirect evidence that two types of localized states might exist in GaAsBi, possibly from short range ordering, Bi clusters, or more than one bismuth compositions [156][157]. If we assume that more than one localized states are in this sample, the activation energies calculated from the Arrhenius plot for two of them are 120 meV and 11 meV, which matches the data from [158].

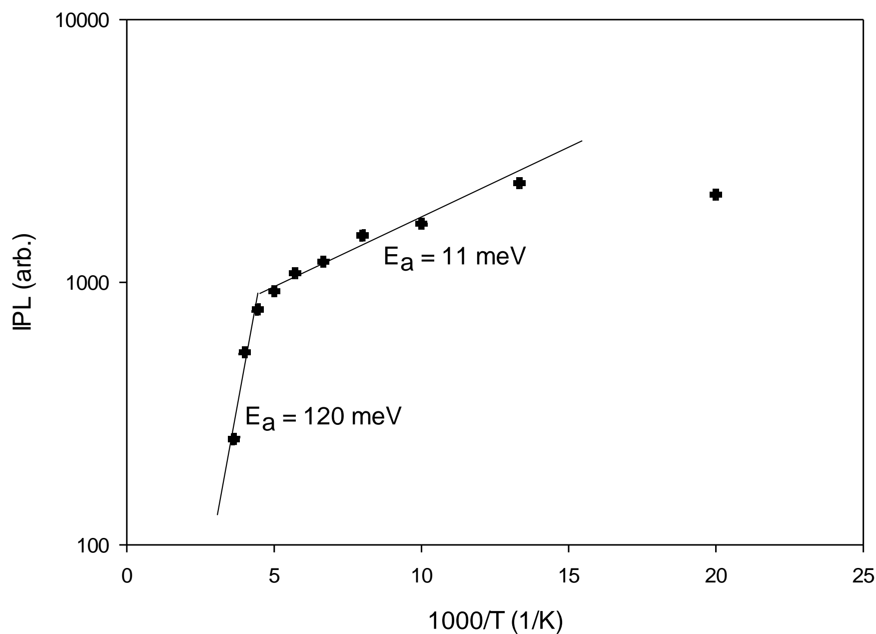

Figure 6.40. Integrated PL of STFA9 as a function of 1000/T with a laser power of ~ 0.2 W

The peak shift for STFA9 as a function of temperature is shown in Figure 6.41. Three fittings of the data are obtained using Equations 6.6, 6.7 and 6.18. The green line is plotted using the standard empirical Varshni shift equation (Equation 6.6). The red line is from the varied Varshni shift with considering the effect of deep levels (Equation 6.7). The black line is from the semi-empirical localized equation which can further unveil the function of deep levels (Equation 6.18). The fitting parameters are $E_0 = 1.32$ eV, $\alpha = 0.371$ meV/K, $\beta = 170$ K, $\sigma = 15.6$ meV, $E_a = 1.3$ eV, $\tau_r = 2.47 \times 10^{-6}$, $\tau_{tr} = 1.67 \times 10^{-7}$. The lower α value than the value reported for a GaAs control sample in [155] (0.56 meV/K) illustrates the temperature dependence reduction of band-gap by incorporating Bi. The activation energy can then be calculated as $E_0 - E_a \approx 20$ meV, which value is in the same order of the one obtained from IPL.

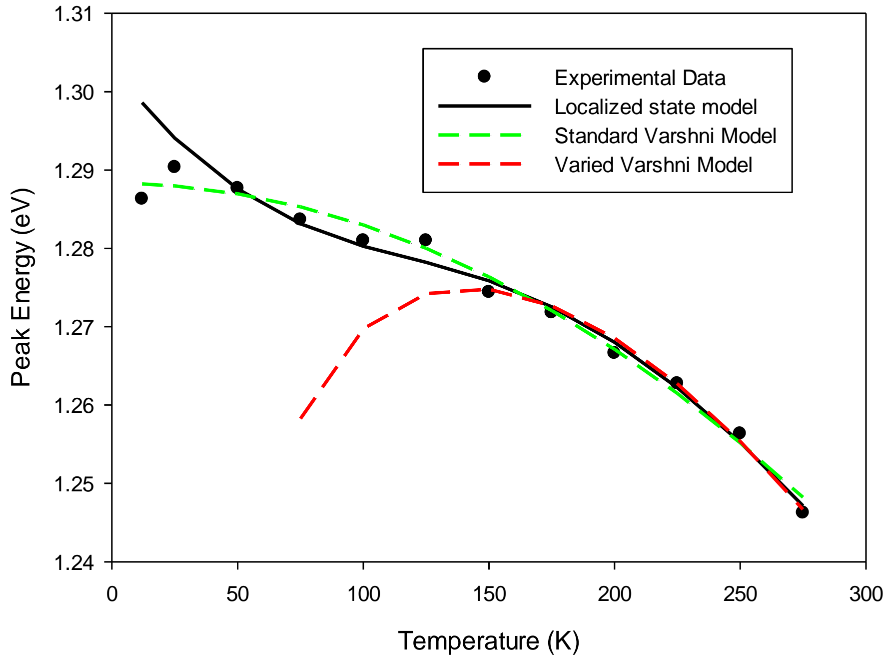

Figure 6.41. Peak shift of STFA9 as a function of temperature

In conclusion, from the previous researches [142][143], the temperature dilation and vibration of lattice are the main reasons for the band-gap change if the band is clear (i.e. without deep level traps). Whereas redistribution of localized states in different temperatures is believed to be the main reason causing the localized related s-shape of band gap change, since the barrier energy is different to different states.

3. Photo-multiplication behaviour

3.1. Background study of photo-multiplication

Avalanche photodiode (APD) is widely used in telecommunication to detect low photon flux due to its high sensitivity. The properties of the impact ionization depend critically on the relative values of the impact ionization coefficients α and β. For low noise APDs, it is important that α and β are very different in magnitude [159]. For instance, after an electron-hole pair is generated by an incident photon, if α is much larger than β, only the primary and secondary electrons keep generating more electron-hole pairs when they travel through the crystal, while the holes have a high probability that will simply be swept out by the electric field in the opposite direction.

On the contrary, considering an extreme situation, if α equals β and $1/\alpha$ and $1/\beta$ exactly equal the length of the multiplication region when the electrical field reaches a certain value, avalanche breakdown is triggered immediately and the current increases abruptly to be simply dependent on the series resistance. In this case, because of the random nature of the process, the breakdown occurs in a noisy uncontrollable manner over a very narrow range of fields.

A ratio β/α (or α/β) of only 5 can improve noise performance by over an order of magnitude if the carrier with the higher, rather than the lower ionization coefficient, is chosen to initiate the avalanche gain. Unfortunately, most APD detectors are facing the problem of relatively high excess noise, especially for III-V materials in which α and β are almost equal, within about a factor of 2.

HgCdTe is a candidate material for low noise APDs operating at 1.27 μm wavelengths for fibre optical communication applications, advanced laser rangefinders and 3D-imaging radars [160]. In the cadmium-rich alloy range of this material, $Hg_{1-x}Cd_xTe$, the spin-orbit splitting energy in the valence band can be equal to the fundamental energy gap ($E_g = \Delta_0$) [161]. In electron-hole recombination processes, this resonance ($E_g = \Delta_0$) is expected to largely increase Auger recombination. The impact ionization phenomena, being the reverse mechanism of the Auger process, is expected to have a minimum threshold energy lowered at the resonance. Either $\Delta_0 > E_g$ or $\Delta_0 < E_g$ would lead to a larger threshold ($E_i > E_g$).

At the resonance, the spin-orbit split-off band becomes a possible source of holes for initiation of impact ionization. In this case, electron-hole pairs are much easier to be created from the high energy holes. As calculated, the hole ionization coefficient depends exponentially on the difference between the threshold energy and band-gap energy ($E_i - E_g$). E_i is defined as the threshold energy for impact ionization. For HgCdTe in resonance state, the hole-initiated impact ionization is improved to $\beta/\alpha \approx 30$ at $x \approx 0.6$. Whereas when the composition makes far from resonance, for example, β/α can be as low as 0.06 at $x \approx 0.41$ [162][163]. This indicates that nearly pure electron or pure hole multiplication occur at some definite composition which has the beneficial effect of making the electron and hole impact ionization rates quite different, which is desirable for low-noise avalanche photodiodes. Similar enhancement of β/α with resonance have been found in the material GaAlSb [164].

InAs, with its band structure sharing similarities with $Hg_{0.7}Cd_{0.3}Te$, is another popular material for APDs with β/α nearly goes down to 0 [165]. The band structure exhibits large inter-valley separations between the minimums of the Γ valley and the L and X valleys, with values in excess of roughtly 0.7 and 1.0 eV, respectively [166]. Since the band gap of InAs is only 0.36 eV, the large separations allow electrons to be accelerated into an energy much greater than the band gap before inter-valley scattering, in which case electrons have greater opportunities to get impact ionization. Meantime, the heavy-hole valence band is relatively flat, leading to a harder acceleration of holes. Therefore, the electron initiated impact ionization is expected to be significantly enhanced over hole initiated impact ionization (ie. $\beta/\alpha \rightarrow 0$).

The dilute nitride, Ga(In)AsN, is well known for its large band gap reduction with only a small fraction of N, which is explained by the band anti-crossing on the conduction band. It is suggested that the modified conduction band of dilute nitrides would hinder electrons from reaching sufficient

energy to impact ionize [159], which makes the material become a potential candidate for low noise hole-initiated APDs [167].

3.2. Multiplication behaviour of GaAs

To investigate the multiplication behaviour of GaAsBi, it is better to have a look at GaAs first. The ideal impact ionisation coefficients of GaAs can usually be expressed as following [168]:

$$\alpha, \beta = A \exp\left[-\left(\frac{B}{F}\right)^{c}\right] \quad (6.19)$$

where α (β) is electron (hole) ionisation coefficient, F is the electrical field strength, and A, B and c are fitting parameters. For GaAs, the fitting parameters A, B, and c are shown in Table 6.6, which are obtained from photo-multiplication measurements on GaAs PINs and NIPs [169].

Table 6.6. The fitting parameters for GaAs ionisation coefficients.

F **(kV/cm)**	**Coefficient type**	***A*** **($\times 10^5 cm^{-1}$)**	***B*** **($\times 10^5 cm^{-1}$)**	***c***
150-500	α	1.45	5	2.1
	β	1.55	5.5	2
500-1110	α	4.7	12	0.9
	β	4	11	1
1110-1400	α	6.39	16	0.9
	β	5.92	15.5	0.95

Ionisation coefficients of GaAs are therefore drawn in Figure 6.42.

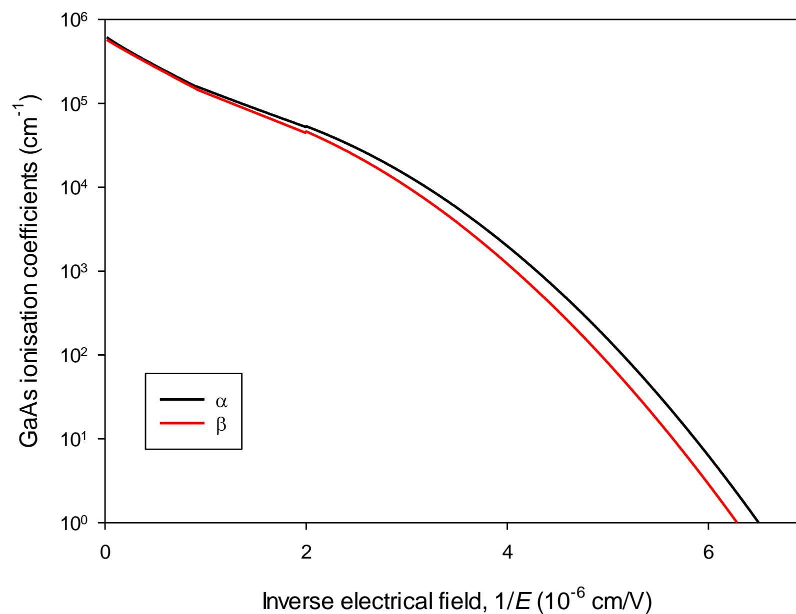

Figure 6.42. Ionisation coefficients of GaAs as a function of inverse electrical field

According to Equations 3.16, the multiplication factors for ideal GaAs PINs at different i-region thicknesses can be calculated when using the ionisation coefficients described above. Multiplication factors for ideal GaAs PINs with 4 different i-region thicknesses (200 nm, 400 nm, 800 nm and 1600 nm) were shown in Figure 6.43 and Figure 6.44.

From Figure 6.43, the breakdown voltage is getting larger with increasing i-region thickness. Besides, for the same i-region thickness, M_e is larger than M_h since $\alpha > \beta$, but eventually (when M_e and M_h go infinity) they breakdown at the same voltage. From Figure 6.44, the required impact ionisation field is smaller with increasing i-region thickness. It is due to that longer i-region would give more space for carriers to accelerate, and hence a larger M can be obtained at the same electrical field.

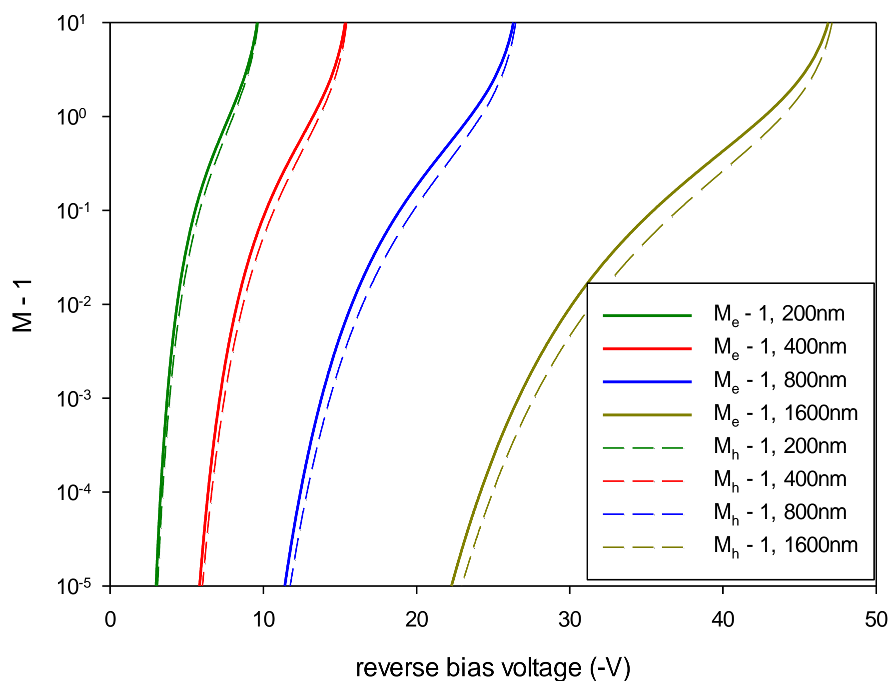

Figure 6.43. Multiplication factors for GaAs as a function of reverse bias at different i-region thicknesses. M_e and M_h are the electron-initiated and hole-initiated multiplication factors respectively

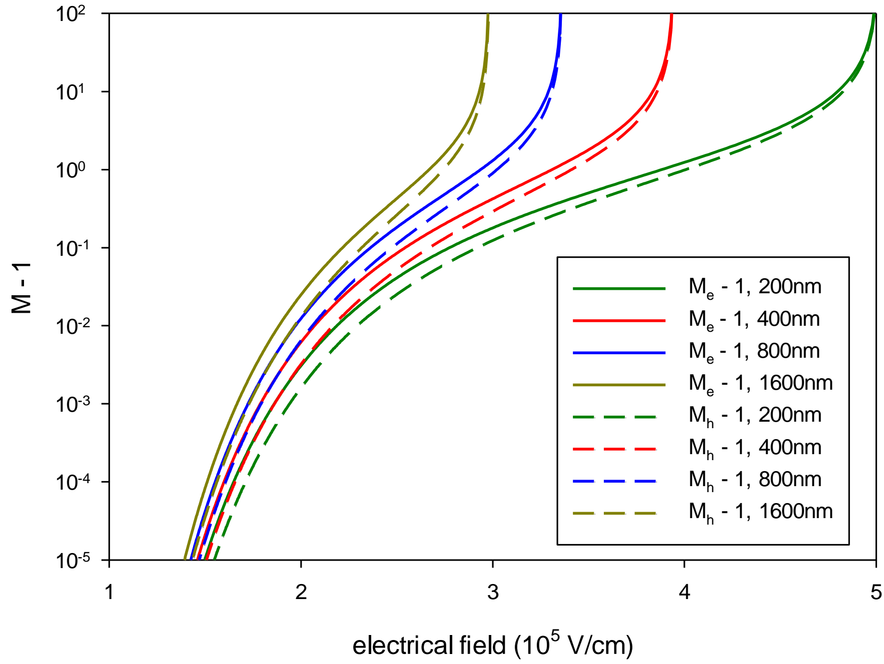

Figure 6.44. Multiplication factors for GaAs as a function of electrical field at different i-region thicknesses

3.3. Experimental Results

To explore the behavior of GaAsBi photo-multiplication, two different lasers with 543.5 nm and 850 nm wavelengths were used to incident on the top optical windows of the diodes, and the generated photocurrents were extracted with a phase-sensitive lock-in amplifier. When adding a high enough reverse bias voltage during the illumination, a measurable multiplication gain can be obtained due to impact ionization. The raw data of photo-multiplication photocurrents are shown in Appendix 6.

Based on the absorption coefficients of doped GaAs, 96% photons would be absorbed in the GaAs cap layer if 543.5 nm laser is used, whereas only 42% photons would be absorbed if 850 nm laser is used. It's fair to regard that it is almost pure injection using 543.5 nm laser. The photo-generated minority carriers would only diffuse from the top p or n layer to the edge of i-region, and get swept by the electric field across the whole region. Depending on the type of injected minority carriers, the gain can be represented as M_e for electrons or M_h for holes. On the contrary, since only 42% photons would be absorbed in the cap layer when 850 nm laser is used, the photo-multiplication gain obtained with the longer wavelength laser (850 nm) is therefore represented by M_{mix}, since carriers would also be generated in the i-region.

A linear extrapolation of the primary photocurrent is used to correct for a small increase in the carrier collection efficiency due to the increasing depletion width and peak electric field with reverse

bias. The avalanche gain or multiplication factor (*M*) is the ratio of the multiplied and primary photocurrent.

Besides, the more meaningful way of looking at the data from photo-multiplication measurements is to plot the avalanche multiplication gain against electrical field. The way of mapping voltage to electrical field in the i-region can be done with a simple method. Since the doping density in the p- and n-regions are high, the contribution of electrical field to the voltage can be ignored (see Figure 6.45).

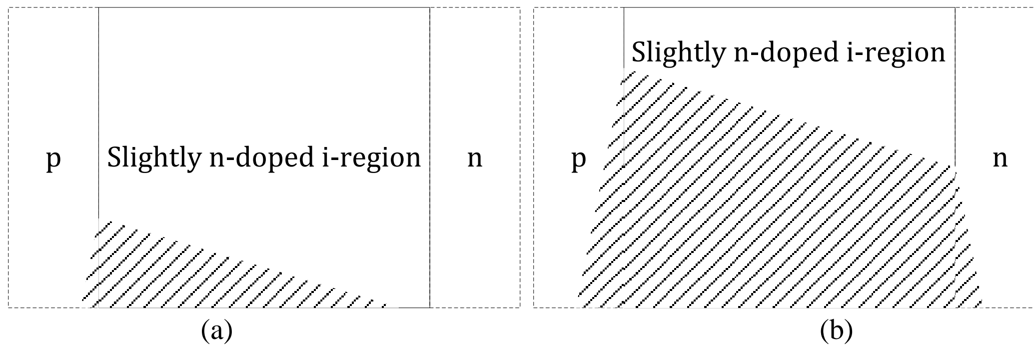

Figure 6.45. The electrical field distribution through p-i-n junction with slightly n-doped i-region, (a) is when the i-region is partially depleted, and (b) is when the i-region is fully depleted. The top edge of the shadow region is the distribution of electrical field, and the area of that region is the accumulated voltage.

According to Gauss Theorem, the relationship between electrical field and doping density in the depletion region is:

$$dE = \frac{qN}{\varepsilon} dx \tag{6.20}$$

where N is the doping density and ε is the permittivity of the material. In this case, if the i-region is at the fully-depleted edge, the maximum electrical field is:

$$E_{\max} = \frac{qN}{\varepsilon} W_i \tag{6.21}$$

where W_i is the i-region thickness. And the accumulated voltage is approximately:

$$V_{th} \approx \frac{qNW_i^2}{2\varepsilon} \tag{6.22}$$

If the built-in potential is ϕ_b, the bias voltage is $V = \phi_b - V_{th}$. If the accumulated voltage is smaller than V_{th}, which means that $V > \phi_b - V_{th}$, i-region is partially depleted, otherwise it is fully depleted. In the situation of partially depleted, the relationship between the maximum electrical field and bias voltage is:

$$E_{\max} = \sqrt{\frac{2qN(\phi_b - V)}{\varepsilon}} \tag{6.23}$$

And the average electrical field can be expressed as:

$$E_{avg} = \sqrt{\frac{qN(\phi_b - V)}{2\varepsilon}} \tag{6.23a}$$

When i-region is fully depleted, the relationship changes to:

$$E_{\max} = \frac{\phi_b - V}{W_i} + \frac{qNW_i}{2\varepsilon} \tag{6.24}$$

And the average electrical field can be expressed as:

$$E_{\max} = \frac{\phi_b - V}{W_i} \tag{6.24a}$$

From CV measurements, ϕ_b is approximately 1, N is about ~ 1.5×10^{16} cm^{-3}, ε is the permittivity of GaAs. For devices with 100 nm, 200 nm, 400 nm, and 800 nm thicknesses, the bias voltages at the fully depleted edge are roughly 0.86 V, 0.44V, -1.25V, and -8V respectively. In this case, the 100 nm and 200 nm ones are fully depleted already with 0 bias. From Equations 6.23 and 6.24, the relationship between electrical field and voltage is obtained. After the baseline correction, the multiplication gain of STF8 and STFA series as a function of electrical field can be obtained as shown in Figures 6.46-6.49. The avalanche gains of ideal GaAs with different i-region thicknesses are also shown in the figures to compare with GaAsBi experimental results.

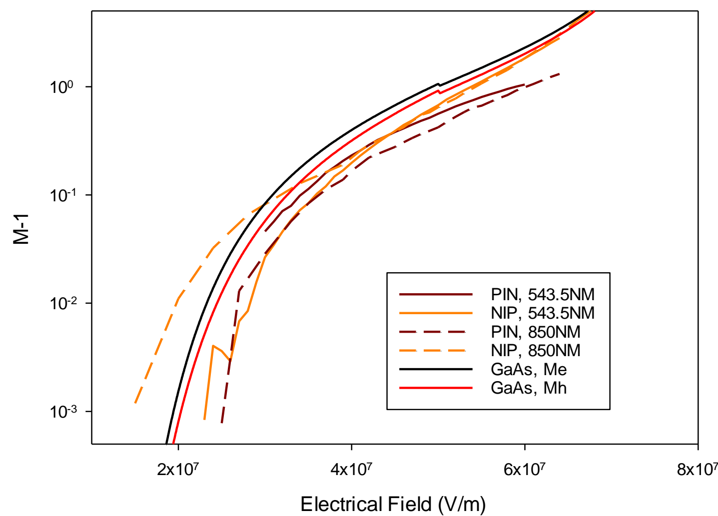

Figure 6.46. The multiplication gain of PIN and NIP with ~ 100 nm i-region thickness as a function of average electrical field compared with GaAs

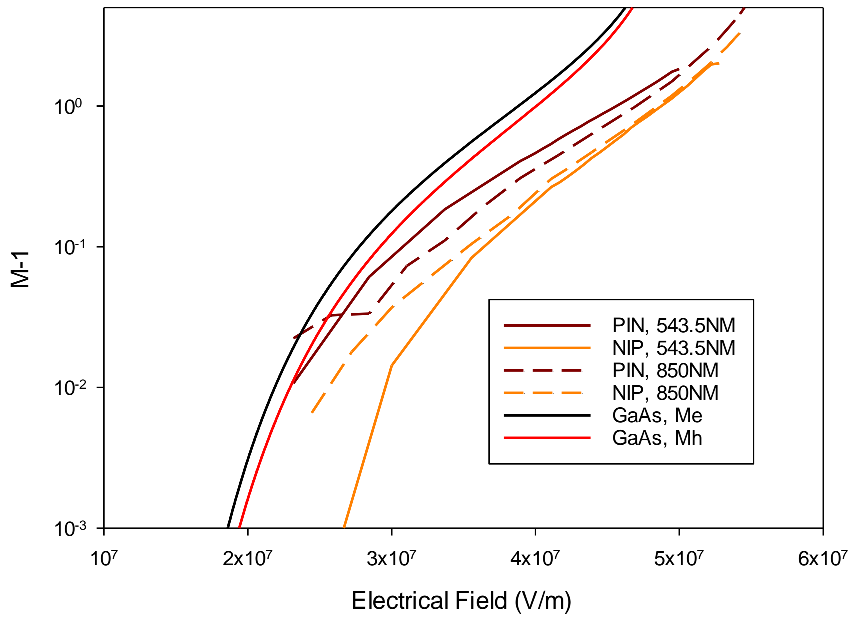

Figure 6.47. The multiplication gain of PIN and NIP with ~ 200 nm i-region thickness as a function of average electrical field compared with GaAs

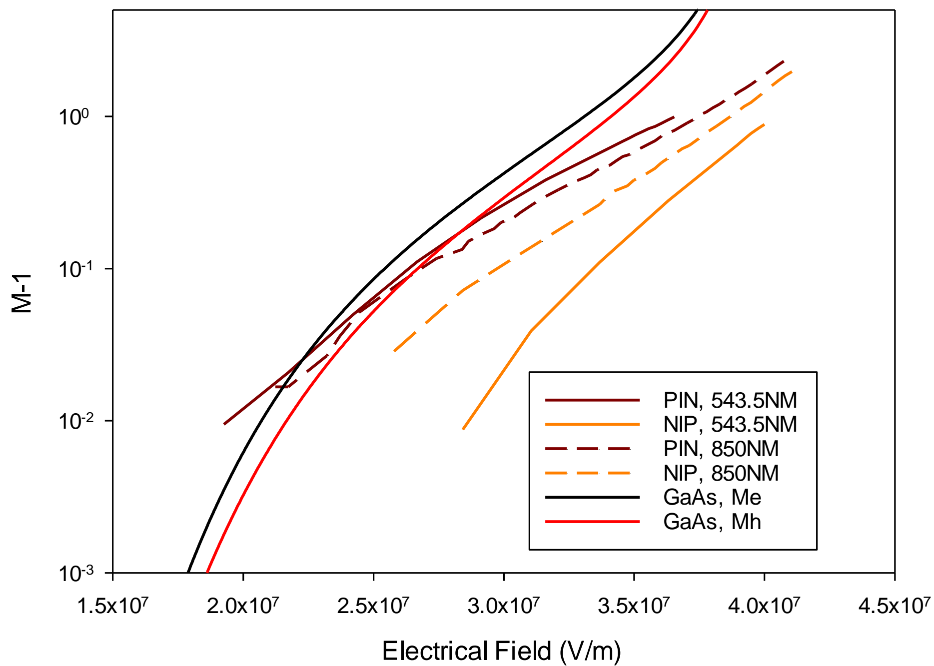

Figure 6.48. The multiplication gain of PIN and NIP with ~ 400 nm i-region thickness as a function of average electrical field compared with GaAs

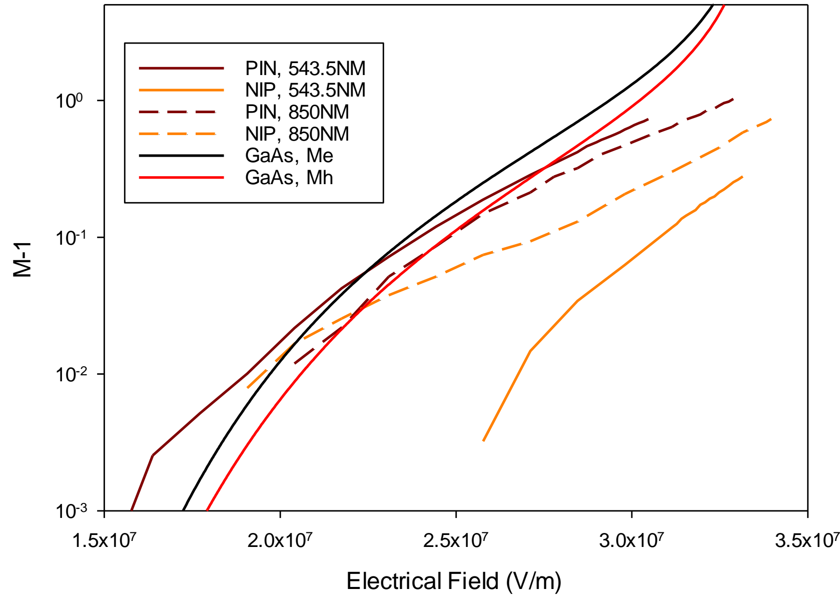

Figure 6.49. The multiplication gain of PIN and NIP with ~ 800 nm i-region thickness as a function of average electrical field compared with GaAs

From Figures 6.47-6.49, it seems like that M_e and M_h were getting closer and closer with the increasing electrical field, and finally converged into one when the electrical field was large enough. Larger breakdown fields were required for GaAsBi samples compared to GaAs, which means either α or β (or both) has been suppressed by incorporating Bi into GaAs. Furthermore, a clear larger difference between electron-initiated and hole-initiated multiplication factors (M_e and M_h respectively) compared to GaAs was observed. The difference between M_e and M_h is also much larger in this thesis compared to the results in [167]. Multiplication gain happened at larger field for hole-initiated situation suggests a considerable suppression of impact ionization of holes. For Figure 6.46, since the i-region thickness of the samples is very thin, the performance would be affected more seriously by side effects such as dead space effect, and the fluctuation of the measurement results can be serious, such as the CV measurements. In this case, the data of 100 nm layer samples is excluded when we analyze the final multiplication factor and ionization coefficients.

Due to the variation of bismuth content and other uncertainties in these samples, comparing pure injection initiated multiplication (M_e or M_h) with mixed injection (M_{mix}) in the same samples can provide a more robust evidence of a large α/β ratio. From Figures 6.48-6.49 (results in samples with thicker i-region thicknesses), a slightly right shift of M-1 towards larger field from M_e to M_{mix} can be observed as well as a significant left shift of M-1 from M_h to M_{mix}. The smaller deviation from M_e to M_{mix} compared to the deviation from M_h to M_{mix} can be explained theoretically. If α and β values are already obtained which has the form of Equations 6.27 and 6.28, and the starting point of avalanche x

is chosen to be half of the avalanche region thickness ($w/2$), the electron-initiated, hole-initiated and mixed avalanche gains can be obtained from Equations 3.16, 3.16a and 3.16b. The simulation results (not shown here) match the experimental results, where M_e to M_{mix} is much smaller than M_h to M_{mix}. From a qualitative view, if β is suppressed, electron ionization plays a major roll. In this case, hole-initiated avalanche gain would be very small, while electron-initiated and mixed-initiated can both get a fairly large gain.

Since $M_e > M_h$ for GaAsBi from Figures 6.56-6.59, the electron ionization coefficient can be estimated in two ways if we assume $M_e = M_h$ and $M_e >> M_h$.

If $M_e = M_h$, Equation 3.16a is changed to:

$$\alpha = \frac{1}{w}\left(\frac{M_e - 1}{M_e}\right) \tag{6.25}$$

If $M_e >> M_h$, Equation 3.16a is changed to:

$$\alpha = \frac{1}{w}\ln\left(M_e\right) \tag{6.26}$$

The estimated electron ionization coefficients for different i-region thickness samples are plotted in Figures 6.50 and 6.51. Figure 6.50 shows the results obtained using Equation 6.25, and Figure 6.51 shows the results using Equation 6.26. From these two figures, the difference of hole-initiated multiplication gain did not affect much about the value of electron ionisation coefficient α, which shows the validation of the estimation. Besides, the measured α of GaAsBi samples is very similar to α of GaAs.

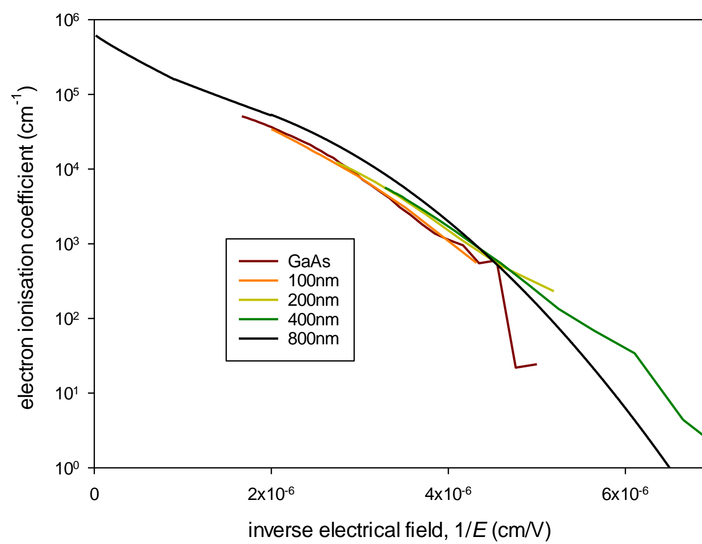

Figure 6.50. The estimated electron ionisation coefficient of GaAsBi using Equation 6.25 compared to GaAs (assume $M_e = M_h$)

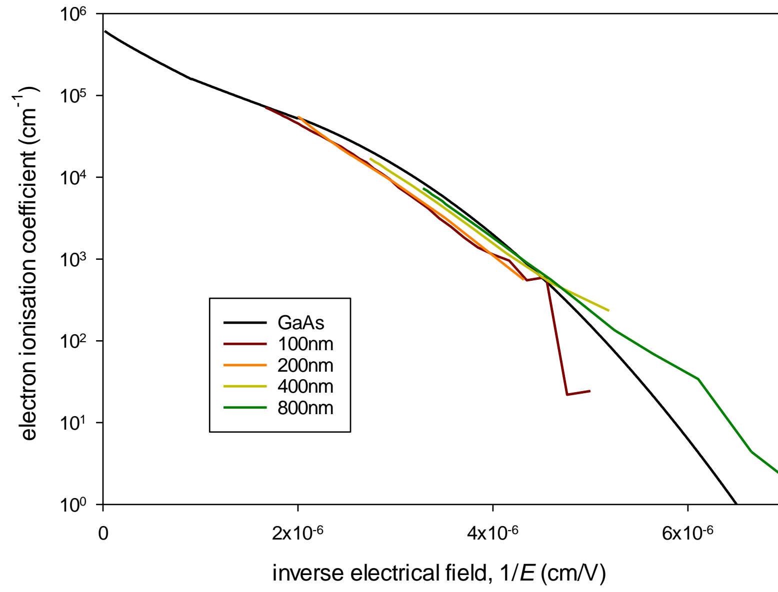

Figure 6.51. The estimated electron ionisation coefficient of GaAsBi using Equation 6.26 compared to GaAs (assume $M_e >> M_h$)

Neglecting small differences in the dimensions, background doping or alloy content in p-i-n and n-i-p structures, α and β can be estimated from multiplication factors M_e and M_h using Equation 3.16 [170], and the results are shown in Figure 6.52. The empirical parametrized expressions for α and β obtained from fitting the results are as follows:

$$\alpha = 1.1\times10^5 \exp\left(-\left[\frac{5.2\times10^5}{E}\right]^2\right) \tag{6.27}$$

$$\beta = 5.4\times10^4 \exp\left(-\left[\frac{4.7\times10^5}{E}\right]^{3.2}\right) \tag{6.28}$$

where E denotes electrical field in V/cm. Equations 6.27 and 6.28 give good fits to the experimental data as shown in Figure 6.52. A relatively large ionization coefficient ratio α/β is observed (especially larger than 10 when the electrical field is small enough). The hole ionization coefficient β is largely suppressed by more than an order of magnitude as predicted based on the valence-band anti-crossing effect with increasing effective hole mass; whereas the electron ionization coefficient α is not so heavily suppressed compared to GaAs.

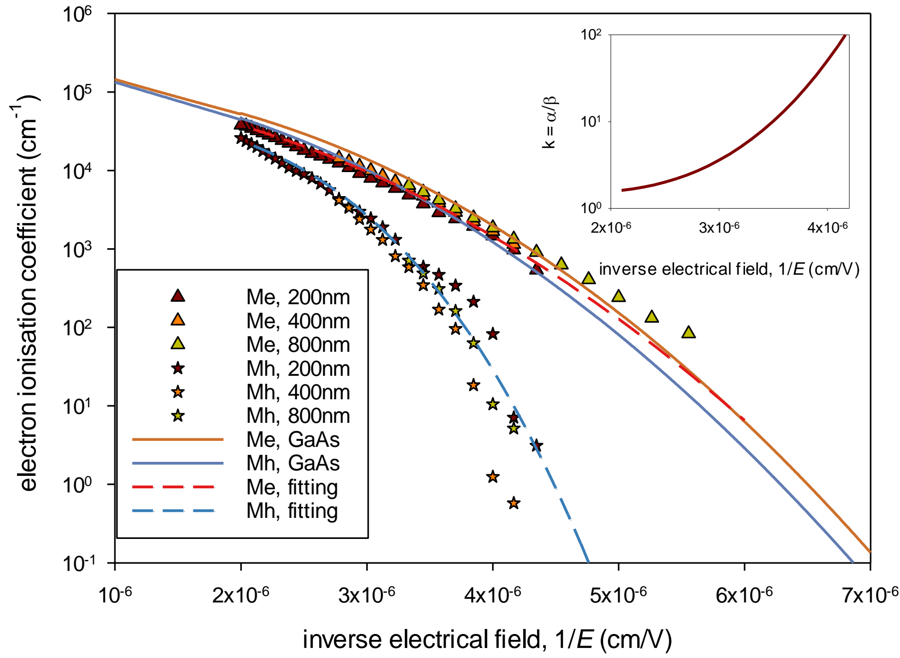

Figure 6.52. The calculated electron and hole ionisation coefficients (α and β) of GaAsBi using Equation 3.16 compared to GaAs

Similar to dilute nitride, the alloy GaAsBi has the property of large band gap reduction as well. The valence band anti-crossing (VBAC) model as shown in Chapter 1 was proposed to explain the band gap reduction, and the valence band was predicted to split into $E_-(k)$ and $E_+(k)$. The change of the heavy-hole band accounts for not only the band gap reduction, but also an increase in the hole effective mass. This change of the band structure is thought to suppress holes from attaining sufficient energy to achieve impact ionization, leading to a smaller hole ionization coefficient. Besides, unlike InAs and HgCdTe, the bismuth content should be larger than 10% in GaAsBi in order to make the spin-orbit splitting energy be equal to the band gap ($E_g = \Delta_0$). In this case, GaAsBi with low Bi content would not be able to provide high energy holes as the source of generating electron-hole pairs from spin-orbit splitting band.

There is no obvious reason for the small reduction of α, since the band structure of the conduction band for GaAsBi is still being discussed. Possible reasons can be due to ionized impurity scattering, residual lattice mismatch, or inhomogeneity of Bi content. It is possible that α/β could be further increased if these extrinsic factors related to the sample quality could be identified and reduced, especially when the unintentional doping density is very high in the GaAsBi i-layer, leading to a relatively high dark current.

4. Summary

In this chapter, two sets of samples (STF8 and STFA) were grown to investigate several properties of GaAsBi. Low temperature current-voltage and photoluminescence measurements were taken on STFA7 and STFA9 respectively to investigate the temperature dependent behaviour of GaAsBi. It seems that both measurements show two different activation energies which can be explained by the existence of localized states. The photo-multiplication measurements were taken on both STF8 and STFA series. A significant suppression of hole-initiated impact ionization was observed as predicted by previous theory related to the valence band anti-crossing. A relatively large ionization coefficient ratio α/β for GaAsBi heterojunctions was obtained from this experiment. The encouraging discovery shows a very promising use of GaAsBi as low-noise electron-initiated avalanche photodiodes.

Chapter 7: Future plan

1. Sample growth

Related to the general MBE machine operation, it will be very useful to verify the relationship between cell temperature and flux rate. Though we know the ideal relationship should obey the Knudsen rule, in real world there must be a deviation. The process is to set different temperatures of the Ga cell, and to find the corresponding beam equivalent pressures (BEPs) and the growth rate related atomic flux rates. The importance of doing this experiment is that it can help to decide the bismuth flux rate by observing the cell temperature and BEP. Previously we think the BEP has a linear relationship with the flux rate, which is not so correct, and this experiment can help to fix this problem.

The surface reconstruction is the most important and most difficult research part in MBE. From the phase changing, lots of information can be found, such as the growth temperature, the As:Ga flux ratio, etc. The GaAs phase diagram in either static or growing situation is quite mature, but there are still loads of unknowns with GaAsBi. Therefore, it can be productive to investigate more about the phase diagram of GaAsBi surface reconstruction.

Several growth models for GaAsBi growth were already investigated in Chapter 4. However, more thorough theoretical models could be established by understanding the fundamental working mechanism of growth. Besides, investigating the growth theory and improving growth models can be very helpful to grow GaAsBi samples with better quality.

Doped GaAsBi layer growth can also be a very interesting task. Furthermore, growth of GaAsBi devices with good qualities and implementing them in useful areas should be the final goal of the research.

2. Photoluminescence measurements

From photoluminescence measurements, usually a broad peak, or even double peaks related to GaAsBi layers can be found. The short range ordering as a possible explanation seems to be very convincing. It is also possible that during the growth, the bismuth content has somehow changed. Some experiments have been done recently in our lab showing that the surface temperature might change with accumulating bismuth layers on the surface. Since the band gap of GaAsBi is shorter than GaAs, the radiation absorption is larger in GaAsBi. If we provide the same heating power, with the increase of the GaAsBi layer thickness, the surface of the sample can absorb more heat and become hotter and hotter, in which case less bismuth can be incorporated. Several other phenomena are worth investigating such as the decrease of GaAsBi PL intensity with the increase of bismuth incorporation.

Besides, more information can be revealed by low temperature PL and time resolved PL (the working mechanism of time resolved PL is recorded in Appendix 2).

3. Device fabrication

Device fabrication is a critical process of semiconductor research. After a good quality structure has been grown, fabrication is used to make the structure into devices. Lithography is to create device pattern during the fabrication by photoresist. The wafer is covered with photoresist, then the selected portions of the wafer by a mask is exposed to short wavelength light, and the exposed regions are washed away by a developer solution. The metal contact is usually made from the deposition of gold and zinc. Etching is used to remove material from the wafer. A mature and rigorous process has been made throughout these years' research, and it is necessary and helpful to be familiar with it.

4. Measurements of device properties

Further investigation of optoelectronic properties of GaAsBi can be on IV, CV and photocurrent measurements. More electronic properties can be revealed from the IV results such as recombination centres in the depletion region and the compositions of leakage current. CV measurements can provide key information about the structure such as the doping density and the depletion width at a certain reverse bias. The information can be used in further analysis. Optical properties can be obtained from photocurrent measurements, and properties such as Franz-Keldysh effect can be further investigated.

Appendices

Appendix 1: Summary of previous GaAsBi samples grown by STM-MBE

The structures of GaAsBi samples grown in our lab are often single GaAsBi layers, bulk p-i-n diodes, or quantum wells. Samples are named ST-L-xx, where ST means scanning tunnelling, and L is a letter which represents the growth year (with A as the year 2010). The first x is a number which shows the series, and the second x is a number showing the position in the series.

The STD5 series were grown in 2013, which electrical and optical properties were discussed in Chapter 5. The structure is shown in Figure A1.1.

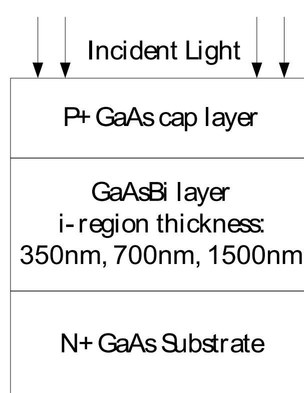

Figure A1.1. the structure of STD5 series

The growth parameters are shown in the following table:

Table A1.1. Growth conditions of STD51-STD5D

<table>
<tr><th>Sample</th><th>t (nm)</th><th>Sub I (A)</th><th>GR (ML/s)</th><th>Bi T</th><th>As:Ga</th></tr>
<tr><td>STD51</td><td rowspan="6">350</td><td rowspan="2">0.8</td><td rowspan="4">0.55</td><td rowspan="6">530</td><td>3.18</td></tr>
<tr><td>STD52</td><td>3.12</td></tr>
<tr><td>STD53</td><td>0.9</td><td>3.32</td></tr>
<tr><td>STD54</td><td>0.7</td><td>3.12</td></tr>
<tr><td>STD55</td><td rowspan="8">0.8</td><td>0.65</td><td>2.44</td></tr>
<tr><td>STD56</td><td>0.45</td><td>2.87</td></tr>
<tr><td>STD57</td><td rowspan="3">700</td><td rowspan="7">0.55</td><td>530</td><td>2.35</td></tr>
<tr><td>STD58</td><td>550</td><td>2.28</td></tr>
<tr><td>STD59</td><td>570</td><td>2.28</td></tr>
<tr><td>STD5A</td><td rowspan="4">1500</td><td>530</td><td>2.24</td></tr>
<tr><td>STD5B</td><td>550</td><td>2.24</td></tr>
<tr><td>STD5C</td><td>570</td><td>2.24</td></tr>
<tr><td>STD5D</td><td>0.7</td><td>530</td><td>2.22</td></tr>
</table>

In Table A1.1, t is the thickness of the i-region, Sub I is the current in the substrate heating element, GR is the growth rate, Bi T is the temperature of the bismuth Knudsen effusion cell, and As:Ga is the As:Ga atomic flux ratio. The heater current is used to represent the growth substrate surface temperature. From a rough calculation, the surface temperature is nearly 325 °C, 375 °C and 425 °C when the current is set to 0.7 A, 0.8 A and 0.9 A respectively. Since As_4 species is used instead of As_2 as a source of arsenic atoms, and considering the sticking coefficient of As_4 is less than 0.5, the As:Ga flux ratio is set around 2. The calculated Bi:Ga atomic flux rate from AFM experiments is approximately 5%, 10%, and 15%, when the bismuth cell temperature is 530 °C, 550 °C and 570 °C, respectively. However, the maximum incorporation from photoluminescence measurements is around 3%, when the growth temperature is 375 °C.

Several sets of samples grown in 2014 are recorded in Table A1.2.

Table A1.2. The summary of grown samples in the year 2014

Sample	Substrate	Sub I	Structure	Purpose of growth
STE2	n+	0.73A	Single GaAsBi layers	Using different bismuth flux rate to find the optimized point with sub current 0.73A
STE3	n+	0.73A	p-i-n diodes	GaAs control pins to investigate the surfactant function of bismuth
STE4	n+	0.73A	quantum well	To find different confinement energy
STE5	n+	0.73A	p-i-n diodes	To check the growth interrupt technique
STE6	n+	0.65A	Single GaAsBi layers	Lower growth temperature to get more bismuth incorporated
STE7	n+	0.73A	p-i-n diodes	GaAs control pins
STE8	n+	0.73A	p-i-n diodes	Growth interrupt technique
STE9	undoped	0.73A	Single GaAsBi layers	Resolve the broad peak problem

The properties of STF8 and STFA series grown in 2015 are discussed in Chapter 6.

Appendix 2: The theory of time resolved photoluminescence

Time resolved photoluminescence (TRPL) is used to study fast transient behaviour (mainly carrier recombination and transport) in materials. A pulsed light source is incident to the sample, and the subsequent decay of PL intensity is measured as a function of time. Since the intensity is proportional to the density of carriers, the decay of intensity can indicate the lifetime of carriers.

Even if non-radiative recombination does not create photons, the change of carrier density by that still alter the TRPL. In this case, the result of TRPL includes all the recombination processes

instead of only the radiative part. There are 3 possible non-radiative recombination processes: Auger recombination, surface recombination, and recombination of defects.

Band-to-band recombination, or direct recombination is radiative. It happens in direct band-gap semiconductors. The recombination rate can be written as:

$$R = rpn \tag{A2.1}$$

Here, p and n are the density of electrons and holes respectively. r = $v_{th} \cdot \sigma$ is the recombination coefficient. v_{th} is the average thermal velocity of carriers, σ is called scattering cross section, which is comparable to the particle size. The spontaneous generation rate is:

$$G = rN_C N_V \exp\left(\frac{E_V - E_C}{kT}\right) = rn_i^2 \tag{A2.2}$$

Recombination is dominated by the excess minority carrier density. If we use n-type semiconductor as an example, the decay of carrier density is:

$$\frac{d\Delta p}{dt} = G - R = -r\left(N_D \Delta p + \Delta p^2\right) \tag{A2.3}$$

At low injection of carriers, if we define $\tau_p = 1/(r \cdot N_D)$, Equation A2.3 is changed to:

$$\frac{d\Delta p}{dt} = -rN_D \Delta p = -\frac{\Delta p}{\tau_p} \tag{A2.4}$$

At high injection, since Δp is comparable to N_D, the decay cannot be a single exponential decay anymore. Equation A2.3 can be solved as:

$$\Delta p(t) = \frac{\Delta p_0 \exp\left(-t/\tau_p\right)}{1 + \frac{\Delta p_0}{N_D}\left[1 - \exp\left(-t/\tau_p\right)\right]} \tag{A2.5}$$

The recombination and generation of carriers at deep levels is named as Shockley-Read-Hall (SRH) recombination mechanism [171]. If we consider only one deep level as a recombination centre, the states on it can either be occupied by holes or electrons, and the state distribution on the level should obey Fermi-Dirac distribution:

$$f_{tn} = \left[1 + \exp\left(\frac{E_t - E_f}{kT}\right)\right]^{-1} \tag{A2.6}$$

Here f_{tn} is the fraction of deep level occupied by electrons, $f_{tp} = 1 - f_{tn}$ is the part by holes correspondingly. E_t is the energy of deep level, and E_f is the Fermi level. Figure A2.1 shows four possible processes on the deep level.

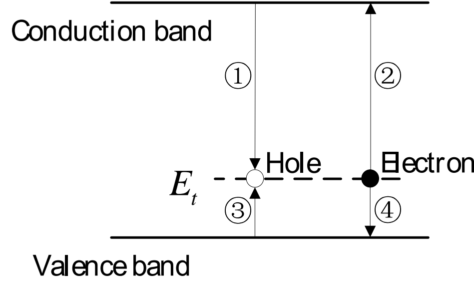

Figure A2.1. 4 processes of SRH recombination (1) recombination of a hole with an electron on conduction band (2) thermal activation of an electron to conduction band (3) thermal activation of a hole to valence band (4) recombination of an electron with a hole on valence band

From Figure A2.1, the change rate of electrons in conduction band depends on process 1 and 2. The decrease rate is:

$$U_n = \sigma_n \upsilon_{th} N_t \left[f_{tp} n - f_{tn} N_C \exp\left(\frac{E_t - E_C}{kT} \right) \right] \tag{A2.7}$$

v_{th} is the thermal velocity of carriers if we assume the thermal kinetic energy of electrons and holes are the same. σ_n is the scattering or capture cross-section area of electron. N_C is the available vacancies in conduction band, and E_C is the conduction band energy.

The decrease rate of holes in valence band is:

$$U_p = \sigma_p \upsilon_{th} N_t \left[f_{tn} p - f_{tp} N_V \exp\left(\frac{E_V - E_t}{kT} \right) \right] \tag{A2.8}$$

Recombination happens when $U_n = U_p$, since electrons and holes diminish in pairs. In this case, if we define

$$p_t = N_V \exp\left(\frac{E_V - E_t}{kT} \right) = n_i \exp\left(\frac{E_i - E_t}{kT} \right) \tag{A2.9a}$$

and

$$n_t = N_C \exp\left(\frac{E_t - E_C}{kT} \right) = n_i \exp\left(\frac{E_t - E_i}{kT} \right) \tag{A2.9b}$$

The following equation is obtained:

$$\exp\left(\frac{E_t - E_f}{kT} \right) = \frac{p\sigma_p + \sigma_n n_t}{n\sigma_n + \sigma_p p_t} \tag{A2.9}$$

And:

$$R_{SRH} = U_p = U_n = \sigma_n \sigma_p \upsilon_{th} N_t \left[\frac{pn - n_i^2}{n\sigma_n + \sigma_p p_t + p\sigma_p + \sigma_n n_t} \right] \tag{A2.10}$$

A logarithmic plot of the recombination rate with E_t - E_i shows a steep peak at $E_t = E_i$ [172]. This means that SRH recombination becomes important when deep level is near mid-gap.

Surface and/or interface recombination is a kind of SRH recombination happened on the surface and/or interface. So Equation A2.11 is adopted to deduce the surface recombination coefficient:

$$S = \sigma \upsilon_{th} N_{st} \exp\left(-\frac{qV_s}{kT} \right) \tag{A2.11}$$

where N_{st} is the area density of deep level states, V_s is a potential represents the bent of band near surface which leads to the change of carrier density on the surface.

Auger recombination is a kind of recombination that an electron passes its potential energy to another carrier during the recombination instead of emitting a photon, and the energy becomes a part of kinetic energy of the carrier. In this case, more than an electron and a hole has been involved in this recombination. It happens mostly on indirect band-gap pure semiconductor (e.g. undoped Silicon). It is also usually observed at high injection condition. Figure A2.2 shows a comparison among radiative, SRH and auger recombination.

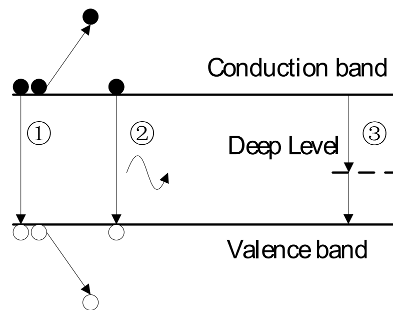

Figure A2.2. Different types of recombination mechanisms (1) Auger recombination (2) radiative recombination (3) SRH recombination

Appendix 3: A simple way of calculating Capacitance

To interpret the relationship between capacitance and bias voltage, a simple p_+n structure is first considered (Figure A3.1). Since the doping in p_+ layer is very heavy, the depletion region in p_+ layer can be ignored.

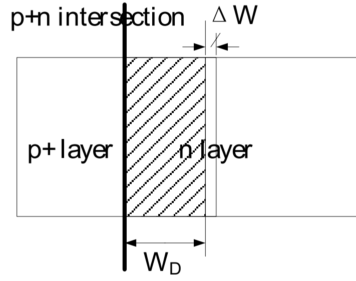

Figure A3.1. p+n junction

When the bias voltage changes slightly by ΔV, the change of depletion width ΔW will be quite small comparing with the depletion width W_D (Figure A3.1). If we define the change of electrical field in depletion region as ΔE (a constant independent to position, based on sheet charge assumption and Gauss's Law), then we get $\Delta V = \Delta E \cdot (W_D + \Delta W) = \Delta E \cdot W_D$.

With Gauss's Law, another equation is obtained: $\Delta Q = \varepsilon \Delta E \times A$. A is the cross-section area of the junction. So the capacitance is:

$$C = \frac{\Delta Q}{\Delta V} = \frac{\varepsilon A}{W_D} \tag{A3.1}$$

The doping density can also be calculated. The change of charge in N-layer can be expressed as $\Delta Q = N_D \cdot q \cdot A \cdot \Delta W$. Combining this expression with Equation A3.1, we can obtain:

$$N_D = \frac{\varepsilon}{W_D q} \frac{\Delta V}{\Delta W} \tag{A3.2}$$

Since $W = \varepsilon A/C \rightarrow \Delta W = -(\varepsilon A/C^2) \cdot \Delta C$, the relationship between doping density and capacitance is obtained:

$$N_D = \frac{2}{q\varepsilon} \frac{\Delta V}{\Delta (C/A)^{-2}} \tag{A3.3}$$

Appendix 4: Photocurrent Calculation

In this appendix, a simple deduction of the Beer-Lambert Law is introduced first. ϕ_x is defined as the incident photon density which is a function of deepness x. If we assume $d\phi_x$, a tiny fraction of the incident photon density, is absorbed through a very thin layer with the thickness of dx, the following equation is obtained:

$$-d\phi_x = \alpha \phi_x dx \tag{A4.1}$$

where α is the absorption coefficient. Solving the above equation, we can obtain:

$$\phi_x = \phi_0 \exp(-\alpha x) \tag{A4.2}$$

$$\phi_{absorb} = \phi_0 - \phi_x = \phi_0 \left[1 - \exp(-\alpha x)\right] \tag{A4.3}$$

where ϕ_0 is the initial incident photon density. Then the situation in the p-n junction is considered. As shown in Figure A4.1, a p-n junction can be divided into depletion region (the region marked as W_D) and diffusion region, which currents are dominated by drift and diffusion respectively. Here ϕ is defined as the incident photon density at the interface of p-n junction. According to the above calculation, ϕ should be:

$$\phi = \phi_0 \exp(-\alpha W_P) \tag{A4.4}$$

Besides, the generation rate of electrons as a function of the deepness can be obtained as:

$$G_e(x) = \phi\alpha \exp(-\alpha x) \tag{A4.5}$$

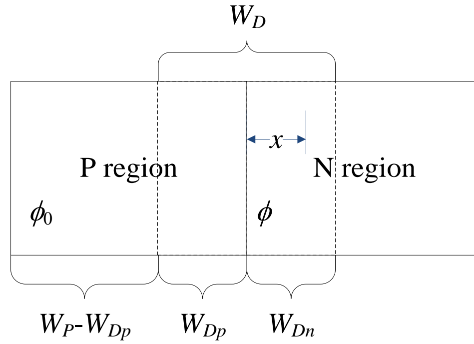

Figure A4.1. The diagram of a typical p-n junction

If all the absorbed photons in depletion region generate electrons in the diode successfully, and all the electrons are collected as drift current, then:

$$J_{drift} = q\phi\left[\exp(\alpha W_{Dp}) - \exp(-\alpha W_{Dn})\right] \tag{A4.6}$$

To solve the diffusion current with incident light, the following continuity equations in p and n diffusion regions with the boundary conditions are established. Continuity equation in p-region:

$$D_n \frac{\partial^2 n_p}{\partial x^2} - \frac{n_p - n_{p0}}{\tau_n} + G_e(x) = 0 \tag{A4.7}$$

Boundary condition:

$$\begin{cases} n_p = n_{p0} & x = -\infty \\ n_p = n_{p0} \exp\left(\dfrac{qV}{kT}\right) & x = -W_{Dp} \end{cases} \quad \text{(A4.8)}$$

If we consider the surface recombination, the boundary condition is:

$$\begin{cases} D_n \dfrac{d\left(n_p - n_{p0}\right)}{dx} = S_n \left(n_p - n_{p0}\right) & x = -W_P \\ n_p = n_{p0} \exp\left(\dfrac{qV}{kT}\right) & x = -W_{Dp} \end{cases} \quad \text{(A4.9)}$$

Continuity equation in n-region:

$$D_p \frac{\partial^2 p_n}{\partial x^2} - \frac{p_n - p_{n0}}{\tau_p} + G_e(x) = 0 \quad \text{(A4.10)}$$

Boundary condition:

$$\begin{cases} p_n = p_{n0} & x = \infty \\ p_n = p_{n0} \exp\left(\dfrac{qV_b}{kT}\right) & x = W_{Dn} \end{cases} \quad \text{(A4.11)}$$

The dark current can be calculated through establishing continuity equations without considering incident light. The continuity equation in p-region can be expressed as:

$$D_n \frac{\partial^2 n_p}{\partial x^2} - \frac{n_p - n_{p0}}{\tau_n} = 0 \quad \text{(A4.12)}$$

If the p-region is long enough, the boundary conditions:

$$\begin{cases} n_p = n_{p0} & x = -\infty \\ n_p = n_{p0} \exp\left(\dfrac{qV}{kT}\right) & x = -W_{Dp} \end{cases} \quad \text{(A4.13)}$$

If we consider the surface recombination, the boundary condition is:

$$\begin{cases} D_n \dfrac{d\left(n_p - n_{p0}\right)}{dx} = S_n \left(n_p - n_{p0}\right) & x = -W_P \\ n_p = n_{p0} \exp\left(\dfrac{qV}{kT}\right) & x = -W_{Dp} \end{cases} \quad \text{(A4.14)}$$

Continuity equation in n-region:

$$D_p \frac{\partial^2 p_n}{\partial x^2} - \frac{p_n - p_{n0}}{\tau_p} = 0 \tag{A4.15}$$

Boundary condition:

$$\begin{cases} p_n = p_{n0} & x = \infty \\ p_n = p_{n0} \exp\left(\dfrac{qV}{kT}\right) & x = W_D \end{cases} \tag{A4.16}$$

The photocurrent can be calculated when adding drift current and diffusion currents in both p and n regions (as shown in Equation A4.17), and using the sum to minus the dark current. The calculation result is recorded in Chapter 5.

$$J_{photo} = J_{drift} + J_{diff-p} + J_{diff-n} - J_{dark-p} - J_{dark-n} \tag{A4.17}$$

If we consider GaAs/GaAsBi/GaAs p-i-n heterojunction, if the i-region is slightly n-doped, it would behave as a p+-n- junction as shown in Figure A4.2. In this case, the photons with wavelength longer than 870 nm cannot be absorbed in p-region, and thus the initial incident photon density would not reduce until it reaches the interface of p-i junction.

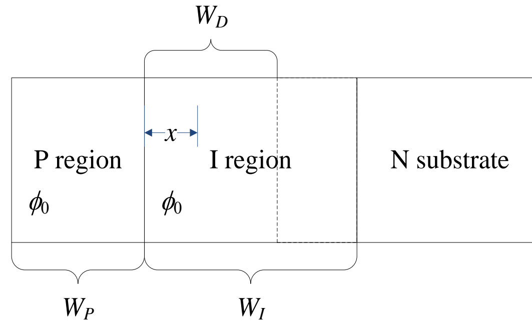

Figure A4.2. The diagram for p-i-n structure when i-region is slightly n-doped.

The light absorbed in depletion region will be collected by the electrical field to form drift current:

$$J_{dr} = q\phi_0\left[1 - \exp\left(-\alpha W_D\right)\right] \tag{A4.18}$$

The continuity equation in i-region outside the depletion region is:

$$D_p \frac{\partial^2 p_n}{\partial x^2} - \frac{p_n - p_{n0}}{\tau_p} + G_e(x) = 0 \tag{A4.19}$$

$$G_e(x)=\phi_0\alpha\exp(-\alpha x) \quad \text{(A4.19a)}$$

The continuity equation in n-region is:

$$D_{p2}\frac{\partial^2 p_n}{\partial x^2}-\frac{p_n-p_{n0}}{\tau_{p2}}=0 \quad \text{(A4.20)}$$

Parts of boundary conditions will be as following, whether it will be forward or reverse:

$$\begin{cases} p_n = p_{n0}\exp\left(\dfrac{qV_b}{kT}\right) & x=W_D \\ p_{left}=p_{right},\ \dfrac{dp}{dx}\Big|_{left}=\dfrac{dp}{dx}\Big|_{right} & x=W_I \\ p_n=p_{n0} & x=\infty \end{cases} \quad \text{(A4.21)}$$

Solving the above equations and eliminating dark current, the photocurrent can be obtained which is shown in Chapter 5.

If the i-region is slightly p-doped, the p-i-n junction can be addressed as a p^--n^+ junction as shown in Figure A4.3.

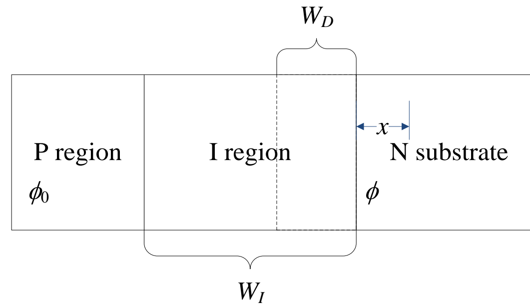

Figure A4.3. The diagram for p-i-n structure when i-region is slightly p-doped

The drift current is:

$$J_{dr}=q\phi\left[1-\exp(-\alpha W_D)\right] \quad \text{(A4.22)}$$

$$\phi=\phi_0\exp(-\alpha W_I) \quad \text{(A4.22a)}$$

The continuity equation in P-region is:

$$D_{n2}\frac{\partial^2 n_p}{\partial x^2}-\frac{n_p-n_{p0}}{\tau_{n2}}=0 \quad \text{(A4.23)}$$

The continuity equation in i-region outside the depletion region is:

$$D_n \frac{\partial^2 n_p}{\partial x^2} - \frac{n_p - n_{p0}}{\tau_n} + G_e(x) = 0 \tag{A4.24}$$

$$G_e(x) = \phi\alpha \exp(-\alpha x) \tag{A4.24a}$$

Boundary conditions will be as following, whether it will be forward or reverse:

$$\begin{cases} n_p = n_{p0} & x = -\infty \\ n_{left} = n_{right}, \left.\frac{dn}{dx}\right|_{left} = \left.\frac{dn}{dx}\right|_{right} & x = -W_I \\ n_p = n_{p0}\exp\left(\frac{qV_b}{kT}\right) & x = -W_D \end{cases} \tag{A4.25}$$

Appendix 5: Measurement results of low temperature photoluminescence

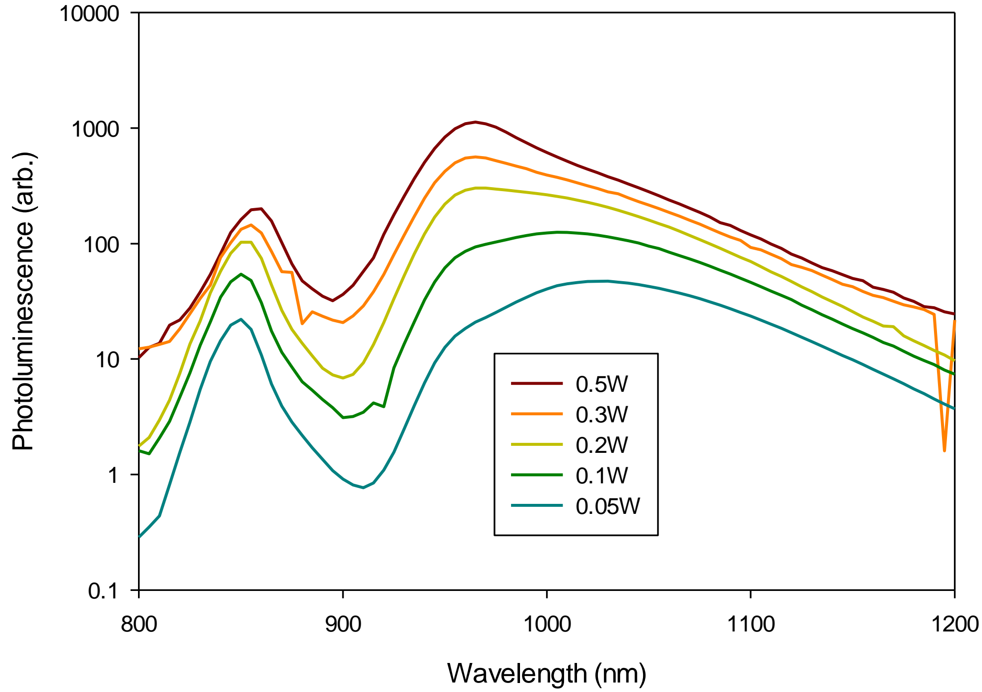

Figure A5.1. photoluminescence of STFA9 at ~12K

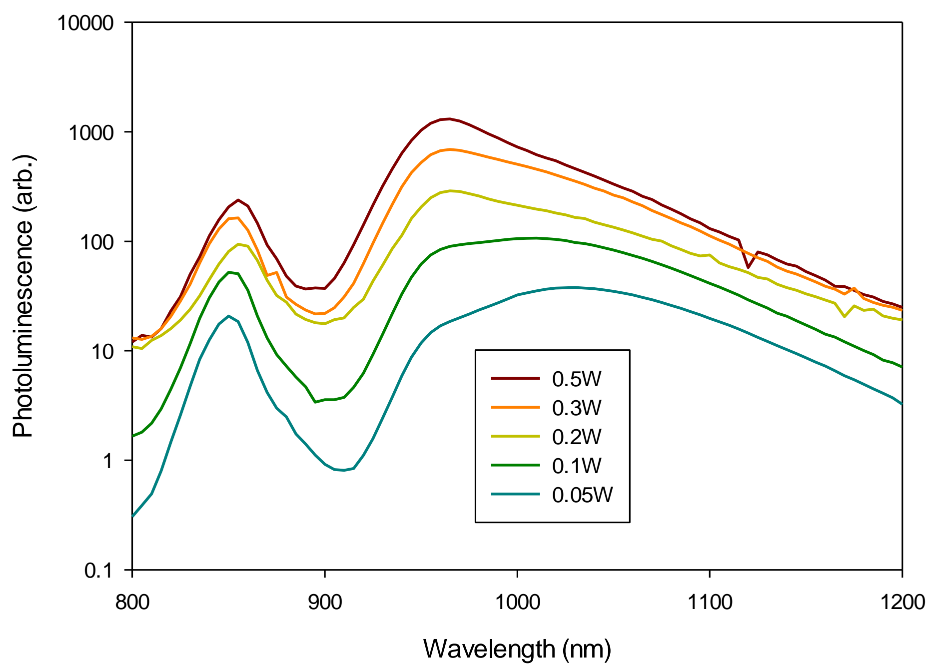

Figure A5.2. photoluminescence of STFA9 at ~24K

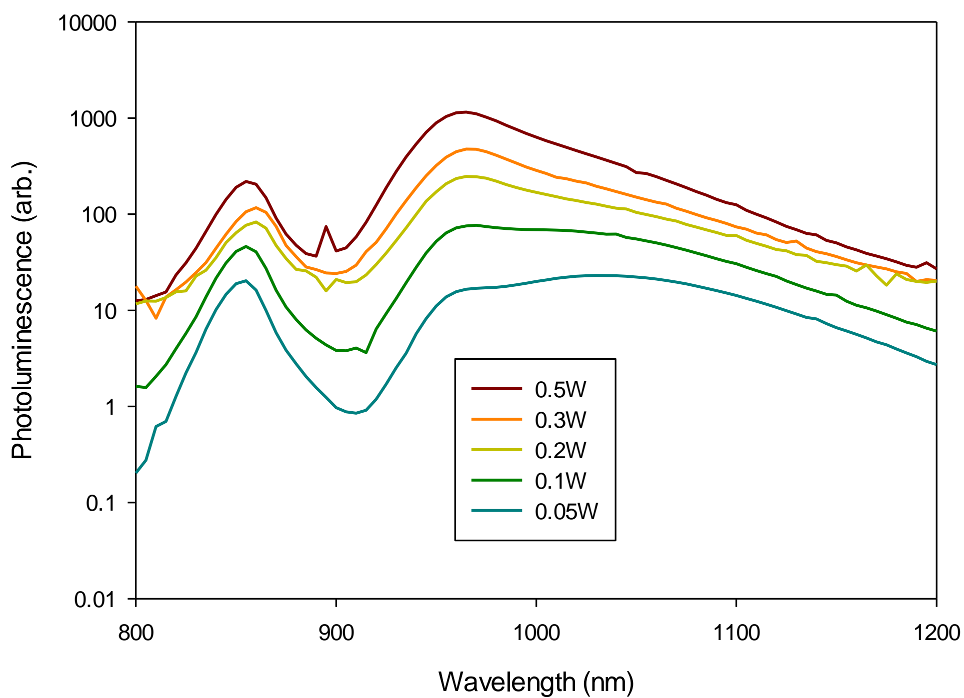

Figure A5.3. photoluminescence of STFA9 at ~49K

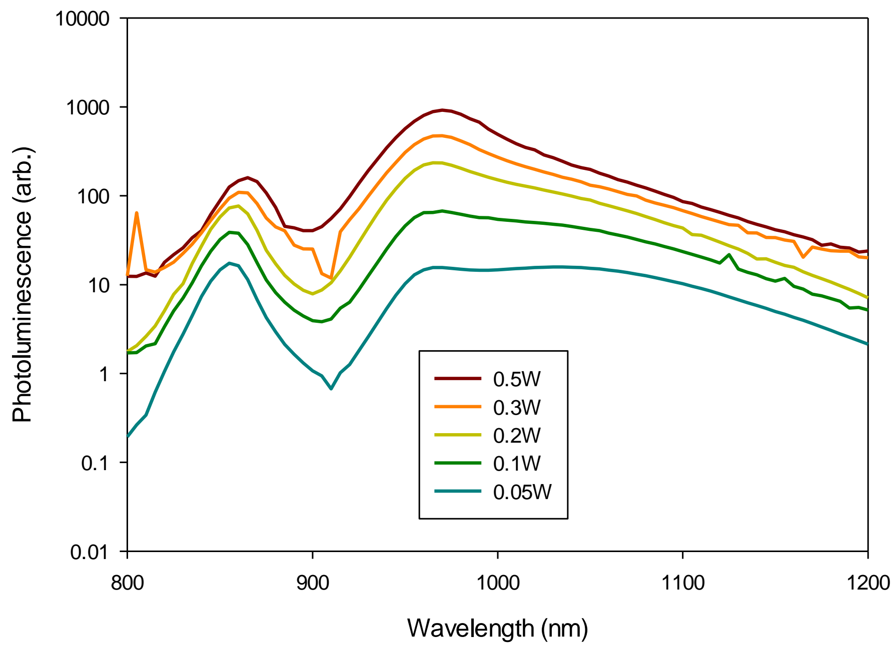

Figure A5.4. photoluminescence of STFA9 at ~74K

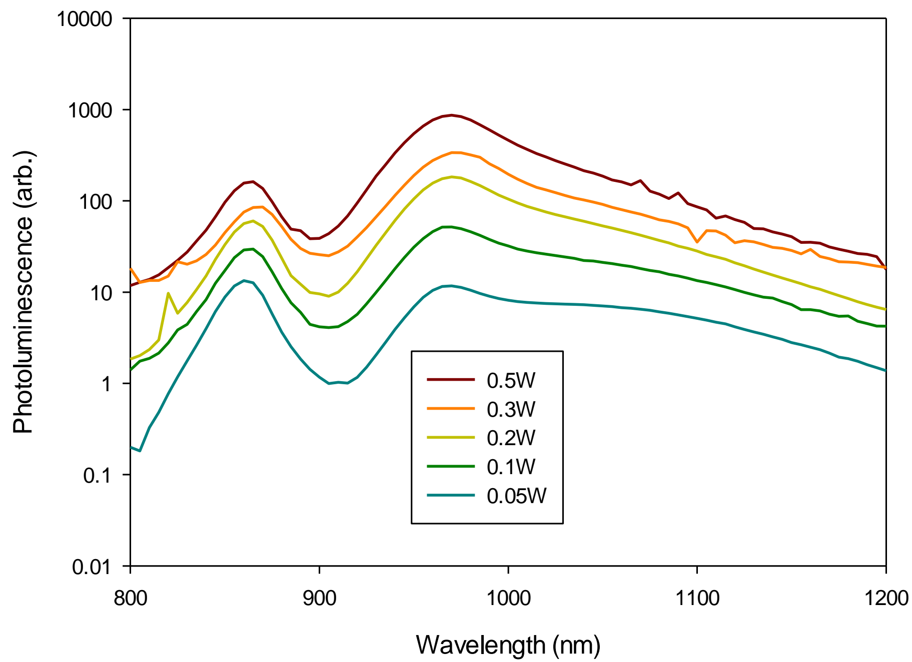

Figure A5.5. photoluminescence of STFA9 at ~99K

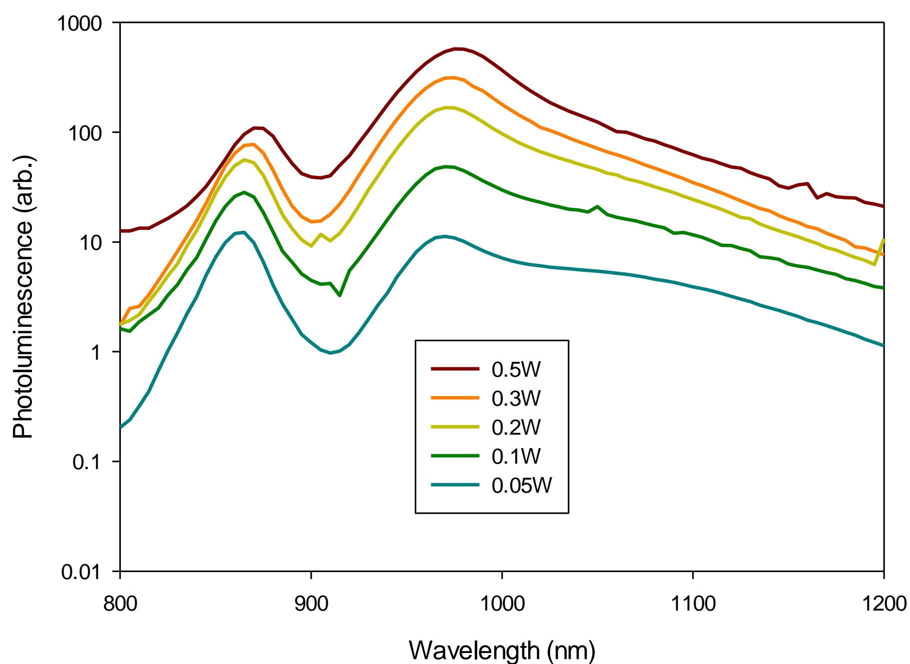

Figure A5.6. photoluminescence of STFA9 at ~124K

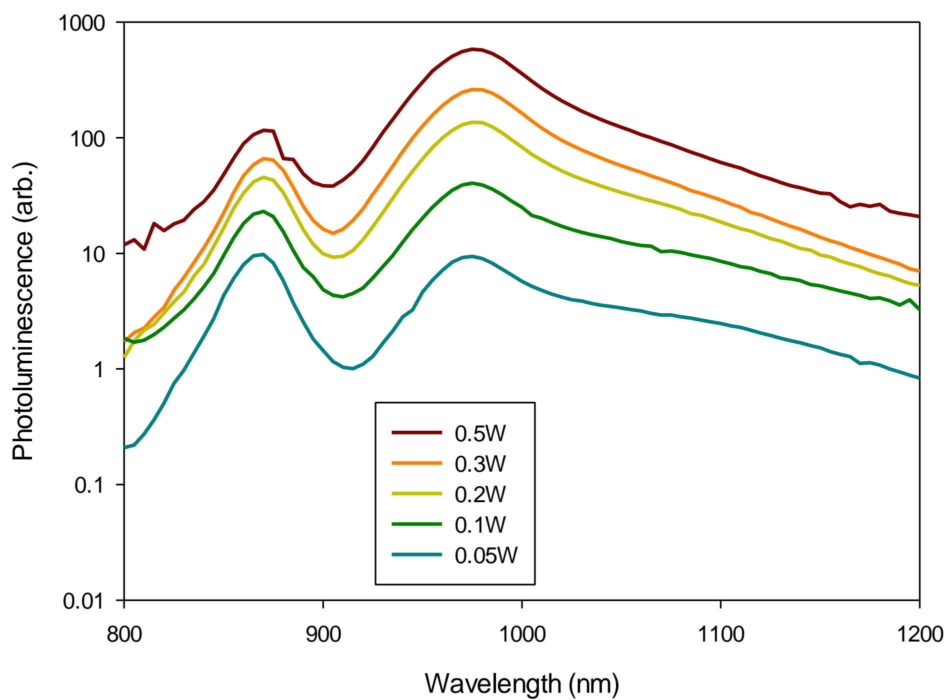

Figure A5.7. photoluminescence of STFA9 at ~149K

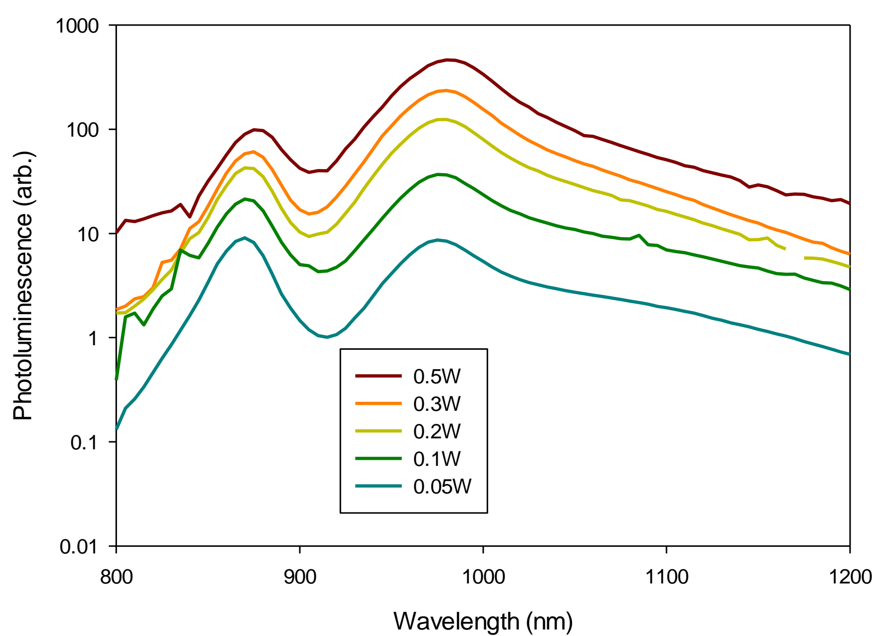

Figure A5.8. photoluminescence of STFA9 at ~174K

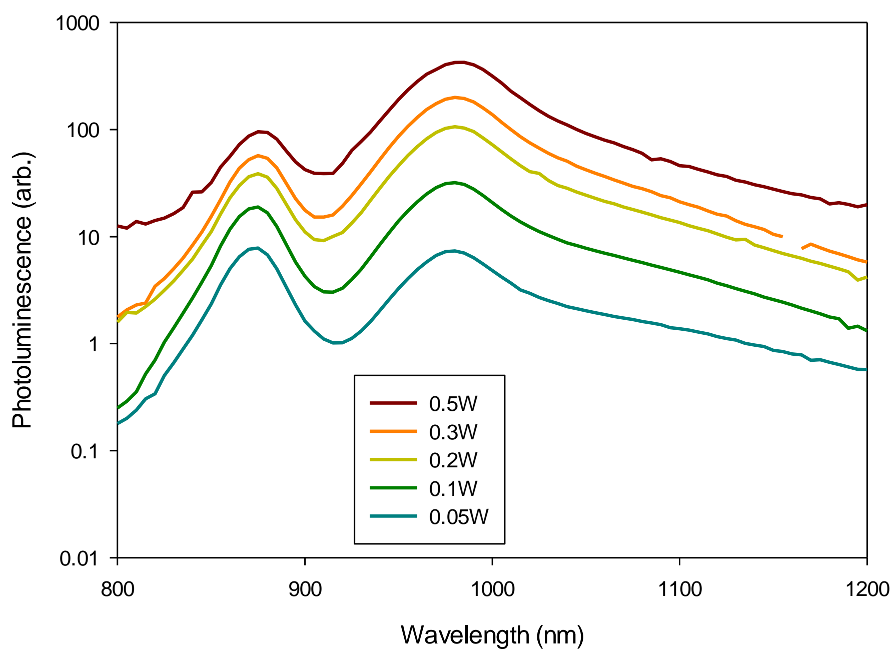

Figure A5.9. photoluminescence of STFA9 at ~199K

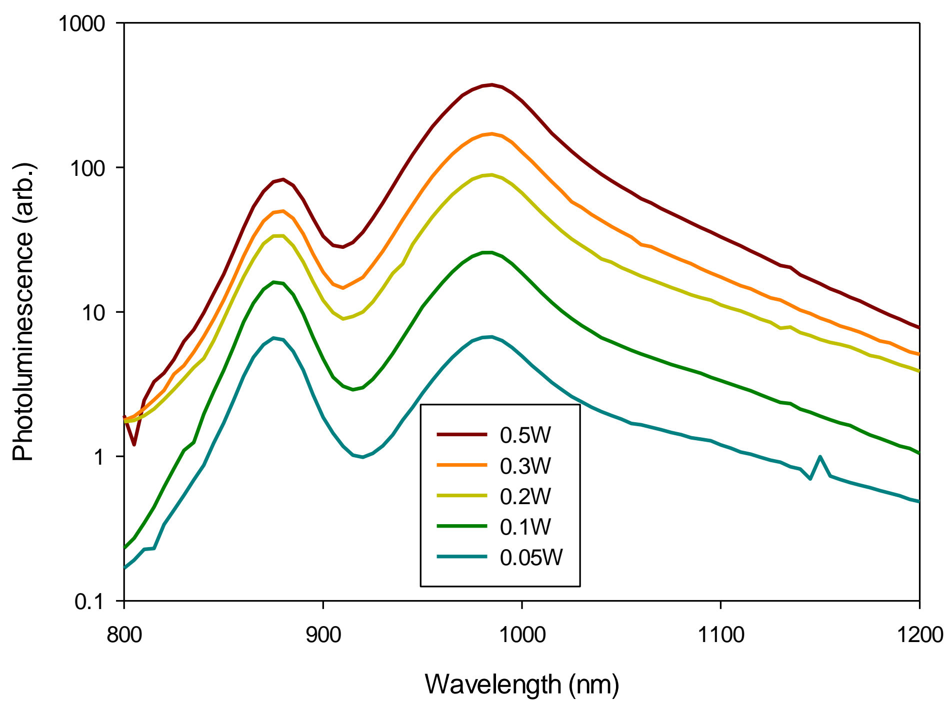

Figure A5.10. photoluminescence of STFA9 at ~224K

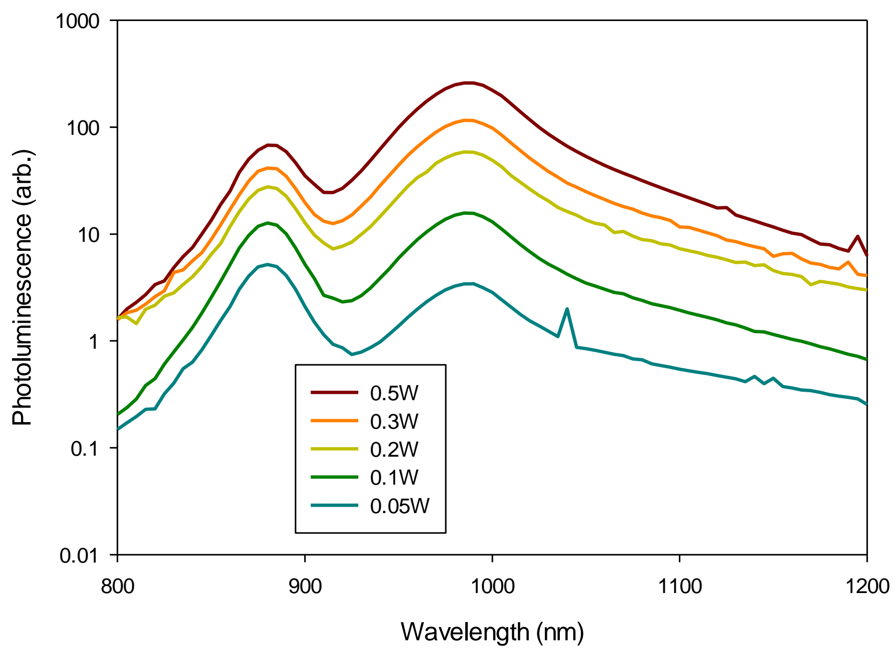

Figure A5.11. photoluminescence of STFA9 at ~249K

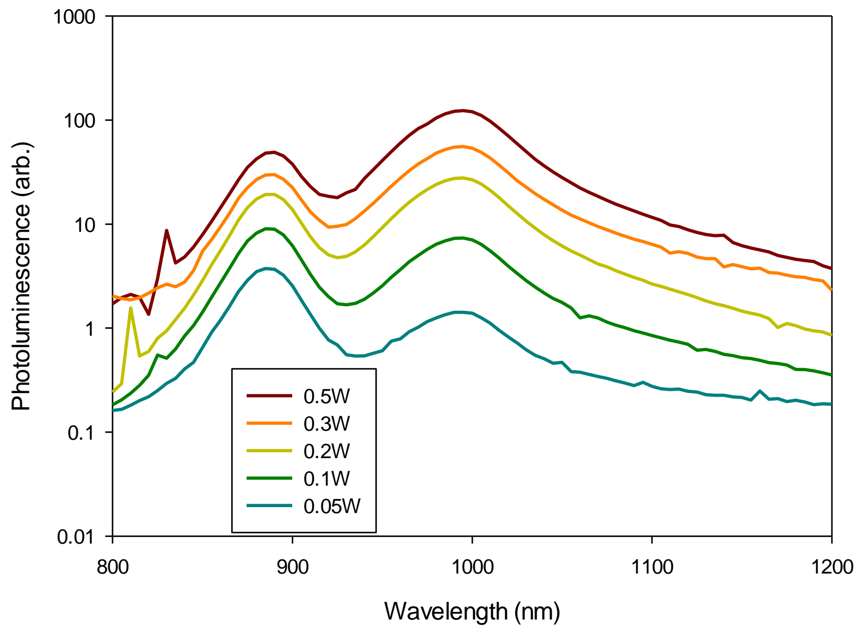

Figure A5.12. photoluminescence of STFA9 at ~274K

Appendix 6: Photo-multiplication results of STF8 and STFA series

When taking photo-multiplication measurements on STF8 and STFA series, lasers with 543.5 nm and 850 nm wavelength were used. The power of the lasers was around 1 mW, and was attenuated to ~ 0.1 mW by mirrors and beam splitter when the beams arrived at the optical window of devices. The level of photocurrent of these samples is about hundreds of nA. A laser power of ~ 0.2 mW was also implemented to verify the results, and multiplication curves under different laser powers match quite well. Figures A6.1 to A6.4 show the normalized raw data of multiplication as a function of bias voltage for PINs and NIPs with different i-region thicknesses.

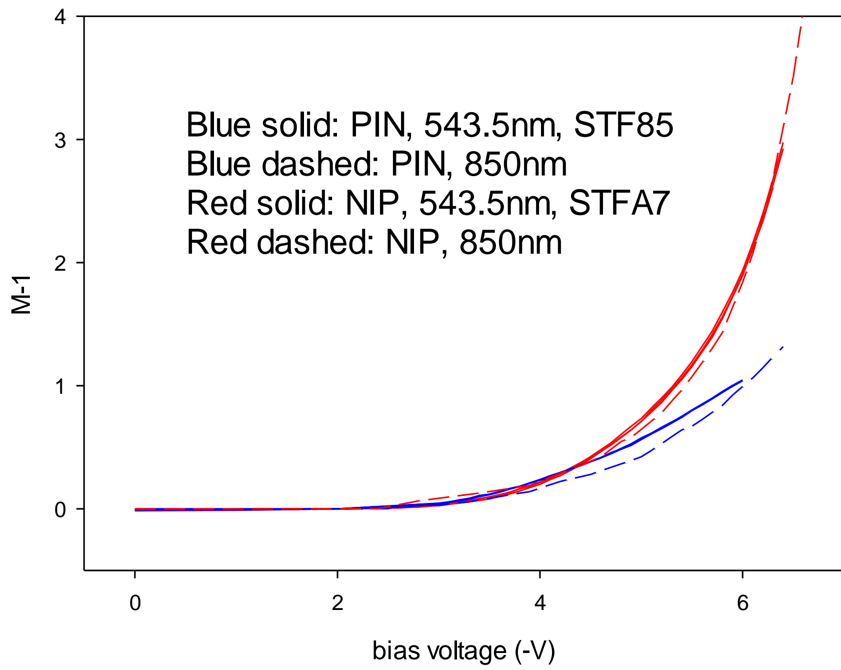

Figure A6.1. Normalized raw multiplication data as a function of bias voltage for STF85 and STFA7 at 543.5 nm and 850 nm lasers (i-region thickness is ~ 100 nm)

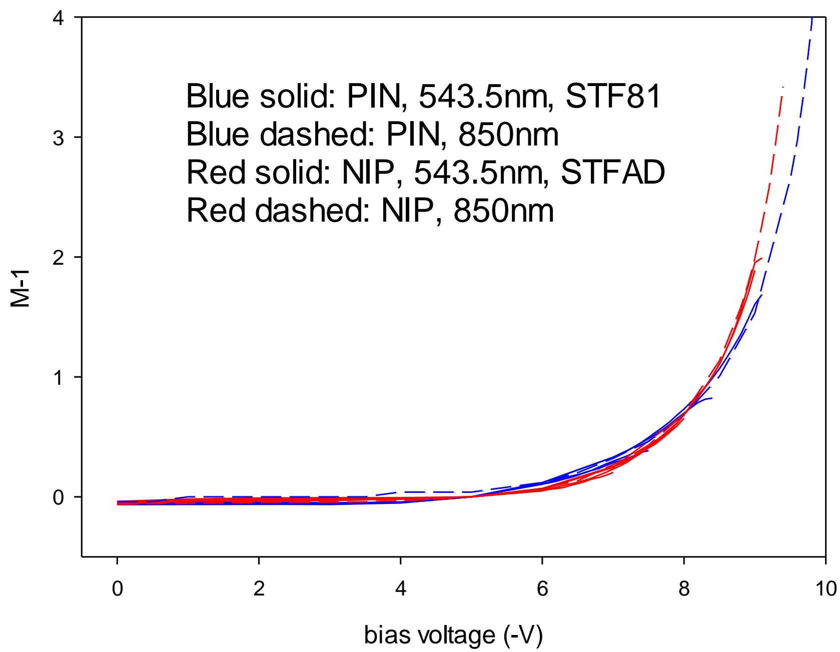

Figure A6.2. Normalized raw multiplication data as a function of bias voltage for STF81 and STFAD at 543.5 nm and 850 nm lasers (i-region thickness is ~ 200 nm)

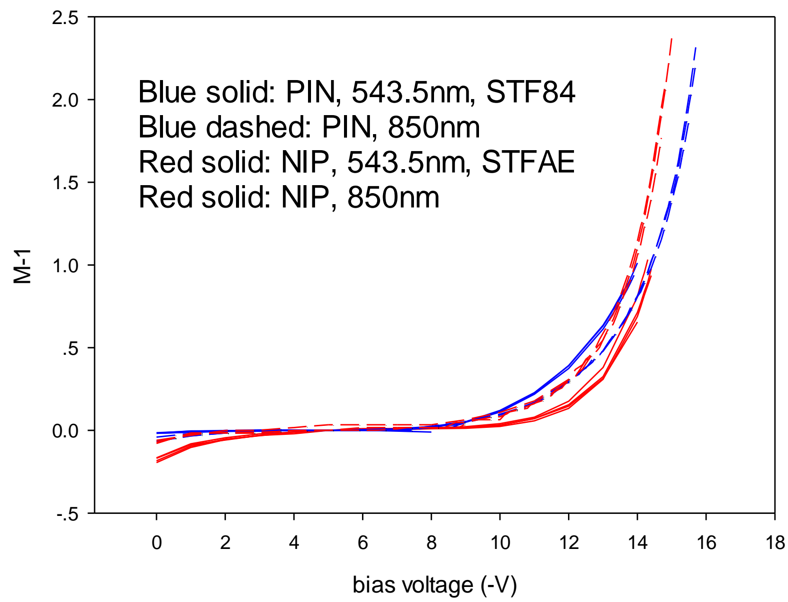

Figure A6.3. Normalized raw multiplication data as a function of bias voltage for STF84 and STFAE at 543.5 nm and 850 nm lasers (i-region thickness is ~ 400 nm)

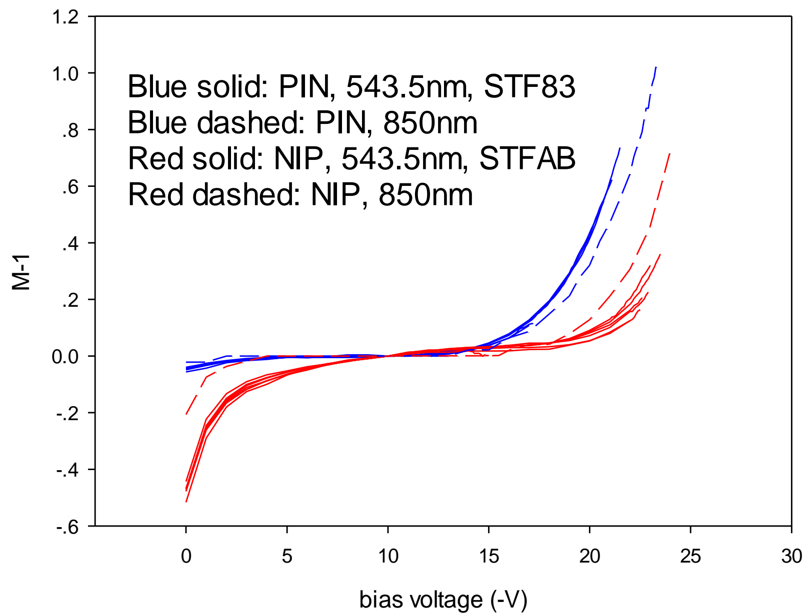

Figure A6.4. Normalized raw multiplication data as a function of bias voltage for STF83 and STFAB at 543.5 nm and 850 nm lasers (i-region thickness is ~ 800 nm)

Bibliography

[1] K. Oe and H. Okamoto, "New Semiconductor Alloy $GaAs_{1-x}Bi_x$ Grown by Metal Organic Vapor Phase Epitaxy," *Jpn. J. Appl. Phys.*, vol. 37, no. Part 2, No. 11A, pp. L1283–L1285, Nov. 1998.

[2] S. Tixier *et al.*, "Molecular beam epitaxy growth of $GaAs_{1-x}Bi_x$," *Appl. Phys. Lett.*, vol. 82, no. 14, p. 2245, 2003.

[3] R. B. Lewis, D. A. Beaton, X. Lu, and T. Tiedje, "Light emitting diodes," *J. Cryst. Growth*, vol. 311, no. 7, pp. 1872–1875, Mar. 2009.

[4] H. Okamoto and K. Oe, "Growth of metastable alloy InAsBi by low-pressure MOVPE," *Jpn. J. Appl. Phys.*, vol. 1608, 1998.

[5] H. Asahi, K. Yamamoto, K. Iwata, S. Gonda, and K. Oe, "New III-V Compound Semiconductors TlInGaP for 0.9 μm to over 10 μm Wavelength Range Laser Diodes and Their First Successful Growth," *Jpn. J. Appl. Phys.*, vol. 35, no. Part 2, No. 7B, pp. L876–L879, Jul. 1996.

[6] A. Mascarenhas, Y. Zhang, J. Verley, and M. J. Seong, "Overcoming limitations in semiconductor alloy design," *Superlattices Microstruct.*, vol. 29, no. 6, pp. 395–404, Jun. 2001.

[7] Y. Zhang, A. Mascarenhas, and L.-W. Wang, "Similar and dissimilar aspects of III-V semiconductors containing Bi versus N," *Phys. Rev. B*, vol. 71, no. 15, p. 155201, Apr. 2005.

[8] B. Fluegel, S. Francoeur, A. Mascarenhas, S. Tixier, E. Young, and T. Tiedje, "Giant Spin-Orbit Bowing in $GaAs_{1-x}Bi_x$," *Phys. Rev. Lett.*, vol. 97, no. 6, p. 67205, Aug. 2006.

[9] B. Pursley, M. Luengo-Kovac, G. Vardar, R. S. Goldman, and V. Sih, "Spin lifetime measurements in GaAsBi thin films," *Appl. Phys. Lett.*, vol. 102, no. 2, p. 22420, 2013.

[10] M. Johnson and R. H. Silsbee, "Interfacial charge-spin coupling: Injection and detection of spin magnetization in metals," *Phys. Rev. Lett.*, vol. 55, no. 17, pp. 1790–1793, Oct. 1985.

[11] M. N. Baibich, J. M. Broto, A. Fert, F. N. Van Dau, and F. Petroff, "Giant Magnetoresistance of (001)Fe/(001)Cr Magnetic Superlattices," *Phys. Rev. Lett.*, vol. 61, no. 21, pp. 2472–2475, Nov. 1988.

[12] G. Binasch, P. Grünberg, F. Saurenbach, and W. Zinn, "Enhanced magnetoresistance in layered magnetic structures with antiferromagnetic interlayer exchange," *Phys. Rev. B*, vol. 39, no. 7, pp. 4828–4830, Mar. 1989.

[13] J. Barnaś, A. Fuss, R. Camley, P. Grünberg, and W. Zinn, "Novel magnetoresistance effect in layered magnetic structures: Theory and experiment," *Phys. Rev. B*, vol. 42, no. 13, pp. 8110–8120, Nov. 1990.

[14] S. Datta and B. Das, "Electronic analog of the electro-optic modulator," *Appl. Phys. Lett.*, vol. 56, no. 7, p. 665, 1990.

[15] C. A. Broderick *et al.*, "Determination of type-I band offsets in $GaBi_xAs_{1-x}$ quantum wells using polarisation-resolved photovoltage spectroscopy and 12-band k.p calculations," *Semicond. Sci. Technol.*, vol. 30, no. 9, p. 94009, 2015.

[16] K. Alberi *et al.*, "Valence-band anticrossing in mismatched III-V semiconductor alloys," *Phys. Rev. B*, vol. 75, no. 4, p. 45203, Jan. 2007.

[17] K. Alberi, O. D. Dubon, W. Walukiewicz, K. M. Yu, K. Bertulis, and A. Krotkus, "Valence band anticrossing in $GaBi_xAs_{1-x}$," *Appl. Phys. Lett.*, vol. 91, no. 5, p. 51909, 2007.

[18] A. Janotti, S.-H. Wei, and S. Zhang, "Theoretical study of the effects of isovalent coalloying of Bi and N in GaAs," *Phys. Rev. B*, vol. 65, no. 11, p. 115203, Feb. 2002.

[19] W. Shan *et al.*, "Band Anticrossing in III-N-V Alloys," *Phys. status solidi*, vol. 223, no. 1, pp. 75–85, Jan. 2001.

[20] A. R. Mohmad *et al.*, "Localization effects and band gap of GaAsBi alloys," *Phys. Status Solidi Basic Res.*, vol. 251, pp. 1276–1281, May 2014.

[21] Y. Tominaga, K. Oe, and M. Yoshimoto, "Low Temperature Dependence of Oscillation Wavelength in $GaAs_{1-x}Bi_x$ Laser by Photo-Pumping," *Appl. Phys. Express*, vol. 3, no. 6, p. 62201, 2010.

[22] P. Ludewig *et al.*, "Electrical injection Ga(AsBi)/(AlGa)As single quantum well laser," *Appl. Phys. Lett.*, vol. 102, no. 24, pp. 3–6, 2013.

[23] H. Cotal *et al.*, "III–V multijunction solar cells for concentrating photovoltaics," *Energy Environ. Sci.*, vol. 2, no. 2, p. 174, 2009.

[24] T. Thomas *et al.*, "Requirements for a GaAsBi 1 eV sub-cell in a GaAs-based multi-junction solar cell," *Semicond. Sci. Technol.*, vol. 30, no. 9, p. 94010, 2015.

[25] C. Hunter, F. Bastiman, A. Mohmad, and R. Richards, "Absorption Characteristics of $GaAs_{1-x}Bi_x$/GaAs Diodes in the Near-infrared," *IEEE Photonics Technol. Lett.*, vol. 24, no. 23, pp. 2191–2194, 2012.

[26] Angelo Mascarenhas, "Boron, Bismuth co-doping of Gallium Arsenide and other compounds for photonic and heterojunction bipolar transistor devices," *United States Patent*, US9076915B2, 2013.

[27] R. N. Kini, A. J. Ptak, B. Fluegel, R. France, R. C. Reedy, and A. Mascarenhas, "Effect of Bi alloying on the hole transport in the dilute bismide alloy $GaAs_{1-x}Bi_x$," *Phys. Rev. B*, vol. 83, no. 7, p. 75307, Feb. 2011.

[28] R. N. Kini, L. Bhusal, A. J. Ptak, R. France, and A. Mascarenhas, "Electron Hall mobility in GaAsBi," *J. Appl. Phys.*, vol. 106, no. 4, p. 43705, 2009.

[29] I. Hase, “Heterojunction bipolar transistor with a base layer that contains bismuth,” *United States Patent* 6936871, 2006.

[30] M. Martin and E. R. Brown, “Critical comparison of GaAs and InGaAs THz photoconductors,” *Proc. SPIE 8261, Terahertz Technology and Applications V*, February 2012, p. 826102.

[31] K. Bertulis *et al.*, “GaBiAs: A material for optoelectronic terahertz devices,” *Appl. Phys. Lett.*, vol. 88, no. 20, p. 201112, 2006.

[32] M. Yoshimoto, S. Murata, A. Chayahara, Y. Horino, J. Saraie, and K. Oe, “Metastable GaAsBi Alloy Grown by Molecular Beam Epitaxy,” *Jpn. J. Appl. Phys.*, vol. 42, no. Part 2, No. 10B, pp. L1235–L1237, Oct. 2003.

[33] M. Yoshimoto *et al.*, “New Semiconductor GaNAsBi Alloy Grown by Molecular Beam Epitaxy,” *Jpn. J. Appl. Phys.*, vol. 43, no. No. 7A, pp. L845–L847, Jun. 2004.

[34] W. Huang, M. Yoshimoto, Y. Takehara, J. Saraie, and K. Oe, “$GaN_yAs_{1-x-y}Bi_x$ Alloy Lattice Matched to GaAs with 1.3 μm Photoluminescence Emission,” *Jpn. J. Appl. Phys.*, vol. 43, no. No. 10B, pp. L1350–L1352, Sep. 2004.

[35] W. Huang, K. Oe, G. Feng, and M. Yoshimoto, “Molecular-beam epitaxy and characteristics of $GaN_yAs_{1-x-y}Bi_x$,” *J. Appl. Phys.*, vol. 98, no. 5, p. 53505, 2005.

[36] L. Vegard, “Die Konstitution der Mischkristalle und die Raumfüllung der Atome,” *Zeitschrift für Phys.*, vol. 5, no. 1, pp. 17–26, Jan. 1921.

[37] K. Sakamoto, K. Kyoya, K. Miki, H. Matsuhata, and T. Sakamoto, “Which Surfactant Shall We Choose for the Heteroepitaxy of Ge/Si(001)? -Bi as a Surfactant with Small Self-Incorporation-,” *Jpn. J. Appl. Phys.*, vol. 32, no. Part 2, No. 2A, pp. L204–L206, Feb. 1993.

[38] K. Sakamoto and H. Matsuhata, “Abrupt Si/Ge/Si (001) Interfaces Fabricated with Bi as a Surfactant,” *Japanese Journal of Applied Physics*, vol. 2307, 1994.

[39] M. Pillai and S. Kim, “Growth of $In_xGa_{1-x}As$/GaAs heterostructures using Bi as a surfactant,” *J. Vac. Scl. Technol*, pp. 1232–1236, 2000.

[40] S. Tixier, M. Adamcyk, E. C. Young, J. H. Schmid, and T. Tiedje, “Surfactant enhanced growth of GaNAs and InGaNAs using bismuth,” *J. Cryst. Growth*, vol. 251, no. 1–4, pp. 449–454, Apr. 2003.

[41] E. C. Young, S. Tixier, and T. Tiedje, “Bismuth surfactant growth of the dilute nitride GaN_xAs_{1-x},” *J. Cryst. Growth*, vol. 279, no. 3–4, pp. 316–320, Jun. 2005.

[42] A. J. Ptak, D. A. Beaton, and A. Mascarenhas, “Growth of BGaAs by molecular-beam epitaxy and the effects of a bismuth surfactant,” *J. Cryst. Growth*, vol. 351, no. 1, pp. 122–125, Jul. 2012.

[43] I. Langmuir, “The Constitution And Fundamental Properties Of Solids And Liquids.,” *J. Am. Chem. Soc.*, vol. 38, no. 11, pp. 2221–2295, Nov. 1916.

[44] M. P. J. Punkkinen *et al.*, "Bismuth-stabilized (2×1) and (2×4) reconstructions on GaAs(100) surfaces: Combined first-principles, photoemission, and scanning tunneling microscopy study," *Phys. Rev. B*, vol. 78, no. 19, p. 195304, Nov. 2008.

[45] P. M. Mooney *et al.*, "Deep level defects in n-type GaAsBi and GaAs grown at low temperatures," *J. Appl. Phys.*, vol. 113, no. 13, p. 133708, 2013.

[46] M. Kunzer, W. Jost, U. Kaufmann, H. Hobgood, and R. Thomas, "Identification of the BiGa heteroantisite defect in GaAs:Bi," *Phys. Rev. B*, vol. 48, no. 7, pp. 4437–4441, Aug. 1993.

[47] G. Ciatto, P. Alippi, A. Amore Bonapasta, and T. Tiedje, "How much room for BiGa heteroantisites in $GaAs_{1-x}Bi_x$?," *Appl. Phys. Lett.*, vol. 99, no. 14, p. 141912, 2011.

[48] G. Pettinari *et al.*, "Compositional evolution of Bi-induced acceptor states in $GaAs_{1-x}Bi_x$ alloy," *Phys. Rev. B*, vol. 83, no. 20, p. 201201, May 2011.

[49] A. Baldereschi and J. Hopfield, "Binding to isoelectronic impurities in semiconductors," *Phys. Rev. Lett.*, vol. 28, no. 1970, pp. 1970–1973, 1972.

[50] S. Francoeur, S. Tixier, E. Young, T. Tiedje, and A. Mascarenhas, "Bi isoelectronic impurities in GaAs," *Phys. Rev. B*, vol. 77, no. 8, p. 85209, Feb. 2008.

[51] E. H.C. Parker, "The technology and physics of molecular beam epitaxy," *Materials Science and Engineering,* p. 699, 1985.

[52] K. Martin, *Vacuum Physics and Technology*. Academic Press, 1980.

[53] D. T. Gerken and J. Calhoun, "Design Review of Cast Aluminum Scroll Compressor Components," *SAE 2000 World Congress,* Mar. 2000.

[54] M. Audi and M. de Simon, "Ion pumps," *Vacuum*, vol. 37, no. 8–9, pp. 629–636, Jan. 1987.

[55] A. Gupta and J. Leck, "An evaluation of the titanium sublimation pump," *Vacuum*, vol. 25, no. 8, 1975.

[56] A. Y. Cho, "Growth of extremely uniform layers by rotating substrate holder with molecular beam epitaxy for applications to electro-optic and microwave devices," *Appl. Phys. Lett.*, vol. 38, no. 5, p. 360, 1981.

[57] M. Knudsen, "Die Gesetze der Molekularströmung und der inneren Reibungsströmung der Gase durch Röhren," *Ann. Phys.*, vol. 333, no. 1, pp. 75–130, 1909.

[58] M. Knudsen, "Experimentelle Bestimmung des Druckes gesättigter Quecksilberdämpfe bei 0° und höheren Temperaturen," *Ann. Phys.*, vol. 334, no. 6, pp. 179–193, 1909.

[59] M. Knudsen, "Die Molekularströmung der Gase durch Offnungen und die Effusion," *Ann. Phys.*, vol. 333, no. 5, pp. 999–1016, 1909.

[60] M. Knudsen, "Eine Revision der Gleichgewichtsbedingung der Gase. Thermische Molekularströmung," *Ann. Phys.*, vol. 336, no. 1, pp. 205–229, 1909.

[61] O. Knacke and I. Stranski, "The mechanism of evaporation," *Prog. Met. Phys.*, no. 1, 1956.

[62] A. Ichimiya and P. I. Cohen, *Reflection High-Energy Electron Diffraction*. Cambridge: Cambridge University Press, 2004.

[63] J. Stroscio, D. Pierce, and R. Dragoset, "Homoepitaxial growth of iron and a real space view of reflection-high-energy-electron diffraction," *Phys. Rev. Lett.*, vol. 70, no. 23, pp. 3615–3618, Jun. 1993.

[64] P. L. Kapitza and P. A. M. Dirac, "The reflection of electrons from standing light waves," *Math. Proc. Cambridge Philos. Soc.*, vol. 29, no. 2, p. 297, Oct. 2008.

[65] P. P. Ewald, "Introduction to the dynamical theory of X-ray diffraction," *Acta Crystallogr. Sect. A Cryst. Physics, Diffraction, Theor. Gen. Crystallogr.*, vol. 25, no. 1, pp. 103–108, Jan. 1969.

[66] J. S. Blakemore, "Semiconducting and other major properties of gallium arsenide," *J. Appl. Phys.*, vol. 53, no. 10, p. R123, 1982.

[67] J. C. M. Hwang, "Growth of high-purity GaAs layers by molecular beam epitaxy," *Appl. Phys. Lett.*, vol. 42, no. 1, p. 66, 1983.

[68] M. Heiblum, E. E. Mendez, and L. Osterling, "Growth by molecular beam epitaxy and characterization of high purity GaAs and AlGaAs," *J. Appl. Phys.*, vol. 54, no. 12, p. 6982, 1983.

[69] E. C. Larkins, E. S. Hellman, D. G. Schlom, J. S. Harris, M. H. Kim, and G. E. Stillman, "Reduction of the acceptor impurity background in GaAs grown by molecular beam epitaxy," *Appl. Phys. Lett.*, vol. 49, no. 7, p. 391, 1986.

[70] N. Chand, "MBE growth of high-quality GaAs," *J. Cryst. Growth*, vol. 97, no. 2, pp. 415–429, Sep. 1989.

[71] A. Y. Cho, H. C. Casey, C. Radice, and P. W. Foy, "Influence of growth conditions on the threshold current density of double-heterostructure lasers prepared by molecular-beam epitaxy," *Electron. Lett.*, vol. 16, no. 2, p. 72, 1980.

[72] R. P. Vasquez, "X-ray photoelectron spectroscopic study of the oxide removal mechanism of GaAs (100) molecular beam epitaxial substrates in in situ heating," *Appl. Phys. Lett.*, vol. 42, no. 3, p. 293, 1983.

[73] A. Y. Cho and J. R. Arthur, "Molecular beam epitaxy," *Prog. Solid State Chem.*, vol. 10, pp. 157–191, Jan. 1975.

[74] C. Kittel and P. McEuen, *Introduction to solid state physics*. 1976.

[75] E. A. Wood, "Vocabulary of Surface Crystallography," *J. Appl. Phys.*, vol. 35, no. 4, p. 1306, 1964.

[76] M. C. Gallagher, R. H. Prince, and R. F. Willis, "On the atomic structure and electronic properties of decapped GaAs(001)(2×4) surfaces," *Surf. Sci.*, vol. 275, no. 1–2, pp. 31–40, Sep. 1992.

[77] K. Kanisawa and H. Yamaguchi, "Extremely long surface diffusion of Ga and critical nucleation on As-rich GaAs(001) surfaces caused by phase transitions," *Phys. Rev. B*, vol. 56, no. 19, pp. 12080–12083, Nov. 1997.

[78] G. Bell, J. Belk, C. McConville, and T. Jones, "Species intermixing and phase transitions on the reconstructed (001) surfaces of GaAs and InAs," *Phys. Rev. B*, vol. 59, no. 4, pp. 2947–2955, Jan. 1999.

[79] C. B. Duke, "Semiconductor Surface Reconstruction: The Structural Chemistry of Two-Dimensional Surface Compounds.," *Chem. Rev.*, vol. 96, no. 4, pp. 1237–1260, Jun. 1996.

[80] J. E. Northrup, "Structure of GaAs(001) surfaces: The role of electrostatic interactions," *Phys. Rev. B*, vol. 50, no. 3, pp. 2015–2018, Jul. 1994.

[81] A. Ohtake, "Surface reconstructions on GaAs(001)," *Surf. Sci. Rep.*, vol. 63, no. 7, pp. 295–327, Jul. 2008.

[82] L. Däweritz and R. Hey, "Reconstruction and defect structure of vicinal GaAs(001) and $Al_xGa_{1-x}As(001)$ surfaces during MBE growth," *Surf. Sci.*, vol. 236, no. 1–2, pp. 15–22, Oct. 1990.

[83] E. Hellman and J. Harris, "Infra-red transmission spectroscopy of GaAs during molecular beam epitaxy," *J. Cryst. Growth*, vol. 81, pp. 38–42, 1987.

[84] K. Regiński, J. Muszalski, V. V. Preobrazhenskii, and D. I. Lubyshev, "Static phase diagrams of reconstructions for MBE-grown GaAs(001) and AlAs(001) surfaces," *Thin Solid Films*, vol. 267, no. 1–2, pp. 54–57, Oct. 1995.

[85] A. Y. Cho, "Morphology of Epitaxial Growth of GaAs by a Molecular Beam Method: The Observation of Surface Structures," *J. Appl. Phys.*, vol. 41, no. 7, p. 2780, 1970.

[86] A. Y. Cho, "GaAs Epitaxy by a Molecular Beam Method: Observations of Surface Structure on the (001) Face," *J. Appl. Phys.*, vol. 42, no. 5, p. 2074, 1971.

[87] J. J. Harris, B. A. Joyce, and P. J. Dobson, "Oscillations in the surface structure of Sn-doped GaAs during growth by MBE," *Surf. Sci. Lett.*, vol. 103, no. 1, pp. L90–L96, Feb. 1981.

[88] C. E. C. Wood, "RED intensity oscillations during MBE of GaAs," *Surf. Sci.*, vol. 108, no. 2, pp. L441–L443, Jul. 1981.

[89] J. H. Neave, B. A. Joyce, P. J. Dobson, and N. Norton, "Dynamics of film growth of GaAs by MBE from Rheed observations," *Appl. Phys. A Solids Surfaces*, vol. 31, no. 1, pp. 1–8, May 1983.

[90] R. Fischer *et al.*, "Incorporation rates of gallium and aluminum on GaAs during molecular beam epitaxy at high substrate temperatures," *J. Appl. Phys.*, vol. 54, no. 5, p. 2508, 1983.

[91] C. Heyn and D. E. Jesson, "Congruent evaporation temperature of molecular beam epitaxy grown GaAs (001) determined by local droplet etching," *Appl. Phys. Lett.*, vol. 107, no. 16, p. 161601, Oct. 2015.

[92] J. R. Arthur, “Gallium Arsenide Surface Structure and Reaction Kinetics: Field Emission Microscopy,” *J. Appl. Phys.*, vol. 37, no. 8, p. 3057, 1966.

[93] J. H. Neave and B. A. Joyce, “Temperature range for growth of autoepitaxial GaAs films by MBE,” *J. Cryst. Growth*, vol. 43, no. 2, pp. 204–208, Mar. 1978.

[94] T. Murotani, T. Shimanoe, and S. Mitsui, “Growth temperature dependence in molecular beam epitaxy of gallium arsenide,” *J. Cryst. Growth*, vol. 45, pp. 302–308, Dec. 1978.

[95] J. R. Arthur, “Interaction of Ga and As_2 Molecular Beams with GaAs Surfaces,” *J. Appl. Phys.*, vol. 39, no. 8, p. 4032, 1968.

[96] C. T. Foxon and B. A. Joyce, “Interaction kinetics of As4 and Ga on {100} GaAs surfaces using a modulated molecular beam technique,” *Surf. Sci.*, vol. 50, no. 2, pp. 434–450, Jun. 1975.

[97] A. Y. Cho, “Bonding direction and surface-structure orientation on GaAs (001),” *J. Appl. Phys.*, vol. 47, no. 7, p. 2841, 1976.

[98] C. E. C. Wood and B. A. Joyce, “Tin-doping effects in GaAs films grown by molecular beam epitaxy,” *J. Appl. Phys.*, vol. 49, no. 9, p. 4854, 1978.

[99] D. K. Bowen and B. K. Tanner, *High Resolution X-Ray Diffractometry And Topography*. Taylor & Francis, 1998.

[100] R. D. Richards, “Molecular beam epitaxy growth and characterisation of GaAsBi for photovoltaic applications,” *University of Sheffield PhD Thesis*, September, p. 197, 2014.

[101] C. R. Wie, “High resolution X-ray diffraction characterization of semiconductor structures,” *Mater. Sci. Eng.*, vol. 13, pp. 1–56, 1994.

[102] D. B. Murphy, M. W. Davidson, “Differential Interference Contrast Microscopy and Modulation Contrast Microscopy,” in *Fundamentals of Light Microscopy and Electronic Imaging*, Hoboken, NJ, USA: John Wiley & Sons, Inc., 2012, pp. 173–197.

[103] T. Gfroerer, *Encyclopedia of Analytical Chemistry*. Chichester, UK: John Wiley & Sons, Ltd, 2006.

[104] S. M. Sze and K. K. Ng, *Physics of Semiconductor Devices*. Hoboken, NJ, USA: John Wiley & Sons, Inc., 2006.

[105] C. T. Dervos, P. D. Skafidas, J. A. Mergos, and P. Vassiliou, “p-n Junction Photocurrent Modelling Evaluation under Optical and Electrical Excitation,” *Sensors*, vol. 4, no. 5, pp. 58–70, Jul. 2004.

[106] S. J. Fonash, “General formulation of the current-voltage characteristic of a p-n heterojunction solar cell,” *J. Appl. Phys.*, vol. 51, no. 4, p. 2115, 1980.

[107] P. A. Wolff, “Theory of Electron Multiplication in Silicon and Germanium,” *Phys. Rev.*, vol. 95, no. 6, pp. 1415–1420, Sep. 1954.

[108] W. Shockley, "Problems related to p-n junctions in silicon," *Solid. State. Electron.*, vol. 2, no. 1, pp. 35–67, Jan. 1961.

[109] S. A. Plimmer, J. P. R. David, G. J. Rees, and P. N. Robson, "Ionization coefficients in $Al_xGa_{1-x}As$ (x=0-0.60)," *Semicond. Sci. Technol.*, vol. 15, no. 7, pp. 692–699, Jul. 2000.

[110] R. J. McIntyre, "Multiplication noise in uniform avalanche diodes," *IEEE Trans. Electron Devices*, vol. 13, no. 1, pp. 164–168, 1966.

[111] A. J. Ptak *et al.*, "Kinetically limited growth of GaAsBi by molecular-beam epitaxy," *J. Cryst. Growth*, vol. 338, no. 1, pp. 107–110, Jan. 2012.

[112] F. Bastiman, A. R. B. Mohmad, J. S. Ng, J. P. David, and S. J. Sweeney, "Non-stoichiometric GaAsBi/GaAs (100) molecular beam epitaxy growth," *J. Cryst. Growth*, vol. 338, no. 1, pp. 57–61, Jan. 2012.

[113] M. Henini *et al.*, "Molecular beam epitaxy of GaBiAs on (311)B GaAs substrates," *Appl. Phys. Lett.*, vol. 91, no. 25, p. 251909, 2007.

[114] E. C. Young, M. B. Whitwick, T. Tiedje, and D. A. Beaton, "Bismuth incorporation in $GaAs_{1-x}Bi_x$ grown by molecular beam epitaxy within-situ light scattering," *Phys. Status Solidi*, vol. 4, no. 5, pp. 1707–1710, Apr. 2007.

[115] A. R. Mohmad, F. Bastiman, C. J. Hunter, J. S. Ng, S. J. Sweeney, and J. P. R. David, "The effect of Bi composition to the optical quality of $GaAs_{1-x}Bi_x$," *Appl. Phys. Lett.*, vol. 99, no. 4, p. 42107, 2011.

[116] P. Laukkanen *et al.*, "Anomalous Bismuth-Stabilized (2×1) Reconstructions on GaAs(100) and InP(100) Surfaces," *Phys. Rev. Lett.*, vol. 100, no. 8, p. 86101, Feb. 2008.

[117] F. Bastiman, A. G. Cullis, J. P. R. David, and S. J. Sweeney, "Bi incorporation in GaAs(100)-2×1 and 4×3 reconstructions investigated by RHEED and STM," *J. Cryst. Growth*, vol. 341, no. 1, pp. 19–23, Feb. 2012.

[118] X. Lu, D. A. Beaton, R. B. Lewis, T. Tiedje, and M. B. Whitwick, "Effect of molecular beam epitaxy growth conditions on the Bi content of $GaAs_{1-x}Bi_x$," *Appl. Phys. Lett.*, vol. 92, no. 19, p. 192110, 2008.

[119] R. B. Lewis, M. Masnadi-Shirazi, and T. Tiedje, "Growth of high Bi concentration $GaAs_{1-x}Bi_x$ by molecular beam epitaxy," *Appl. Phys. Lett.*, vol. 101, no. 8, p. 82112, 2012.

[120] A. G. Norman, R. France, and A. J. Ptak, "Atomic ordering and phase separation in MBE $GaAs_{1-x}Bi_x$," *J. Vac. Sci. Technol. B Microelectron. Nanom. Struct.*, vol. 29, no. 3, p. 03C121, 2011.

[121] R. D. Richards *et al.*, "Molecular beam epitaxy growth of GaAsBi using As2 and As4," *J. Cryst. Growth*, vol. 390, pp. 120–124, Mar. 2014.

[122] J. W. Matthews and A. Blakeslee, "Defects in epitaxial multilayers," *J. Cryst. Growth*, vol. 27, pp. 118–125, Dec. 1974.

[123] A. S. Kyuregyan and S. N. Yurkov, “Room-temperature avalanche breakdown voltages of p-n junctions made of Si, Ge, SiC, GaAs, GaP, and InP,” *Sov. Phys. Semicond.*, vol. 10, no. 23, pp. 1126–1132, 1989.

[124] H. I. Ralph, “On the theory of the Franz-Keldysh effect,” *J. Phys. C Solid State Phys.*, vol. 1, no. 2, pp. 378–386, Apr. 1968.

[125] J. Tauc, Ed., *Amorphous and Liquid Semiconductors*. Boston, MA: Springer US, 1974.

[126] F. Urbach, “The Long-Wavelength Edge of Photographic Sensitivity and of the Electronic Absorption of Solids,” *Phys. Rev.*, vol. 92, no. 5, pp. 1324–1324, Dec. 1953.

[127] S. R. Johnson and T. Tiedje, “Temperature dependence of the Urbach edge in GaAs,” *J. Appl. Phys.*, vol. 78, no. 9, p. 5609, 1995.

[128] M. V. Kurik, “Urbach rule,” *Phys. Status Solidi*, vol. 8, no. 1, pp. 9–45, Nov. 1971.

[129] H. C. Casey, “Variation of minority-carrier diffusion length with carrier concentration in GaAs liquid-phase epitaxial layers,” *J. Appl. Phys.*, vol. 44, no. 3, p. 1281, 1973.

[130] D. E. Aspnes, “Recombination at semiconductor surfaces and interfaces,” *Surf. Sci.*, vol. 132, no. 1–3, pp. 406–421, Sep. 1983.

[131] J. Požela and A. Reklaitis, “Electron transport properties in GaAs at high electric fields,” *Solid. State. Electron.*, vol. 23, no. 9, pp. 927–933, Sep. 1980.

[132] B. Bouzazi, H. Suzuki, N. Kojima, Y. Ohshita, and M. Yamaguchi, “Relationship between a nitrogen-related hole trap and ionized acceptors density in p-type GaAsN grown by chemical beam epitaxy,” *Phys. Status Solidi*, vol. 8, no. 2, pp. 616–618, Feb. 2011.

[133] A. V. Drigo *et al.*, “On the mechanisms of strain release in molecular-beam-epitaxy-grown $In_xGa_{1-x}As$/GaAs single heterostructures,” *J. Appl. Phys.*, vol. 66, no. 5, pp. 1975–1983, 1989.

[134] D. Madouri, A. Boukra, A. Zaoui, and M. Ferhat, “Bismuth alloying in GaAs: a first-principles study,” *Comput. Mater. Sci.*, vol. 43, no. 4, pp. 818–822, Oct. 2008.

[135] H. Achour, S. Louhibi, B. Amrani, a. Tebboune, and N. Sekkal, “Structural and electronic properties of GaAsBi,” *Superlattices Microstruct.*, vol. 44, no. 2, pp. 223–229, Aug. 2008.

[136] R. People and J. C. Bean, “Calculation of critical layer thickness versus lattice mismatch for Ge_xSi_{1-x}/Si strained-layer heterostructures,” *Appl. Phys. Lett.*, vol. 47, no. 3, pp. 322–324, 1985.

[137] E. A. Fitzgerald, “Dislocations in strained-layer epitaxy: theory, experiment, and applications,” *Mater. Sci. Reports*, vol. 7, no. 3, pp. 87–140, 1991.

[138] A. Fischer, H. Kühne, and H. Richter, “New Approach in Equilibrium Theory for Strained Layer Relaxation,” *Phys. Rev. Lett.*, vol. 73, no. 20, pp. 2712–2715, Nov. 1994.

[139] F. Huang, “Comment on ‘New Approach in Equilibrium Theory for Strained Layer Relaxation,’” *Phys. Rev. Lett.*, vol. 85, no. 20, pp. 4411–4411, Nov. 2000.

[140] C. H. Belgacem and M. Fnaiech, "Exact Analytical Solution for the Critical Layer Thickness of a Lattice-Mismatched Heteroepitaxial Layer," *Journal of Electronic Materials*, vol. 39, no. 10, pp. 2248–2250, 2010.

[141] S. Tan, "Optoelectronic Characterisation of III-V Antimonide and Nitride Alloys Grown on GaAs," *University of Sheffield PhD Thesis*, 2012.

[142] H. Fan, "Temperature Dependence of the Energy Gap in Monatomic Semiconductors," *Phys. Rev.*, vol. 78, no. 6, pp. 808–809, Jun. 1950.

[143] T. Muto and S. Oyama, "Theory of the Temperature Effect of Electronic Energy Bands in Crystals," *Prog. Theor. Phys.*, vol. 5, no. 5, pp. 833–843, Sep. 1950.

[144] Y. P. Varshni, "Temperature dependence of the energy gap in semiconductors," *Physica*, vol. 34, no. 1, pp. 149–154, Jan. 1967.

[145] K. P. O'Donnell and X. Chen, "Temperature dependence of semiconductor band gaps," *Appl. Phys. Lett.*, vol. 58, no. 25, p. 2924, 1991.

[146] P. G. Eliseev, P. Perlin, J. Lee, and M. Osiński, "'Blue' temperature-induced shift and band-tail emission in InGaN-based light sources," *Appl. Phys. Lett.*, vol. 71, no. 5, p. 569, 1997.

[147] Q. Li *et al.*, "Thermal redistribution of localized excitons and its effect on the luminescence band in InGaN ternary alloys," *Appl. Phys. Lett.*, vol. 79, no. 12, p. 1810, 2001.

[148] Q. Li, S. J. Xu, M. H. Xie, and S. Y. Tong, "A model for steady-state luminescence of localized-state ensemble," *Europhys. Lett.*, vol. 71, no. 6, pp. 994–1000, Sep. 2005.

[149] C. Hunter, "Growth and characterization of bulk $GaAs_{1-x}Bi_x$/GaAs diodes," *University of Sheffield PhD Thesis*, January, 2014.

[150] Z. Y. Xu *et al.*, "Thermal activation and thermal transfer of localized excitons in InAs self-organized quantum dots," *Superlattices Microstruct.*, vol. 23, no. 2, pp. 381–387, Feb. 1998.

[151] T. Prutskij, C. Pelosi, and G. Attolini, "Temperature quenching of photoluminescence of ordered GaInP2 alloy under different excitation densities," *Cryst. Res. Technol.*, vol. 46, no. 2, pp. 127–134, 2011.

[152] Y. I. Mazur *et al.*, "Effects of spatial confinement and layer disorder in photoluminescence of $GaAs_{1-x}Bi_x$/GaAs heterostructures," *J. Phys. D. Appl. Phys.*, vol. 46, no. 6, p. 65306, Feb. 2013.

[153] S. Mazzucato *et al.*, "Low-temperature photoluminescence study of exciton recombination in bulk GaAsBi.," *Nanoscale Res. Lett.*, vol. 9, no. 1, p. 19, Jan. 2014.

[154] D. Fan *et al.*, "MBE grown GaAsBi/GaAs double quantum well separate confinement heterostructures," *J. Vac. Sci. Technol. B, Nanotechnol. Microelectron. Mater. Process. Meas. Phenom.*, vol. 31, no. 3, p. 03C105, May 2013.

[155] A. R. Mohmad, F. Bastiman, J. S. Ng, S. J. Sweeney, and J. P. R. David, "Photoluminescence investigation of high quality $GaAs_{1-x}Bi_x$ on GaAs," *Appl. Phys. Lett.*, vol. 98, no. 12, p. 122107, 2011.

[156] G. Ciatto, E. Young, F. Glas, J. Chen, R. Mori, and T. Tiedje, "Spatial correlation between Bi atoms in dilute $GaAs_{1-x}Bi_x$: From random distribution to Bi pairing and clustering," *Phys. Rev. B*, vol. 78, no. 3, p. 35325, Jul. 2008.

[157] G. Ciatto, M. Thomasset, F. Glas, X. Lu, and T. Tiedje, "Formation and vanishing of short range ordering in $GaAs_{1-x}$Bix thin films," *Phys. Rev. B*, vol. 82, no. 20, p. 201304, Nov. 2010.

[158] S. Imhof *et al.*, "Clustering effects in Ga(AsBi)," *Appl. Phys. Lett.*, vol. 96, no. 13, p. 131115, Mar. 2010.

[159] A. R. Adams, "Band-structure engineering to control impact ionisation and related high-field processes," *Electron. Lett.*, vol. 40, no. 17, p. 1086, 2004.

[160] A. Rogalski, "Infrared detectors: Status and trends," *Prog. Quantum Electron.*, vol. 27, no. 2–3, pp. 59–210, 2003.

[161] C. Verie, F. Raymond, J. Besson, and T. Nguyen Duy, "Bandgap spin-orbit splitting resonance effects in $Hg_{1-x}Cd_xTe$ alloys," *J. Cryst. Growth*, vol. 59, no. 1–2, pp. 342–346, Sep. 1982.

[162] G. Leveque, M. Nasser, and D. Bertho, "Ionization energies in CdxHg1-xTe avalanche photodiodes," *Semicond. Sci. Technol.*, vol. 8, no. 7, pp. 1317–1323, 1993.

[163] J. Beck *et al.*, "The HgCdTe electron avalanche photodiode," *J. Electron. Mater.*, vol. 35, no. 6, pp. 1166–1173, 2006.

[164] O. Hildebrand, W. Kuebart, and M. H. Pilkuhn, "Resonant enhancement of impact in $Ga_{1-x}Al_xSb$," *Appl. Phys. Lett.*, vol. 37, no. 9, pp. 801–803, Nov. 1980.

[165] A. R. J. Marshall, C. H. Tan, M. J. Steer, and J. P. R. David, "Electron dominated impact ionization and avalanche gain characteristics in InAs photodiodes," *Appl. Phys. Lett.*, vol. 93, no. 11, pp. 13–16, 2008.

[166] A. R. J. Marshall, J. P. R. David, and C. H. Tan, "Impact ionization in InAs electron avalanche photodiodes," *IEEE Trans. Electron Devices*, vol. 57, no. 10, pp. 2631–2638, 2010.

[167] S. L. Tan *et al.*, "Experimental evaluation of impact ionization in dilute nitride GaInNAs diodes," *Appl. Phys. Lett.*, vol. 103, no. 10, p. 102101, 2013.

[168] M. A. Saleh *et al.*, "Impact-ionization and noise characteristics of thin III-V avalanche photodiodes," *IEEE Trans. Electron Devices*, vol. 48, no. 12, pp. 2722–2731, 2001.

[169] S. A. Plimmer, J. P. R. David, and D. S. Ong, "The merits and limitations of local impact lonization theory," *IEEE Trans. Electron Devices*, vol. 47, no. 5, pp. 1080–1088, 2000.

[170] G. E. Stillman and C. M. Wolfe, "Avalanche Photodiodes,", *Semiconductors and Semimetals*, Vol. 12, 1977, pp. 291–393.

[171] C. Sah, R. Noyce, and W. Shockley, "Carrier Generation and Recombination in P-N Junctions and P-N Junction Characteristics," *Proc. IRE*, vol. 45, no. 9, pp. 1228–1243, Sep. 1957.

[172] R. K. Ahrenkiel, "Minority Carriers In III-V Semiconductors: Physics and Applications," *Semicond. Semimetals*, vol. 39, pp. 39–150, 1993.

Publications

Journals

1. **Z. Zhou**, D. F. Mendes R. D. Richards, F. Bastiman, J. P. R. David. Absorption Properties of GaAsBi Based p-i-n Heterojunction Diodes. Semiconductor Science and Technology, 30: 094004, 2015.
2. T. B. O. Rockett, R. D. Richards, Y. Gu, F. Harun, Y. Liu, Z. Zhou, J. P. R. David. Influence of growth conditions on the structural and opto-electronic quality of GaAsBi. Journal of Crystal Growth, in press, 2017
3. **Z. Zhou**, R. D. Richards, Y. Liu, T. B. O. Rockett, F. Harun, J. P. R. David. The investigation of photo-multiplication in GaAsBi diodes. (in preparation)

Conferences

4. **Z. Zhou**, D. F. Mendes, R. D. Richards, F. Bastiman, J. P. R. David. Poster presentation: The opto-electronic characteristics of GaAs/GaAsBi/GaAs p-i-n diodes. The 5th International Workshop on Bismuth-Containing Semiconductors, Cork, Ireland, 21-23/7/2014.
5. R. D. Richards, **Z. Zhou**, D. F. Mendes, F. Bastiman, J. P. R. David. Oral presentation: Characterisation of bulk GaAsBi p-i-n diodes. UK Semiconductors, Sheffield, England, 9-10/7/2014.
6. F. Harun, T. B. O. Rockett, A. R. Mohmad, R. D. Richards, **Z. Zhou**, F. Bastiman, J. P. R. David. Poster presentation: Polarised photoluminescence study of GaAsBi grown by molecular beam epitaxy. UK Semiconductors, Sheffield, England, 1-2/7/2015.
7. **Z. Zhou**, R. D. Richards, T. B. O. Rockett, F. Bastiman, J. P. R. David. Poster presentation: Investigation of bismuth incorporation into GaAs based on growth conditions. UK Semiconductors, Sheffield, England, 1-2/7/2015.
8. R. D. Richards, C. J. Hunter, F. Bastiman, **Z. Zhou**, F. Harun, T. B. O. Rockett, J. P. R. David. Oral presentation: GaAsBi LEDs emitting at 1,200nm. UK Semiconductors, Sheffield, England, 1-2/7/2015.
9. **Z. Zhou**, R. D. Richards. Oral presentation: Investigation of the Mechanism of Bismuth Incorporation into GaAs, 6th International Workshop on Bismuth Containing Semiconductors, Madison, Wisconsin, USA, 19-22/7/2015
10. T. B. O. Rockett, R. D. Richards, F. Harun, Y. Gu, **Z. Zhou**, J. P. R. David. Poster presentation: Optimizing the Opto - Electronic Properties of GaAsBi by Tuning Growth Conditions. 19th International Conference on Molecular Beam Epitaxy, 4-9/9/2016

11. **Z. Zhou**, R. D. Richards, Y. Gu, T. B. O. Rockett, F. Harun, Y. Liu, J. S. Cheong, A. Baharuddin, J. P. R. David. Poster presentation: Investigation of Photo-multiplication in GaAsBi Diodes. 7th International Workshop on Bismuth Containing Semiconductors, Shanghai, China, 24-27/7/2016
12. T. B. O. Rockett, R. D. Richards, F. Harun, Y. Gu, **Z. Zhou**, J. P. R. David. Poster presentation: Optimising the Structural and Optical Quality of GaAsBi. UK Semiconductors, Sheffield, UK, 6-7/7/2016